

**Lateral Variability of Sedimentology, Mineralogy and  
Geochemistry in the HYC Zn-Pb-Ag deposit, Northern Territory,  
Australia; *implications for ore genesis.***

A thesis presented as partial fulfilment of the degree of  
Bachelor of Science with Honours.

**Tim Ireland (B.Sc.)**



UNIVERSITY OF TASMANIA  
SCHOOL OF EARTH SCIENCES

and



November, 2001

## I Abstract

An understanding of the lateral variability of sedimentology, mineralogy and geochemistry at HYC has the potential to contribute to improved ore genesis models, and to facilitate better mine planning and grade control at the McArthur River Mine. HYC is the largest of the north-Australian Proterozoic sediment hosted stratiform base metal deposits (>230 mT @ >12%Zn), and is hosted by the reduced sub-wave base marine carbonate-siliclastic Barney Creek Formation.

Macroscopic planar sulphide laminae consist of variable intergrowths of two distinct sphalerite and pyrite phases, galena, arsenopyrite, quartz, ankerite and dolomite, and disguise significant microscopic textural complexity. Sphalerite 1 (sp1) and pyrite 1 (py1) are paragenetically early, fine grained and volumetrically dominant in the deposit, whereas sphalerite 2 (sp2) occurs as late stage, relatively coarse grained replacement of carbonates, and pyrite 2 (py2) is coarse grained, volumetrically minor, and is the last sulphide phase to form. The deposit fringe is characterised by systematic changes of microscopic sp1 texture with concomitant stratigraphic thinning and declining base metal grade that is unrelated to the distribution of iron. Characteristic anastomosing microscopic textures are explained by pelagic fallout of pyrite crystallites from the water column (py1) with simultaneous seafloor precipitation of basemetal sulphides (sp1).

Sheet-like mass flow deposits that separate ore lenses and dilute ore at HYC exhibit rapid lateral transition from erosive boulder-bearing debris flows to non-erosive normally-graded turbidites. Turbidites formed by elutriation of fines into a turbid flow that followed and outran the primary debris flows. Plastically deformed sulphidic intraclasts and sulphidic matrices of these breccias are texturally and isotopically identical to *in-situ* laminated sulphide ore, and constrain mineralisation to the upper few metres of the unconsolidated marine sediments.

Nodular carbonates occur on all preserved fringes of the deposit, and are the direct lateral equivalent of the mineralised stratigraphy. The S/C ratio of unmineralised siltstone reveals primary differences in shallow diagenetic processes between the nodular and laminar sulphide ore facies. Bacterially triggered carbonate precipitation probably took place at shallow depth during base-metal mineralisation, and resulted in Fe-Mn-calcite nodule formation in a zone concentric about the local depocentre. Dolomitisation and partial replacement by sphalerite (sp2) occurred shortly after nodule formation, as modified ore fluids permeated the sediment pile. The  $\delta^{13}\text{C}$  of these carbonates is

consistent with that of detrital carbonates in the host unit, which indicates that oxidised organic carbon (a major product of inorganic sulphate reduction) was not incorporated into the nodular carbonates.

The  $\delta^{34}\text{S}$  values of sp1 and py1 are heavier in the deposit centre (5-8‰) than in the deposit fringe (0 to -2‰). This suggests a gradient of  $^{34}\text{S}$  fractionation concentric around the focus of mineralisation, interpreted to be largely due to bacterial processes that were limited spatially by physicochemical gradients in a stratified water body. Fine grained pyrite textures closely resemble contemporaneous microfossils and microbially laminated pyritic sediments elsewhere, and confirm the presence of a prolific benthic microbial fauna spatially related to the mineralising system. Sp2 defines a  $\delta^{34}\text{S}$  population (mean = 9.3‰) that is distinct from, and always heavier than coexistent sp1, interpreted to arise from partial closed-system sulphate reduction in the sediment pile.

The textural, geochemical and sedimentological data demonstrate that the stratiform HYC Zn-Pb-Ag deposit at McArthur River is a vent-distal sedimentary exhalative deposit, in which the contemporaneous benthic microbial fauna played an important role in mineralisation. The HYC sub-basin was probably not significantly more extensive than the deposit, and restriction of the water body, including 'plugging' of the northern end by a fanglomerate wedge, were crucial to establishment of a stratified aqueous environment amenable to extreme concentration of metals. Metalliferous fluids were introduced into the basin via hydrothermal pluses from a structural conduit related to the Emu Fault.

## **II Acknowledgements**

Supervision for this project has been at all times tolerant, supportive and intelligent, and my already high regard for my supervisors Ross Large and Stuart Bull has risen through the course of the year. Particularly invaluable were Ross' contribution to on site trouble shooting at McArthur River and last-minute reviewing, and Stu's permanent aire of relaxation. I would also thank other University of Tasmania staff: Peter McGoldrick for discussions of microbial processes; Mike Blake and June Pongratz for their tireless logistical support; Andrews Rae, Wurst and Stewart, Darryl Clark, Neil Martin, and Alan Wilson for comedic and constructive discussions. Staff of the University's Central Science Laboratory have lent their valuable time and expertise toward analyses performed during this research; Dr. Graham Rowbottom, Dr. Dave Steele, and Mr Keith Harris. Adam Duritz, Shakira, and Valhalla kept me entertained and fed through the less gripping moments.

This project would also have not have eventuated without the support of several staff at the McArthur River Mine. I thank most sincerely Damien Nihill, Steve Pevely, and Matt Furness, for taking time out of their hectic working lives to entertain my academic whims even if the answers might not make the mine run any more smoothly. One day I'll shout you each that carton Harry keeps talking about. Special thanks also to Ian Irlam and Ron Dean for logistical support and interesting conversation, and to Toby for shifting miles of core I never actually looked at.

To Pam Allen and Bruno Cayoun I give enormous thanks, for helping me keep up the pretence of worthwhile linguistic study through the course of the year. I also extend my gratitude to my friends Narelle, Celeste, Tyrone, Steve, Siobhan, Jane and Bron, for happily enduring my company despite all my selfish antics this year (at least you gave that impression, anyway). With your support, I managed.

### **III Contents**

I. Abstract.....	i
II. Acknowledgements.....	iii
III. Contents.....	iv
IV. List of Figures.....	vi
1. INTRODUCTION.....	1
1.1. Regional Geology.....	5
1.2. Local Geology .....	8
2. SEDIMENTOLOGY OF THE INTER-ORE BRECCIAS.....	13
2.1 Introduction.....	13
2.2 Methods.....	13
2.3 Mass Flow Lithofacies.....	17
2.4 Flow Geometry and Spatial Relationships.....	24
2.5 Sediment Gravity Flow Processes.....	33
2.6 Sedimentological Model for the HYC Inter-Ore Mass Flow Facies.....	36
3. SULPHIDE TEXTURES.....	48
3.1 Background.....	48
3.2 Methods.....	50
3.3 Sulphide Textures.....	50
3.4 Sulphide Spatial Distribution.....	67
3.5 Mechanisms for Sulphide Genesis.....	70
4. NODULAR CARBONATES.....	70
4.1 Introduction.....	70
4.2 Methods and Sampling.....	72
4.3 Composition and Mineralogy.....	74
4.4 Distribution.....	81
4.5 S-C-Fe Relationships.....	84

---

4.6 Discussion.....	92
4.7 Summary.....	97
5. SULPHUR ISOTOPES OF THE #3 AND #4 ORE LENSES.....	100
5.1 Introduction.....	100
5.2 Methods and Sampling.....	102
5.3 Results.....	106
5.4 Sulphur Geochemistry and Marine Chemical Environments.....	110
5.5 Discussion.....	113
5.6 Conclusion.....	119
6. CONCLUSIONS.....	121
6.1 Constraints for Mineralisation and Conclusion.....	121
6.2 Implications for Exploration and Further Work.....	123
7. REFERENCES.....	125
Appendices .....	138

## IV List of Figures

### 1. INTRODUCTION

Figure 1.1	Location maps.....	2
Figure 1.2	Tectonic and metallogenic maps.....	4
Figure 1.3	Tectonostratigraphic summary diagram. ....	6
Figure 1.4	Stratigraphy of the southern McArthur Basin.....	7
Figure 1.5	Local geology map of the HYC area.....	9
Figure 1.6	E-W section through the HYC deposit and environs.....	10
Figure 1.7	Graphic logs of HYC mine stratigraphy and host sequence.....	11

### 2. SEDIMENTOLOGY OF INTERORE BRECCIAS

Figure 2.1	N-S drillhole-correlated section through the Barney Creek .....	14
Figure 2.2	Cumulate isopach map of interore and hangingwall breccias at HYC .....	14
Figure 2.3	Tables of breccia characteristics. ....	15
Figure 2.4	Location map of drillholes used in this study. ....	16
Figure 2.5	Photographs of mass flow breccias. ....	19
Figure 2.6	Photographs of breccia clasts and matrices. ....	21
Figure 2.7	Photographs of distal mass flow facies. ....	23
Figure 2.8	Correlated graphic logs of the 8 major mass flow units.....	25-7
Figure 2.9	Contoured images of mass flow deposit geometry and scour depth. ....	28
Figure 2.10	Isopach maps of the major interore mass flow units.....	30
Figure 2.11	Stratigraphic section of #3 lens and I3/4, and isopach map of tubidite silty tops.....	32
Figure 2.12	Diagrams of mass flow transformation processes. ....	35
Figure 2.13	Maximum particle size / bed thickness calculation for three mass flow units. ....	39
Figure 2.14	Seafloor slope calculations for three interore mass flow units. ....	39
Figure 2.15	Summary diagrams of spatial and stratigraphic relationships of the major sedimentary facies at HYC. ....	40

### 3. SULPHIDE TEXTURES

Figure 3.1	Plan view of metallogenic zonation at HYC, and $fO_2$ -pH diagram for the probable ore fluid composition. ....	43
Figure 3.2	Photographs of laminated sulphide ore and component sulphide phases. ....	45
Figure 3.3	Microphotographs of pyrite 1. ....	48
Figure 3.4	Microphotographs of py1 macroframboids and visually similar microfossils. ....	49
Figure 3.5	Microphotographs of sphalerite 1 textures. ....	51
Figure 3.6	Microphotographs of sphalerite 1 textural relationships. ....	52
Figure 3.7	Microphotographs of sphalerite 1 mineralogical relationships. ....	53
Figure 3.8	Microphotographs of mineralised and unmineralised siltstones. ....	54
Figure 3.9	Microphotographs of sphalerite 2. ....	56
Figure 3.10	Microphotographs of pyrite 2. ....	57
Figure 3.11	Microphotographs of sphaleritic siltstone fragments in various clastic facies. ....	60
Figure 3.12	Plan view contoured maps of sulphide abundance and textural distribution. ....	63
Figure 3.13	Wholerock geochemical data presented as plan view interpolated surfaces, bivariant plots, and net mass changes plots. ....	65
Figure 3.14	Diagram of important elements of the proposed SEDEX mechanism. ....	67

### 4. NODULAR CARBONATES

Figure 4.1	Photograph of nodular carbonate-type mineralised siltstone, and introductory C-O isotope plots. ....	71
Figure 4.2	Microphotographs of nodular carbonates. ....	73
Figure 4.3	Carbonate compositional tables. ....	76
Figure 4.4	Plot of lateral variation of Fe and Mn substitution into nodular carbonates. ....	77
Figure 4.5	Bivariate plots of cation ratios and bulk substitution in nodular carbonates. ....	77
Figure 4.6	Images of compositionally zoned calcite nodules, and plot of variation of elemental composition within a single crystal. ....	78
Figure 4.7	C-O isotope and isotope ratio-substitution plots for nodular carbonates. ....	80
Figure 4.8	Plan view contoured plots of nodular carbonate distribution. ....	82
Figure 4.9	Stratigraphic correlation of nodular carbonates across the southern fringe of the #3 ore lens. ....	83

---

Figure 4.10	Type example S-C-DOP-Fe plots used to explain diagenetic processes in anoxic basins.....	86
Figure 4.11	Microphotographs of unmineralised siltstones used for S/C analyses. ....	86
Figure 4.12	Bivariate S-C-Fe plots from this study and for the McArthur Basin. ....	88
Figure 4.13	$fO_2$ -pH diagrams for ore system fluid conditions.....	94
Figure 4.14	C-O isotope plot of modeled trends for varying water-rock ratio and temperature ....	96
Figure 4.15	Schematic diagrams of a hydrothermally-fed stratified water body.....	96
Figure 4.16	Interpreted map of nodular carbonate, sphalerite 1 and pyrite 1 distribution.....	98

## 5. SULPHUR ISOTOPES

Figure 5.1	Sulphur isotope data from previous studies at HYC.....	101
Figure 5.2	Table of interpretations of HYC sulphur isotope data.....	101
Figure 5.3	Microphotographs of laser ablation targets for sulphur isotope analysis.....	103
Figure 5.4	Table of calculated precision for sulphur isotope analyses.....	103
Figure 5.5	Stratigraphic correlation diagram used for sulphur isotope sampling.....	105
Figure 5.6	Histograms of bulk sulphur isotope data .....	107
Figure 5.7	Plans and sections showing lateral variability of sulphur isotope data.....	109
Figure 5.8	Statistical calculations for sp1 and sp2 populations. ....	112
Figure 5.9	Summary diagram of the the physicochemistry of stratified water bodies.....	112
Figure 5.10	Schematic diagram of processes relevant to the marine and diagenetic sulphur cycle during mineralisation at HYC. ....	117
Figure 5.11	Compilation of bulk sulphur isotope data from HYC. ....	119

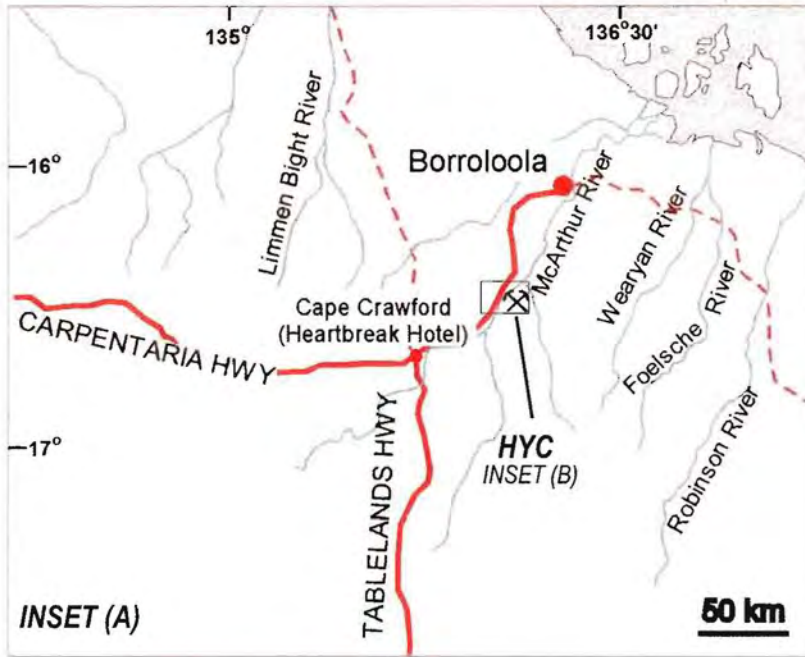
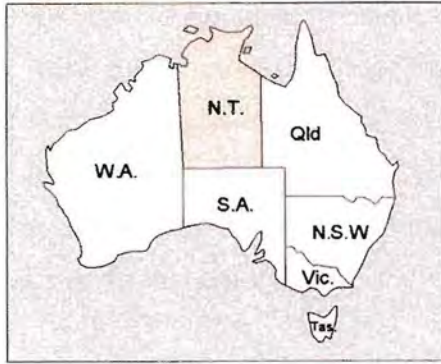
# 1 INTRODUCTION

The HYC Ag-Pb-Zn deposit is located approximately 50 km southwest of Borroloola, Northern Territory (fig 1.1). It is the largest known member of the 'stratiform sediment-hosted' class of deposits (227 million metric tons 9.2% Zn, 4.1% Pb, and 41g/t Ag), which collectively represent more than 50% of world lead and zinc resources (Goodfellow *et al.* 1993). Currently, McArthur River Mining (MRM) are working the richest two of eight ore lenses, and calculate underground mining reserves of 22.9 million tonnes of 13.6% zinc, 6.3 % lead, and 65 g/t silver (D. Nihill, pers. comm. 2001).

Previous research into north Australian stratiform sediment-hosted base metal deposits has been focussed in the zones of greatest metal enrichment or regionally in the McArthur Basin. This approach has defined empirical exploration criteria for SHS deposits, but has led to debate about the deposit genesis. In either the sedimentary or diagenetic scenarios proposed (Large *et al.* 1998; Hinman, 1996, respectively), spatial variation toward the deposit fringes are likely to show distinctive characteristics, as sulphide depositional processes diminish in intensity and grade into the ambient sedimentary system. The broad aim of this study is to describe lateral geological variability within the HYC deposit, and to integrate the findings with current knowledge and ideas on ore formation processes. MRM may also benefit from better understanding of the ore dilution, ore mineralogy changes, and breccia sedimentology investigated in this study.

Lateral variations are described in detail, for sedimentology and sulphide occurrence in sedimentary breccias, microscopic sulphide textures, the distribution and chemistry of nodular carbonates, and sulphide isotope ratios of sphalerite and pyrite. These parameters were selected because of their potential to constrain theories on mineralisation processes and timing, and to aid the mining operation. Twenty three diamond drillholes were studied that span the economic mineralisation, and relevant underground exposures were also mapped to complement the drillhole data. Sedimentological investigations were made across the entire mineralised stratigraphy, whereas the #3 ore lens is the focus of sulphide textural and geochemical studies because it occurs in the largest number of recent drillholes.

*Figure 1.1 – Maps and aerial photo showing location and situation of the McArthur River Mine. The mine is located in the subtropical climatic zone of northern Australia, and experiences a hot dry season and a hot wet season that peaks in February. The area supports subtropical open forest and grassland, and riverine forest in the immediate floodplains of the McArthur River.*



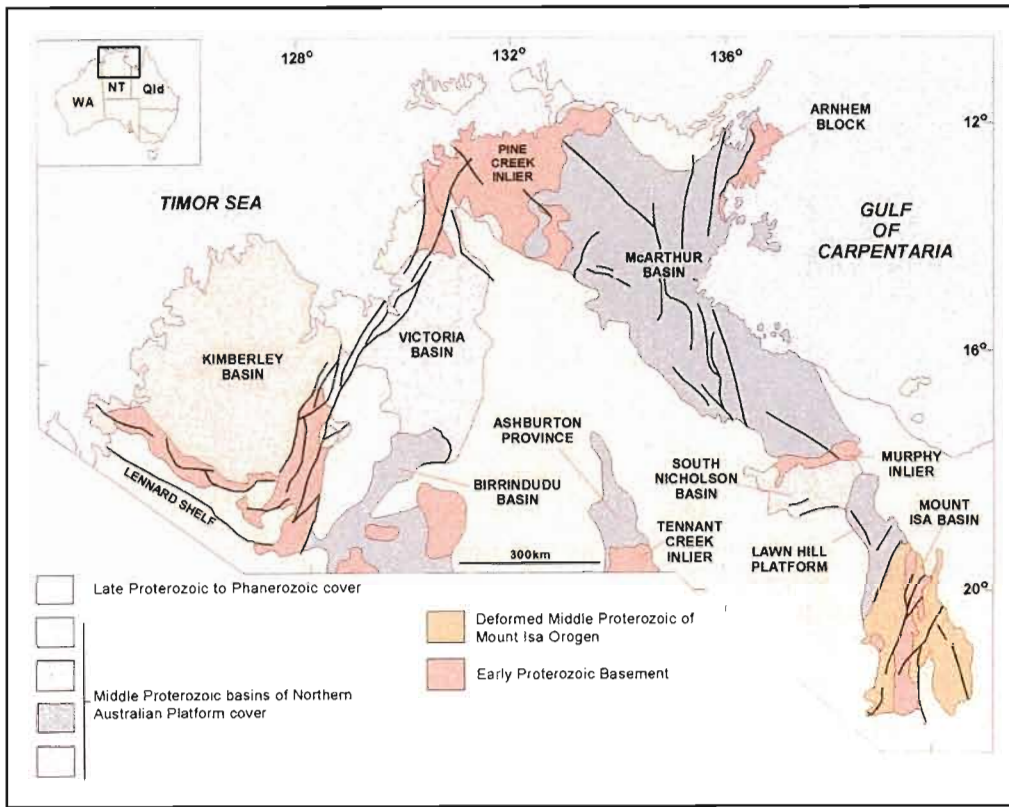
Inter-ore breccias are an important part of the HYC sedimentary system, and an important control on grade dilution in the mine. Previous work (Walker 1977, Logan 1990) has documented gross geometric trends and described breccia clast lithologies, but has stopped short of determining individual flow geometry and formative processes. The nodular carbonate ore texture has been mentioned by many workers (e.g. Rye and Williams, 1981; Perkins and Bell, 1998; Large *et al.* 1998; Logan *et al.* 2001) but has not been studied rigorously. This is warranted since it represents both an integral part of the ore system and another important control of grade dilution in the mine. Sulphide sulphur isotope ratios have been the subject of protracted discussion (Smith & Croxford, 1973; Rye & Williams, 1981; Eldridge *et al.* 1993) but it is hoped that consideration of lateral variations will aid progress toward a conclusive interpretation. Hypotheses on the formation of HYC have swung in popularity between sedimentary exhalative (Croxford and Jephcott, 1972; Large *et al.* 1998), variations on the theme of syn-diagenetic replacement (Williams, 1978; Hinman, 1996; Logan *et al.* 2001), and post-diagenetic replacement (Perkins and Bell, 1998). Ultimately, this is a descriptive study that is specifically aimed at filling holes in our understanding of ore genesis at HYC.

### 1.1 **Regional Geology**

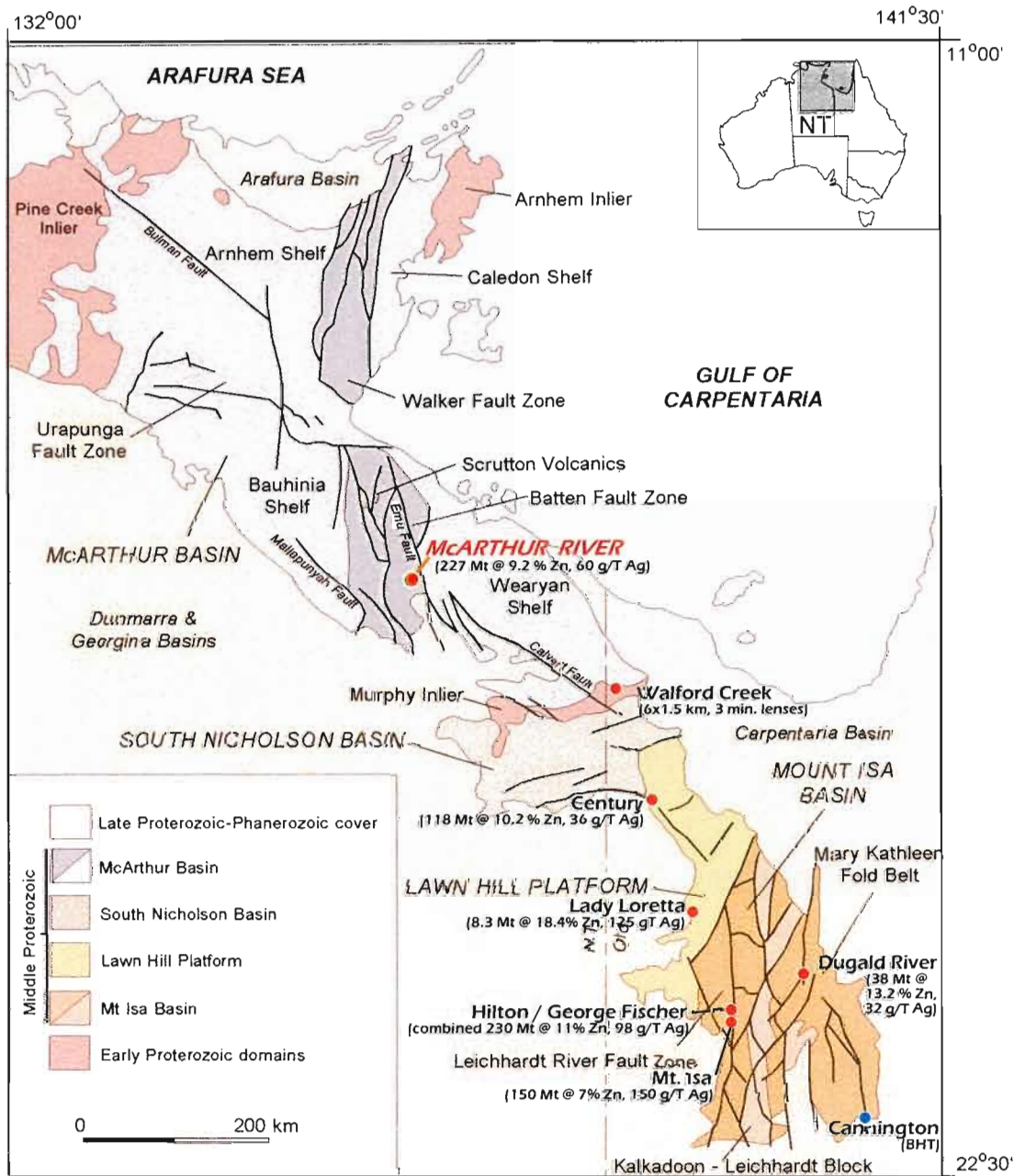
The Palaeo- to Mesoproterozoic McArthur Basin is the western subdivision of a 180 000 km<sup>2</sup>, multiphase, north Australian intracratonic superbasin system (fig.1.2a) that was active through the 375 million years from 1815 to 1450 Ma (Rawlings, 1999; Jackson *et al.* 2000). An 80-100 km-wide north-south-trending relatively moderate-strain corridor, the Walker and Batten Fault Zones, transects the basin and accommodates greater thickness of sediment than elsewhere (Plumb & Wellman, 1987; fig.1.2b). The McArthur Basin comprises a mixed siliclastic and platformal carbonate succession with minor volcanic lithologies toward the base (but see Leaman, 1998). It is bound by older Palaeoproterozoic rocks of the Pine Creek Inlier in the northwest, by the Arnhem Inlier in the north, and by the Murphy Inlier in the southeast. Subsurface extent of the McArthur Basin is poorly constrained, but it probably continues offshore to the northeast and may also extend beneath outcropping Neoproterozoic and Phanerozoic rocks in the southwest (Pietsch *et al.* 1991). Beyond the Murphy Inlier lie the other important basin terranes of the Carpentaria Zinc Belt (fig.1.2). At least seven other stratiform base metal deposits similar in style to HYC are hosted in these central and eastern Proterozoic marine terranes (McGoldrick & Large 1998). U-Pb isotope

*Figure 1.2 - (a) Major tectonic elements of northern Australia showing the extent of exposed Proterozoic rocks. (b) Tectonic map of the 'Carpentaria Zinc Belt' showing major structures of the McArthur Basin, the Batten Fault Zone, and details of large base metal deposits of the province (compiled from McGoldrick and Large, 1998; Winefield, 1999).*

(A)



(B)



dating of zircons from volcanic and volcanogenic rocks constrain the absolute age host rocks to mineralisation at HYC at  $1640 \pm 3$  Ma (Carr *et al* 1996). Throughout the Carpentaria Zinc Belt, stratiform base-metal mineralisation occurs entirely within a 65 million year window between 1660 and 1595 Ma. (McGoldrick & Large 1998).

### 1.1.1 Tectonic Evolution of the McArthur Basin

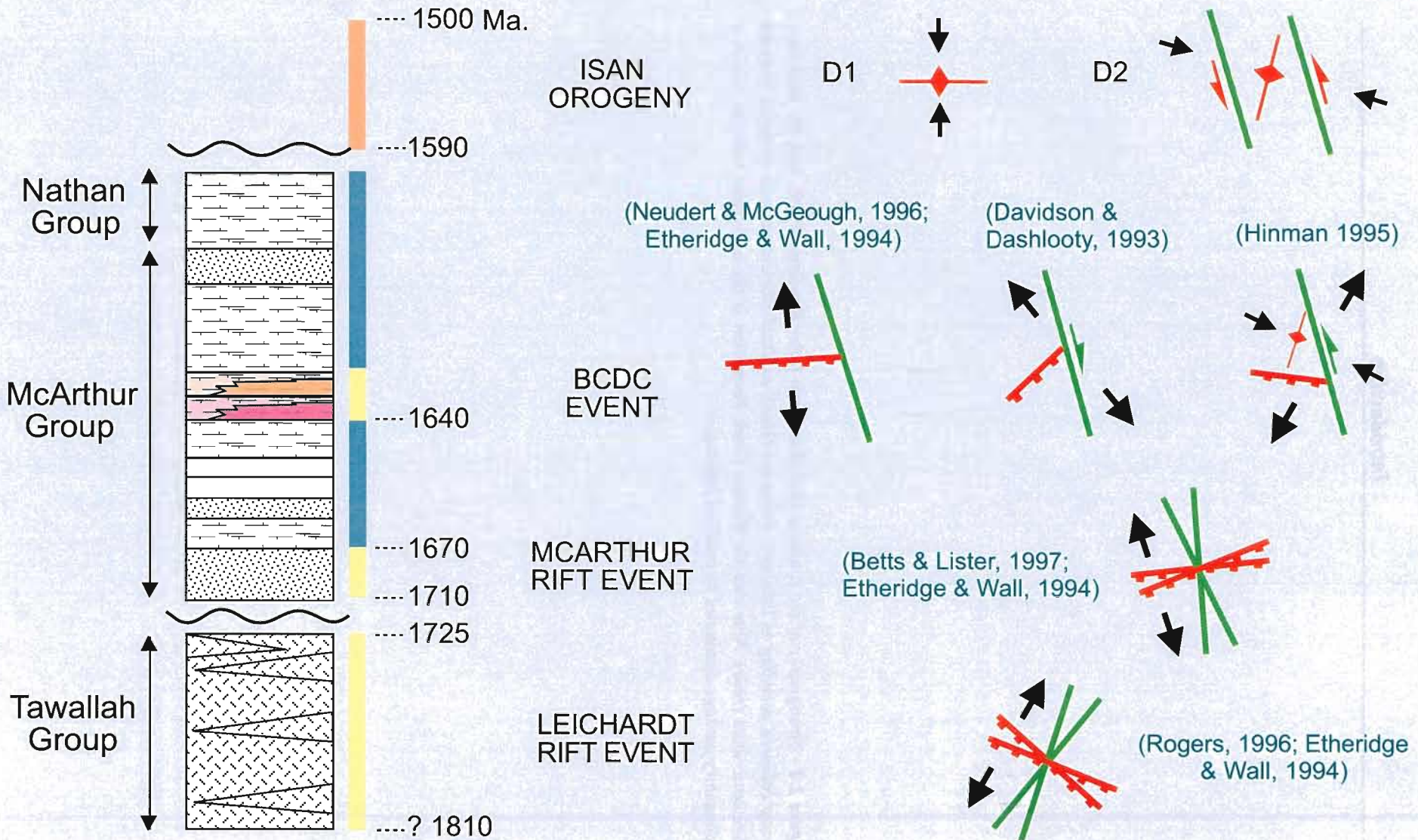
The tectonic evolution of the McArthur Basin was dominated by a deep seated N-S framework Barramundi-age structures that disguise dominantly north-northwest- to north-northeast-directed extension (Selley, 1998). The McArthur Basin has never undergone complete inversion, but the tectonic history has been difficult to determine because of repeated structural reactivation (fig.1.3; Etheridge and Wall, 1994; Hinman, 1995; Bull and Rogers, 1996). Several important structures in basin evolution, such as the Tawallah and Emu Faults, are anastomosing zones that consist of series of smaller structures in two or more orientations, and are sinuous at regional scale. Strike-slip motion along these major sinuous structures during McArthur Group time led to local transtensional sub-basin development at releasing bends, and local transpressional uplift at restraining bends in the Batten Fault Zone (Selley, 1998).

### 1.1.2 McArthur Basin Stratigraphy

The most complete sedimentary record in the McArthur Basin occurs in the Batten Fault Zone, in which up to 10 km of stratigraphic section are preserved in contrast to less than 4 kilometres on the adjacent 'shelves' (Plumb & Wellman, 1987; fig.1.4). Shallow- to marginal marine and fluvial sandstone and dolostone dominate the McArthur Basin stratigraphy. The Tawallah Group is laterally extensive and is not influenced by the Batten Fault Zone, and is mostly oxidised siliclastic lithologies and mafic volcanic rocks that are interpreted to have been deposited in terrestrial and shallow marine settings. Outcrop of the McArthur Group is restricted to the Batten Fault Zone, where it varies in thickness (up to 4.5 kilometres) between several sub-basins within this zone. It comprises cyclical stromatolitic and evaporitic dolostone with subordinate fine siliciclastics. These represent mostly shallow-emergent, but also sub-wave base marine environments. HYC is hosted toward the middle of the McArthur Group within the dolomitic siltstone-dominated Barney Creek Formation, which records the deepest-water sedimentation anywhere in the McArthur Basin (Bull,

*Figure 1.3 - Schematic summary of the tectonic evolution of the McArthur Basin showing the geometry of rift phases during McArthur Group time. Repeated transgression in the Barney Creek Formation, referred to as the Barney Creek Depositional Cycle (BCDC) is related to localised differential rifting and subsidence along sinuous major structures (Selley, 1998).*

# McArthur Basin Tectonostratigraphy



rift phase

thermal sag phase

basin inversion

deep water facies

*Figure 1.4 - Stratigraphy of the southern McArthur Basin (after Rawlings, 1999), with the McArthur Group coloured according to lithology; dolomites (blue), oxidised siliciclastic units (yellow), reduced siliciclastic units (reds). Note that the Barney Creek Formation is the lowermost reduced unit in a sedimentary package dominated by oxidised lithologies.*



1998). The Nathan and Roper Groups comprise quartz sandstone and dolomite deposited in marginal marine and peritidal shelf environments of a stable epicratonic platform. Both groups are laterally extensive across the southern McArthur Basin and mark the cessation of depocentral conditions along the Batten-Walker Fault Zone (descriptions from Murray, 1975; Jackson *et al.* 1987; Logan *et al.* 1990; Kruse *et al.* 1994; Rawlings, 1999).

## 1.2 **Local Geology**

HYC occurs in the middle McArthur Group, within and adjacent to the eastern margin of the southern Batten Fault Zone. Stratiform base-metal mineralisation has been recognised in several sub-basins in a linear array extending west from HYC across the Batten Fault Zone (fig.1.5), but only the HYC sub-basin contains economic resources (Walker *et al.* 1977). The HYC sub-basin is a fault-controlled, north-south oriented, synclinal structure, adjacent to, and approximately one kilometre from, the Emu Fault (fig.1.6). The western margin of the sub-basin is truncated at surface, and the eastern margin is complexly faulted against the discordant transpressive Cooley Dolomite breccia. The northern and southern margins are preserved; and the mineralised sequence interfingers with thickened sedimentary breccias and dolomitic siltstones, respectively (Perkins and Bell, 1998; Logan *et al.* 2001).

HYC is hosted by the HYC Pyritic Shale Member of the Barney Creek Formation, which is the lowermost significant reduced unit in the McArthur Basin. Carbonate geochemistry and sedimentology record a transgressive-regressive cycle from shallow marine/emergent conditions (Teena Dolomite and W-Fold Shale), to sub-wave base conditions during Barney Creek time, and return to shallow conditions afterwards (Reward Dolomite; Winefield, 1999; Pietsch *et al.* 1991), referred to as the Barney Creek Depositional Cycle (BCDC; Bull, 1998). Basin tectonism, rather than eustatic change, is regarded as the primary control over the Barney Creek Depositional Cycle (Bull, 1998). Massive to graded, thin to thick, sedimentary mass flow breccias are abundantly interspersed with mineralisation at HYC (fig.1.7; Walker *et al.* 1977), and are seen as evidence for rapid fault-controlled subsidence of sub-basins within the Batten Fault Zone.

*Figure 1.5 - Local geology of the Batten Fault Zone near HYC (after Winefield, 1999). Sub-basin outlines and axes are shown; the three depressions extending west from HYC all contain sub-economic basemetal mineralisation.*

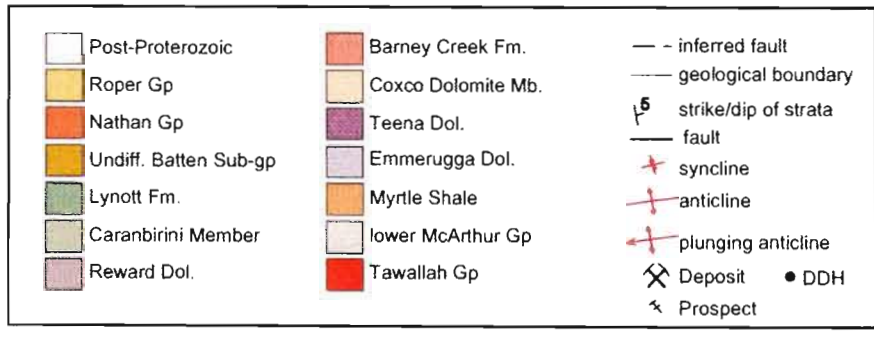
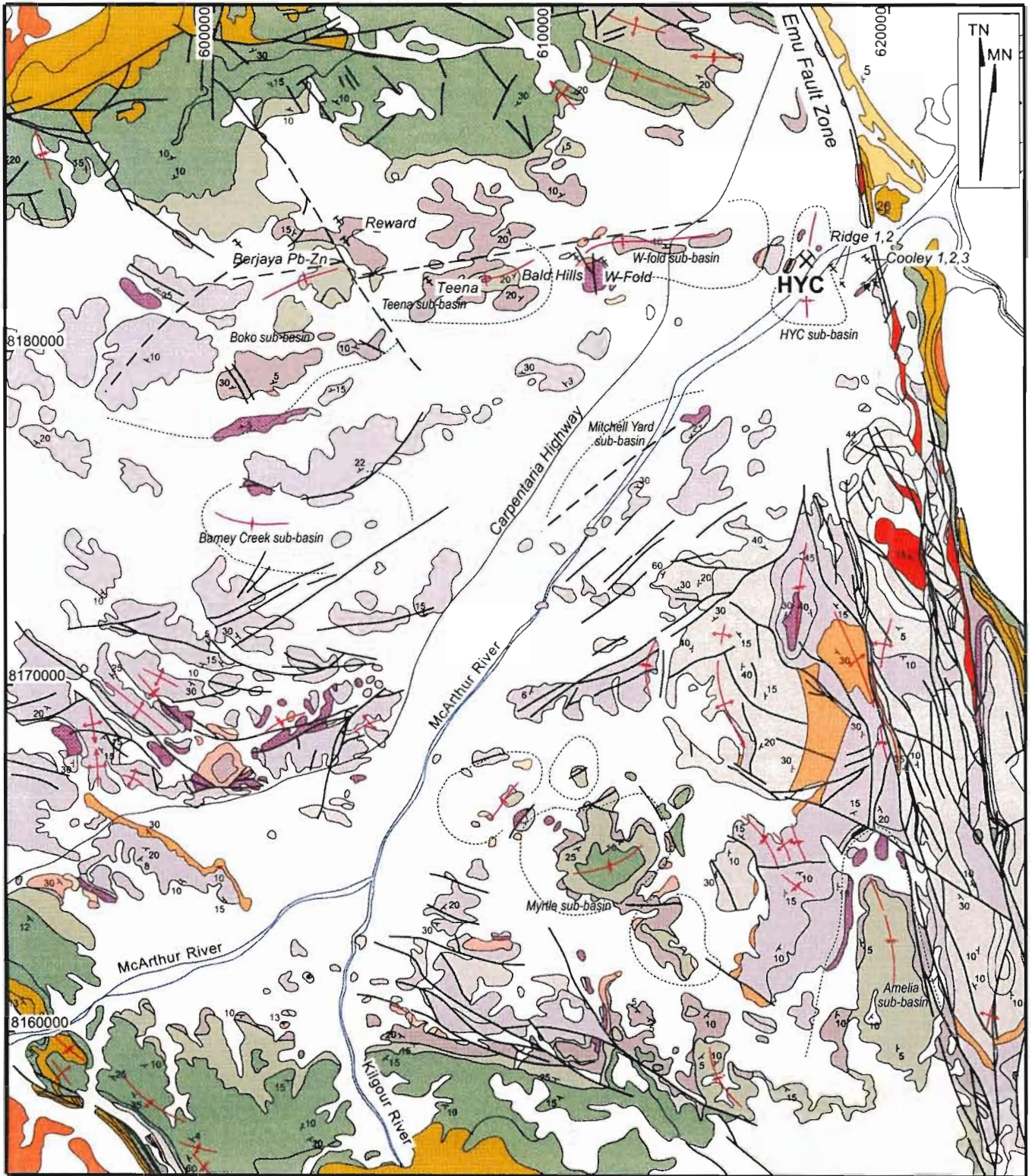
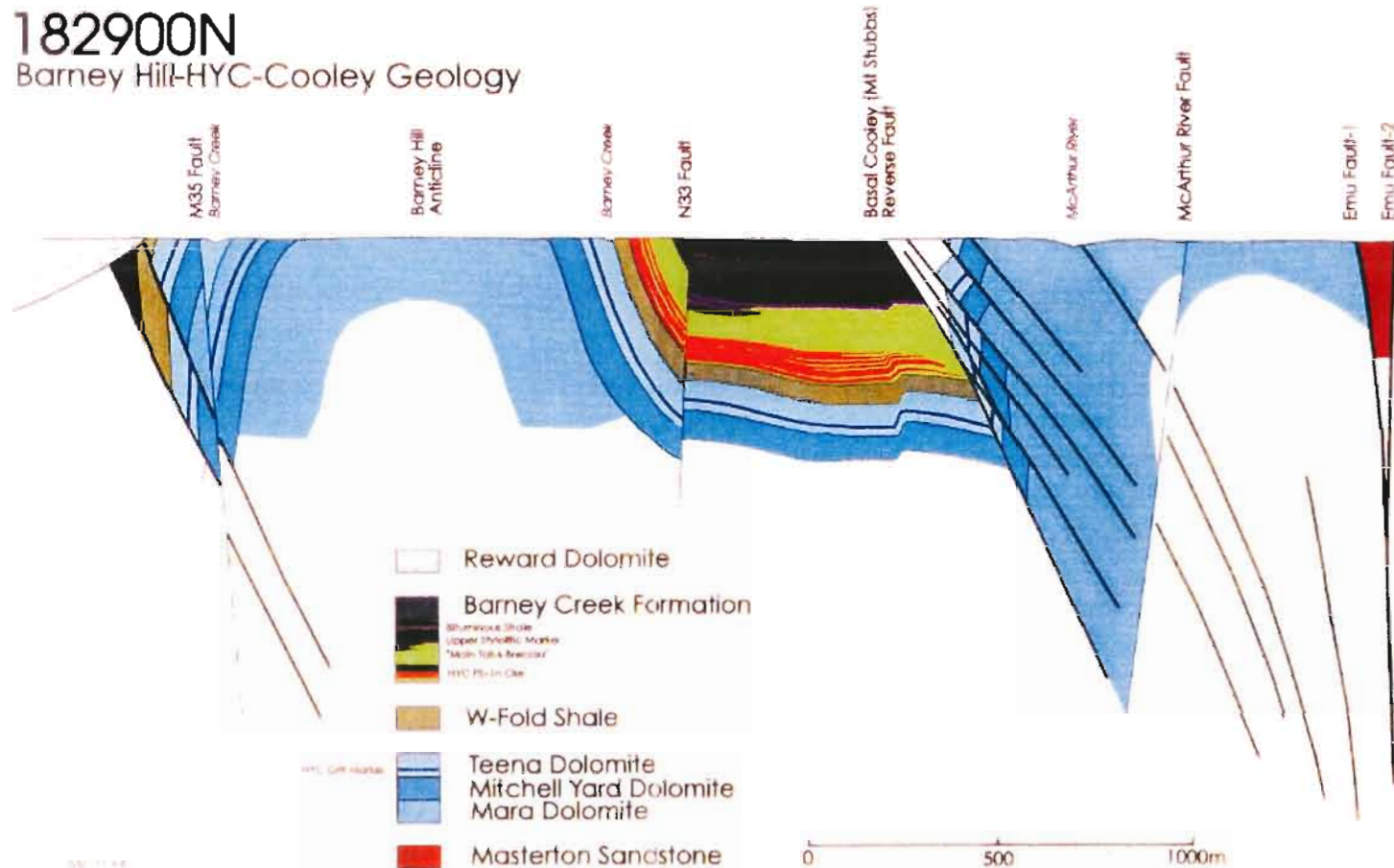


*Figure 1.6 - E-W section through the HYC deposit and environs, showing broad fault-controlled synclinal geometry of the HYC sub-basin, transpressive geometry of the Cooley Breccia, and 'step' folded eastern extension of the deposit (after Hinman, 1994).*

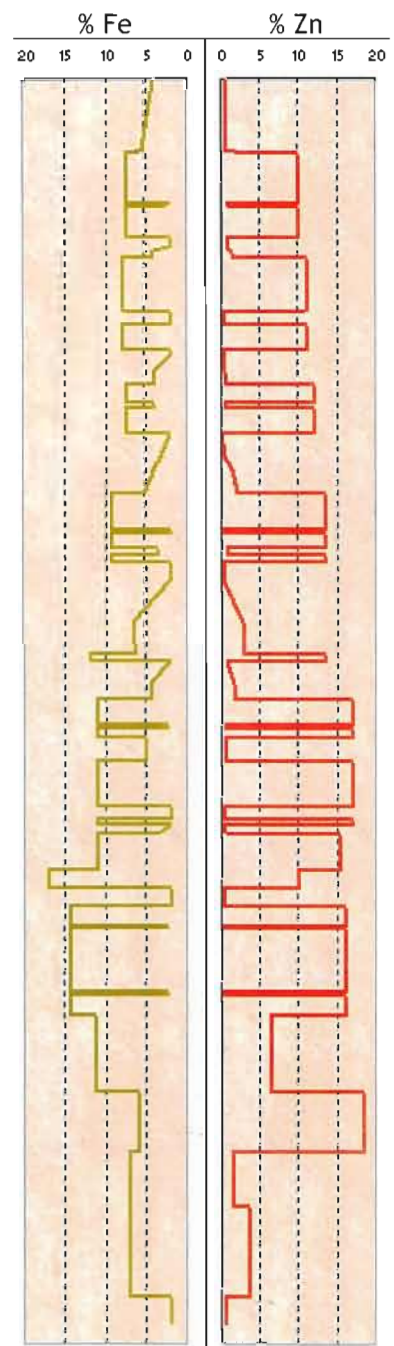
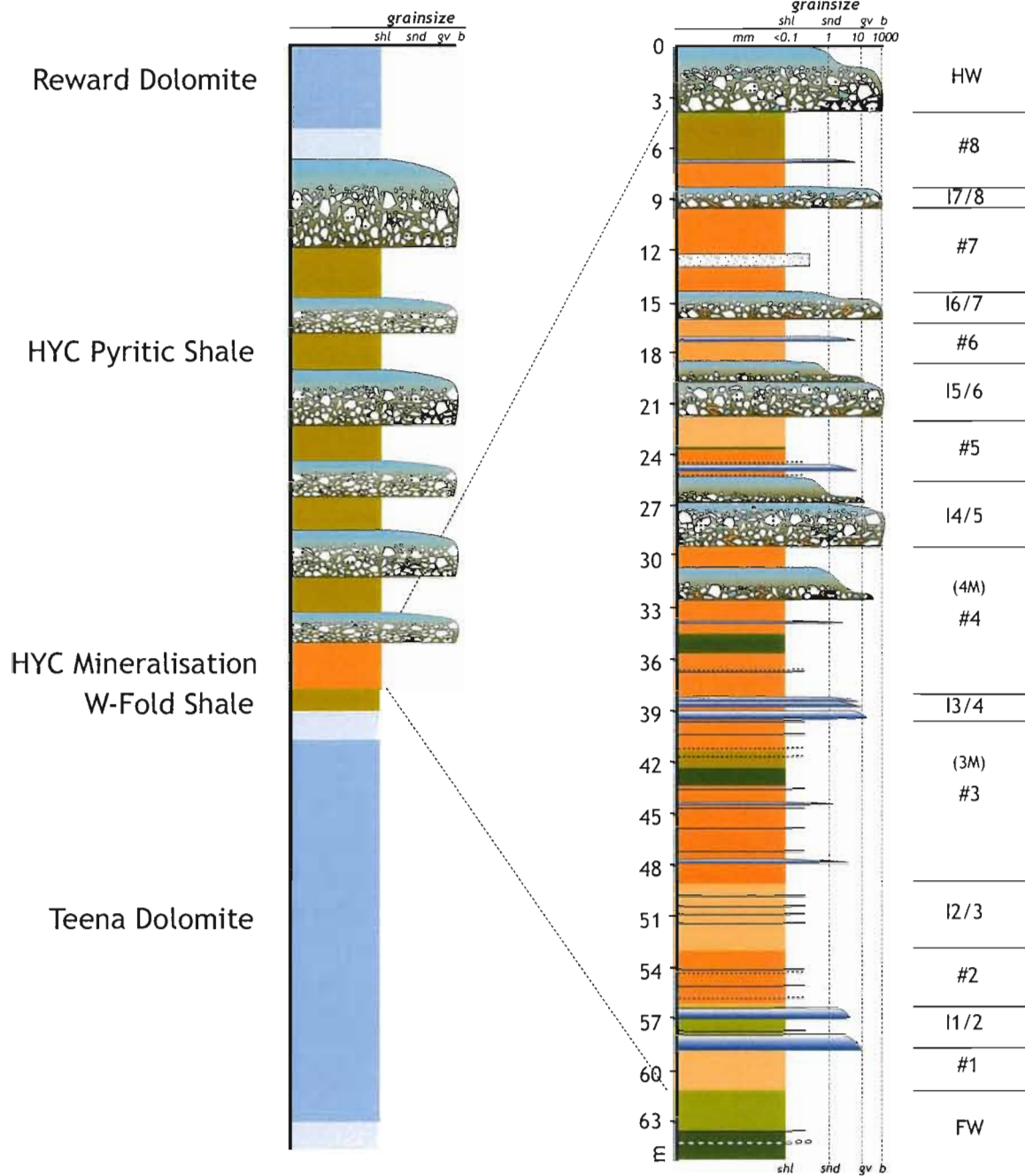
# 182900N

## Barney Hill-HYC-Cooley Geology



182900N

*Figure 1.7 - Graphic representation of the ~60m mineralised interval at HYC showing the mine stratigraphic nomenclature, average metal grades, the location and characteristics of the mass flow units (drawn for the northern central part of the mine), and the position of the orebody in the local stratigraphy. Mass flow sedimentation persisted throughout Barney Creek Time until cessation of rapid subsidence along the Batten Fault Zone, marked by deposition of the Reward Dolomite.*



- Black chert: pod-like and discontinuous.
- Tuffaceous clay (dashed line if too thin for scale).
- Diagenetic carbonate concretions 2-10cm.
- Pervasive nodular carbonate.
- Nodular carbonate-dominated laminated siltstone.
- Incipient nodular carbonate development in mineralised shale.
- Laminated py-sp-gn mineralised carbonaceous siltstone-shale.
- Laminated massive pyrite-dominated shale.
- Laminated pyritic carbonaceous siltstone.
- Massive dolomitic siltstone.
- Laminated to massive, graded fine dolarenite.
- Massive-graded medium-coarse dolarenite.
- Chaotic, polymict, dolomite matrix, dolomite-dominated breccia
- Chaotic, polymict, dark (variably sulphidic) matrix, dolomite-laminated sulphide breccia. Clasts drawn are faithful to stratigraphic thickness scale, and approximate real shapes and framework organisation.

Primary geochemical halos of anomalous Zn, Pb, Tl and Fe and  $^{18}\text{O}$ -enriched, and  $^{13}\text{C}$ -depleted carbonate surround the HYC deposit and extend laterally along the 'favourable horizon' for at least 15 kilometres to the southwest (Large *et al.* 2000, 2001). Anomalous manganese-enrichment in carbonates defines a separate halo that is stratigraphically offset below the deposit in the underlying W-Fold shale. This is the broadest geochemical signature related to mineralisation and is traceable for at least 23 kilometres southwest of the deposit (Large *et al.* 2000). Alkali metasomatism is also recognised in the HYC area, including adularia-ankerite alteration associated with mineralisation (Davidson, 1998) and regional potassium metasomatism and transition-metal depletion in the Tawallah Group near HYC (Cooke *et al.* 1998).

Total organic carbon (TOC) in the Barney Creek Formation ranges up to 2% and shows greater maturity (vitrinite reflectance, Rock Eval pyrolysis) within the mineralised zone than can be explained by a simple burial-related maturation gradient (Crick, 1992). Likewise, kerogen from HYC has unusual hydrocarbon molecular distribution, analagous to that produced during inorganic oxidation of organic matter (Logan *et al.* 2001). Filamentous and spheroidal microfossils occur in black cherts and sulphide aggregates in the deposit (Oehler & Logan, 1977; Logan *et al.* 2001) and also in 'lamalginites' elsewhere in the McArthur Basin (Crick 1992). Biomarkers indicative of cyanobacteria, archaeobacteria and lesser algae occur throughout the Barney Creek Formation, and combined biomarker and carbon isotope evidence suggests the presence of sulphur oxidising eubacteria in the HYC sub-basin (Logan *et al.* 2001). There are other unusual biomarker compounds of unknown (but probably of organic origin) common to both the HYC and Mt Isa Pb-Zn ore environments, but which occur exclusively in unmineralised laminae, and suggest further complexity of bacterial marine ecosystems during Barney Creek time (Logan *et al.* 2001).

## **2 SEDIMENTOLOGY OF THE INTER-ORE BRECCIAS**

### **2.1 Introduction**

The ore lenses at HYC are separated by thick sedimentary breccia beds that thin and fine toward the south and west. Hinman (2001) has shown that to the north of HYC the breccias amalgamate and thicken, and that the breccias/turbidites within the HYC deposit occupy a position toward the foot of a larger fan of sediment gravity flow deposits (fig.2.1). It has generally been accepted that individual flows grade laterally from proximal boulder-bearing clast-supported breccias into gravelly and sandy turbidites in the distal basinal environment (Logan, 1979; Perkins and Bell, 1998). Logan (1979) described the deposits as 'chaotic slump' and 'debris' flows 'followed by a graded bed', and showed that there is directional variability between provenance in the north and northeast within the 'inter-ore' breccias.

Breccia clasts represent the range of lithologies recognised in older McArthur Group stratigraphy, as well as intraclasts of mineralised siltstone, nodular dolomite-mineralised siltstone, and black cherts from the Barney Creek Formation itself (Logan 1979, fig.2.3). Walker (1977) described a loose reverse McArthur Group stratigraphy within breccia clasts and concluded that the breccias had formed in response to activity on basin-bounding faults. He also separated the HYC breccias into three types based on provenance and clast type (fig.2.2): type 1 breccias have northeastern provenance and contain characteristic turquoise dolomitic shale clasts, type 2 breccias have southeastern provenance and include clasts of distinctive Coxco Dolomite Member, and type 3 breccias (which only occur in the hangingwall to HYC) have northeastern provenance and contain siliciclastic clasts of the Masterson Sandstone. This work considers only breccias of type 1 classification because they impinge most heavily on base metal mineralisation.

### **2.2 Methods**

Breccia architecture and composition has been studied here in 23 drillholes across the HYC deposit (fig.2.4). Graphic stratigraphic logs were drawn of these drillholes and selected intervals are represented to demonstrate aspects of the type 1 'interore' breccias. Because the mining operation at

*Figure 2.1 - N-S drillhole-correlated section through the Barney Creek Formation and the HYC deposit, extending several hundred metres north of the limit of economic mineralisation. The south-thinning wedge geometry of coarse clastic deposits is apparent (from Hinman, 2001).*

*Figure 2.2 - Cumulate isopach map of type 1 (interore) and type 2 (hangingwall) breccias at HYC. The NE and SE provenances are clear, but grouping individual flows conceals any variation within each group (from Walker, 1977).*

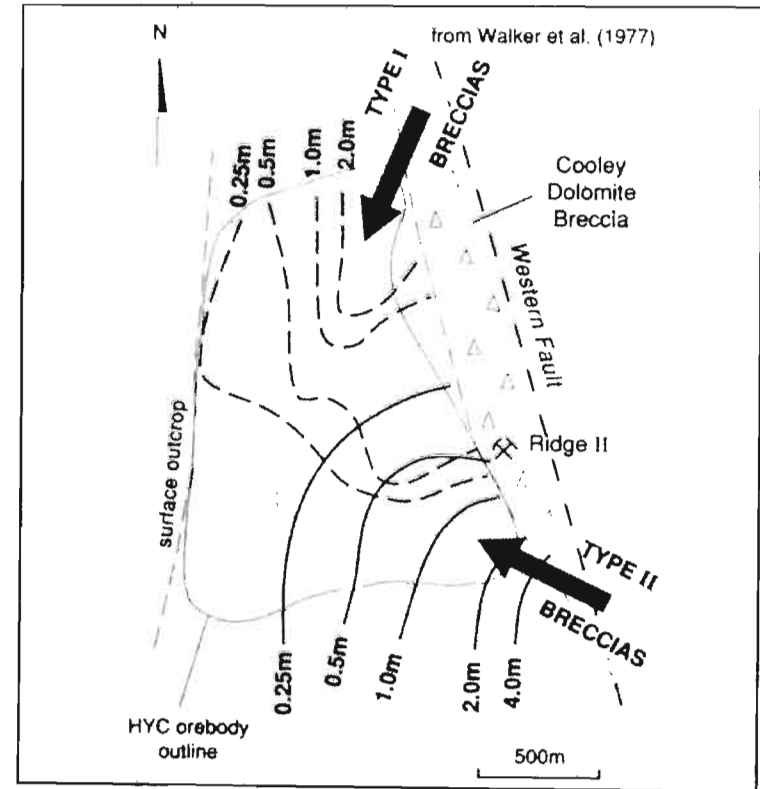
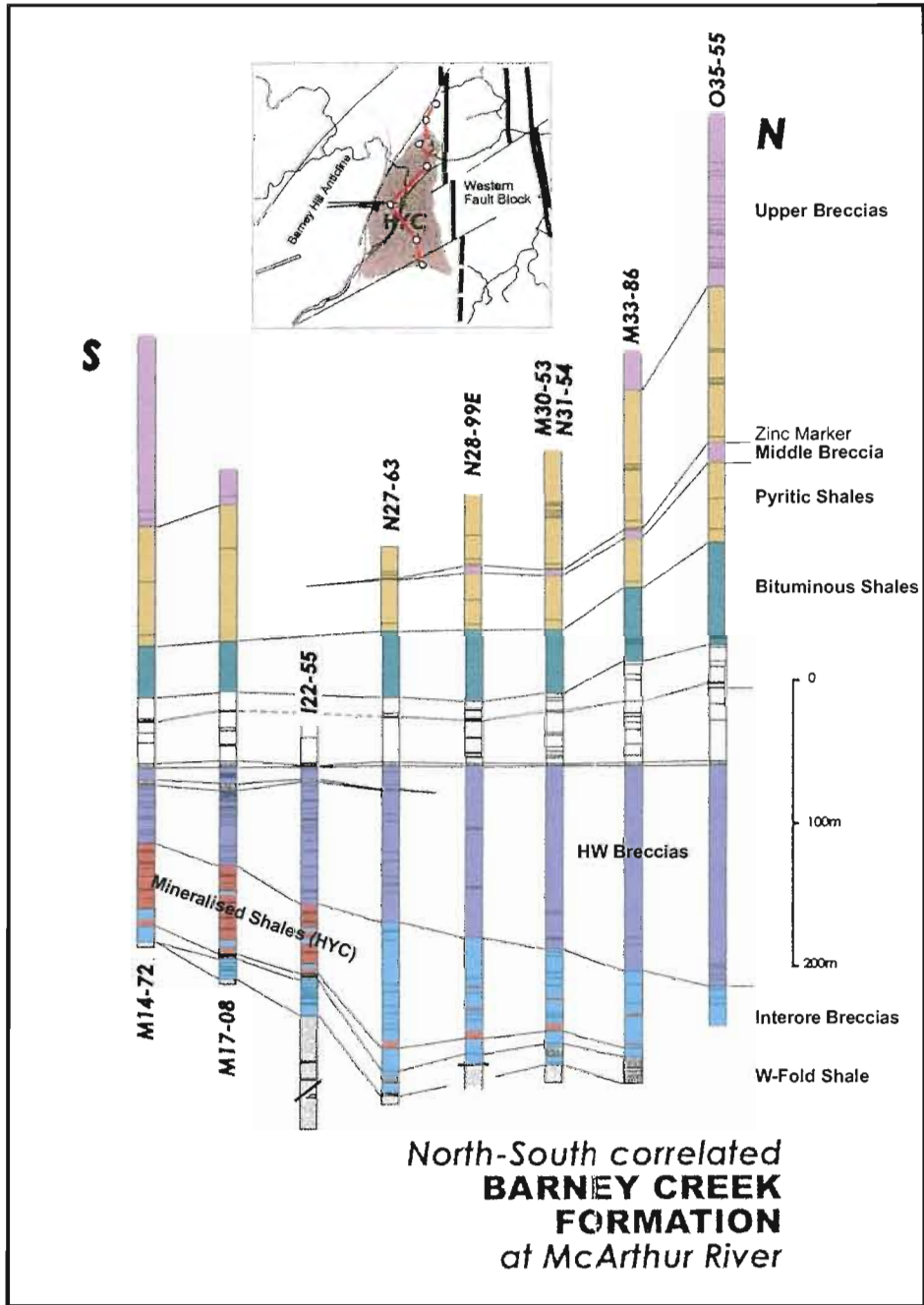


*Figure 2.3 - Descriptions of the clast populations and sedimentological features of the HYC interore mass flow facies (from Logan, 1979). Note that all the characteristic features of in situ laminated base metal mineralisation are recognised as clasts in the mass flow deposits.*

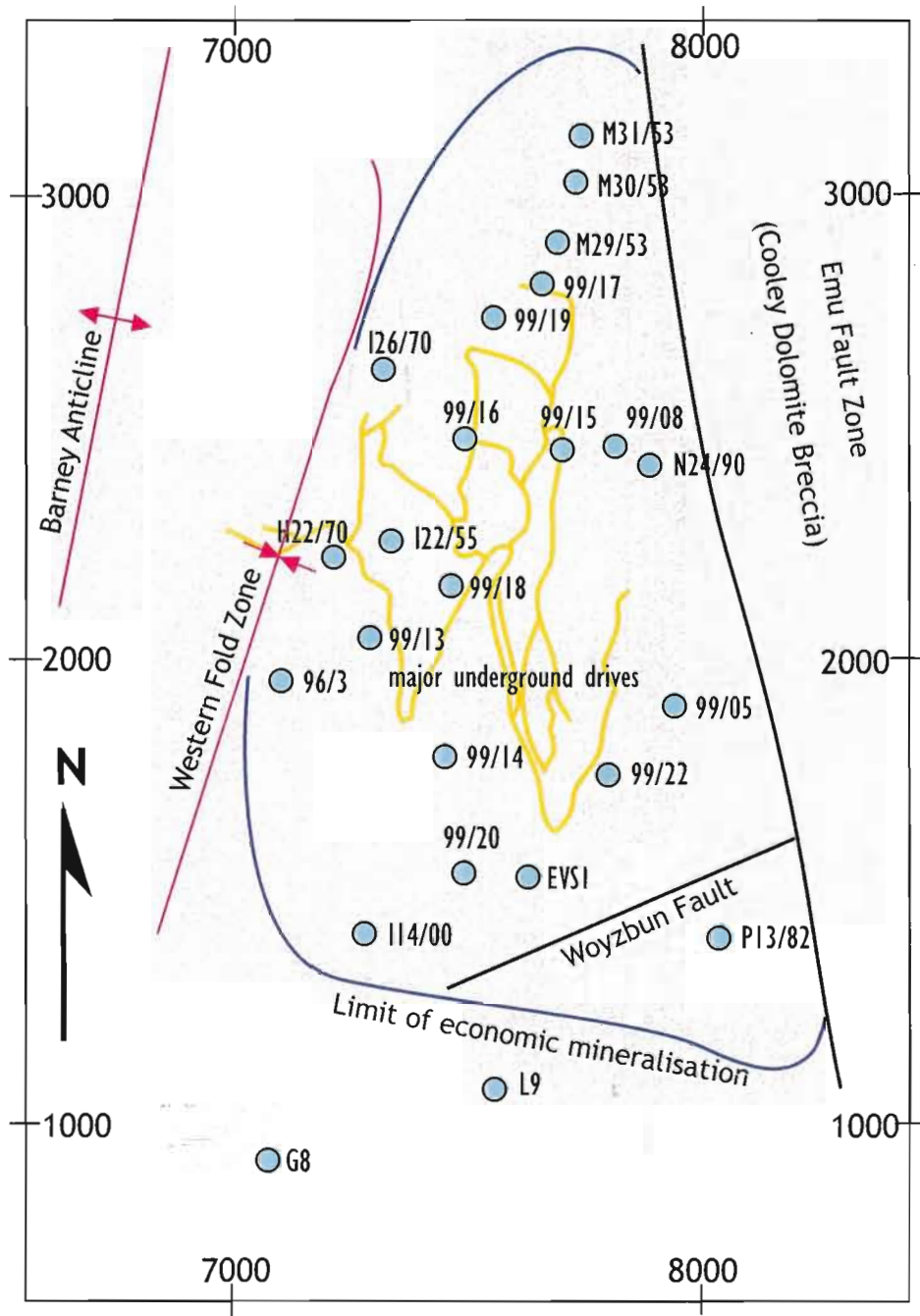
### Breccia Clast Descriptions (after Logan 1979)

<i>Common</i>	<i>Frequent</i>	<i>Rare</i>	<i>Intraclast</i>
<p>Stromatolitic dolomite.</p> <p>Algal mat-textured dolomite.</p> <p>Grey, pink, green and white laminated to massive dolomite.</p> <p>Dolomite with pseudomorphs after discoid gypsum.</p> <p>Grey, green and pink dolomite breccia.</p> <p>Siliceous dolomite.</p> <p>Light grey recrystallised dolomite.</p> <p>Light and dark grey dolomitic siltstone.</p> <p>Green dolomitic mudstone.</p> <p>Intraformationally brecciated dolomite.</p>	<p>Turquoise mudstone.</p> <p>Algal mat-textured dolomite with pseudomorphs after discoid gypsum.</p> <p>Pink, grey and green quartz dolarenite.</p> <p>Siliceous algal-mat textured dolomite.</p> <p>Intraformationally brecciated green dolomitic mudstone.</p> <p>Greenish grey thin to medium bedded dolomite.</p> <p>Light grey thinly bedded interbedded dolomitic siltstone and dolarenite.</p> <p>White weakly cherty dolomite.</p>	<p>Red and green quartz dolarenite.</p> <p>Oncolitic dolomite.</p> <p>Light grey massive dolomite with cryptocrystalline silica blebs.</p> <p>Siliceous algal debris beds.</p> <p>Grey massive dolomite with pseudomorphs of a cubic mineral.</p> <p>Orange-pink dolomite.</p> <p>Dark grey highly porous dolomite.</p> <p>Saccharoidal dolomite.</p> <p>Oolitic dolomite.</p> <p>Green mudstone with fragments of red mudstone.</p> <p>Dolomite with chalcopyrite blebs.</p>	<p>Black chert with sphalerite rims.</p> <p>Pyritic shale with nodular dolomite texture.</p> <p>Pyritic carbonaceous shale.</p> <p>Pyritic, sphalerite-mineralised laminated carbonaceous shale.</p>

### HYC Interore Mass Flow Facies Descriptions (after Logan 1979)

Environment	Bed Thickness	Clast Size	Grading and Sorting	Scouring and Erosion	Mud/Sand Ratio	Shale Disturbance	Erratic Clasts	Laminations and Ripples
<b>Proximal</b>	Thick	Large	Ungraded, chaotic and unsorted	Common evidence	Low	Underlying shale often contorted	Common	Usually disturbed and eroded.
<b>Distal</b>	Thin	Sands and silts	Strong grading and poor sorting	Rare evidence	High	Underlying shale rarely disturbed	Rare	Usually complete.

*Figure 2.4 - HYC deposit location map of drillholes logged during this study. These were selected based on core availability, stratigraphic intersections, and quality of core preservation.*



McArthur River is highly ore-selective, there are very few useful underground exposures of the breccias, but these have been used to augment drill hole data where possible. Polished sections of selected samples were used for detailed petrological investigation of matrices and sulphidic clasts. The stable sulphur isotope ratios of sulphidic clasts and matrices were analysed at the University of Tasmania Central Science Laboratory's laser ablation facility (ch.5).

Implicit in the use of drill cores for interpretation of sedimentology is the restriction of data collection to a small number of points within a wider laterally extensive deposit. Thus, for this work it has at times been necessary to make informed guesses in extrapolation and correlation between holes, and it can only be assumed that any one drill intersection is representative of the unit in a particular area.

### **2.3 Mass Flow Lithofacies**

The term 'inter-ore breccia' is used loosely to cover all mass flow facies within the ore sequence at HYC. These can be subdivided into four lithofacies: boulder-bearing sedimentary breccias, matrix-supported pebble breccias, and gravel-rich and sand-rich graded beds.

#### **2.3.1 Sedimentary Boulder Breccia**

Thick-bedded, erosive, massive and chaotic unsorted breccias dominate the mass flow facies in the northern third of the HYC deposit. These range from 1-19m in thickness and contain clasts that range in size from fine silt to tens of metres (fig.2.5). They may scour up to 5 metres into the underlying fine grained sediment, and in the northern part of the mine may completely truncate the mineralised stratigraphy such that multiple flows amalgamate together. The coarse (>1cm) clast fraction comprises a variety of largely dolomitic lithologies as sub-angular to sub-rounded fragments, and decimeter scale soft-sediment-deformed siltstone intraclasts are common. The largest dolomite blocks occur consistently in the top half of each flow, and the lower half characteristically shows weak inverse grading and exponential increase in intraclast abundance toward the base. Breccia packing is generally tight, with volumetric dominance of large clasts and

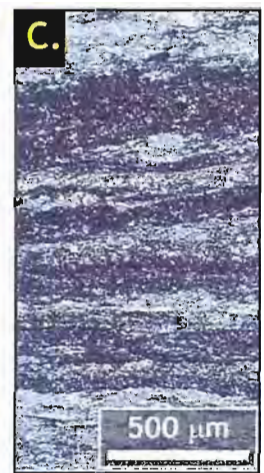
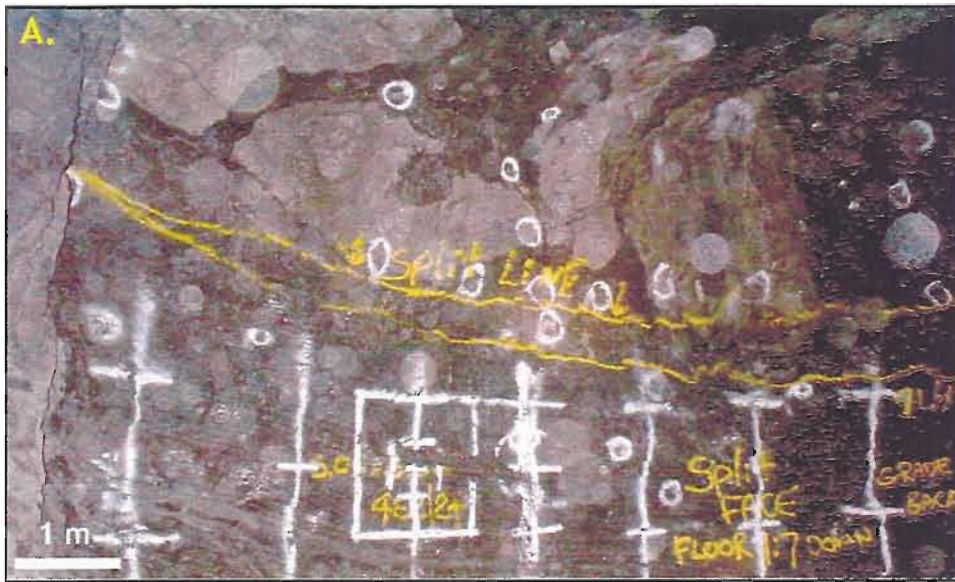
block separation usually less than 10% of the local maximum particle size (fig.2.5). The absence of clast organisation except for basal reverse grading, extreme poor sorting, large maximum particle size relative to bed thickness, and volumetric dominance of large clasts define these units as clast-rich debris flow deposits (definition of Sohn, 2000).

Isolated dolomite blocks occur within the mine stratigraphy, usually <10 metres wide, but up to a maximum of 45 metres (the 'Rock from Mars'). One such boulder, 4 metres wide, in the 4E2-2 decline part of the mine, occurs immediately under the '4M' breccia, but is enveloped in soft-sediment deformed mineralised siltstone instead of breccia matrix. Another block, 2.5 metres wide, occurs in coarse pebble breccia of the 4M stratigraphic unit, laterally separated from coherent boulder breccia by about 30 metres. These isolated blocks are either boulders that have slid down into the basin independently, or which have rolled off the unstable steep front of a breccia deposit as the mass flow process terminates (outrunner blocks).

Intraclasts usually make up less than 10% of the total clast population in the boulder breccias, but account for greater than 50% near the base of some units. They include all the distinctive features of HYC ore mineralisation: stratiform pyritic and sphaleritic dolomitic siltstone, nodular dolomite dolomitic siltstone, and sphalerite-galena-replaced black chert (figs.2.5-2.7). In thin section these appear identical to similar in-situ mineralised facies. Rare intraclasts reach a metre in length, but most are less than 20cm long, due to disaggregation during flow progress. Similarly, most siltstone intraclasts show strong soft-sediment deformation: tight to isoclinal folding, and variable plastic extension or shortening.

Matrices to the boulder breccia facies are highly variable in composition, and are dominated by clean, light grey dolomitic siltstone and dark grey-brown carbonaceous, pyritic, and sphaleritic dolomitic siltstone (fig.2.6). In thin section the dark matrix contains disseminated very fine-grained euhedral pyrite (<10 $\mu$ ), pyrite framboids, and very fine grained (<10 $\mu$ ) sphalerite as ragged aggregates interstitial to dolomite silt grains. Pyrite accounts for up to 15% of the matrix, and sphalerite up to 30%. There is little gradation between the two matrix types, and the transition typically occurs over 10-20 cm. The two matrix types are similar in abundance, with dark matrices more common in thicker flows. Within a flow unit, the dark matrix always underlies the grey matrix, and the interface between the two is not strictly bed-parallel. There is an inexact relationship

*Figure 2.5 - (a) View of underground exposure of the basal 4M breccia in the 4E2-2decline mine area. (b) reflected light microphotograph (RLM) of a laminated sulphide clast in a dark-matrix breccia, compare (c); in situ laminated sulphide ore, for similarity. (d) Breccia specimen showing laminated sulphide intraclast and dense clast packing. (e) Drill core specimen dominated by sulphidic intraclasts. (f) Polished thin section showing plastic deformation and variable shortening of sulphidic siltstone intraclast. Beneath the grey dolomite clast, part of the same original siltstone clast is markedly shortened due to compaction.*

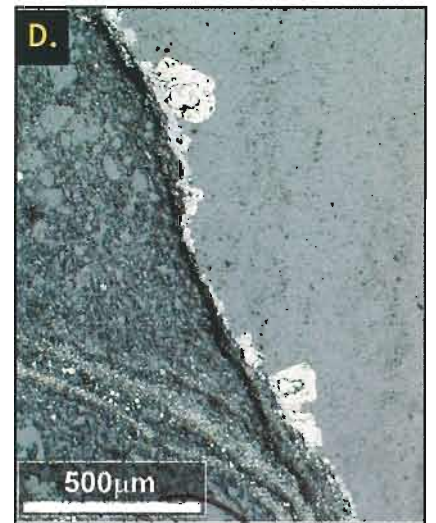
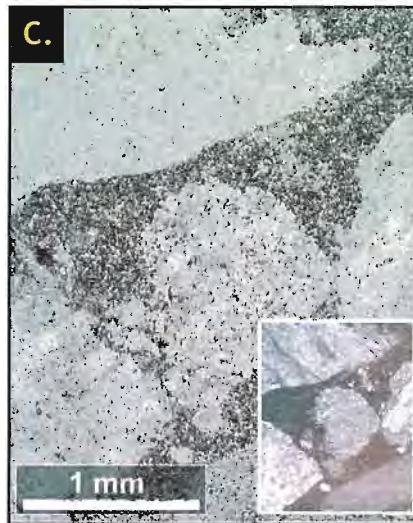
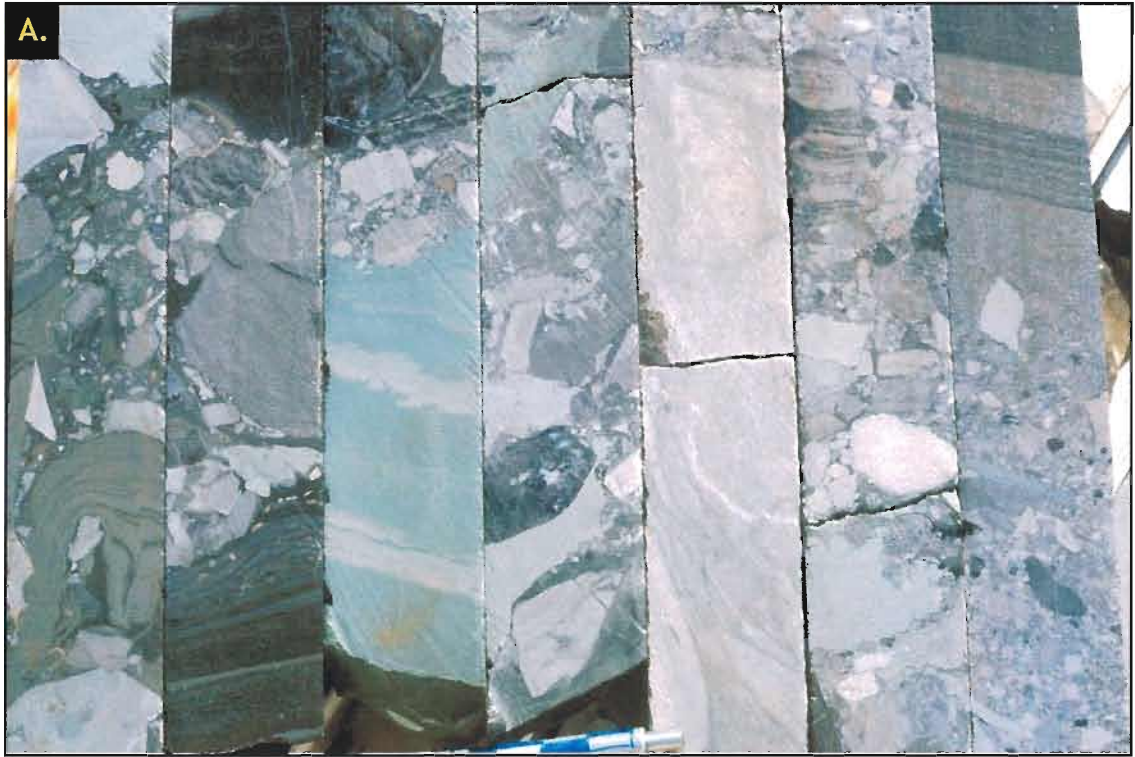


between the underlying sediment-type and the amount of dark matrix: the dark matrix usually occupies more than 80% of breccias that overlie laminated mineralised siltstone, whereas those that overlie the nodular dolomite ore facies (or other breccias) have less, or no, dark matrix. This suggests that dark matrices are a product of direct incorporation of unconsolidated sediment into the mass flow during sedimentation.

Base-metal sulphide replacement of clasts in the breccia facies is common (fig.2.6), usually as coronas of sphalerite, and blebs of galena  $\pm$  chalcopyrite  $\pm$  euhedral arsenopyrite crystals concentrated at the edges of larger clasts. Rarely, entire grains are replaced by sulphide minerals. The sulphide textures shown by these clasts are distinct from those of *in situ* laminated HYC mineralisation, and consist of relatively large continuous monomineralic domains, often with subhedral crystal forms. There is distinct selectivity in clast replacement and adjacent clasts that appear identical in thin section may have suffered very different levels of replacement. Hinman (2001) has suggested that it is the siliceous clasts that undergo the most severe replacement, but there is also definite selectivity between replacement of different carbonate clasts. Large *et al.* (1998) considered these coarse-grained sulphides to be primary clasts sourced in the discordant mineralisation of the Emu Fault Zone.

We analysed the sulphur isotope composition of sphalerite (ch.5) in an 'intraclast', in the matrix, and in a 'replaced' clast that occur within 2 cm of each other in a breccia sample (991712), to constrain ideas on the origin of sphalerite in the mass flow facies. The sphalerite-'replaced' clast has  $\delta^{34}\text{S}_{\text{CDT}} = 3.3 \pm 0.2 \text{‰}$ , the laminated 'intraclast' sphalerite has  $\delta^{34}\text{S}_{\text{CDT}} = 0.68 \pm 0.2 \text{‰}$ , and the matrix sphalerite has  $\delta^{34}\text{S}_{\text{CDT}} = 1.56 \pm 0.2 \text{‰}$ . Throughout the deposit, laminated sphalerite (sp1, ch.3,5) is isotopically lighter than replacement sphalerite (sp2, ch.3,5) by  $\sim 4 \text{‰}$ . The consistency of this relationship between breccia clasts differentiated on textural bases confirms that the laminated sphalerite is indeed intraclastic, and has not formed by mimetic replacement contemporaneous with other, more obvious replacement. The similarity between the isotopic composition of unequivocal replacement sphalerite in the breccia and that of replacement sphalerite in the nodular carbonate ore facies (sp2) suggests that these replacement processes are likely to be contemporaneous and are due to the same mineralising fluid. Intermediate isotopic composition of the matrix material suggests a mixed origin, including diagggregated laminated sphalerite and replacement sphalerite.

**Figure 2.6** - (a) selected pieces of drillcore in sequence (L to R) demonstrating variation from dark sulphidic matrix at the base to clean grey dolomite silt matrix at the top. The location of the transition is occupied by a large white dolomite block. Note the dense clast packing, turquoise siltstone clast, and plastically deformed laminated sulphide intraclast. Scale is centimetres. (b) RLM of dark breccia matrix showing fine grainsize and ragged form of sphalerite component. (c) RLM of dolomite matrix, and inset, the same view in transmitted light showing significant opaque organic component. (d) Subhedral and domainal cpy-sp-gn replacement of a ?dolomite clast in a dark-matrix breccia (DMB). Note truncative juxtaposition of a pyrite-laminated siltstone intraclast against a dolomite clast. (e) Strong domainal sp-gn replacement of a dolomite clast and a pyrite 'macroframboid' in DMB. Sphalerite content of the matrix is indicated by colour contrast with barren siltstone (lower left). (f) Texture-selective replacement of ooidal laminae in a dolomite clast in DMB. (g) Crystal-selective replacement of a dolomite clast in DMB.



### 2.3.2 Matrix-supported Pebble-Breccia

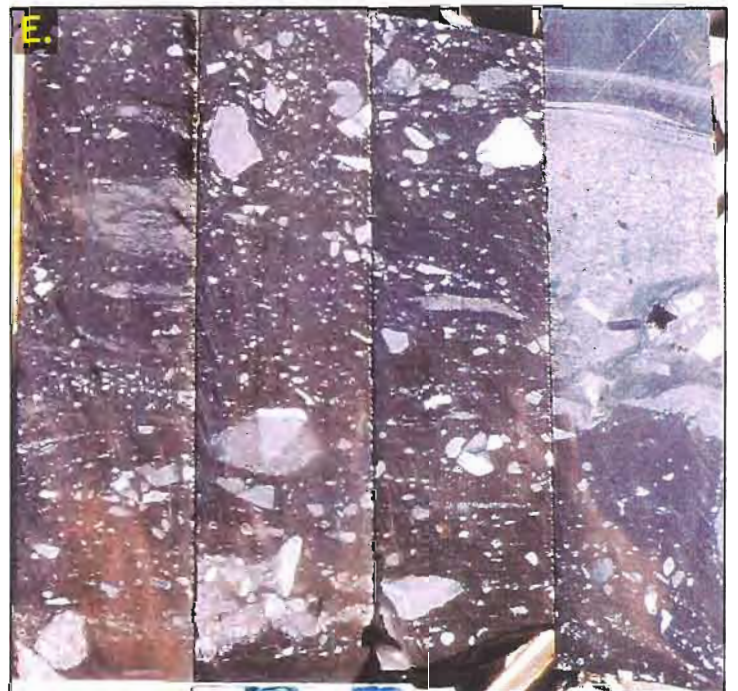
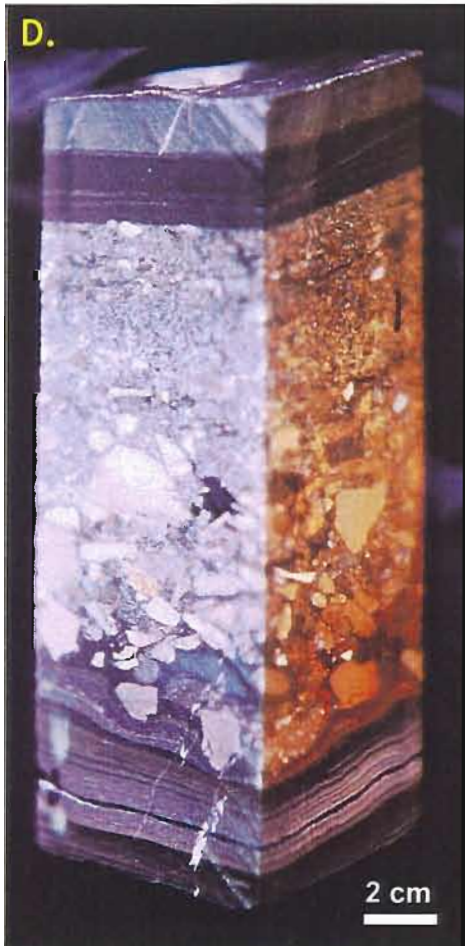
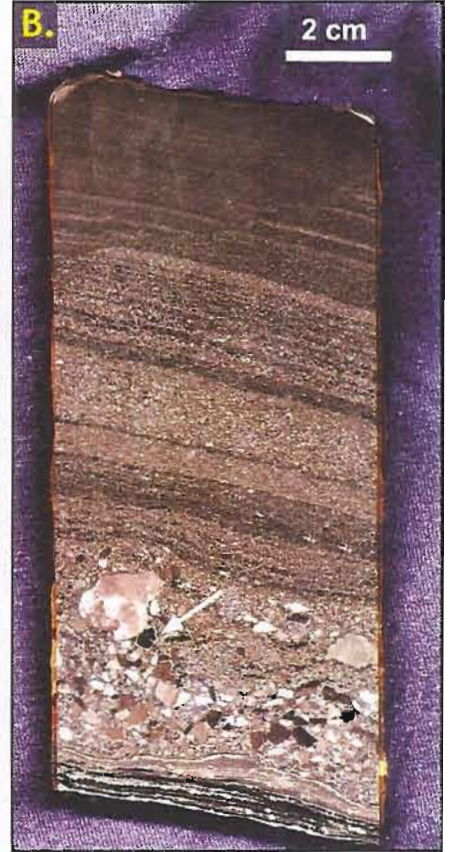
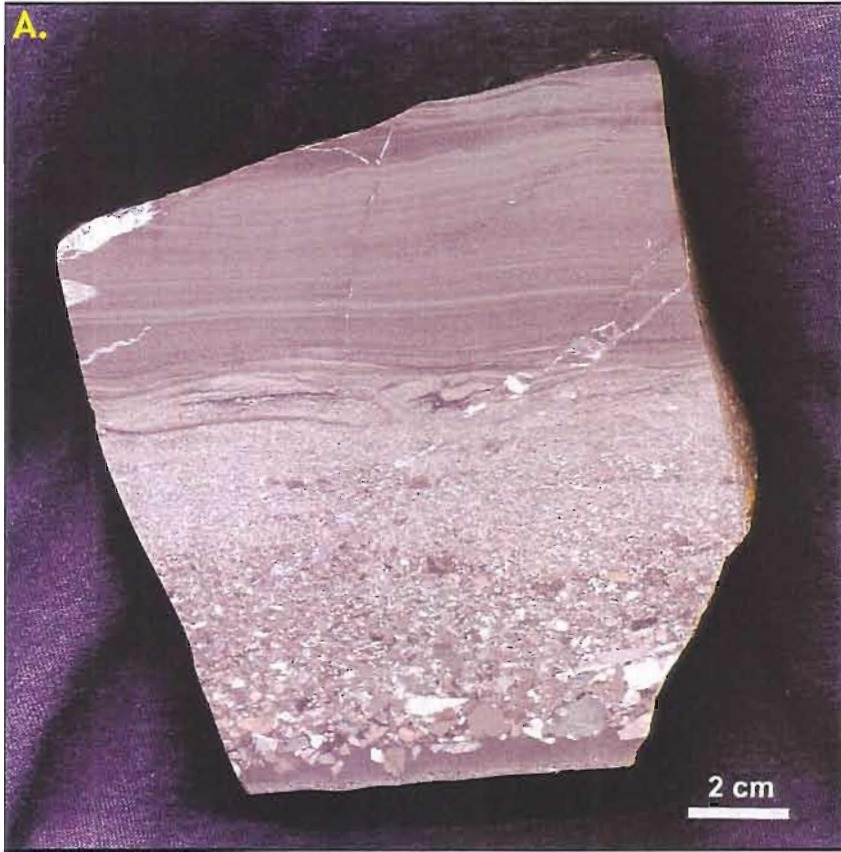
Weakly to chaotically stratified granule and pebble-bearing dark pyritic siltstone occurs in the medial and distal facies of the I3/4d mine stratigraphic unit (units named sequentially bottom to top, fig.1.7). It consists of 70-95% massive to poorly-stratified dark grey-brown dense (pyritic) siltstone, with 5-20% coarse sand, granule and pebble clasts of dolomite, quartz and rare siltstone intraclasts. The coarse clasts show no preferred orientation (fig.2.7), and define discontinuous and wavy stratification through the siltstone. Where the proportion of coarse clasts is very low, an irregular anastomosing mm-scale lamination is developed in the silt. In the medial environment, I3/4d becomes more tightly packed and coarser grained toward the base, and is capped by a normally graded sandstone. Further from source, the base is a normally graded granular sand and irregular granular stratification persists in a thick silty top.

### 2.3.3 Graded Beds

Thick to thin-bedded cobble-bearing to sandy normally graded beds dominate the mass flow facies in the southern two thirds of the HYC deposit, but also occur with boulder breccias in the north and northeast. Normal grading and strong clast size stratification define these beds as turbidites (fig. 2.7, Lowe 1982). In this study, deposits with pebble-size (or coarser) clasts and a massive base are referred to as high-density turbidites because the flow responsible for forming the deposit probably underwent gravitational flow transformation (Fisher 1983) to generate a clast-rich basal zone. Those with granule-sized (or finer) clasts at the base that were probably entirely turbulent are referred to as low-density turbidites.

High density turbidites are characteristically associated with boulder breccias, either as a normally graded capping over a breccia flow, or as an adjacent apron. As the cap to a boulder breccia they comprise 10cm-1m thick beds, which are composed of sub-angular clasts of various dolomite lithologies with a dolomite-quartz-orthoclase siltstone and sandstone matrix. Massive, unordered, framework-supported coarse to fine-grained gravel grades rapidly through granular sandstone and sometimes a moderately well-sorted sandy top. There is no sharp division between the base of such a high-density turbidite and the underlying breccia; the boundary is defined by a change in dominant grainsize from  $> 0.5\text{m}$  to  $\leq 10\text{cm}$ .

*Figure 2.7 - (a) Low-density turbidite showing normal grading from pebbles to coarse sand, a laminated fine sand central zone, and a coarse silt top. (b) Turbidite with pebble-rich reverse graded base including a chert intraclast with a sphalerite corona (arrow), and a normally graded sand to silt top. (c) RLM of a thin sandy turbidite <1cm thick. Thin dolomitic and carbonaceous graded beds like this are ubiquitous throughout the HYC stratigraphy, but are most abundant in the east and north. (d) High-density turbidite dominated by pebble-sized clasts and showing weakly graded, poorly stratified sandy top. (e) Chaotic, weakly stratified matrix-supported pebble breccia from I3/4d. Cores make a continuous section from bottom left to top right. The breccia is capped by a low-density turbidite that contains a chert intraclast.*



Laterally adjacent to the breccia flows are high-density well stratified gravelly turbidites that characteristically show the 'A', 'B', and 'F' Bouma subdivisions as defined by Lowe (1982). These have a massive, chaotic very poorly sorted silt-cobble base up to 1.5m thick that shows the same clast, intraclast and matrix characteristics, packing, and composition as the boulder breccias. Close to genuine boulder breccias, rare large blocks up to 2 m occur within this massive basal zone. Above it there is better clast sorting, and grainsize grades rapidly through granular to fine sand which is occasionally laminated. A massive to weakly laminated silty top of highly variable thickness overlies the fine sandstone.

Low-density turbidites occur throughout the HYC ore-deposit, but are most evident in the southern third of the orebody. They resemble the stratified high density turbidites without the chaotic gravelly base, and are usually thinly bedded (<20cm). They have a strongly normally graded fine-gravel to coarse sand base, comparatively thick laminated fine sand middle zone, and massive silty top of highly variable thickness (cm-m). Most turbidites are grey and dominated by sub-angular dolomite, quartz and orthoclase clasts, but there are also numerous very thin (<5cm), sandy, strongly carbonaceous dark grey and black graded beds interpreted to represent local sediment slump-derived turbid flows.

## **2.4 *Flow Geometry and Spatial Relationships***

### **2.4.1 *Debris Flow Geometry***

There is agreement between all previous workers that the inter-ore breccias are sourced broadly from the northeast and thin to the south and west (Walker 1977, Logan 1979, Perkins and Bell 1998, Hinman 2001). However, this conclusion is drawn from contoured plots of stratigraphic data for the entire deposit, in which all breccias greater than 2 or 3 metres thick plot in the same contour interval, i.e., the interval representing the thickest beds, because the plot includes the thin laterally equivalent turbidites of the distal environment. Considered individually, the debris flow deposits in fact thicken gradually to the south-southwest, i.e., down-flow (fig.2.8a,b,c). In DDH M29/53, the 'I4/5' and 'I5/6' flows thicken and amalgamate, and truncate the entire #5 ore lens. After attaining maximal thickness, commonly between 5 and 10 metres, the debris flow breccias then abruptly thin and degrade into high-density turbidites less than 4 metres thick. In the 4E2-2 decline part of the

*Figure 2.8 - (a) Correlated graphic logs of HYC interore mass flow units I1/2 and I3/4, showing the difference in character and geometry between boulder-bearing debris flow deposits and distal turbidites. The debris flows have sharp frontal geometry, variable dark matrix development, and variable intraclast content. There is a general trend to greater intraclast content closer to source (i.e. to the left of the diagram).*



*Figure 2.8 - (b) Correlated graphic logs of HYC interore mass flow units I4/5 and I5/6, showing entrainment of primary intraclasts, dark matrix development that is loosely related to the nature of the substrate, erosive amalgamation of debris flow deposits, and steep frontal geometry. Maximum clast sizes depicted are faithful to drill intersections. The 1m block at the base of I4/5 in DDH 99/16 is probably an outrunner block that has tumbled from the flow front.*

# 15/6 DEBRIS FLOW

## LEGEND

-  Laminated mineralisation
-  Nodular dolomite mineralisation
-  Massive dolomitic siltstone
-  Graded dolarenite
-  Polymict sedimentary breccia with dolomitic silt matrix
-  Polymict sedimentary breccia with dark sulphidic matrix

M31/53

M30/53

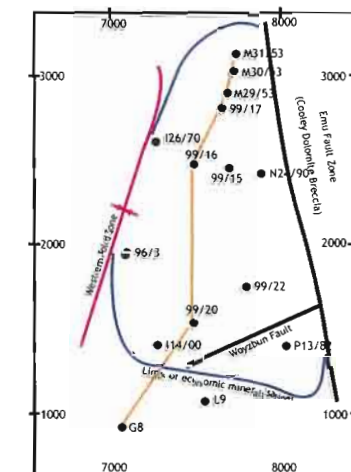
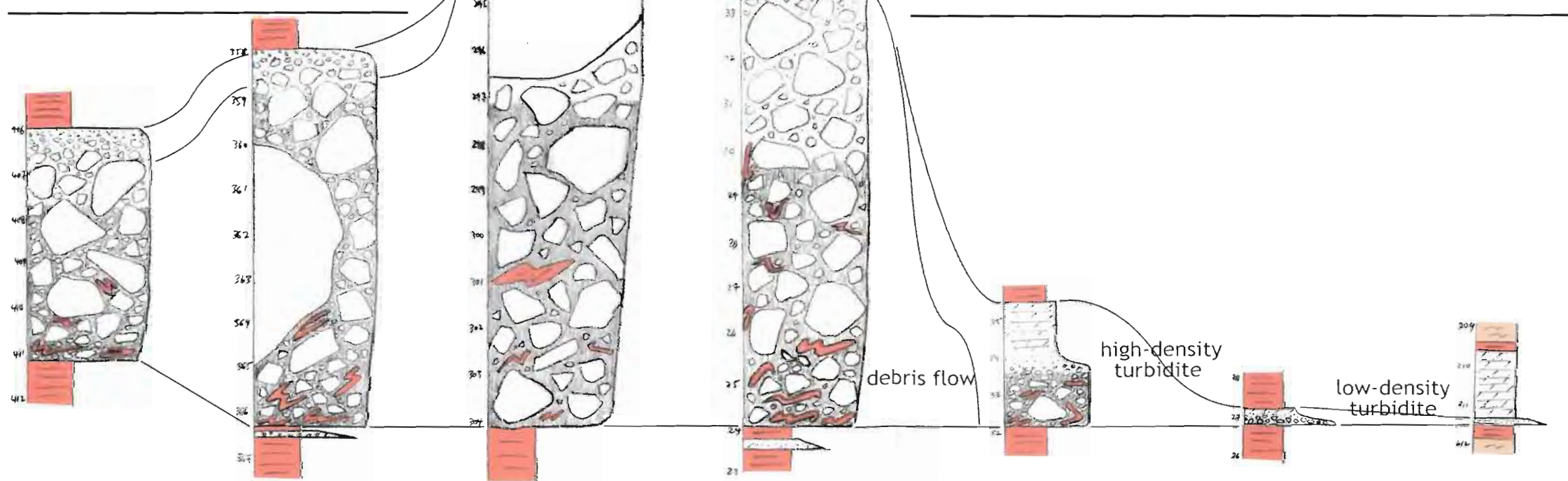
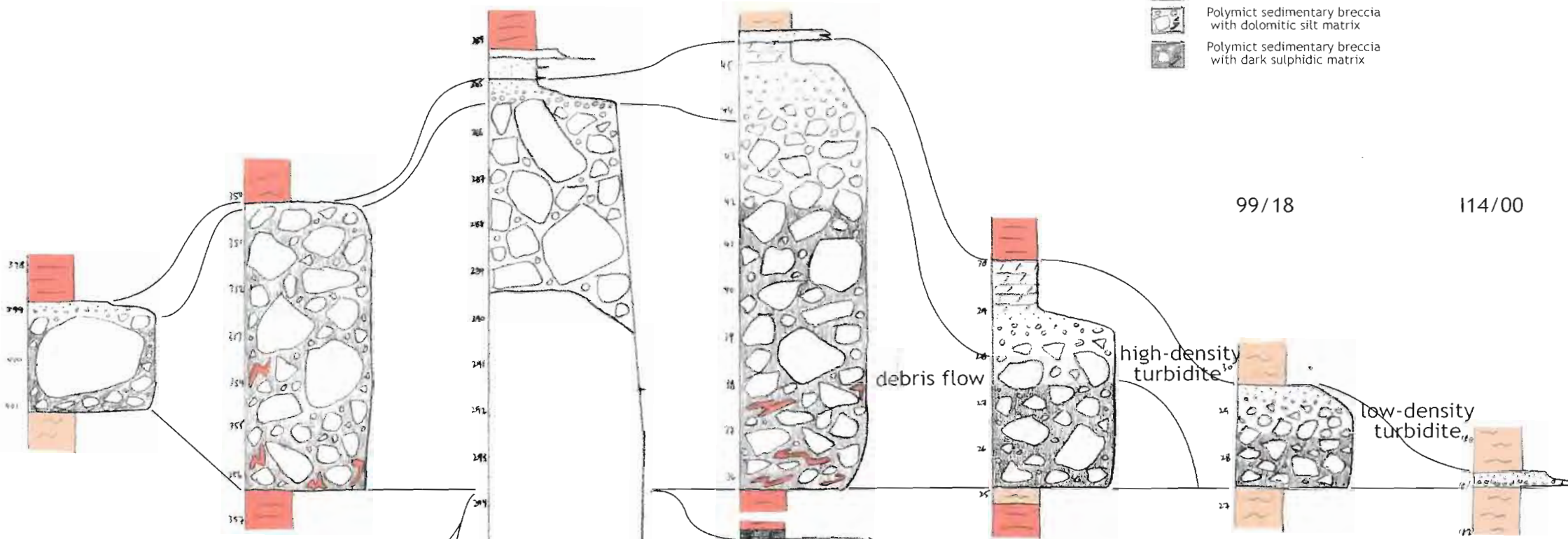
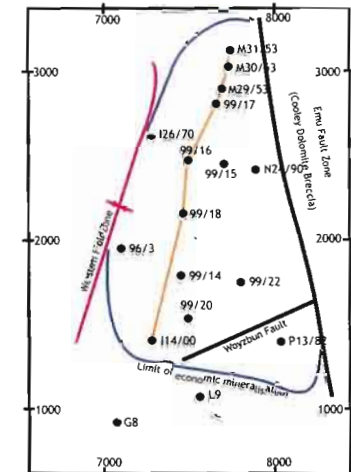
M29/53

99/17

99/16

99/18

114/00



M31/53

M30/53

M29/53

99/17

99/16

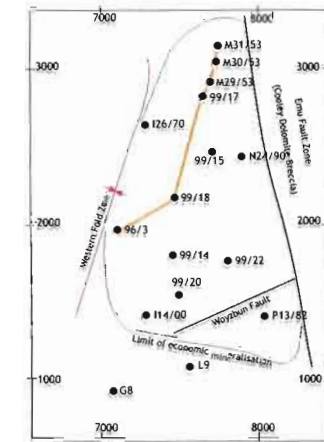
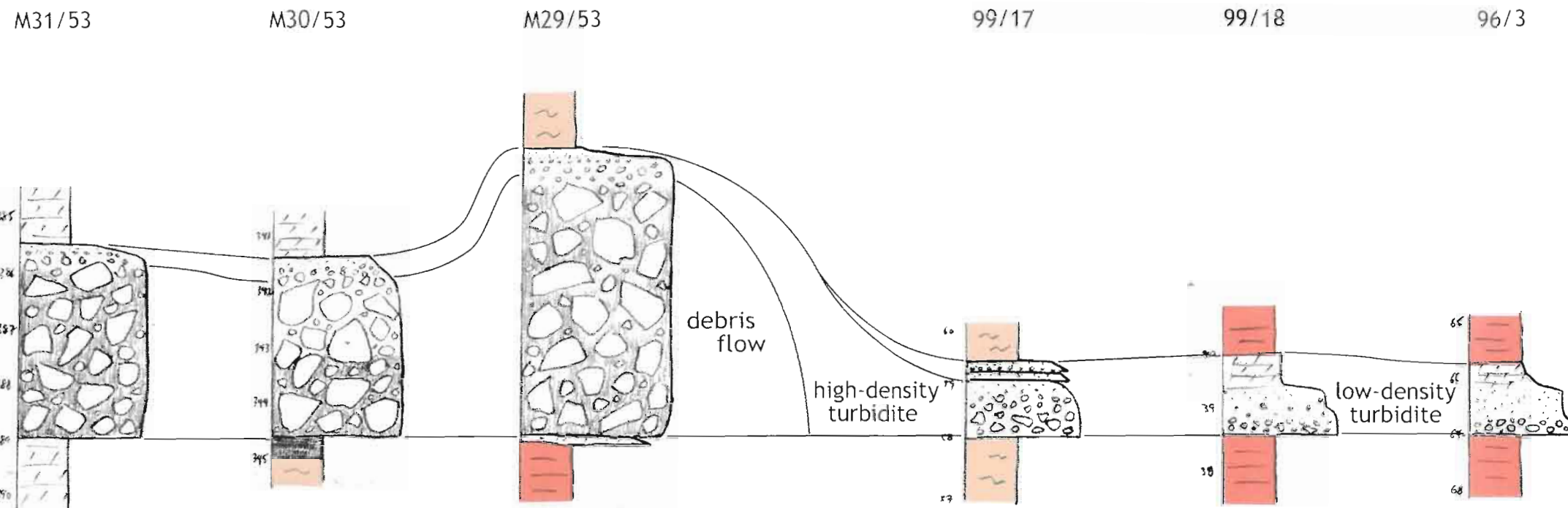
99/20

G8

# 14/5 DEBRIS FLOW

*Figure 2.8 - (c) Correlated graphic logs of HYC interore mass flow units 16/7 and 17/8, showing (again) steep flow fronts, capping turbidites, and variable dark matrix development.*

# 17/8 DEBRIS FLOW



M31/53      M30/53      N24/90      99/17      H22/70      99/18

## LEGEND

- Laminated mineralisation
- Nodular dolomite mineralisation
- Massive dolomitic siltstone
- Graded dolarenite
- Polymict sedimentary breccia with dolomitic silt matrix
- Polymict sedimentary breccia with dark sulphidic matrix

# 16/7 DEBRIS FLOW

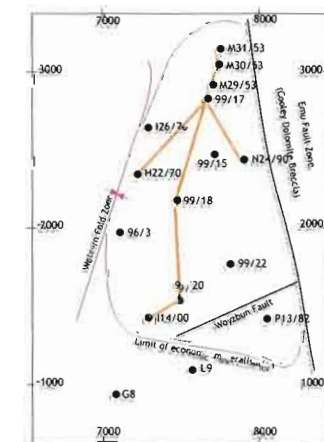
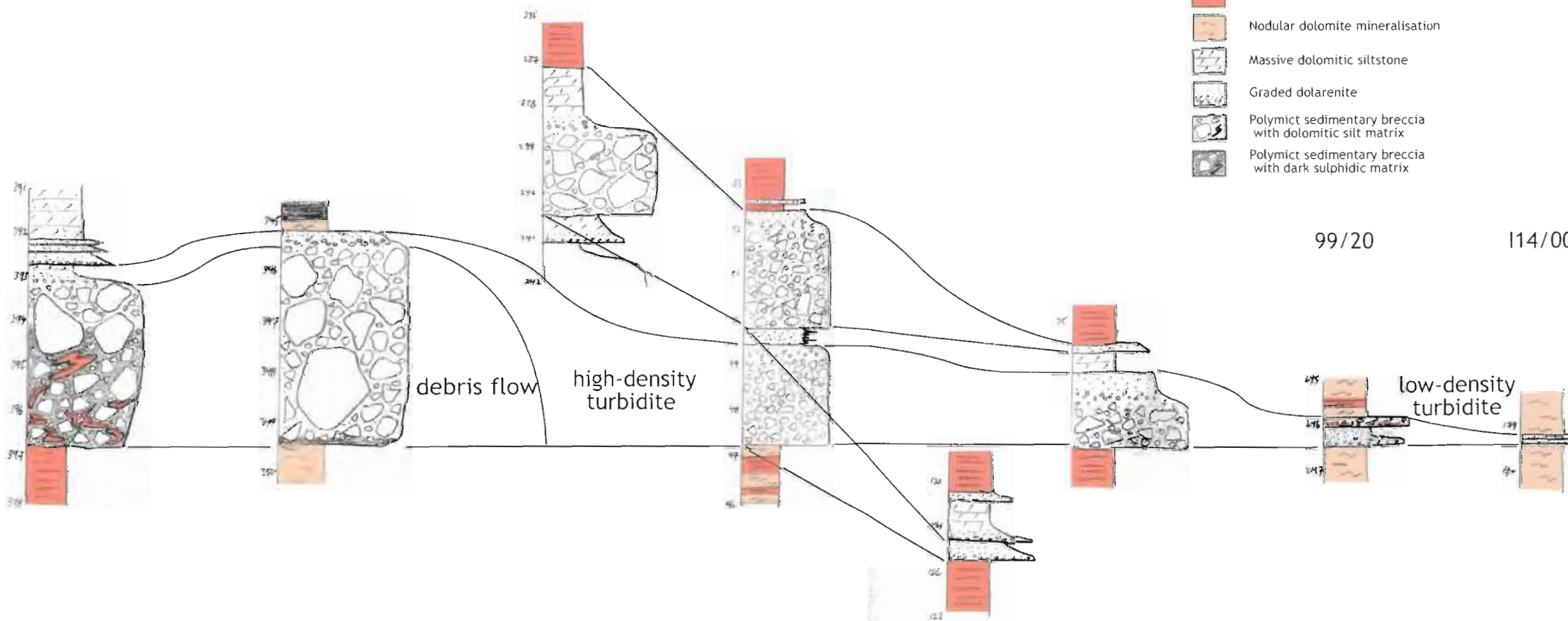
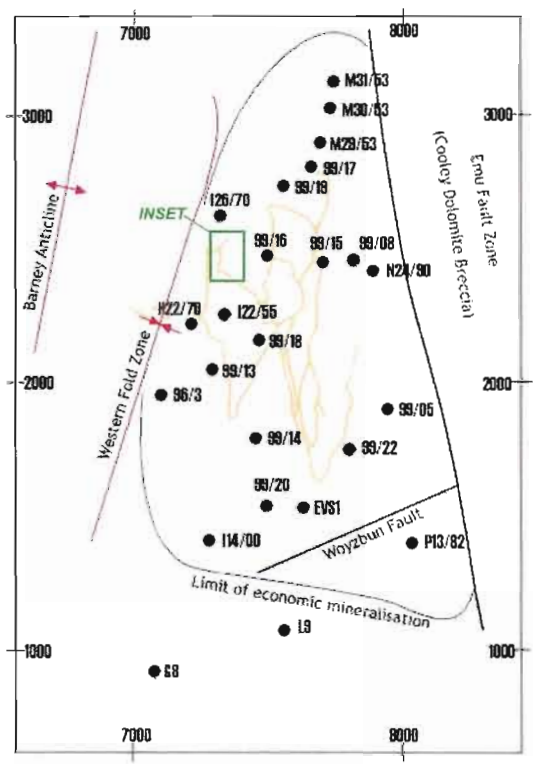
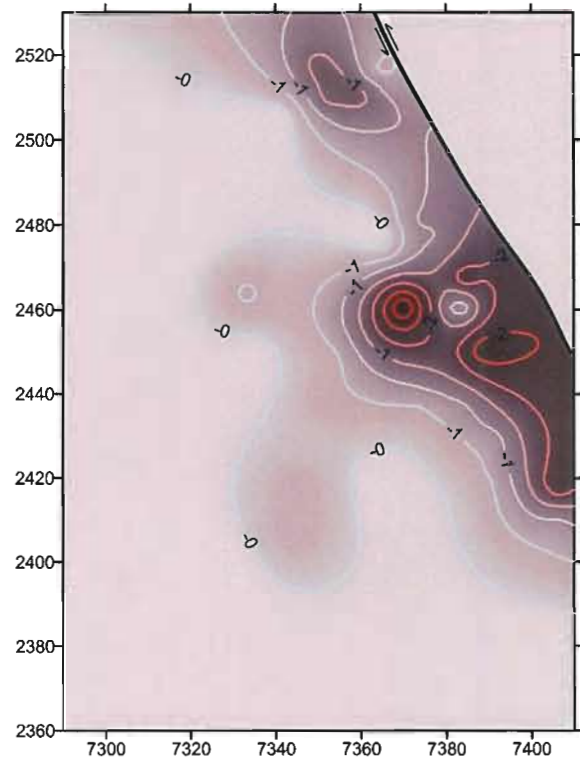
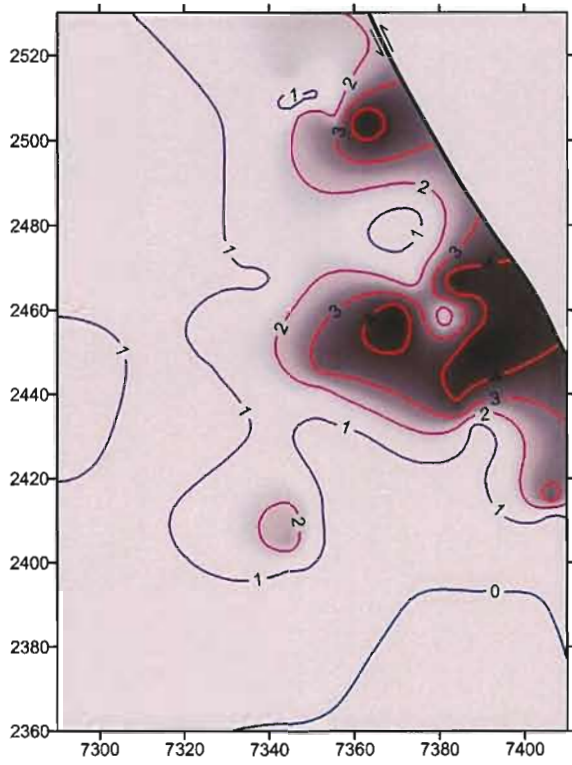


*Figure 2.9 - Contoured images of (a) maximum boulder dimension, and (b) scour depth, for the 4M debris flow in the 4E2-2decline part of the mine. The breccia bed is truncated by a strike-slip fault immediately behind its frontal termination. A large outrunner block (just south of the centre of the plot) has travelled ~40 metres from the debris flow front and has sunk more than a metre into the underlying sediment.*



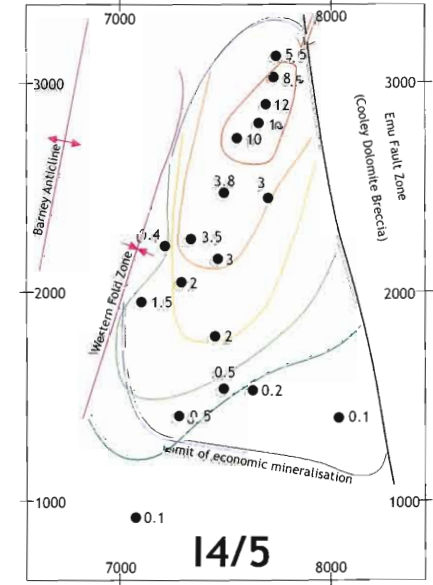
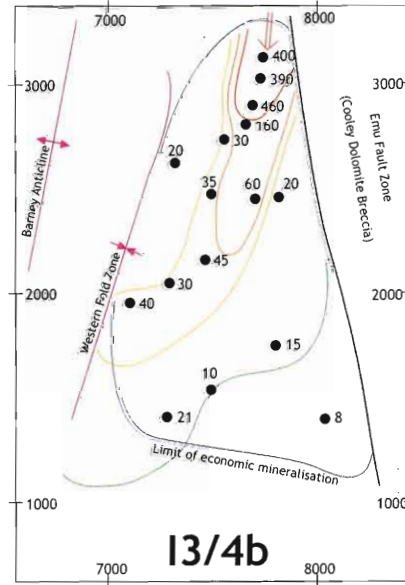
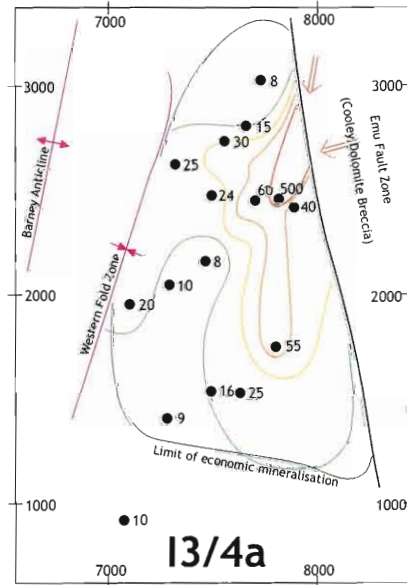
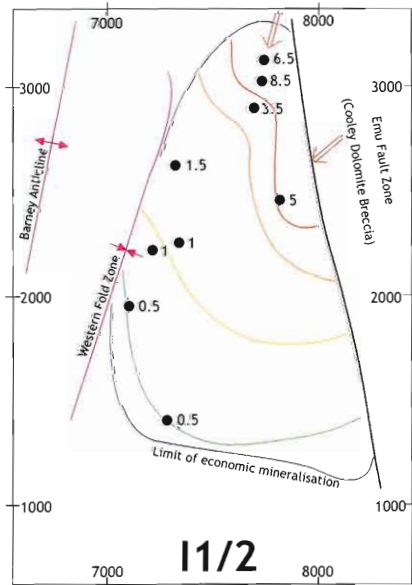
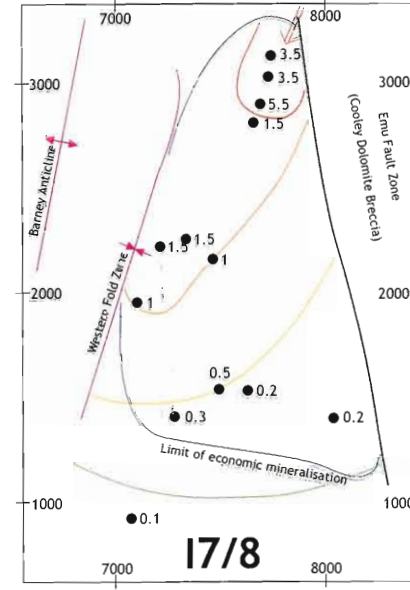
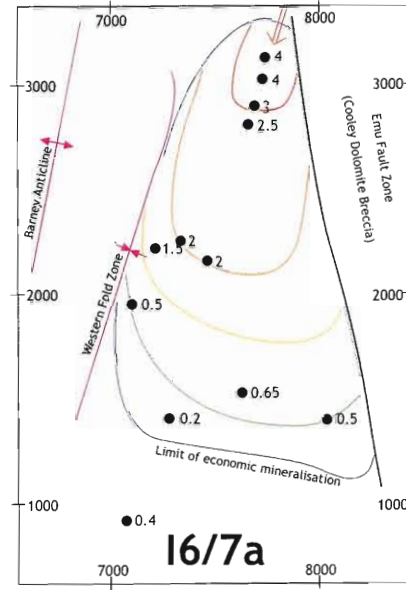
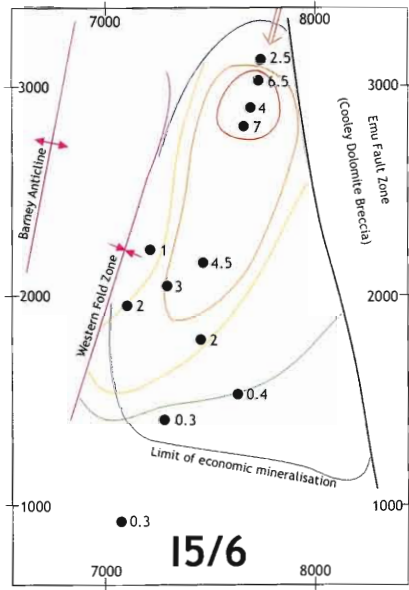
mine, the '4M' breccia changes from a breccia hosting 5 m blocks to a gravelly turbidite with maximum clast size <20cm, over a distance of ~100m (fig.2.9). The transition can probably occur more rapidly for thinner flows (~50m), and correlation between drillholes (eg DDH 99/17 to DDH 99/16) constrains the maximum length of transition to ~200 m.

More regionally, the debris flow deposits within the HYC ore sequence and those that dominate the hangingwall become more abundant and amalgamate to the north-northeast of the deposit. In N-S section they constitute a southward-thinning wedge-shaped accumulation of sediment gravity flow deposits that extends at least as far north as DDH O35/55 (fig.2.1, Hinman 2001), approximately 400 metres north of the northern limit of economic mineralisation. There is a general relationship between maximum flow thickness and the distance any given flow penetrates southward into the HYC subbasin; the 'I4/5' breccia is the thickest inter-ore breccia and extends the furthest south. However, the majority of the inter-ore debris flow deposits abruptly terminate in the vicinity of the 2700mN mine grid northing. Thus, the flows are at least 800 metres long, and interrogation of the mine database shows that they are usually 300-500 metres wide. The linear configuration of northern drillholes analysed in this study does not permit rigorous description of the nature of the lateral edges. Nonetheless, the persistence of SW-directed flows present in DDH M29/53 (northern) as far as DDH N24/90 (eastern), suggests that there is some degree of lateral thinning in contrast to the abrupt frontal termination. Extremely abrupt (<5 m) lateral changes from boulder-bearing debris flow to high density turbidite are observed in some parts of the mine. These are always coincident with late-stage faults and represent an artefact of brittle deformation of the deposit rather than a primary sedimentological feature such as flow channelisation. Disregarding the effects of late deformation, the flows have sheet-like morphology and are probably broadly lensoidal in section.

#### 2.4.2 Mass Flow Direction

There are no flow direction indicators at HYC, and all interpretation of provenance is based on mass-flow deposit geometry, the direction of the long axis of a flow and the direction of frontal thinning. Previous work on the inter-ore breccias (Walker, 1977; Logan, 1979) demonstrated an overall north-northeast provenance and showed variability between NE and N provenance within the type 1 breccias. Correlation of stratigraphy logged during this study indicate systematic variation in the flow direction. Breccias of the lower part of the sequence; the I1/2 and I3/4 inter-ore mass flow units, have NE provenance (fig.2.10), whereas all major units higher in the sequence

*Figure 2.10 - hand-contoured isopach maps of the major interore mass flow units, from the lowermost interore unit 11/2 (bottom left), upsection to 17/8 (top right). Note that flows with ENE and NE provenance are confined to the stratigraphy below the #4 orebody, and that above this level all the units have to NE provenance.*



have NNE provenance (I6/7 is a possible exception, but is difficult to correlate because of flow amalgamation). The mine database suggests that the 4M unit has due N provenance, but the orientation of the flow front as mapped in 4E2-2decline suggests a NNE flow direction. Therefore, the type 1 inter-ore mass flows were not point-sourced in the northeast, but instead had spatially continuous (line) source that spanned the northeastern boundary of the HYC deposit and shifted northward during mineralisation at HYC.

### 2.4.3 Spatial Relationships of the Mass Flow Facies

High density, clast-supported gravel-dominated dolarenite-matrix turbidites with thin sandy tops overlie most debris flow deposits. These capping turbidite beds are thinned or absent where the debris flows are thickest, and are themselves thickest beyond the lateral edges of the debris flows (fig.2.8).

Beyond the frontal termination of the debris flow breccias, strongly stratified high-density turbidites with chaotic, gravelly, dark-matrix bases occupy the equivalent stratigraphic intervals (fig.2.8). The massive bases of this facies become more distinct with distance away from the debris flow deposits, and persist with little decrease in thickness up to 600 metres past the debris flow front. After that, some bases abruptly terminate and the deposit evolves into a low-density sandy turbidite, whereas others entirely lose their fine-grained upper subdivisions and persist into the distal environment. Rarely, in the proximal environments of the east and north, both types of high-density turbidite appear to occur independent of debris flows (eg I6/7b, I3/4c-e), but may in fact be associated with debris flows that do not reach the HYC orebody. In these cases, cap-style turbidites in the proximal environment grade down-flow into stratified turbidites.

Low-density granular to sandy dolomitic turbidites are ubiquitous throughout the HYC deposit, and are particularly abundant within the ore lenses near the northern and eastern limits of the deposit. In the distal environments of the south and west, stratified low density turbidites occupy the stratigraphic positions of the proximal debris flows, and are the down-flow equivalent of the high-density turbidites. In contrast, in the proximal and medial environments there are numerous thin (<10cm), graded, unstratified dolomitic turbidites within the mineralised siltstone lenses. Similar

*Figure 2.11 - (a) Corellated stratigraphic section of the #3 ore lens and I3/4 mass flow units, showing thickening of turbidite silty tops in the central southeastern part of the deposit, and overall distal stratigraphic thinning beyond the southern edge of the deposit. Grading and lateral variation of the I3/4d unit is also apparent. (b) Isopach map of the average thickness (cm) of silty top material per mass flow unit. (c) Isopach map of the average thickness of ore lenses, corrected for bias caused by incomplete intersection of the mine stratigraphy. The coincident geometry of (b) and (c) suggest primary sedimentological control on mineralisation.*

99/17

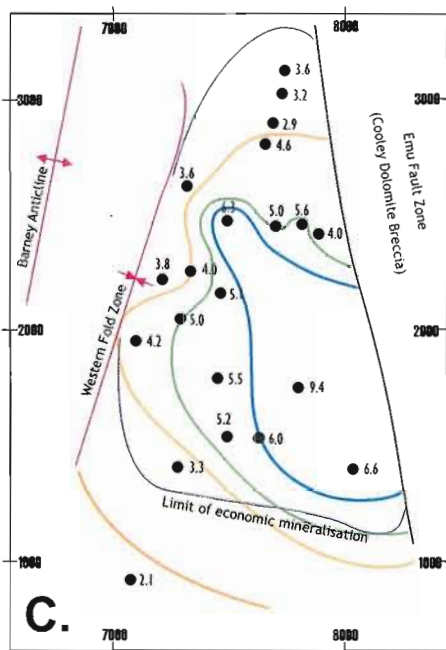
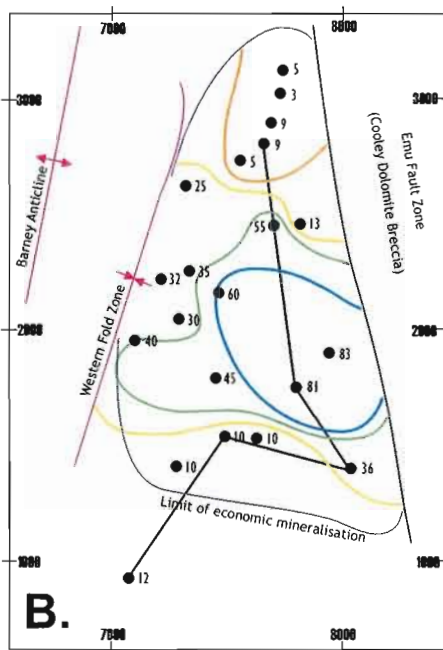
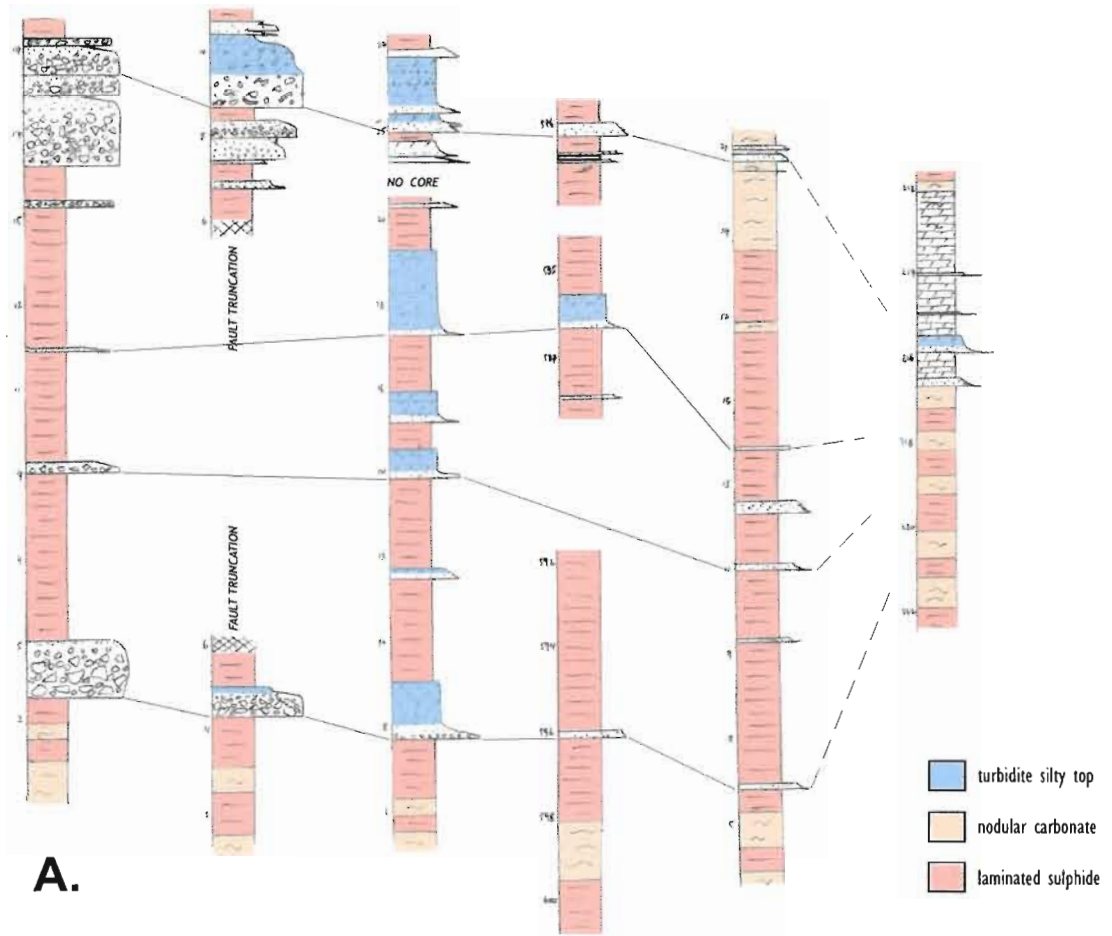
99/15

99/22

P13/82

99/20

G8



thin (<5cm), graded, carbonaceous turbidites occur throughout the deposit and are spatially unrelated to the major mass-flow deposits.

Both high- and low-density turbidites have massive dolomitic-carbonaceous silty tops; the turbidite 'F' subdivision of Lowe (1982). Pelagic (suspension) fallout was the dominant background sedimentary process during periods of mass flow quiescence, and siltstone laminae unaffected by mass flow processes are ungraded and become generally finer grained away from the Emu Fault Zone. The turbidite silty tops are therefore interpreted as the product of suspension deposition of large amounts of fine grained material elutriated from mass flows after the cessation of lateral flow. They vary in thickness within the deposit, but are consistently thickened in the southeastern quarter of the deposit (fig.2.11). In DDH P13/82 and 99/22, the silty tops of most turbidites are thicker than their granular or sandy bases. The mine stratigraphy of the lower ore lenses is also anomalously thickened in this part of the mine (S. Peverly, pers. comm.), and it is interpreted as the local depocentre during formation of ore lenses 2 and 3.

## 2.5 ***Sediment Gravity Flow Processes and Deposits***

Debris flows are defined as gravity driven flows of sediment-water mixtures in which the gravitational clast motion drives motion of the interstitial fluid (Fisher, 1983), as distinct from turbulent flows in which fluid turbulence supports the clastic load. The characteristic reverse graded base develops due to a shear strain gradient which is itself the result of laminar flow dynamics (Johnson, 1970). Debris flows range between mud-rich and clast-rich end-members, which behave as viscoplastic fluids and dilatant granular substances respectively (Sohn, 2000). Debris flows of the clast-rich type flow as a 'rigid plug', in effect lubricated by a more mud-rich 'flow body', and preceded by a boulder-rich flow 'snout' (Padgett *et al*, 1977). When the kinetic energy of this type of flow falls below some critical threshold, frictional interaction between clasts causes the flow to freeze (Gorsline 1984), thus leaving a deposit that attains greatest thickness and contains its largest boulders near the front, and then abruptly terminates. This down-flow geometry has been demonstrated for debris flows across a variety of scales both smaller and larger than those observed at HYC (Padgett *et al* 1977, Prior *et al*. 1984, Sohn 2000). In lateral section, subaqueous debris flows are generally lensoidal with aspect ratios (bed thickness:width) around 1:150 (Gloppen and Steel, 1981). However they may be laterally constrained by the basin architecture in the manner

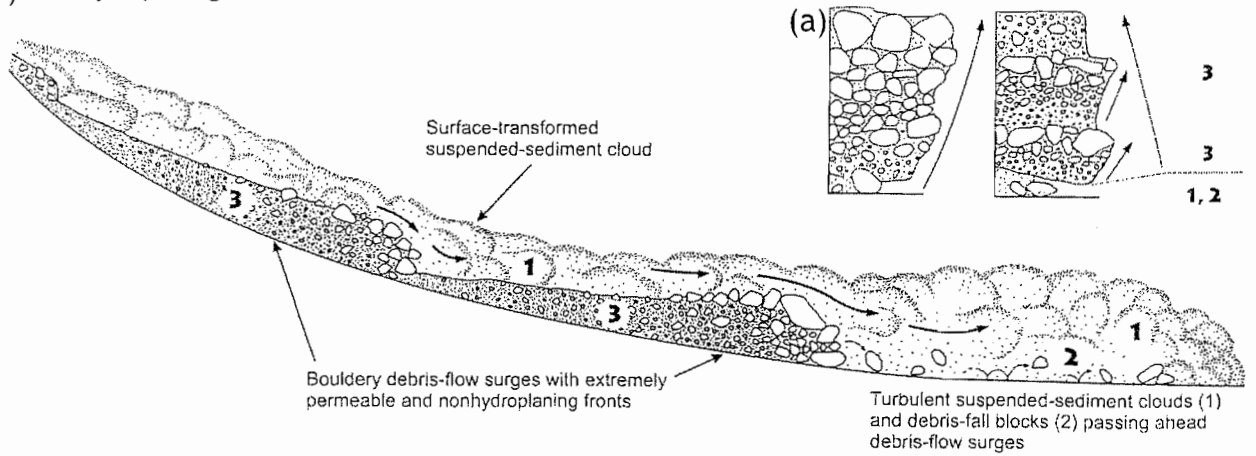
described for the fjord-hosted Kitimat Debris Flow in Alaska (Prior *et al.* 1984). Commonly, blocks dislodged from the boulder-rich flow front tumble down onto the substrate in front of the terminated debris flow and are preserved in isolation amid the ambient sediment (Prior *et al.* 1984; Sohn, 2000). Further, debris flow breccias often contain soft-sediment-deformed intraclasts of the ambient sediment in the rigid plug, while the matrix composition of the boulder-rich snout indicates disaggregation of unconsolidated sediment entrained therein (Padgett *et al.* 1984).

Fisher (1983), introduced the concept of flow transformations between laminar and turbulent flow that applies to a variety of mass flows. Debris flows may transform ‘surficially’ by yielding fine particles to a turbulent flow following above the main laminar flow, or they may transform via ‘fluidisation’; by ingestion of water and elutriation of fine particles yielding a high-density turbulent flow. In contrast, turbulent flows may transform ‘gravitationally’ by fallout of the coarse fraction and subsequent laminar flow of this fraction beneath the originally turbulent flow. Flow transformation has also been attributed to ‘hydroplaning’ of both turbulent and laminar flows on a fluid wedge, that eventually becomes gravitationally unstable and collapses, rapidly depositing a poorly sorted sediment load (Sohn, 2000). Debris flows and related mass flows may undergo constantly changing flow transformation in response to changes in the substrate gradient, flow velocity, and particle concentration (Fisher, 1984), and hence it is possible for a flow to transform several times in different ways.

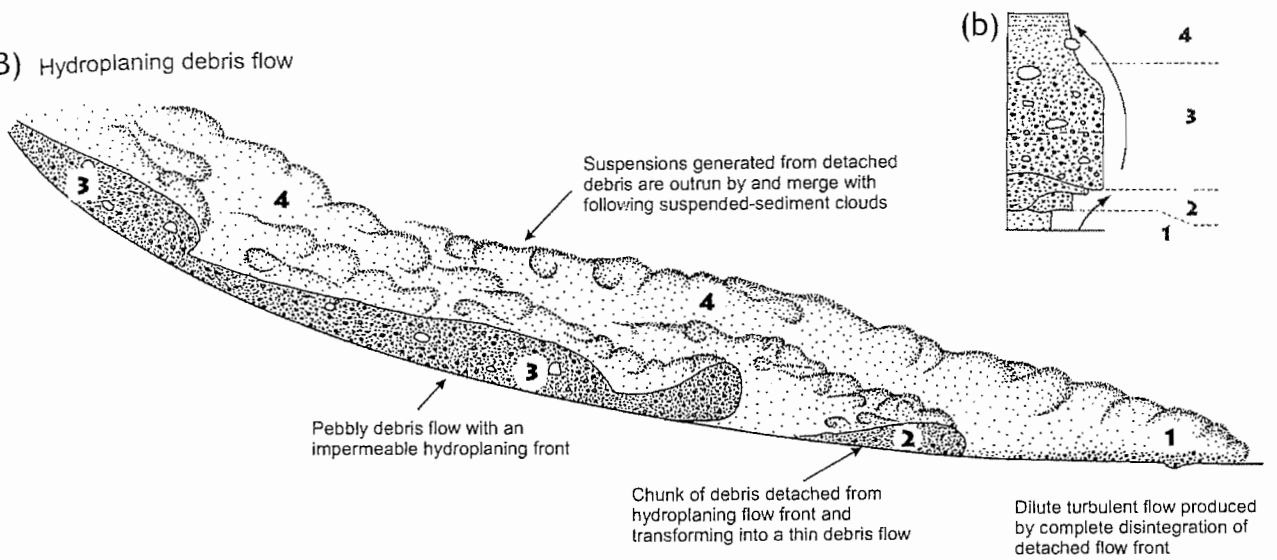
Due to the difficulty in observing modern examples, and the paucity of experimental work (Hampton 1972, Mohrig 1998), little is known about subaqueous debris flows compared to subaerial flows. Taking the assumption that surficial transformations are highly likely in subaqueous environments due to shear between the flow and water, Sohn (2000) effectively explained the features of two types of mass flow associations in the Miocene of South Korea. Reverse-graded boulder-rich flows capped by graded gravels were attributed to surficial transformation of a primary debris flow (fig.2.12), to generate a following higher-velocity turbulent flow that covered and eventually outran its precursor. These capping graded beds thicken as the debris flow thins, and are pebble-dominated. Distinctive poorly-stratified pebbly sand and silt deposits were attributed to rapid deposition from collapse of hydroplaning fine grained debris flows (fig.2.12). Similarly, Gloppen and Steel (1981) describe turbidity currents that follow, flow on top of, and outrun debris flows, as forming a turbiditic “facies belt...between the alluvial fan conglomerates

*Figure 2.12 - Diagrammatic representation of mass flow process transformations, after Sohn (2000). (A) Boulder-rich debris flow showing thickening down-flow, 'outrunner' blocks, and surficial generation of a following turbid flow. (B) Fine-grained debris flow showing hydroplaning behaviour above a thin wedge of water and subsequent collapse of the flow and rapid deposition. Idealised stratigraphic sections are presented; (a) reverse-graded clast-rich boulder bed; (b) irregularly stratified matrix-supported pebble breccia with capping turbidite.*

(A) Nonhydroplaning debris flow



(B) Hydroplaning debris flow



proper and the impinging fine deposits of the basin's axial system", in reference generally to subaqueous debris flow depositional systems (p 51).

Many debris flows occur in environments of major fluvial or submarine channel effluence into a basin, i.e in a deltaic setting, amid progradational arenitic lithologies and overbank lutites (e.g. Prior *et al.* 1984, Sohn 2000). However, debris flows are equally, if not more common in fault-scarp (line-source), 'fanglomerate'-type settings, that may penetrate into adjacent deep water basins amid laminated hemipelagic silts and sands (Padgett *et al.* 1977; Gloppen and Steel, 1981; Davis, 1983; Kessler and Moorhouse, 1984). Both the breccia and host sediment textures shown by Kessler and Moorhouse (1984) from the fault-controlled basins of the upper Jurassic of the British North Sea bear a striking resemblance to those found at HYC. In scarp-source settings, the ratio of maximum particle size/bed thickness (MPS/Bth) has been used to separate subaerial from subaqueous flows (Gloppen and Steel, 1981; Kessler and Moorhouse, 1984). In subaqueous settings there is strong covariance of bed thickness with maximum clast size, and the ratio MPS/Bth is greater than 2. This parameter should be used in conjunction with textural observations to identify subaerial flows. Indeed it is likely that in subaqueous settings MPS/Bth is very low close to source, and increases as a flow evolves and transforms such that low values may be interpreted more generally to indicate short transport distances.

## 2.6 ***Sedimentological Model for the HYC Interore Mass Flow Units.***

### 2.6.1 **Sedimentary Processes**

The mass flow units at HYC, collectively called 'interore breccias', comprise four distinct sedimentological facies (in order of proximity to source): boulder breccias, high-density turbidites, matrix-supported pebble breccias, and low density turbidites. These facies are related and occupy equivalent stratigraphic position, yet rapid transition between facies indicates that the HYC mass flows evolved stage-wise via surficial, gravitational, and hydroplaning flow transformations.

In the proximal environment, the major mass flow units that subdivide the HYC orebody are clast-rich debris flow units, represented by the closed-framework boulder-breccia facies. Debris flows penetrated the deep (100's of metres) marine environment of mineralisation, and scoured

unconsolidated and partly lithified sediment from the seafloor. All the recognised mineralisation facies are represented as intraclasts in the debris flow deposits, and hence mineralisation occurred sufficiently close to the seafloor (<5m depth) for laminated sulphidic siltstones to be available for entrainment by the debris flows. Unconsolidated sulphidic sediment was incorporated into the flow in response to highly variable internal clast reorganisation, resulting in irregular development of sulphidic (dark) matrices to the subsequent breccias. Advancing at a few metres per second, interaction between the flow surface and the standing water body caused turbulent entrainment of fine (sub-cobble) clasts in a zone immediately above the debris flow; a surficial flow transformation responsible for the generation of all the other mass flow facies. The boulder-rich flows slowed and stopped in response to a change in the basin-floor gradient, leaving a thick unsorted boulder-bed with a steep frontal geometry. The front of the deposit was in places unstable, and blocks tumbled down onto the seafloor in front of the flow. The largest of these blocks sank into the unconsolidated sediment and were completely enveloped.

Moving more rapidly than the primary debris flow, the turbulent flow continued past, and outran the breccia deposit. The dense pebbly turbidity current scoured seafloor and entrained small amounts of partly consolidated sediment. Upon loss of kinetic energy, the flow underwent a gravitational transformation in which coarse clasts ceased to be turbidly entrained, and a pebble-rich zone of laminar flow developed at the base. This zone of laminar flow also slowed and stopped at some kinetic threshold, depositing an intraclast-bearing pebbly layer. Close to the debris flow front, this layer envelops 'outrunner' blocks displaced from the top of the boulder breccia. Rarely (eg I3/4d), and probably during unusually rapid flow, such a gravitationally transformed high-density turbidity current hydroplaned, became unstable, and collapsed to rapidly deposit both the coarse sediment of the basal laminar flow and the fine sediment of the turbid flow above it.

A low density, granular-sandy turbidity current is the final product of all three flow transformations for which there is evidence at HYC. These dominate in the distal environment, and also cap all the other mass flow facies. After the higher-energy flows have dissipated, the fine turbulently entrained sediment is deposited as stratified graded beds with characteristic sedimentary structures. If several flows occur in close succession, the local fluid energy does not fall low enough for deposition of the finest silt fraction, and conversely, the greatest thickness of silt accumulates in the deepest, quietest part of the basin. Low-density turbidites that do not correspond to the inter-ore stratigraphic positions occur throughout the HYC ore sequence and are most abundant in the north and east.

These may be minor mass flow events that are restricted to a zone proximal to the major basin-controlling structure, the distal equivalent of larger mass flows that did not extend into the deeper basin environment, or may be sourced from the ramp side of the basin to the southwest.

### 2.6.2 Architecture of the HYC Sub-basin

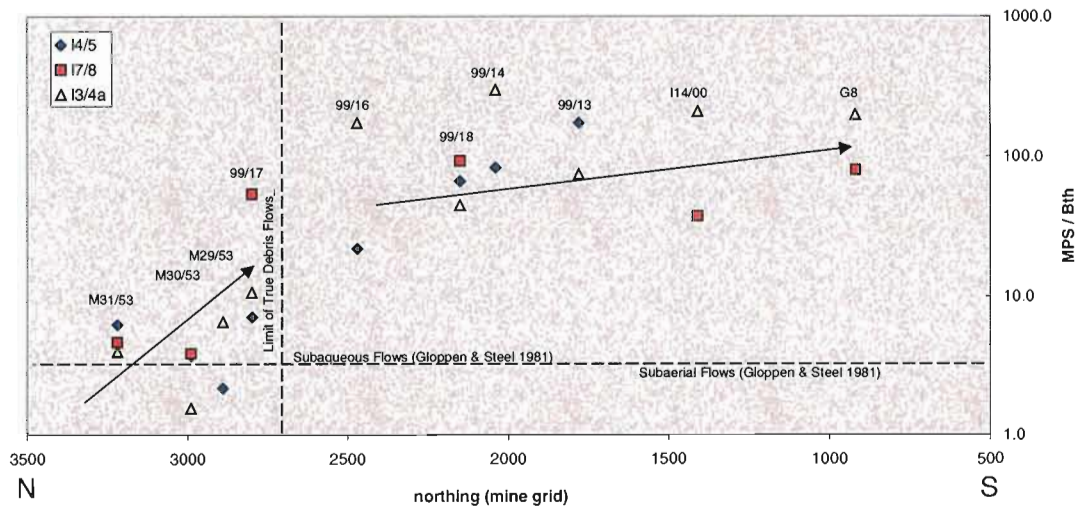
All the mass flow facies at HYC have broadly lenticular cross section, and there is no evidence for flow channelisation. The sedimentary geometry of these units was therefore controlled in the proximal environment by the initial flow composition, direction and velocity, and by the basin architecture in the distal environment.

The type 1 breccia mass flows entered the HYC sub-basin from a range of locations along its northeastern margin (fig.2.10), and flowed generally south-southwest. During the early stages of mineralisation, mass flows (e.g I1/2, I3/4b) originated northeast of the sub-basin, and the dominant flow source shifted northward (to north-northeast) during deposition of the #4 orebody and continued from that direction thereafter. Bedding thickness – clast dimension relationships of the boulder breccia facies suggest short subaqueous transport distance (fig.2.13), which together with the spatial variability of flow origins preclude a fluvial (deltaic) point source. Flow initiation is therefore thought to have occurred via slope failure along the fault-controlled eastern margin of the HYC sub-basin. The inter-ore breccias represent the toe of a S-thinning wedge of coarse clastic deposits that extends north of HYC, and marks the northern boundary of the HYC sub-basin. An inferred E-W structure that controls several other sub-basins of the Batten Fault Zone intersects the controlling eastern structure of the HYC sub-basin approximately a kilometre north of the HYC deposit. However, the prevailing flow directions are inconsistent with this intersection being the ultimate source of the fan (fig.2.15). As type 2 and 3 breccias in the hangingwall to HYC show distinct SE and NE provenance respectively, mass flow initiation occurred at a number of sites along the western margin of the Emu Fault Zone (the eastern extent of the Batten ‘Trough’) throughout the Barney Creek time, apparently unrelated to cross-cutting structures. One such clastic fan projecting west into the basins of the Batten Trough impinged upon the northern extent of the HYC sub-basin and may have served to confine mineralisation processes within the sub-basin. In the southwest the influence of the mass flows is strongly diminished, however massive dolomitic siltstone and markedly thinned stratigraphy indicate shallowing of the sub-basin in that direction beyond DDH G8. As these sedimentary trends coincide with gradual decline of base metal grade,

*Figure 2.13 - Maximum particle size / bed thickness (MPS/Bth) data for three mass flow units on a N-S section. In the proximal environment north of 2600mN this ratio describes a log-linear trend (arrow) from MPS/Bth < 2, to MPS/Bth ~ 10 that demonstrates apparent close proximity to source in the north and more fluid-like flow behaviour down-flow. South of 2600mN, values are an order of magnitude greater, representing the transition from debris flow to turbidity current.*

*Figure 2.14 - Slope calculations for three interore mass flow units. The equations presented are (i) approximated determination of yield strength  $k$  from clast size, clast density  $\nu_b$ , and flow density  $\nu_{fl}$ ; (ii) determination of theoretical yield strength from the gradient of the substrate; (iii) combination of the two previous formulae to determine likely gradient of the substrate from clast characteristics (after Johnson, 1970). Results show a  $\sim 2^\circ$  difference in gradient between the breccia-dominated fan toe and the turbidite-dominated basin.*

Max. Particle Size / Bed Thickness, HYC N-S section



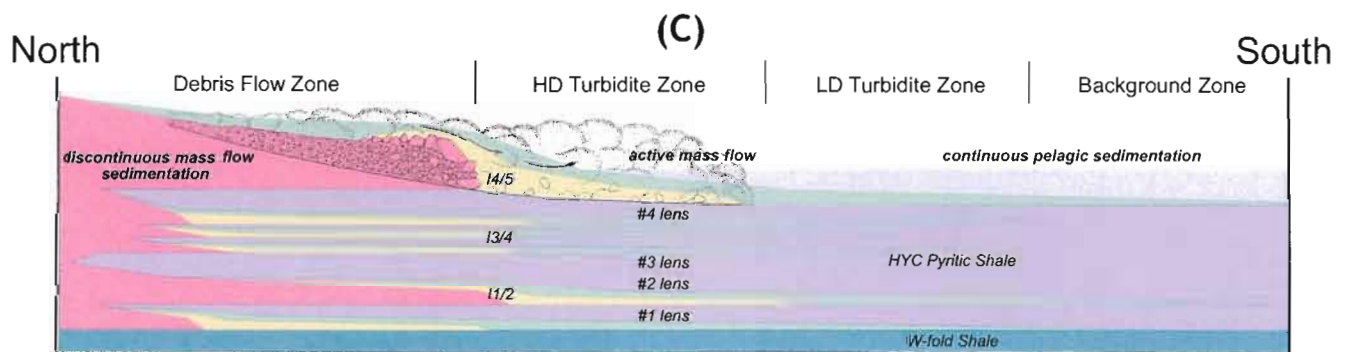
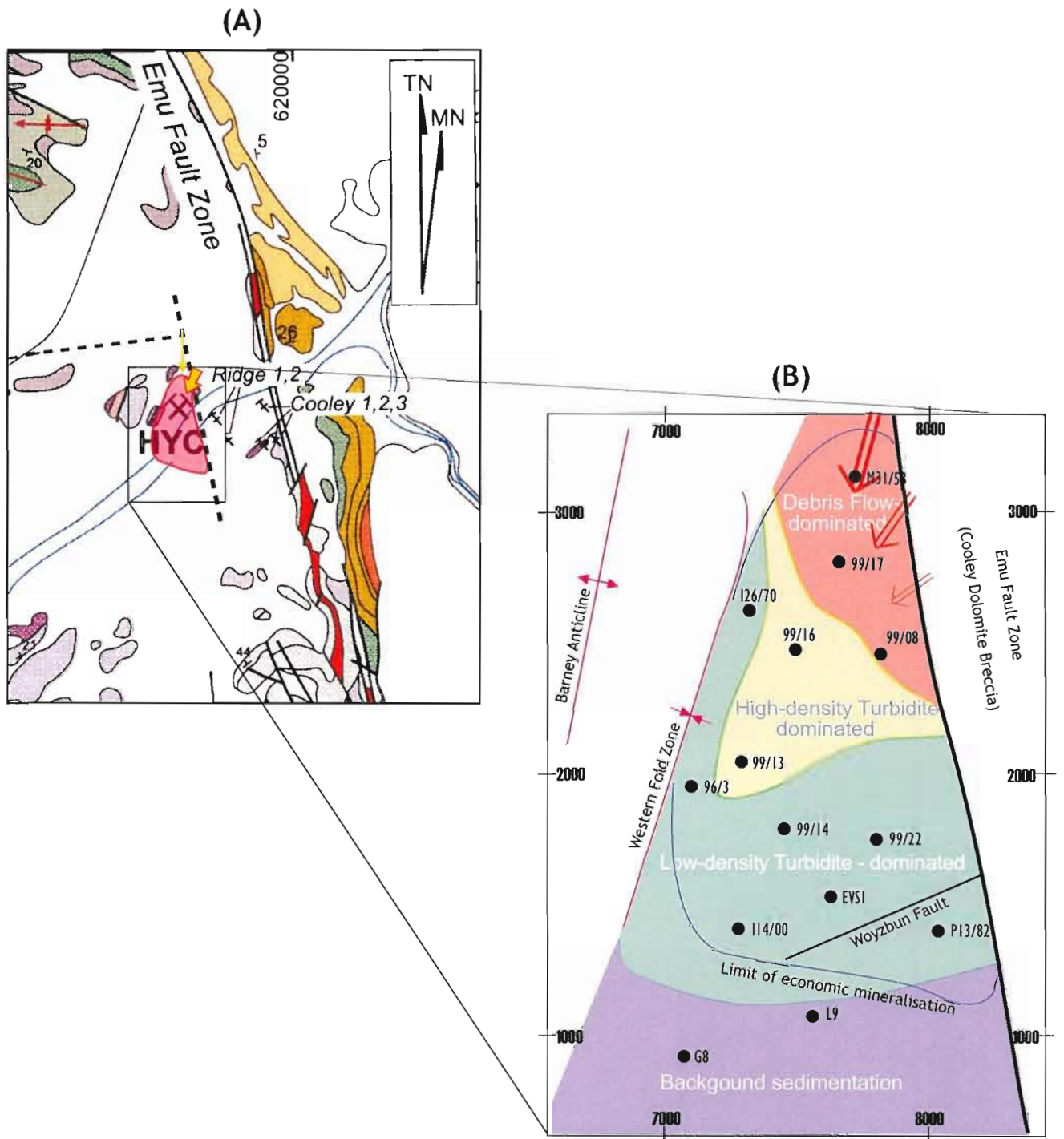
$$(i) \quad k = \frac{1}{4} MPS(v_b - v_d)$$

$$(ii) \quad k = (Bth) \cdot v_d \cdot \sin \delta$$

$$(iii) \quad \delta = \arcsin \left[ \frac{MPS(v_b - v_d)}{4(Bth)v_d} \right]$$

Mass Flow	MPS (m)	Bth (mm)	MPS/Bth	slope (deg)	flow density (g/cc)	matrix %
I5/6	2.5	2300	1.1	<b>2.7</b>	2.5	90
	3.5	850	4.1	<b>1.2</b>	2.4	43
	0.4	10	40	<b>0.2</b>	2.2	0
I4/5	4.9	2200	2.2	<b>1.5</b>	2.5	80
	8.5	3800	2.2	<b>1.2</b>	2.6	95
	1.0	16	62	<b>0.1</b>	2.3	30
I6/7a	3.0	650	4.6	<b>1.51</b>	2.19	0
	4.1	1400	2.9	<b>1.30</b>	2.47	71
	0.4	20	20	<b>0.35</b>	2.19	0

*Figure 2.15 - (a) Geology of the immediate HYC vicinity showing basin-controlling structures and the intersection of an inferred fault intersection north of the deposit. Mass flows are sourced almost a kilometre closer to the deposit than this intersection (arrows), but the E-W structure may have articulated basin subsidence. (b) HYC deposit map showing spatial relationship of mass flow facies. The edge of the debris-flow zone marks the location of a break in slope at the fan toe. Mass flows were sourced in the NE during deposition of the basal mine stratigraphy, and shifted to NNE provenance (red arrows) after the I4/5 debris flow event. The I4/5 debris flow unit marks a shift in basin architecture after which pelagic sedimentation was not focussed in the central southeastern part of the deposit. (c) Schematic N-S section showing intercalation of sedimentary facies in the HYC sub-basin. Mineralisation occupies the fine grained (blue) units in between mass flow events.*



---

mineralisation at HYC was confined to the deepest part of the HYC sub-basin.

The majority of debris flows that interfinger with mineralised shale in the deep part of the basin terminate approximately in the same location (fig.2.15), a phenomenon also borne out by the MPS/Bth data. This suggests the presence of a break in slope in that part of the basin during mass flow sedimentation; application of quantitative sedimentological equations for flow yield strength suggests slopes up to  $3^{\circ}$  on the fan, and  $<1^{\circ}$  on the basin floor (fig.2.14). Within the HYC sub-basin, the distribution of fine turbidite silty tops, and the thickness of mineralised shale describe a local depocentre in the southeast of the deposit. This has the most influence in the strata below the #4 ore lens, and the change lower grade mineralisation (ore lenses 5-8) is coincident with a shift in the source of mass flows into the basin. A discrete phase of basin evolution therefore occurred toward the end of #4 ore lens formation, the unusually intense structural activity perhaps also indicated by the greater volume and particle size of the I4/5 breccia than the other debris flow deposits. The change in mass flow provenance from type 1 to type 2 breccias takes place at the top of the HYC mineralised sequence, and a major shift in basin architecture associated with relocation of the mass flow source may have caused the decline of the HYC hydrothermal system.

### 3 SULPHIDE TEXTURES

#### 3.1 *Background*

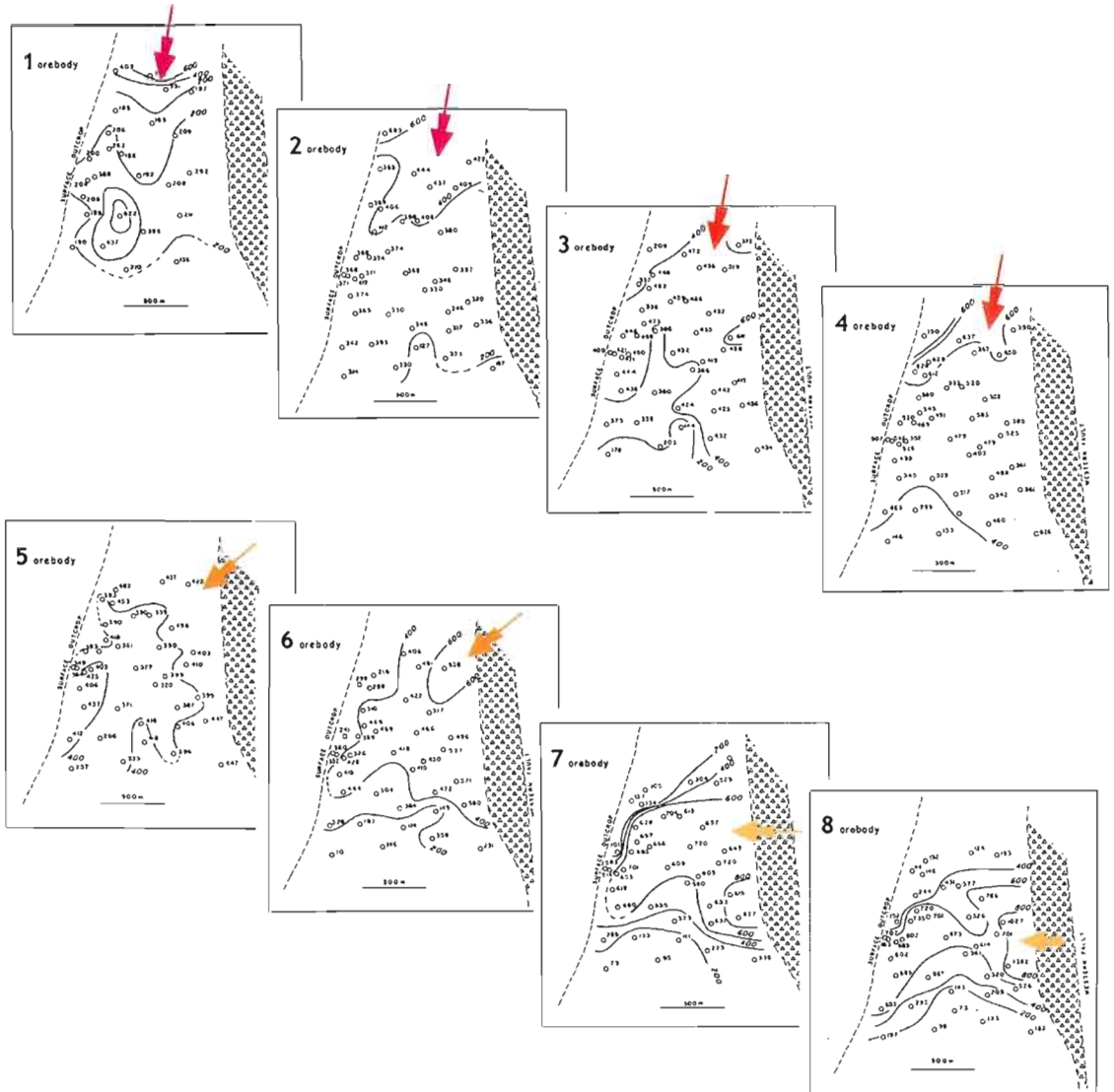
The HYC orebody has never undergone deep burial or been subject to significant tectonic stress, and primary mineral textures are well preserved (Logan *et al.* 1990). There is a broad, overlapping lateral metal zonation from Cu-Pb-Zn-Fe, the orientation of which shifts incrementally from N-S in the lower ore lenses to E-W in the uppermost ore lenses (fig.3.1a; Logan 1979). This has previously been interpreted as a manifestation of the prevailing thermal gradient during formation of each lens (Hinman 1995, 2001), but is just as likely to be caused by chemical kinetics, or subtle pH or oxidation gradients related to fluid flow geometry, independent of temperature (fig.3.1b; Cooke *et al.* 1998).

Base metals occur primarily as discrete, very fine grained sphalerite-galena laminae (<1mm thick), interspersed with quartz-orthoclase-carbonate-illite silt laminae, organic-rich mud laminae, or hybrid laminae of these end-members (Large *et al.* 1998; Blake *et al.* 2001). Pyrite is abundant throughout the mineralised intervals as fine grained euhedral crystals and as modally subordinate subhedral crystals and masses. Approximately a fifth of the base-metal sulphides occur as fine to medium-grained crystalline aggregates associated with, and possibly replacing, 'nodular' carbonates. A much smaller proportion of the base metal sulphides consists of sulphidic clasts in sedimentary breccias (Large *et al.* 1998).

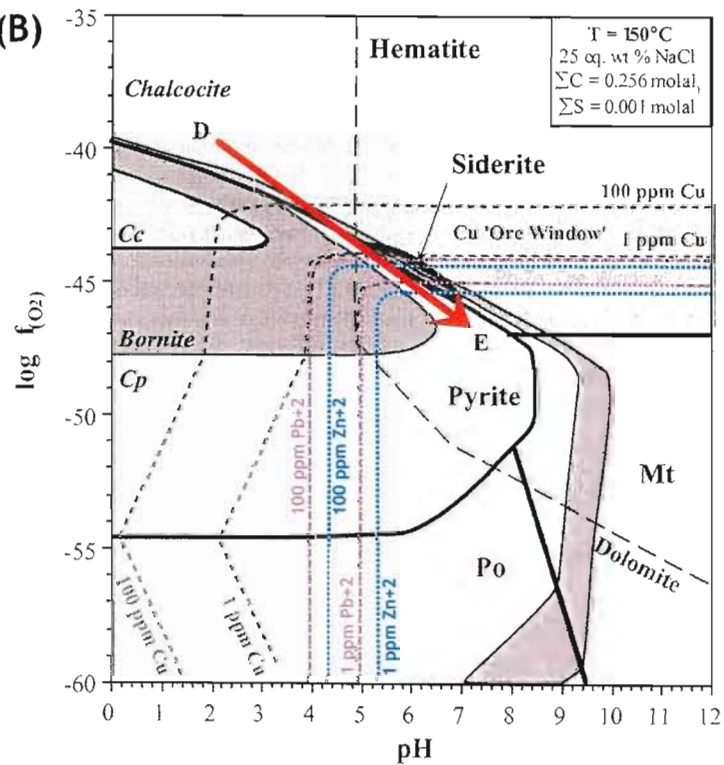
Strongly mineralised HYC siltstone appears in hand specimen, to consist of monomineralic, bedding-parallel planar laminae (fig.3.2a), but these observations are not borne out by microscopic examination. The sulphide-rich laminae are complex aggregates of up to seven variably-intergrown sulphide modes (sp1, sp2, py1, py2, cpy, gn, aspy) and locally contain intergrown quartz and ankerite (Eldridge *et al.* 1993). Likewise, apparently planar macrolaminae commonly contain distinct and characteristic internal textures (Hinman, 1996; Blake *et al.* 2001). Individual siltstone beds are continuous across the deposit (Perkins & Bell 1998), but this cannot be demonstrated for sulphide laminations because of disruption by ubiquitous cm-scale thrusts and folds, and by locally abundant gravity-driven soft-sediment deformation (Hinman, 1995).

*Figure 3.1 - (a) Plan view of metal zonation in each ore lens at HYC expressed as  $1000 \cdot \text{Pb}/\text{Zn}$ , and the interpreted direction of ore fluid entry into the mineralising system, after Logan (1979). Note the shift in orientation from N-S to E-W upsection through the mine stratigraphy. (b)  $f\text{O}_2$ -pH diagram for predicted HYC ore fluid temperature and salinity showing the solubility of copper, lead and zinc, and the likely direction of changing chemical conditions during mineralisation (red arrow). Interpretation of fluid flux geometries (a) is based on the relative solubility of the various metals that predicts sequential precipitation  $\text{Cu} \rightarrow \text{Pb} \rightarrow \text{Zn}$ .*

(A)



(B)



The interpretation of microscopic textures has been used to support various conflicting genetic models (Eldridge *et al.* 1993, Perkins & Bell 1998, Large *et al.* 1998). It is crucial to recognise that in any large geochemical system like HYC, there exists the potential locally for the development of an infinite number of textural relationships. Therefore, to characterise the most important and dominant aspects of the system overall, and draw inferences for mineralisation processes, it is necessary to examine a large number of samples from representative locations throughout the deposit.

### 3.2 **Methods**

Textures and sulphide modal abundances were described from 58 polished thin sections by visual estimation using a standard petrological microscope and reflected light illumination. The results were compiled with drillhole data to demonstrate the distribution and spatial relationships between phases, and contoured manually (due to the inability of automated interpolation algorithms to yield sensible results for widely spaced datasets of 10-20 points). Gangue mineralogy was identified using the backscattered x-ray spectra produced in the scanning electron microscope facility of the University of Tasmania's Central Science Laboratory (CSL). The metal zonation images presented are interpolated surfaces (kriging algorithm) from the McArthur River Mine metallurgical database.

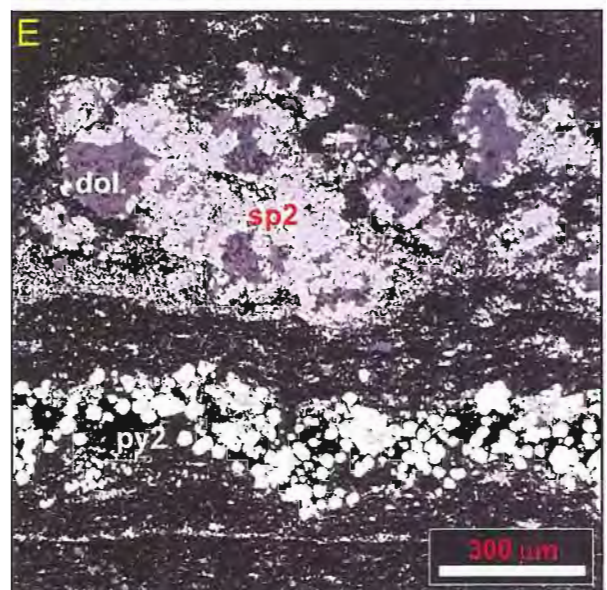
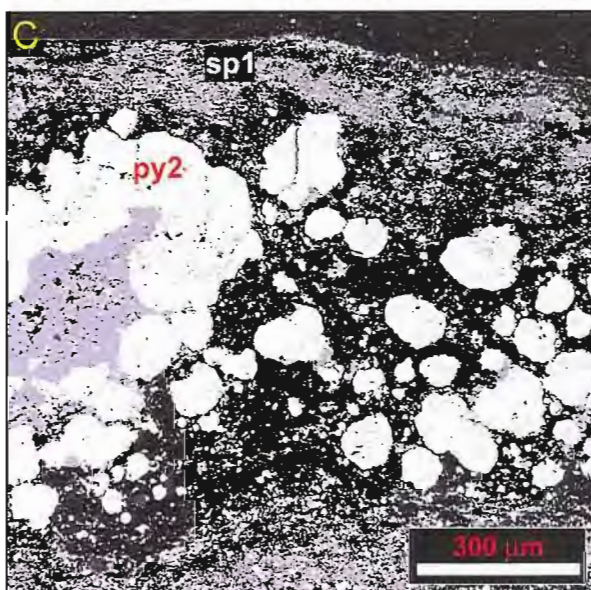
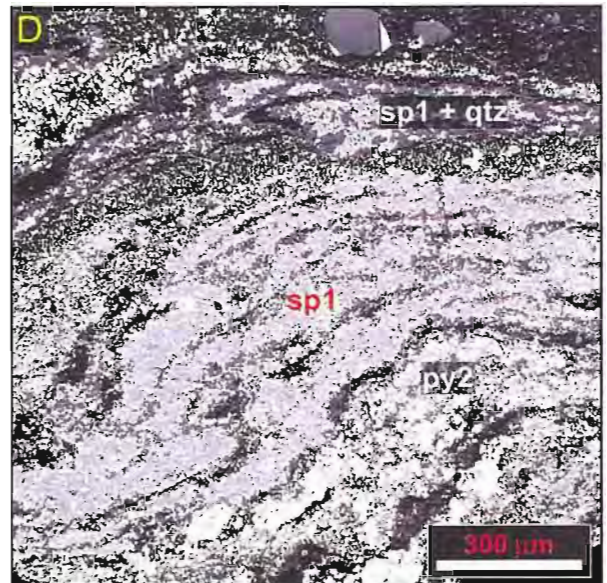
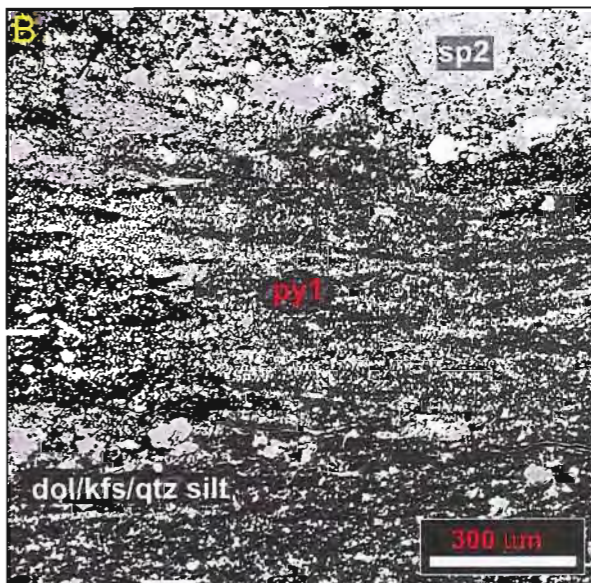
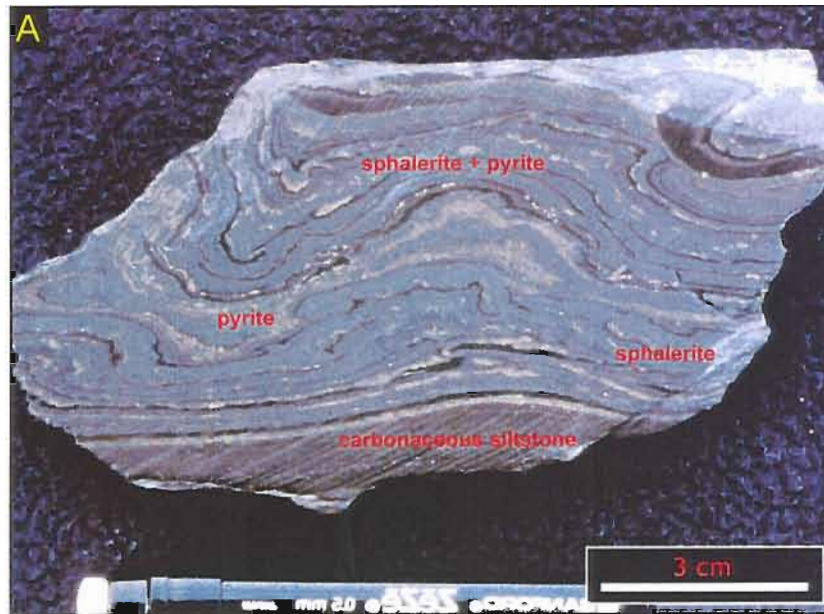
### 3.3 **Sulphide Textures and Distribution**

#### 3.3.1 **Definition of Sulphide Modes**

##### **Pyrite Mode 1** (fig.3.2b)

Mode 1 pyrite (py1; Williams, 1978; Eldridge *et al.* 1993) is ubiquitous in the HYC stratigraphy and makes up about 90% of all pyrite in the zone of economic mineralisation. Py1 occurs as euhedral to subhedral, octahedral (and rarely cubic) crystals 5-10  $\mu\text{m}$  wide, as disseminated single crystals, loosely packed spherical framboids, tightly packed round to ellipsoid "macroframboids" (Croxford and Jephcott, 1972), and as wispy strings of crystals subparallel to the sedimentary lamination. It is distinguished from pyrite 2 by its consistent fine grain size and sharp crystal shapes.

*Figure 3.2 - (a) Hand specimen of laminated sulphide ore from HYC showing apparent monomineralic nature of sulphide laminae and pre-lithification folding. (b-e) Reflected light microphotographs (RLM) of typical HYC sulphide modes; (b) wispy trails of py1 in barren siltstone; (c) coarse pyrite 2 aggregates in a sphalerite 1 lamina; (d) sphalerite 1 with strong anastomosing internal lamination defined by quartz crystals; (e) nodular carbonate lamina strongly replaced by sphalerite 2 and a discrete pyrite 2 lamina.*



**Pyrite Mode 2** (fig.3.2c)

Mode 2 pyrite (py2; Williams, 1978; Eldridge *et al.* 1993) is volumetrically minor, but is a distinctive sulphide phase confined to the base metal-mineralised stratigraphy at HYC. Based on textural indications that suggest a common post-basemetal mineralisation relative age, all pyrite that is not py1 has been included in this category. Py2 occurs as fine to coarse (10µm – 1mm), anhedral to subhedral crystals, crystal aggregates, blebs and as also as overgrowths on py1. Sulphur isotope data (chapter 7) support the validity of grouping the highly variable non-py1 pyrites in this way.

**Sphalerite Mode 1** (fig.3.2d)

Mode 1 sphalerite (sp1) is the most abundant form of this mineral at HYC, representing >80% of all sphalerite in the deposit (Large *et al.* 1998). Sp1 often commonly as an “apparent grain cement...which may enclose many non-sulphide grains” (Eldridge *et al.* 1993). Sp1 is here defined as very fine grained (1-10µm) cryptocrystalline sphalerite that takes the form of irregular elongate and blebby, fine-grained aggregates (2-200 µm thick) that coalesce and combine to define sphalerite-dominated laminae (0.2-1mm thick) within carbonaceous siltstone. It is characteristically associated with euhedral ankerite crystals (100-500 µm wide,  $\text{Ca}_{52}\text{Mg}_{30}\text{Fe}_{13}\text{Mn}_4$  – chapter 6) and euhedral quartz crystals (10-200 µm wide).

**Sphalerite Mode 2** (fig.3.2e)

Mode 2 sphalerite (sp2) is the second most abundant sphalerite mode at HYC, comprising 15-20% of all sphalerite (Large *et al.* 1998), and locally up to 100% in zones of abundant nodular carbonate development. Sp2 consists of 10µm-1mm crystalline aggregates that are, by definition, associated with nodular, micritic or clastic carbonates. Sp2 usually occurs as variable replacement of sparry to micritic ‘nodular’ carbonate aggregates (0.5-4mm thick).

### 3.3.2 Microscopic Sulphide Textures

**Pyrite 1**

Pyrite 1 is a minor component of the entire deep-water facies of the Barney Creek Formation, but is abundant (5-60 vol.%) in and around the HYC deposit. Siltstones of varying py1 abundance are described here as *weakly pyritic* (2-10 vol.%), *pyritic* (10-30 vol.%), or *pyrite-flooded* (30-60 vol.%).

*Weakly pyritic* siltstones contain py1 as sparse disseminations and isolated macrolaminae (0.5-2mm wide) defined by abundant py1. The py1 in these laminae occurs as random disseminations and as discrete wispy trails of crystals (fig.3.3a,b), which are locally associated with similar wispy domains of micritic carbonate (fig.3.3c,d). The laminae edges (both top and base) are variably sharp or diffuse. Sphalerite in weakly pyritic siltstones is restricted to py1-rich laminae. *Pyritic* siltstones account for most of the strongly Zn-mineralised stratigraphy. Planar to crenulated lamination is defined by local absence of py1, or by the nature of co-occurrent sphalerite (fig.3.3e,f,g). Py1 is locally more abundant in fine-grained and organic-rich laminae, and is intimately associated with sphalerite and nodular carbonates in the deposit fringe. *Pyrite-flooded* siltstones occur as discrete laterally continuous layers within the mineralised stratigraphy. Gradation from *pyritic* to *pyrite-flooded* usually occurs over a stratigraphic thickness of 15-30 cm at base of *flooded* layers. Py1 occurs as very abundant disseminated crystals in siltstone that has minimal internal texture (fig.3.4h) except for widely spaced irregular laminae described by low py1 abundance (fig.3.3i,j).

Py1 is variably framboidal, and occurs both as loose round frambooids with diffuse edges (<50 $\mu$ m), and as dense circular to ellipsoidal frambooids with sharp edges ('macroframbooids', <200 $\mu$ m; Croxford and Jephcott, 1972). There is a complete range of macroframbooid shapes (seen in 2 dimensions) from circles (fig.3.4a), to true ellipses (fig.3.4b,c,d), to parallel-sided ellipses (fig.3.4e), which is probably an artefact of variable orientation of one elongate morphology relative to the section observed. Rarely, elongate macroframbooids have several nodes along their length, and appear segmented (fig.3.4f). The macroframbooids are morphologically very similar to some Mesoproterozoic bacterial microfossils (fig.3.4g; Horodyski and Donaldson, 1980), and pyrite replacement of *tasmanites* cysts produces similar sharp-edged forms (fig.3.4h; Schieber and Baird, 2001). Macroframbooids are usually either abundant (20-50%) or absent, whereas diffuse true frambooids are rare overall and only occur in weakly pyritic siltstones. Laminae of high py1 abundance, and often highly macroframbooidal py1, occur adjacent to the base of many nodular carbonate laminae.

*Figure 3.3 - RLMs of pyrite 1; (a) wispy trails of py1 in weakly pyritic siltstone. Note that py1 reaches maximum abundance immediately below a nodular carbonate lamina; (b) detail of py1 trails and a diffuse, water-column-generated framboid in a weakly pyritic siltstone; (c) wispy carbonate domains in highly carbonaceous, weakly pyritic siltstone; (d) coexisting laminae of abundant disseminated py1 (top & bottom) and weakly pyritic laminae with wispy carbonate domains; (e) macrolamination defined by py1 abundance or absence and internal 'crinkly' lamination; (f) typical crinkly py1 laminae in pyritic siltstone; (g) pyritic siltstone showing lamination defined by low py1 abundance in sp1 and coarse silt laminae, and characteristic wispy transition of py1 abundance between laminae; (h) uniform flooding of siltstone with py1; (i) pyrite-flooded siltstone with plastic ?load deformation on a lamina base; (j) thin wispy anastomosing organic-rich, py1-poor laminae in py-flooded siltstone.*

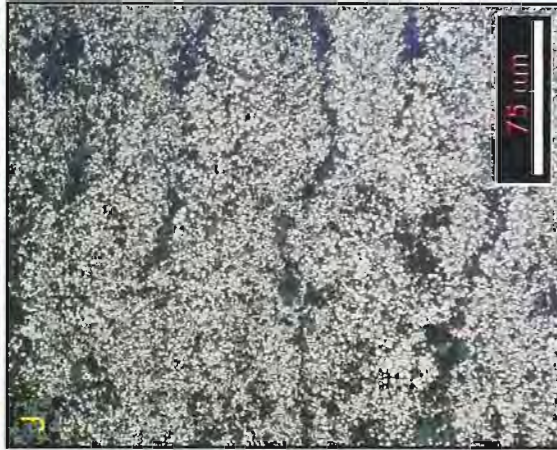
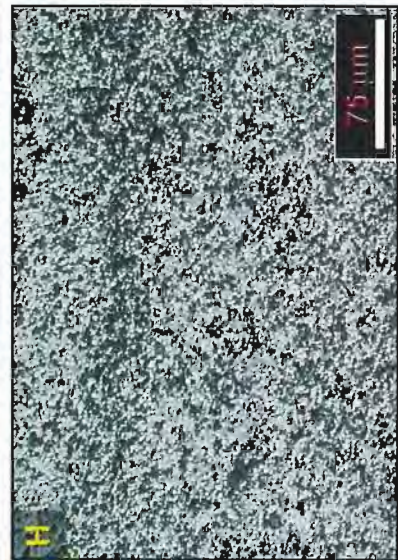
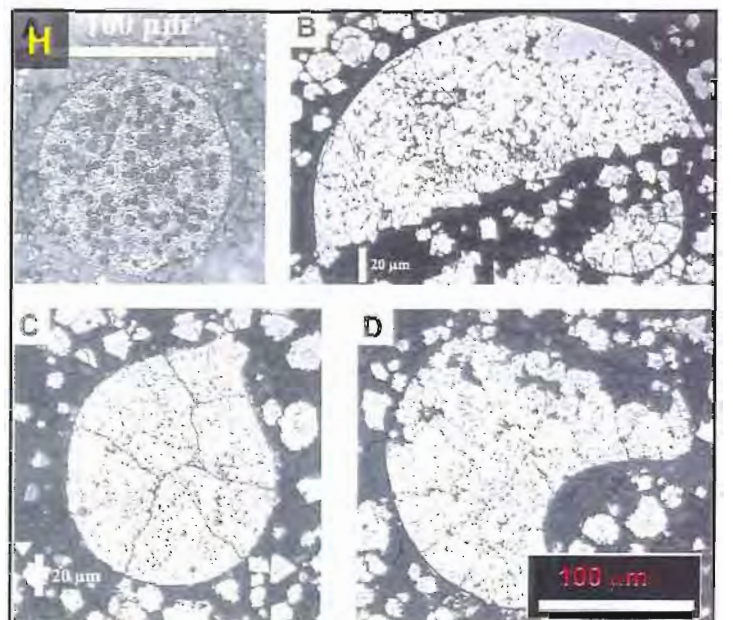
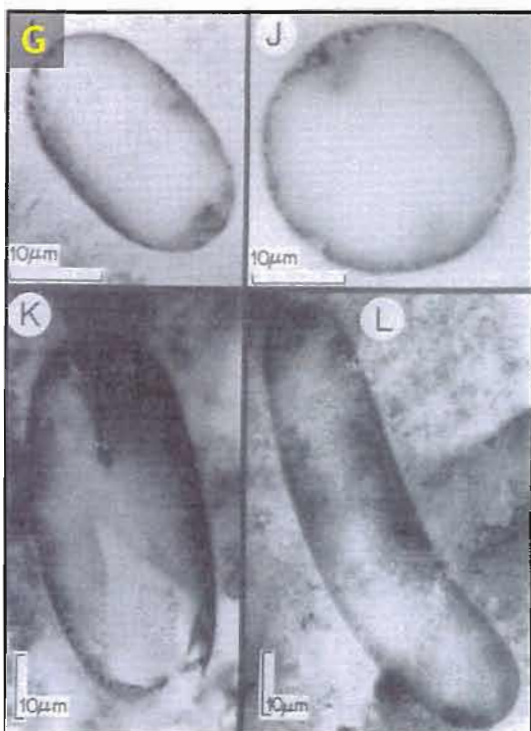
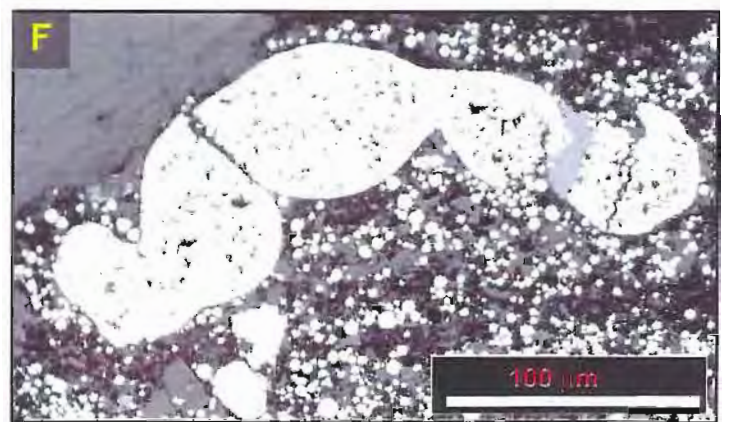
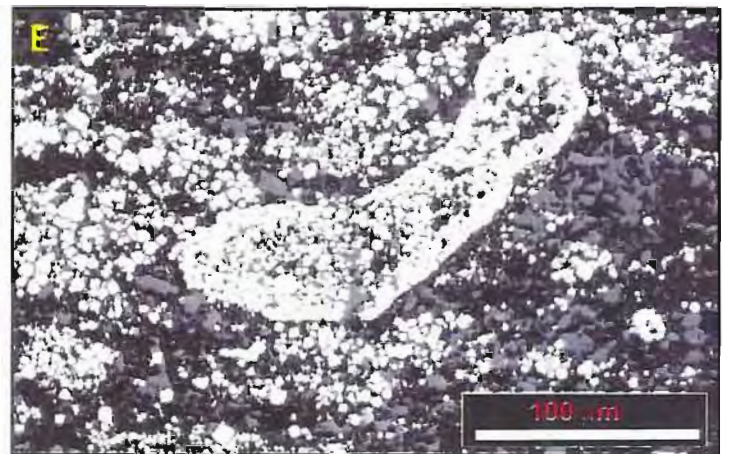
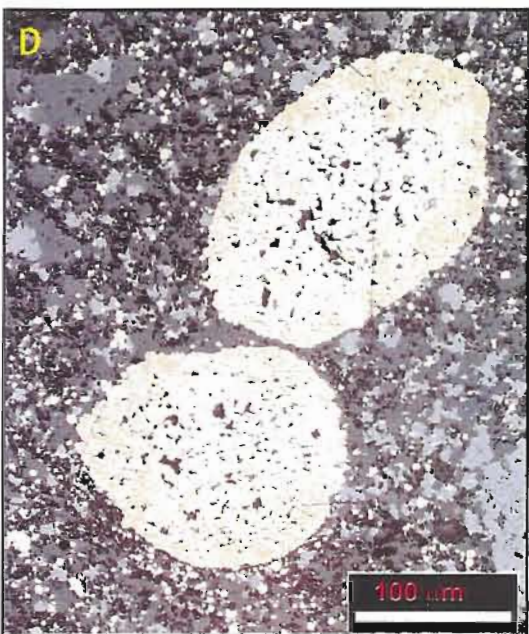
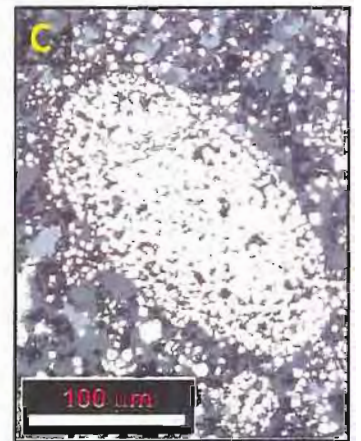
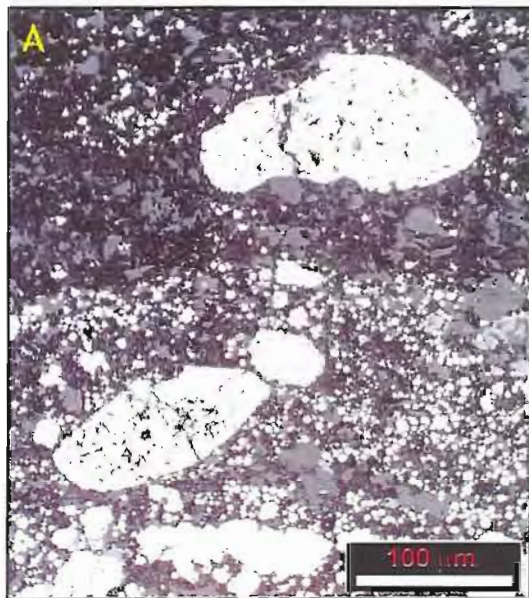


**Figure 3.4** - A variety of pyrite I 'macroframboids' and visually similar microfossils; (a) ellipsoidal macroframboids in adjacent pyritic and weakly pyritic laminae; (b) diffuse macroframboid, but note persistent sharp edges; (c,d) common round and ellipsoidal massive macro-framboids with sharp boundaries; (e) elongate macroframboid with diffuse centre; (f) elongate and globular 'segmented' massive macroframboid; (g) round, ellipsoidal and elongate *Oscillatoriaceae* microfossils preserved in chert from the Mesoproterozoic Dismal Lakes Group (Horodyski and Donaldson, 1980); (h) massive pyritised *tasmanites* cysts from Devonian black shales of the Chattanooga Shale, USA (Scheiber and Baird, 2001).



### *Sphalerite 1*

Sphalerite 1 is characterised by its extremely fine grain size, an abundance of inclusions of both sulphide and non-sulphide minerals, and by the presence of distinctive anastomosing internal lamination within the macroscopic plane lamination.

The internal texture of the macrolaminae has been referred to as 'stylolaminated' (Hinman 1996), alluding to a possible origin by dissolution, and as 'interlaminar gangue fabric' (ILGF; Blake *et al.* 2001), describing the concentration of inclusions that define the internal lamination. The texture is not consistently developed throughout the deposit, nor is it simply defined. There are two characteristics of sp1 that are variable throughout the deposit: the strength and 'density' of ILGF anastomosing lamination, and the apparently inverse relation between abundances of pyrite 1 and quartz-ankerite inclusions. The ILGF lamination varies systematically throughout the deposit (fig.3.5), whereas the type and abundance of inclusions shows either subtle, or no lateral zonation, and therefore the genetic processes responsible for each are not directly linked.

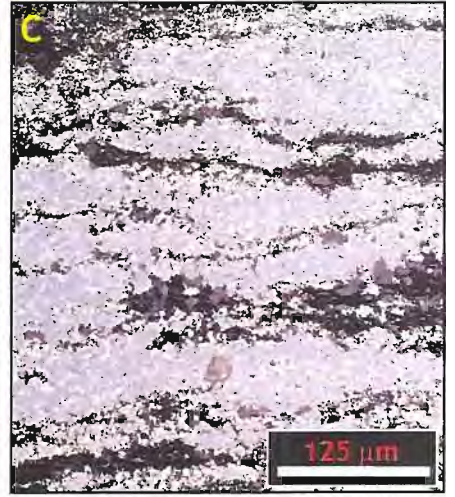
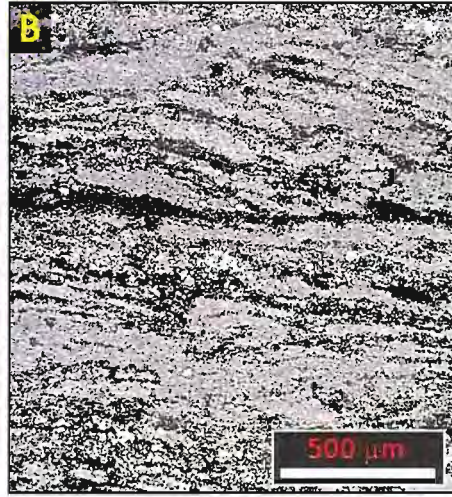
Strongly developed ILGF texture is ubiquitous in the high grade part of the deposit. Each macrolamina consists of irregularly stacked and amalgamated lensoidal sphaleritic domains (100-500  $\mu\text{m}$  long) that are separated by thin trails of organic and clastic material, and py1 (fig.3.5a,b,c). Peripheral to the high grade zone, the lensoidal sp1 domains are more dispersed within each macrolamina (fig.3.5d,e). In the extreme fringe of the deposit, sp1 domains include numerous silt clasts and occur as ragged elongate zones of silt cementation by sp1 (fig.3.5h,i). Untextured, laterally continuous planar laminae of sp1 as thin as a single domain described above are also irregularly developed in the low grade fringes of the deposit (fig.3.5f,g). Sp1 also occurs as a pervasive grain cement in laminae with sharp tops and diffuse bases, and which sporadically includes round structures reminiscent of py1 macroframboids (fig.3.6a). Sp1 laminae that exhibit different textural styles occur adjacent to each other (fig.3.6b,c,d), and have been mapped according to subjective determination of the dominant texture in any one sample. The gradational change of internal textures across the deposit fringe give the impression of declining intensity of the same domain-generative process.

The textural variety of sp1 is accompanied by variation in the associated gangue mineralogy. All the textural variations of sp1 may include between 0 and 50 vol% py1 crystals (fig.3.6e,f,g), and up to

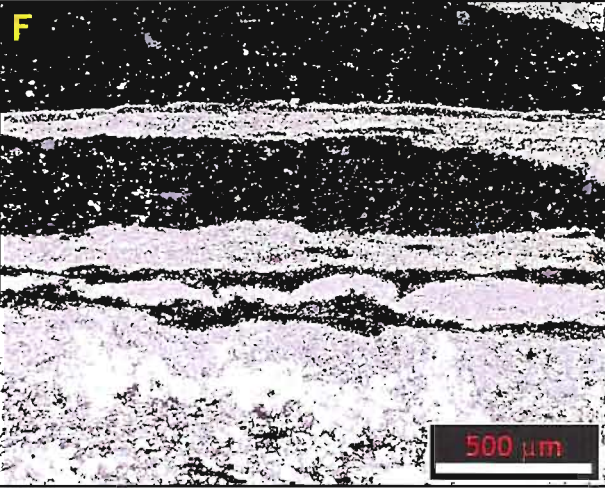
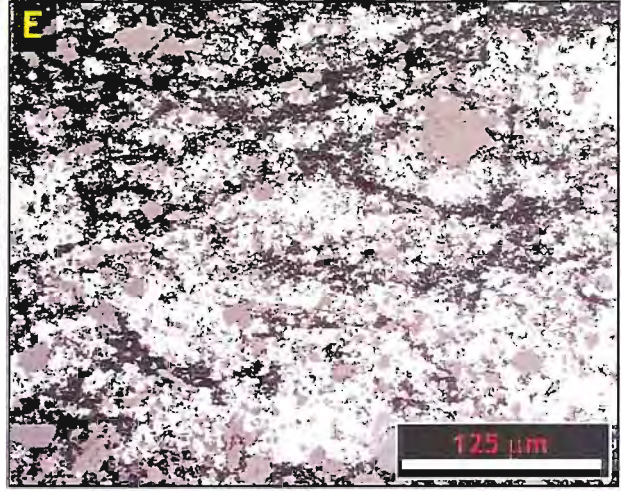
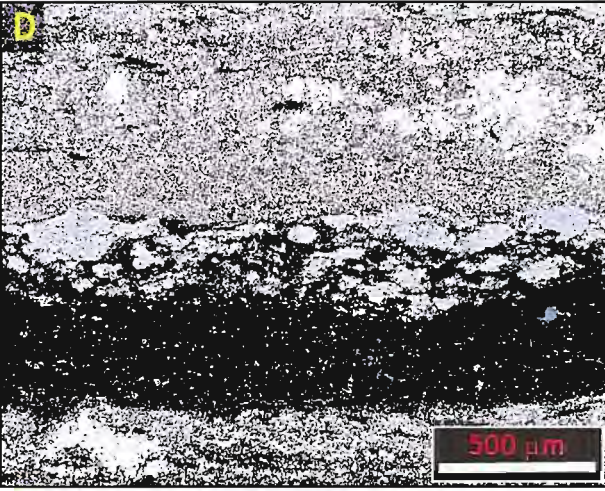
*Figure 3.5 - Detail of sp1 textural variation; strong to weak interlaminar gangue fabric (ILGF) vertically top to bottom, with increasing magnification L to R; sphalerite is light grey, silicate and carbonate silt is dark grey, and pyrite is white-yellow. (a-c) Pervasive sp1 with strong anastomosing ILGF; (d,e) abundant sp1 with weak ILGF and separate sp1 domains; (f,g) isolated discrete continuous plane laminae of sp1; (h,i) sparse, diffuse laminae of small wispy sp1 domains. Note that the extreme deposit periphery is represented by either the plane-laminar or wispy laminae textures.*

increasing magnification →

high grade (centre)



moderate grade (proximal fringe)



low grade (distal fringe)

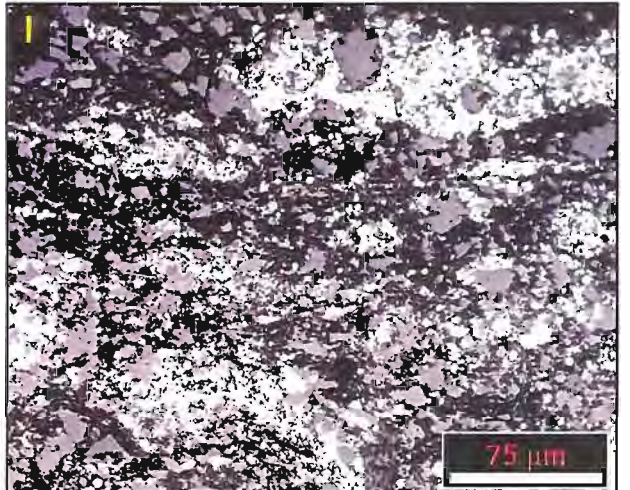
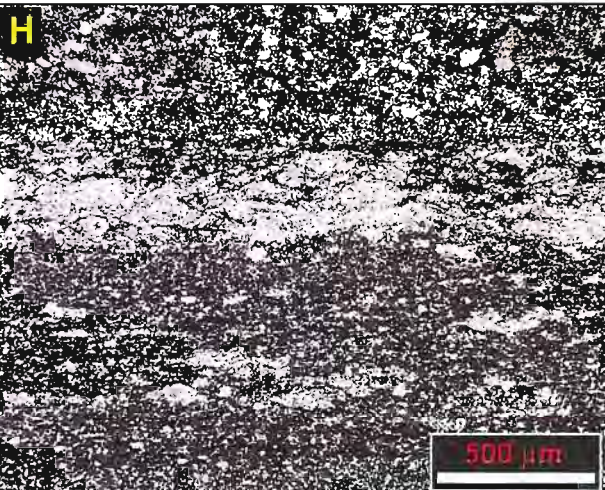


*Figure 3.6 - Sphalerite mineralogical and textural relationships; (a) flooded sp1 lamina with unusual round sp1 form similar to py1 'macroframboids'; (b) coexisting flooded and strong ILGF sp1 laminae. Note the random 'cement'-like behaviour of sp1 in flooded laminae, bottom; (c) coexisting laminae of 'laminar' sp1 and sp1 with intermediate ILGF typical of the deposit fringe; (d) strong ILGF sp1 showing sharp tops and bases of individual planar macrolaminae; (e-g) sp1 laminae of strong ILGF, laminar, and diffuse textures, respectively, showing insensitivity of the the abundance of py1 inclusions to sp1 texture.*

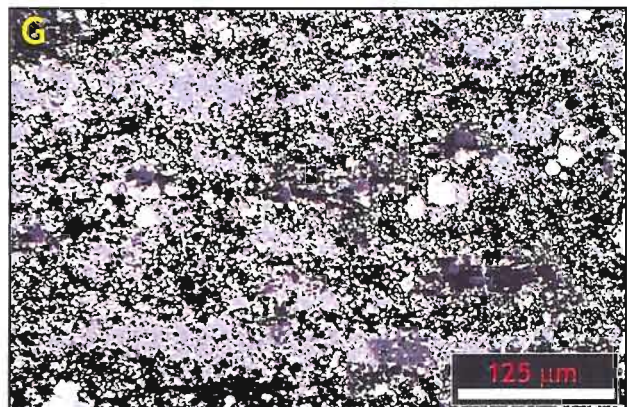
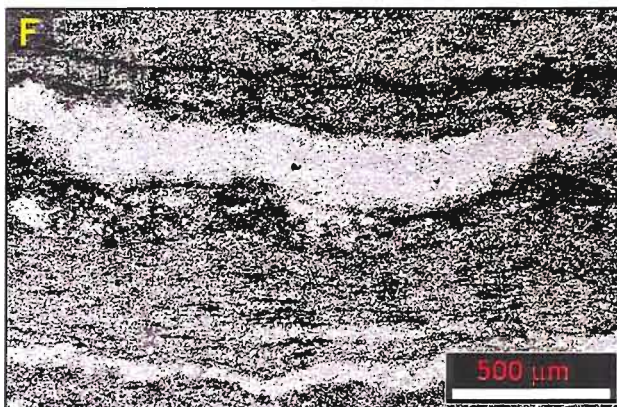
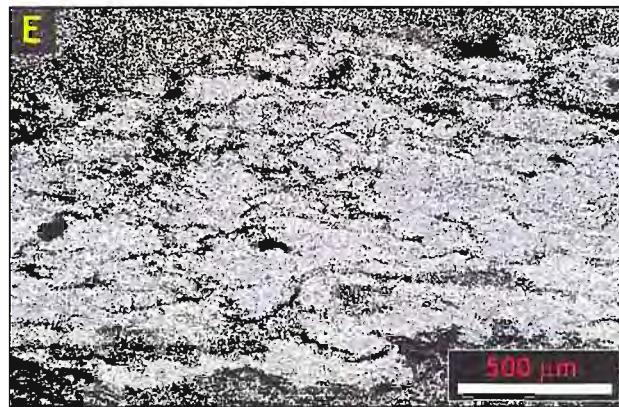
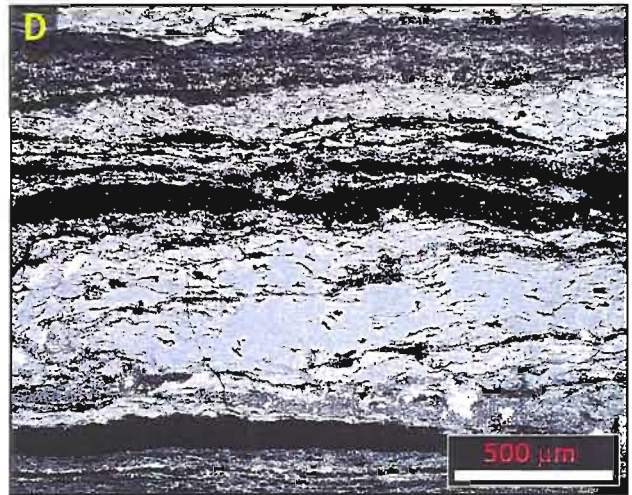
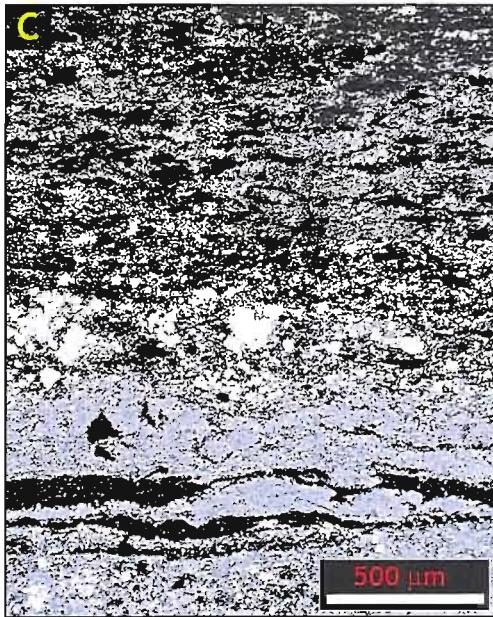
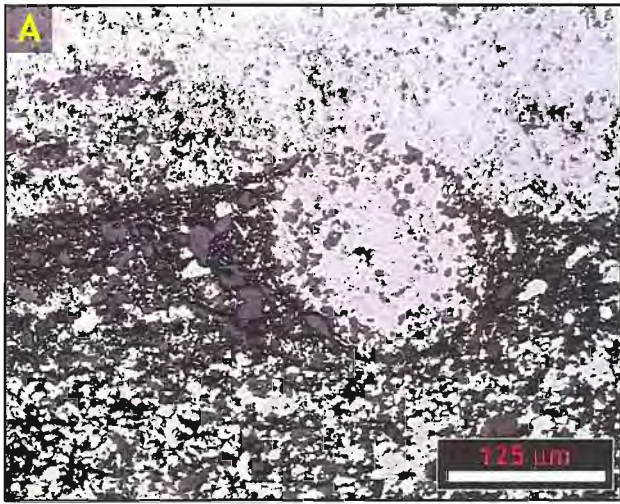


*Figure 3.7 – Textural relationships between sp1 and gangue phases; (a) ILGF internal lamination in sp1 defined by concentration of quartz crystals, clastic grains, and organic material; (b) adjacent laminae of apparently exclusive quartz-rich and pyrite-rich sp1; (c) quartz nucleation on the base and top of an sp1 lamina; (d) detail of a quartz-rich sp1 lamina showing exclusion of pyl relative to adjacent siltstone lamina; (e) zonation of sp1 lamina from quartz-rich base to pyritic top; (f) another zoned lamina, with prismatic euhedral quartz crystals and a large ankerite rhomb that is truncated at the edges of the lamina; (g) pyl and arsenopyrite (aspy) inclusion in euhedral quartz crystal, and chalcopyrite (cpy) replacement of ankerite rhomb; (h) ankerite rhombs in an sp1 lamina showing numerous sphalerite inclusions and nucleation on an internal lamination (top).*

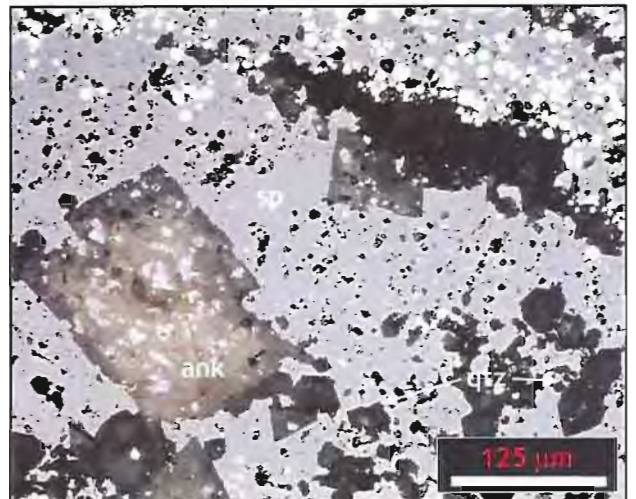
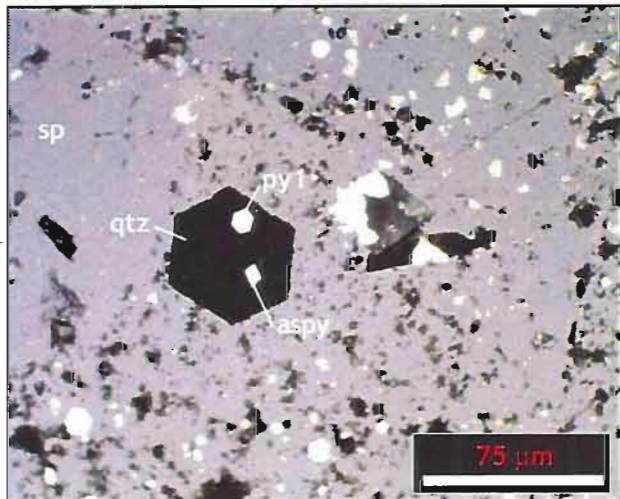
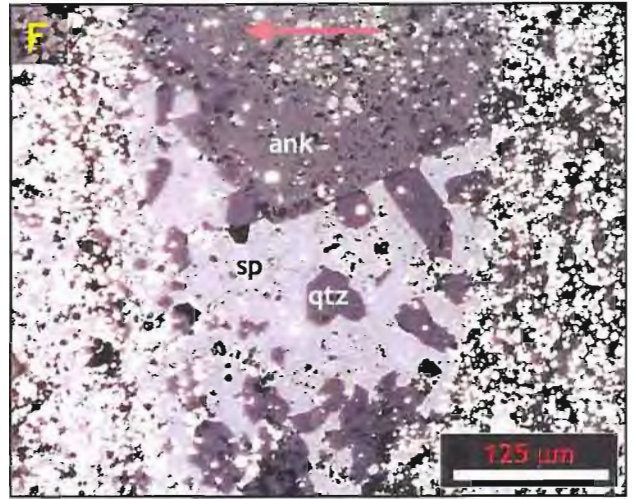
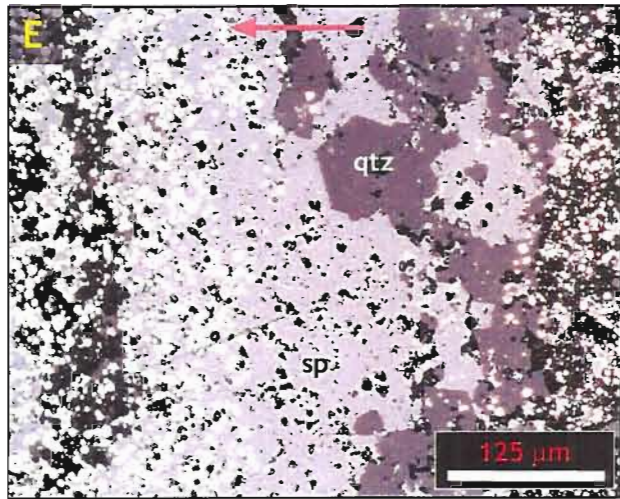
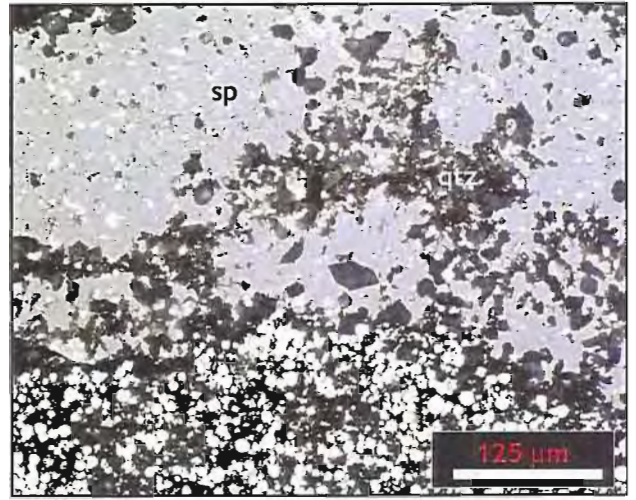
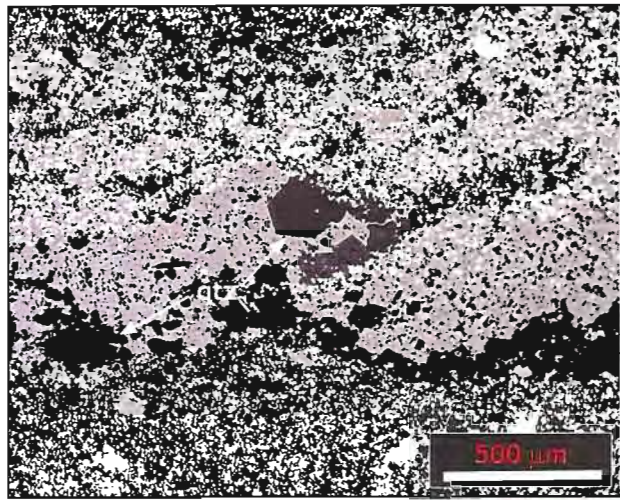
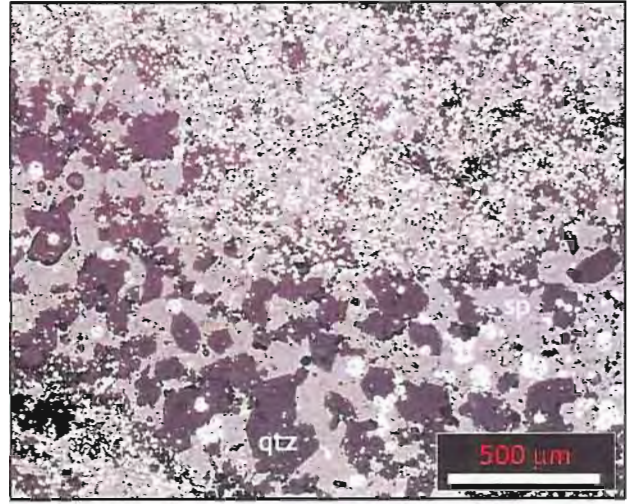
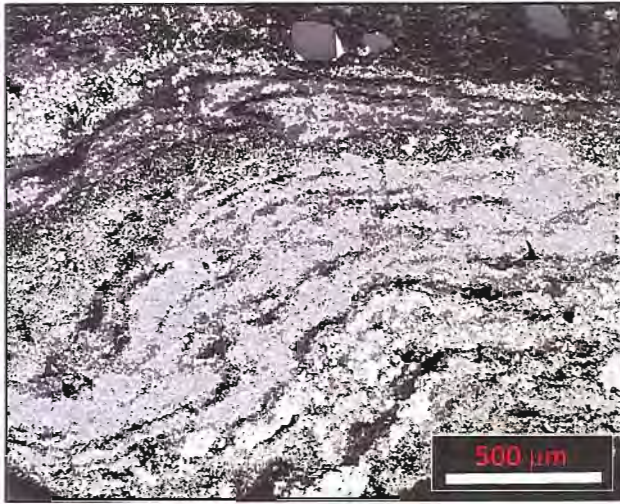
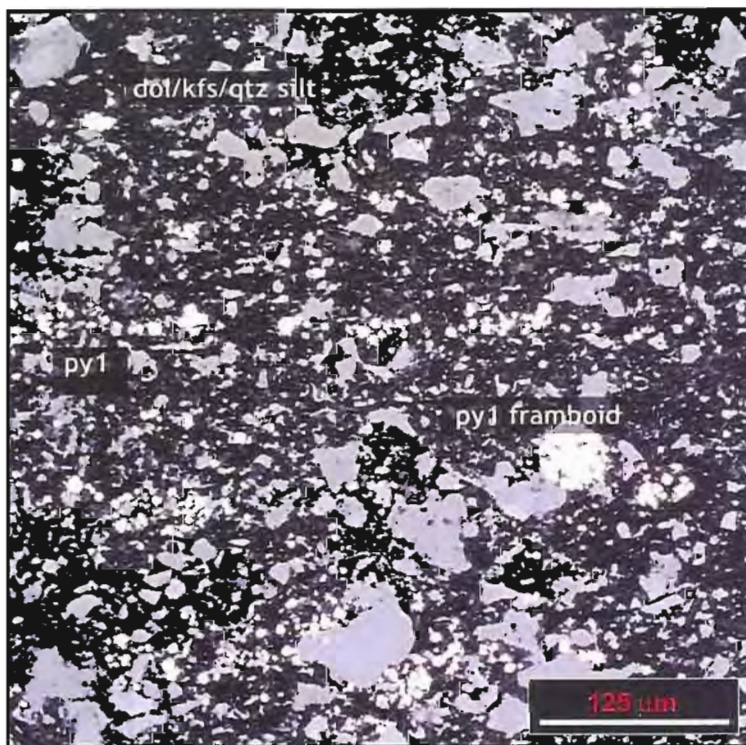
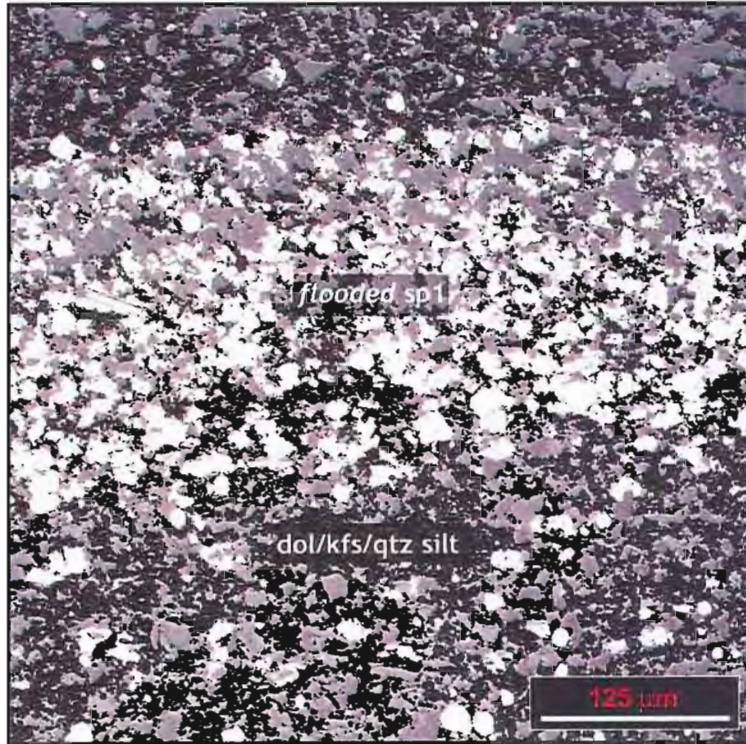


*Figure 3.8 - Comparison of (a); a sp1-flooded lamina dominated by inorganic silt clasts, and (b); a barren carbonaceous siltstone lamina that is markedly more coarse-grained than (a) and also contains abundant dark ?organic material, to demonstrate the insensitivity of sp1 occurrence to grainsize or organic content of individual laminae. Laminae of unmineralised silt are variably of the same grainsize, finer, or coarser, than adjacent mineralised laminae, and consequently there is not likely to be permeability control on laminated base metal mineralisation.*



50 vol% euhedral quartz and ankerite crystals up to 100 $\mu$ m and 400 $\mu$ m long, respectively (fig.3.7 all plates). Quartz and ankerite crystals tend to nucleate on the laminae bases and internal laminations in sp1 (fig.3.7a,c,d,e), and ankerite crystals are commonly truncated at the boundaries of a sp1 lamina or domain (fig.3.7f). Quartz commonly encloses py1 crystals, whereas ankerite usually contains numerous inclusions of sp1 (fig.3.7g,h). Quartz and ankerite occur together, but occur specifically in sp1 that has few py1 inclusions (fig.3.7b,c,d) or in which py1 is confined to the ILGF internal laminations. Similarly, strongly pyritic sp1 is never accompanied by quartz and ankerite crystals. Further still, there is distinct and consistent zonation in untextured laminar sp1, from quartz-ankerite-bearing sp1 at the base, up to quartz-ankerite-poor (strongly pyritic) sp1 at the top (fig.3.7e,f). This gangue mineral zonation has consistent orientation and is recognised in discrete planar sp1 laminae throughout the deposit fringe. Overall, there is a weak trend to more abundant silicate and carbonate inclusions in sp1 (and fewer py1 inclusions) in the high grade part of the deposit. Several genetic models invoke subtle permeability variations in the laminated siltstone to control lamination of sp1. However, no clear relationship between sphalerite abundance and siltstone grain size has been recognised in this study, and barren siltstone laminae (fig.3.8a) are commonly more coarse-grained than adjacent mineralised laminae (fig.3.8b).

### ***Sphalerite 2***

Sphalerite 2 (sp2) has relatively uniform texture. It occurs with, and appears to mimetically replace, nodular carbonates, micrite laminae, and carbonate clasts of mass flow units. Carbonate nodules and clasts are usually rimmed with sp2 and retain a carbonate core (fig.3.9a,b,c,d), but may occasionally be completely replaced (fig.3.9b, top) or have internal textures selectively replaced. Sp2 domains are usually monomineralic and clean of inclusions except for the py1 and ?organic inclusions of the precursor carbonate (fig.3.9e), and rarely contain euhedral quartz and ankerite. Diffuse sp1 and sp2 commonly occur in adjacent laminae and retain textural distinction (fig.3.9d,f), and all phases are uniformly overprinted by py2 (fig.3.9g).

### ***Pyrite 2***

Although texturally variable, py2 shares consistent relationships with the host sulphidic siltstone and is usually confined to discrete laminae (fig.3.10a,b). Acid etching has shown that where possible, py2 selectively nucleates on py1 crystals (Eldridge *et al* 1993, Blake *et al.* 2001). Anhedral crystals clotted aggregates of py2 displace the enclosing laminations (fig.3.10c,d), and are

*Figure 3.9 – RLMs of sp2; (a) fine sp2 rims on nodular carbonates (NC); (b) almost complete sp2 replacement of NC; (c) strong sp2 coronas around lone carbonate nodules in a py1-rich laminae; (d,f) adjacent occurrence of sp1 and sp2, and displacement of sp1 laminae by NC; (e) detail of sp2 replacement of NC showing lack of sp2 influence on py1 distribution; thick sp2 coronas on NC; (g) laminar py2 overprint of NC and sp2.*

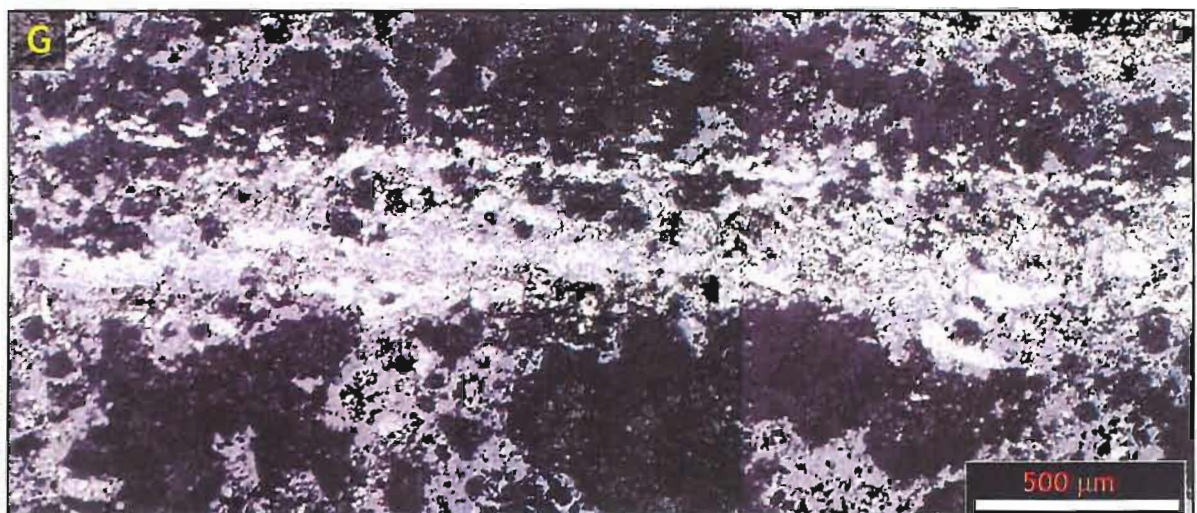
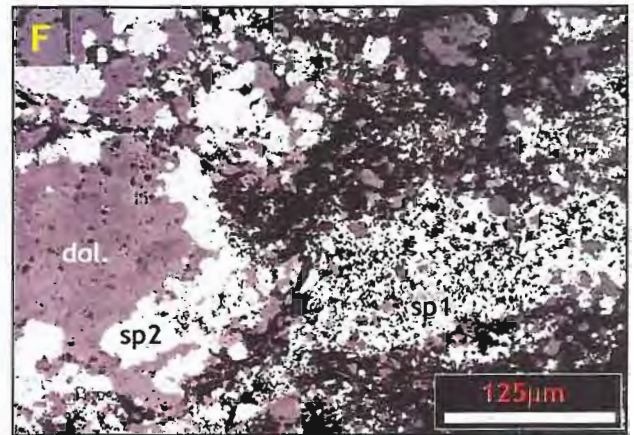
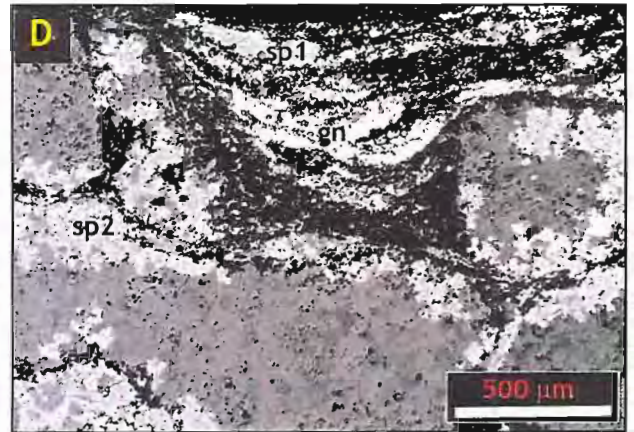
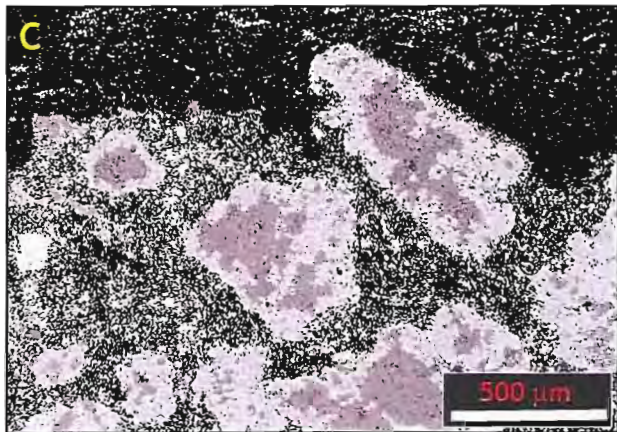
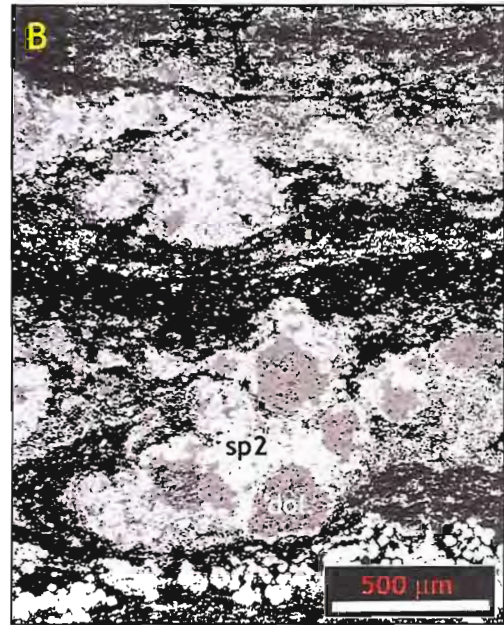
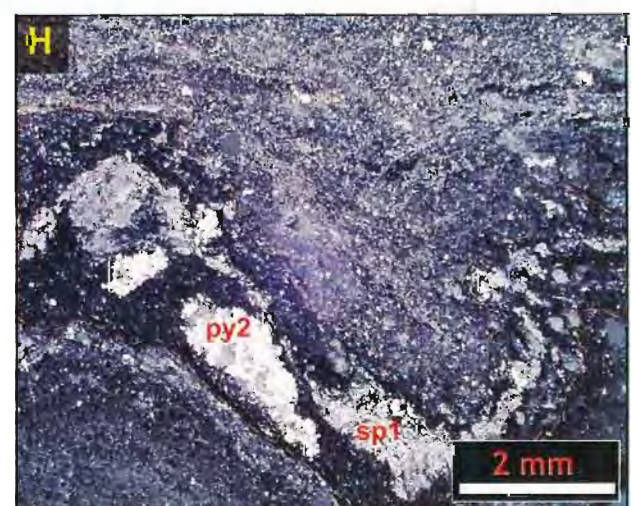
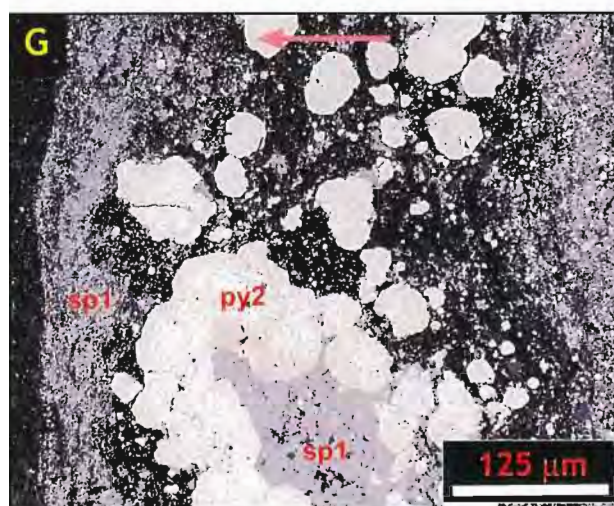
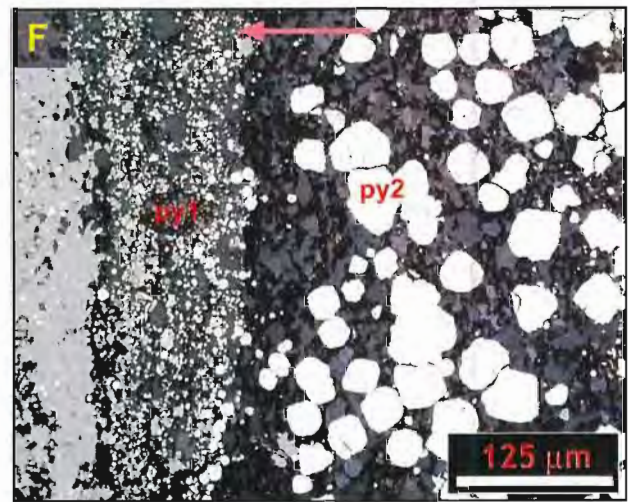
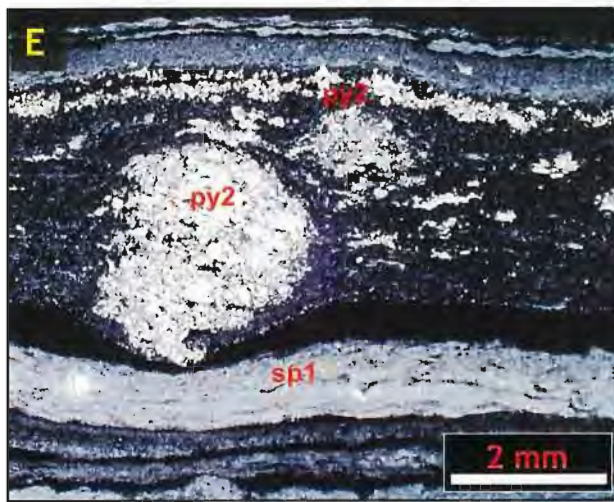
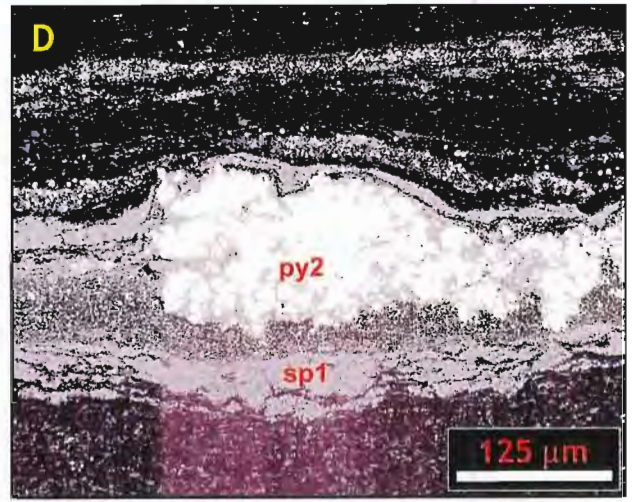
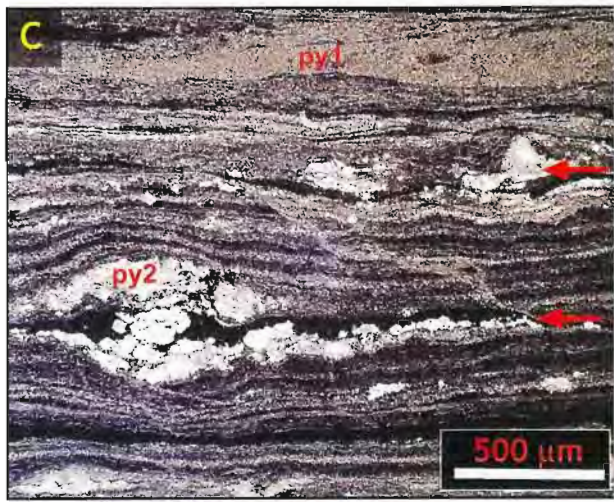
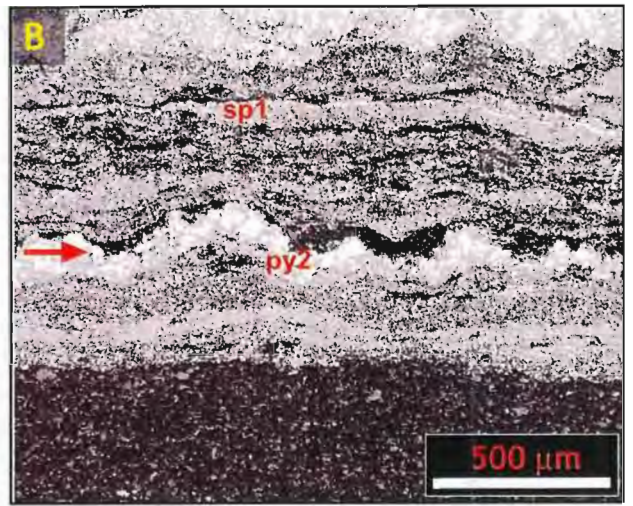
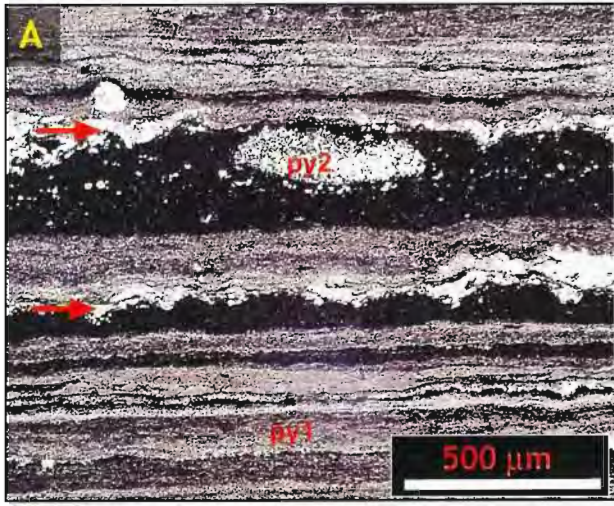


*Figure 3.10 - RLMs of py2; (a) concentration of py2 aggregates in discrete laminae (red arrows) and in the upper part of siltstone laminae; (b) sp1 laminae strongly overprinted by py2 (red arrow). Note the preferential buckling of py2-bearing lamina, which suggests rheological contrast between py2 aggregates and surrounding sediment; (c) discrete py2-bearing laminae (red arrows) in siltstone flooded by py1, with several displacive py2 clots; (d) clotted py2 growth in a sp1 laminae showing accommodation of displacement by the immediately adjacent siltstone; (e) large displacive py2 clot and concentration of py2 at the top of a siltstone lamina; (f) subhedral py2 crystals at the top of a siltstone lamina, showing confinement of py2 to this lamina, and grainsize contrast between pyrite modes. Pink arrow is up. (g) py2 growth in a sp1 laminae associated with clean recrystallised sp1 (left), and subhedral crystals of py2 (pink arrow is up); (h) laminated sulphide clast (orange line) from a mass flow breccia containing all the characteristic sulphide modes at HYC. Mineralisation was complete prior to seafloor erosion by the debris flows.*



commonly concentrated in a discrete lamination near the top of otherwise barren siltstone laminae (fig.3.10a,e,f), or in embayments of the underside of nodular carbonate laminae. Py2 also nucleates in, permeates, and locally expands sp1 laminae, associated with recrystallisation of sphalerite to clean monomineralic domains (fig.3.10g; Blake *et al.* 2001). The relationships between sulphide phases, including py2, are unchanged in sulphidic clasts in the mass flow facies (fig.3.10h).

### 3.3.3 Intergrowth Relationships and Paragenesis

#### *Pyrite 1*

Py1, both as individual crystals and framboids, occurs as inclusions in sp1, sp2, py2, nodular carbonates and micritic carbonates. Laminations, defined by variability in py1 abundance are displaced by carbonate nodules and py2 aggregates. These observations confirm previous conclusions that py1 is the earliest sulphide phase to form in the HYC mineralising system (Eldridge *et al.* 1993, Large *et al.* 1998). The framboidal nature of some py1 indicates formation in aqueous suspension via the ferromagnetic iron sulphide greigite (Kribek, 1975; Wilkin & Berner 1997), and therefore syn-sedimentary timing of py1 precipitation is suggested. However, there is a consistent and complex relationship between gangue minerals that accompany sp1 and the abundance of disseminated py1 inclusions in sp1 (section 3.3.2) that suggests an intimate temporal relationship between formation of py1 and sp1, and possibly even contemporaneous formation.

#### *Sphalerite 1*

Lamination defined by the abundance or texture of sp1 is consistently displaced by py2 and by nodular carbonates that precede sp2. The relationships between sp1 and py1 are considered to indicate spatially separated simultaneous formation, but sp1 is displaced by nodular carbonates and is consequently an early phase in the paragenetic sequence, even if considered independent of py1.

#### *Ankerite*

Ankerite occurs with sp1, and rarely with sp2, as non-corroded euhedral rhombic crystals that contain abundant sp1 inclusions. As ankerite crystals are often truncated by the boundaries of sp1 laminae, it formed after establishment of the laminated texture, but was not crystallographically inhibited by the sphalerite itself and therefore probably formed very shortly after, and before consolidation of coexistent sp1.

**Quartz**

Quartz occurs intimately associated with sp1, and rarely sp2, but includes py1 and nucleates on the base of sp1 laminae. It therefore formed after py1 and sp1, but before the nodular carbonates, sp2 and py2.

**Sphalerite 2**

Sp2 occurs with and replaces nodular carbonates, and preserves the patterns of py1 internally within the precursor carbonate nodules. Py2 overprints both nodular carbonates and sp2. Since the nodular carbonates displace py1 and sp1, sp2 must form after these phases, but precedes py2.

**Pyrite 2**

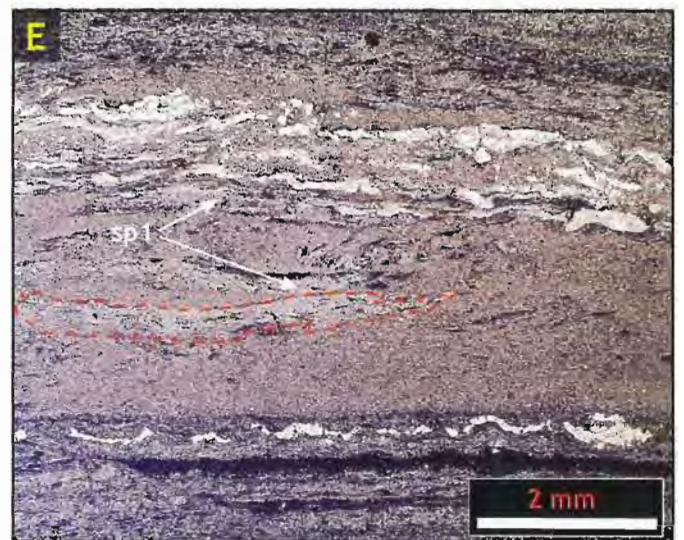
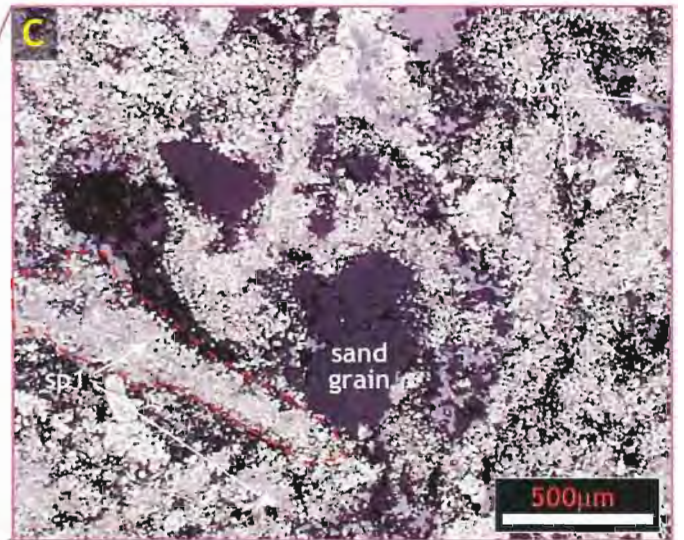
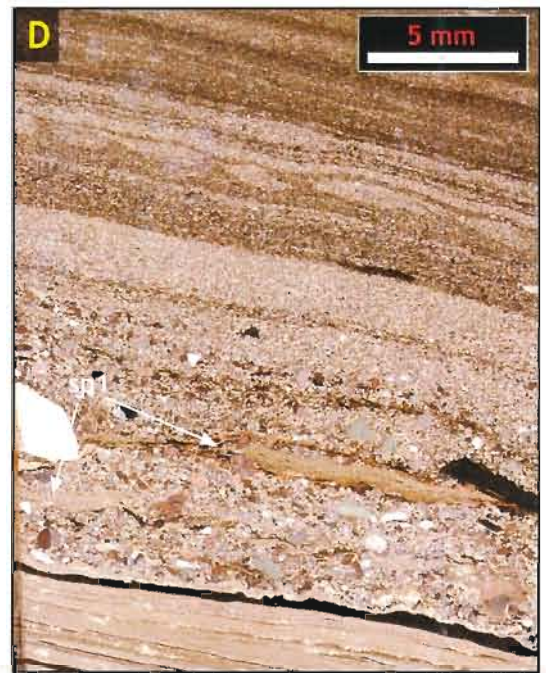
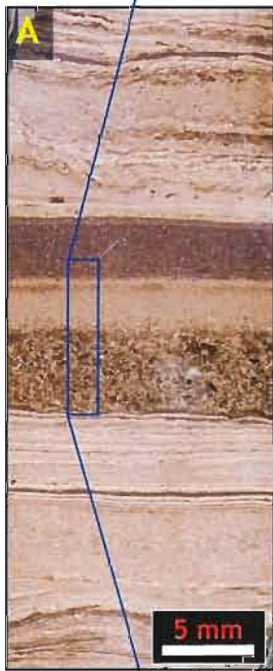
Py2 displaces or overprints all other minerals associated with mineralisation at HYC. It is therefore the latest sulphide phase in the paragenetic sequence.

**3.3.4 Timing of Mineralisation**

Mass flow breccias contain intraclasts of laminated sulphide material that are texturally and isotopically identical to in-situ laminated mineralised siltstone (ch.2). These intraclasts contain the entire suite of minerals associated with mineralisation (fig.3.10h), and therefore the entire sequence of sulphide deposition had finished prior to erosion of the seafloor sediments. Because the mass flow breccias scour up to 5 metres into the unconsolidated sediment pile, mineralisation is constrained to this uppermost part of the sediment pile. Preservation of the fine laminated sulphide structure in coherent clasts further suggests that mineralisation was associated with localised early diagenetic consolidation of the sediment.

Intraformational slump breccias up to 5mm thick are common in the laminated sulphidic siltstones, and indicate that minerals precipitated during mineralisation formed competent laminae within a largely unconsolidated sediment pile. Py2, nodular carbonates and sp1 all occur as clasts in these breccias (fig.3.11e). There are also rare thin stratified and graded turbiditic beds <20mm thick that are dominated by fragments of sp1 laminae texturally identical to primary laminated sp1 (fig.3.11a,b,c). Disaggregated sp1 in the matrices of larger mass flow units (ch.2) indicate that coherent pieces of sp1 are not preserved in high energy flows, and therefore, these thin turbidites

*Figure 3.11 - Detail of sp1 intraclasts in various clastic facies (an example is traced in orange on each plate); (a-c) progressively closer view of a 1cm-thick stratified turbidite bed. The basal layer is composed almost entirely of elongate and plastically deformed fragments of py1-bearing sp1, whereas the middle layer is largely made up of fine sulphide particles, and the upper layer is fine-grained organic, carbonate and silicate clasts. The small scale of this bed, and the preservation of sp1 clasts is interpreted to reflect local sediment source and a relatively low-energy flow. Consequently, mineralisation is constrained to the top few decimetres of the sediment pile; (d) laminated sp1-bearing siltstone clast in a low density turbidite; (e) sp1 fragments in an intraformational breccia layer. The ability of laminated sp1-bearing siltstone to remain coherent in such dynamic sedimentary and diagenetic environments suggests that mineralisation was associated with localised partial lithification of sulphidic laminae as 'hardgrounds' in the largely unconsolidated sediment pile.*



represent material from local events, such as minor slumping of unconsolidated sediment containing sphaleritic hardgrounds. They are unlikely to contain material from deeper than half a metre below the sediment-water interface. The hardgrounds have been coarsely fragmented during turbulent flow and are deposited in the base of the small turbidite because they comprise the coarse fraction of the sediment load. Unconsolidated fragments remain in suspension longer and settle out as the upper strata of the turbidite; first a fine sulphidic layer, then a fine organic-rich silt layer. Consequently, basemetal mineralisation can be constrained to the uppermost few decimetres of the sediment pile; a conclusion which coincides with unequivocal syn-sedimentary timing of framboidal py1.

### 3.4 *Sulphide Spatial Distribution*

All laterally oriented spatial data applies to the 3LC mine stratigraphic interval, except framboidal py1 occurrence, for which data from the 3M interval is presented. As 3LC is a laterally persistent and high grade (Zn) interval, it is assumed that work sufficiently characterises the whole #3 ore lens, and that the observations are also broadly applicable to other ore lenses.

#### *Pyrite 1*

Py1 is least abundant in the north of unit 3LC, and increases toward the south (fig.3.12a). It is stable throughout the strongly base-metal mineralised zone, and increases again south of economic mineralisation where it is the dominant sulphide present. Variation of wholerock iron grades, and therefore of py1 abundance, averaged for the #3 ore lens, show no relationship to the distribution of base metals (MRM database). In unit 3M, which is by definition pyrite-flooded, macroframboidal py1 is strictly confined to the northern and southern peripheries of the deposit (fig.3.12b). There is no recognisable E-W variation in either modal abundance or texture across the spread of drillholes used in this study.

Upsection, py1 is the only common sulphide mineral in the pyrite-flooded siltstones of the stratigraphic hangingwall. Laterally extensive py1-dominated zones such as 3M, and another in the #4 ore lens show gradual upsection increase in py1 abundance concomitant with decrease in sp1, and abrupt py1 decrease at the top of the pyrite-rich zone. These are considered analogous to the larger scale relationship between high grade base metal mineralisation and the hangingwall pyritic

'shales' (Hinman 2001, Blake *et al.* 2001), and show that the mechanisms of py1 and sp1 formation are fundamentally different.

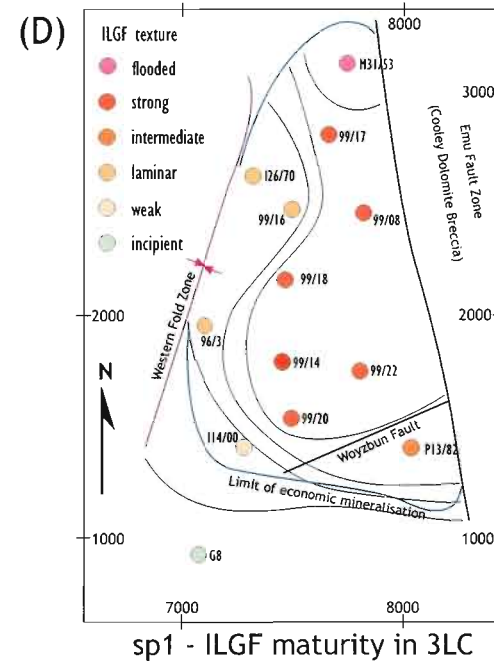
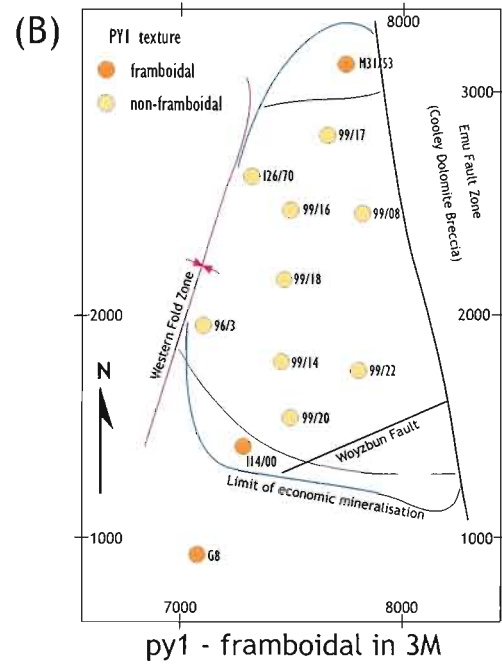
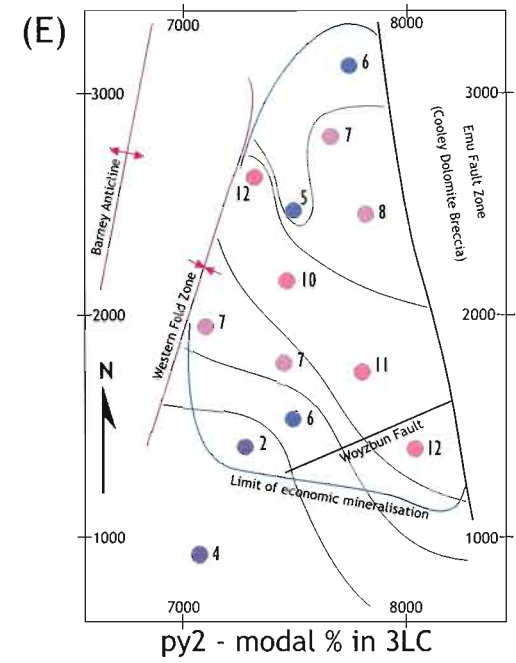
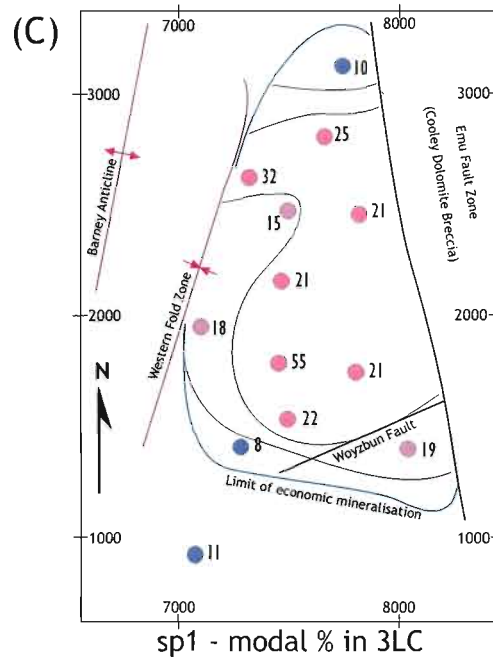
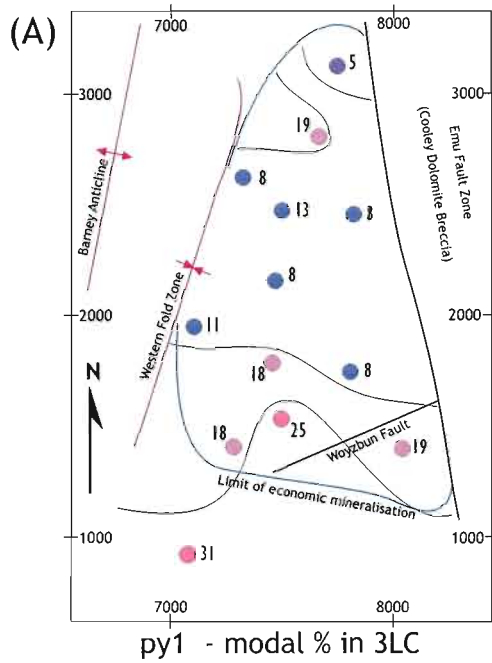
### *Sphalerite 1*

Sp1 abundance is greatest in the central, high grade, part of the deposit, and decreases markedly to the north and south, and subtly to the east and west (fig.3.12c). The lateral boundaries of base-metal mineralised lenses are not abrupt, but consist of a zone of gradual decline in sp1 abundance at least 500m wide that is associated with stratigraphic thinning of the mineralised interval by ~50%. There is an apparent inverse relationship between abundance of sp1 and py1. However, the marked southern decrease of sp1 abundance does not occur until 300-500m further south than the increase in py1 abundance in the same direction (fig.3.12a,c), and wholerock metal distributions show that the occurrence of py1 (iron) and sp1 (zinc) are decoupled (fig.3.13a,b).

The western and southern peripheries of the deposit are characterised by a sharp textural sp1 gradient from strong ILGF in the centre, to weaker, more diffuse and more thinly laminated sp1 textures distally (fig.3.12d). This textural gradient reveals more pronounced E-W variation than is apparent for sp1 modal abundance, and also begins closer to the centre of the deposit than marked increase in nodular carbonate abundance. Therefore, peripheral decrease in zinc grade is a result of less intense sp1 precipitation in the edges of the mineralising system, rather than dilution by nodular carbonates. This is borne out by wholerock geochemistry that shows decline in zinc content at calcium grades lower than is usual for the nodular carbonate facies (fig.3.13b). Furthermore, the edge of the mineralised zone is not clearly defined in the style of classical replacement ores, and sparse sphalerite laminae persist in the extreme distal environment (such as DDH G8). Independent textural changes in the west suggests that the mineralising system did not ever extend far beyond the current erosional truncation of the deposit, and that the "Western Fold Zone" is likely to be a long-lived structure important in basin evolution.

Pervasive grain-cementing (*flooded*) sp1 textures are restricted to the northern margin of the deposit, and share no spatial relationship with increase in nodular carbonate abundance on the same margin. Asymmetry of sp1 texture in the north instead coincides with the location of fluid influx into the system during formation of the #3 ore lens, interpreted from metal zonations (fig.3.1a; Logan, 1979).

*Figure 3.12 - Hand contoured plan view maps of sulphide abundance and textural distribution; (a) py1 modal abundance in the high grade 3LC unit; (b) distribution of macroframboids in the pyrite-flooded 3M unit; (c) sp1 modal abundance in 3LC, showing declining abundance in all the preserved deposit fringes. Note the geometric differences between py1 and sp1 distribution in this unit that suggest precipitation of the two are decoupled. (d) Distribution of internal textures in sp1 laminae, as described in the text and fig.5.5. Changes of sp1 texture follow a pattern similar to modal abundance, but begin to change closer to the geographic centre of the deposit. Mineralisation processes in the deposit fringe therefore varied independent of the bulk flux of metal in the system (e) Modal abundance of py2 in unit 3LC. The distribution of py2 is broadly similar to sp1, but is irregular and locally highly variable.*



### ***Pyrite 2***

Pyrite 2 has a strong spatial association with base-metal mineralisation (fig.3.12c,e). It is closely related to sp1 abundance in the north and central parts of the deposit, and likewise becomes less abundant with distance south of the deposit centre. However, towards the southern margin of the deposit, the decline in py2 abundance begins 300-500 metres north of the equivalent decline in sp1 abundance.

### ***Sphalerite 2***

The occurrence of sp2 is controlled by the distribution of the host nodular carbonates. Qualitatively, sp2 is more abundant, and carbonate nodules are more completely replaced, on the internal edge of the nodular carbonate zone adjacent to laminated mineralisation.

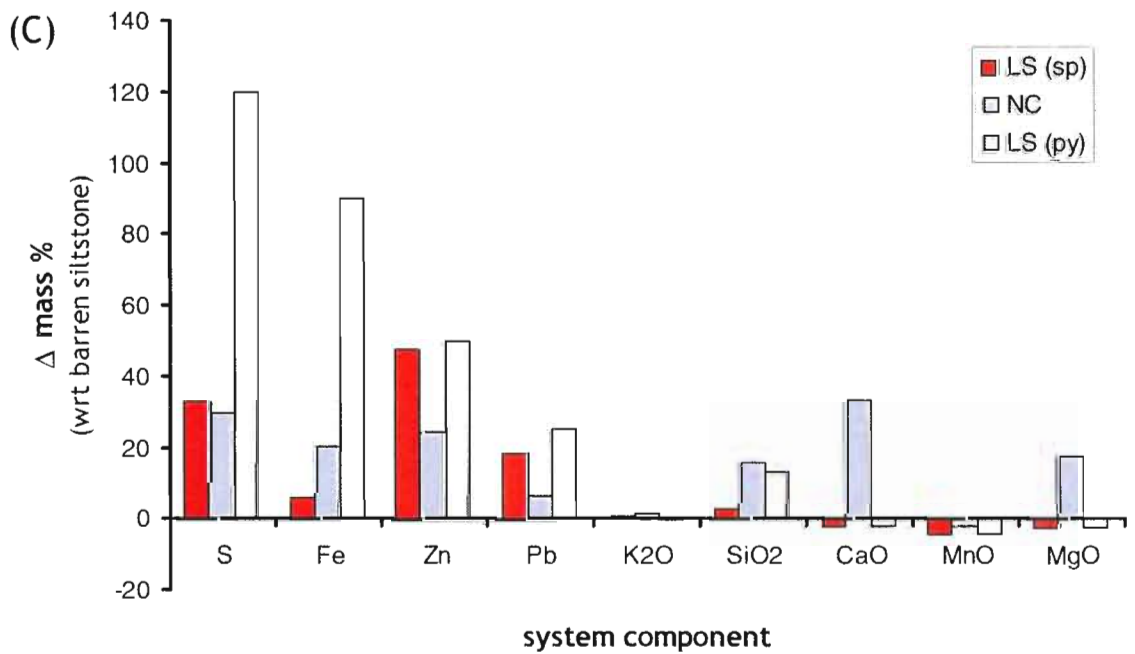
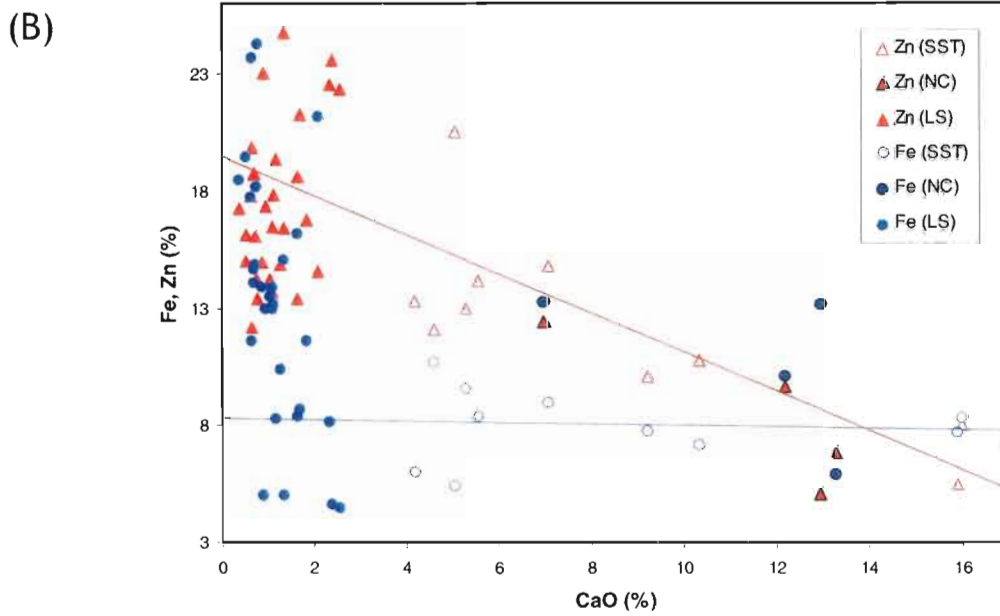
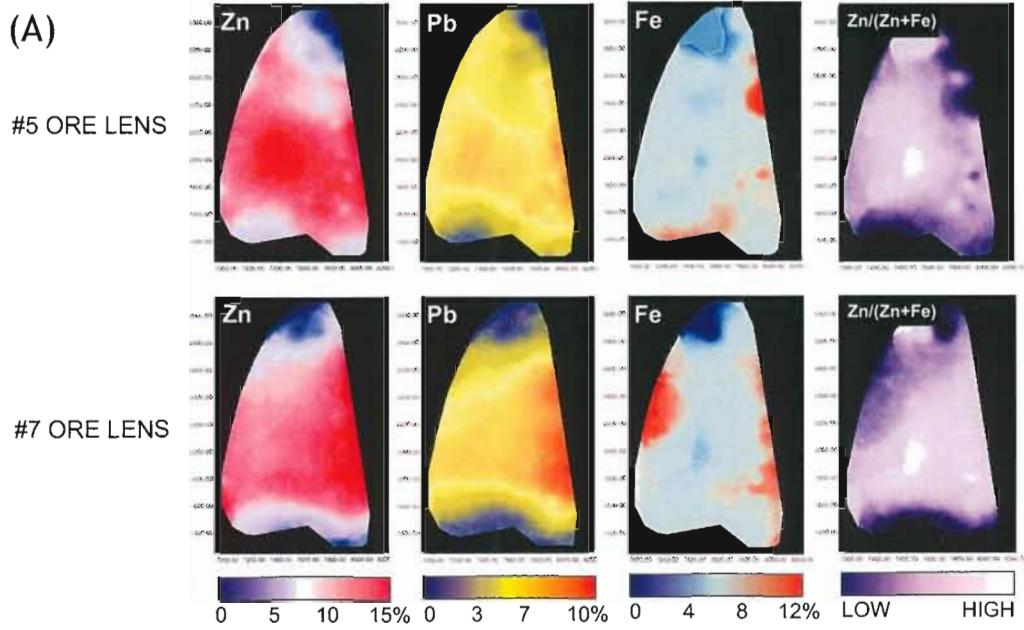
## **3.5 Mechanisms for Sulphide Genesis**

The ultra-fine grained, complex laminated texture of sulphides has been the subject of much conjecture by almost all previous researchers at HYC. Mass balance calculations that compare unmineralised ore-zone siltstones with strongly mineralised samples show that carbonate dissolution is not a major process (fig.3.13c) and precludes a volume-loss stylolite-type origin for the ILGF texture. The mechanism proposed here (fig.3.14) challenges conventional wisdom to accept the simplest explanation, but accounts for all the observed textural complexity and is supported by petrological and geochemical features of the deposit. It is a refinement of the original SEDEX model of Smith and Croxford (1972), in keeping with the laterally extensive, planar laminated sedimentology of the rocks (fig.3.2a).

There are two methods of forming extremely fine mineral grains; settling from aqueous suspension once a critical bouyancy threshold is exceeded by gravity, and rapid precipitation caused by extreme solubility disequilibrium. The former is likely to yield euhedral crystals because of uninhibited precipitation from solution, whereas the latter is likely to form anhedral aggregates. It is proposed that these two scenarios are precisely analagous to formation of py1 and sp1 at HYC.

Consider a stratified water body in which a basal anoxic (no free oxygen) dissolved sulphide-bearing layer is separated from a surficial oxic layer (abundant oxygen) by a dysoxic mixing zone.

**Figure 3.13** - (a) Plan view images of bulk metal grades and ratios for the 5 and 7 ore lenses with colours adjusted individually to show patterns; colour bars are approximate. Note decoupled iron and basemetal distributions shown by different patterns for those metals, and subsequent decoupled *pyl* and *sp1* distribution. The ratio  $Zn/(Zn+Fe)$  matches the pattern of *Zn%*, and indicates that iron is relatively consistent in abundance throughout the deposit. (b) Scatterplot of iron and zinc against calcium showing the insensitivity of iron concentration in the laminated sulphide facies (LS), to 'dilution' by siltstone (SST), or nodular carbonates (NC) – blue line is average unmineralised HYC pyritic siltstone. In contrast, zinc decreases systematically with increasing calcium (red line is approximate Zn-CaO regression), even at calcium contents below that of nodular samples, showing that *sp1* becomes less abundant independent of dilution by nodular carbonates. (c) Histogram of net mass changes for important components of HYC siltstones, calculated using the method of Barrett and McClean (1989) using Ti and Al as immobile reference elements and wholerock XRF data for unmineralised ore-zone siltstones collected in this study as the unmineralised reference rock composition. Note the complete absence of large decreases of the common carbonate elements (Ca, Mg, Mn) that would be anticipated if in situ carbonate dissolution had been a major process.



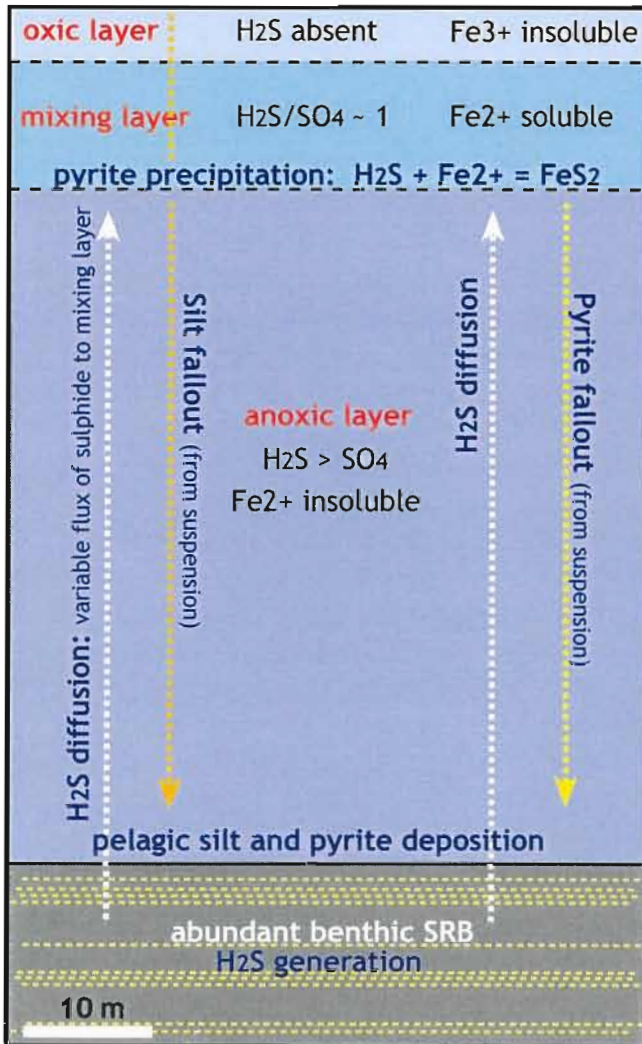
Due to pyrite and hematite solubility near the  $\text{H}_2\text{S}$ - $\text{SO}_4$  predominance boundary, iron is highly soluble in the mixing layer, but not in either of the others (Cooke *et al.* 1998b). In the modern Red Sea, mixing layers above the warm Atlantis Deep brine pools contain two orders of magnitude more dissolved iron than the basal brine or the oxic surface layer. Hydrogen sulphide produced biogenically in the sediment pile escapes and diffuses into the anoxic layer (Berner, 1970), and reacts with dissolved iron at the interface with the mixing layer. Iron sulphide crystals form and fall to the seafloor once their weight exceeds the buoyant force of the water. Basinwide lamination of pyrite abundance develops in response to time-variant flux of dissolved sulphide to the interface between aqueous strata, i.e., pyrite-flooded units represent periods of prolific bacterial sulphate reduction and unusually high sulphide flux to the mixing layer. The gradual increase in pyrite abundance at the base of these pyrite-flooded siltstones occurs over the same scale as facies transitions between iron-poor and iron-rich chemical sediments in the anoxic deep basins of the Red Sea (Craig, 1969), and further supports the notion that pyrite is (at least in part) formed in the water column and is deposited pelagically. Where the mixing layer impinges on the seafloor around the basin periphery, a benthic bacteria restricted to that layer is directly replaced by pyrite and becomes the 'macroframboids' (Croxford and Jephcott, 1972; Eldridge *et al.* 1993; this chapter).

Into this environment of background pelagic silt deposition and fluctuating deposition of pyrite crystallites, warm, hypersaline and dense, sulphate-predominant metalliferous brines (Cooke *et al.* 2000) are introduced in discrete pulses (Large *et al.* 1998). The brine pulses flow downslope and remain largely unmodified until the seafloor slope and flow velocity decrease near a local depression (Sangster, 2001). Integration of lead isotope chronology for the host sequence and detailed stratigraphy suggests that brine pulses enter the basin approximately once every 20 years (R. Large, pers. comm.). Sufficient chemical communication is predicted to occur between the brine and the anoxic water column over this duration, that effectively unmodified brine does not permanently pool in the depression. Instead, it contributes to a dynamic physicochemical gradient within the anoxic zone; from more brine-like in the deepest part of the depression, to ambient anoxic seawater higher in the water column. When a new brine pulse enters the basin, it does not override a classical 'brine pool' (e.g. McDougall, 1984) but is likely to reach neutral buoyancy somewhere near the deepest part of the basin and mix with the highly saline ambient anoxic water there. Mixing and diffusion of hydrogen sulphide into the brine (from the sediment pile and from the anoxic water column) drives spontaneous and rapid sphalerite and galena precipitation (pyrite

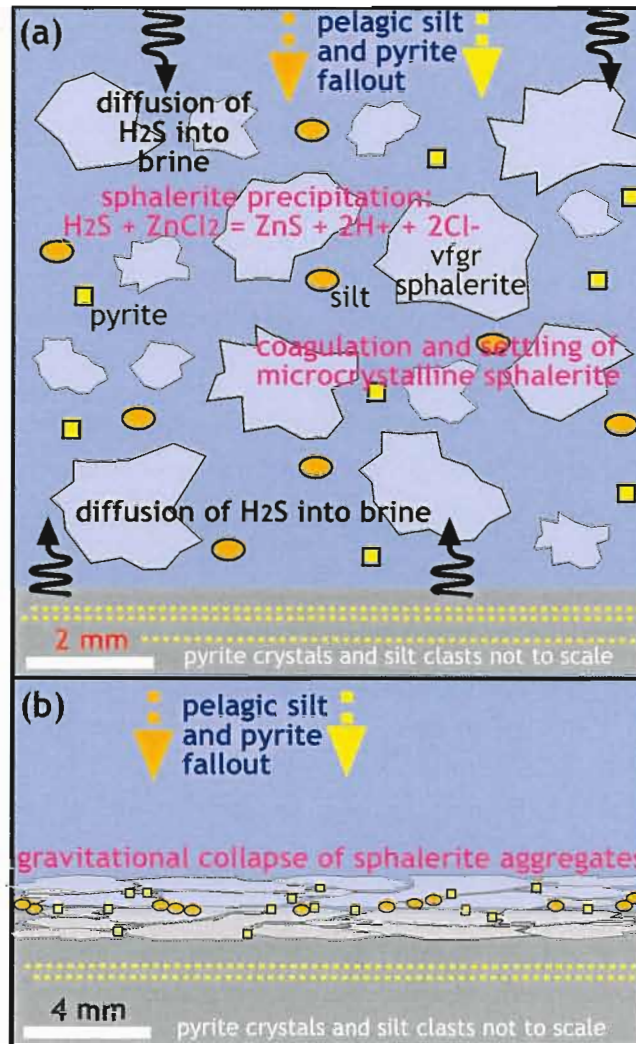
*Figure 3.14 - Diagrammatic representation of the proposed SEDEX genetic mechanism. (I) sediment and chemical fluxes involved in the ambient pelagic silt-pyrite 'background' sedimentation. (II-a) Instantaneous situation after influx of a new brine pulse into the deep basin. Diffusion of hydrogen sulphide into the brine, and unquantified mixing with reduced anoxic seawater cause rapid base metal sulphide precipitation. High ionic strength of the solution causes the precipitate to flocculate, and these aggregates are deposited on the seafloor (II-b) where they collapse under their own weight, trapping pyrite and silt along the boundaries between aggregates. (III) Repetition of the process after tens of years of background deposition gives rise to the planar laminated macroscopic texture. In the deposit fringe, nodular carbonates form in the shallow sub-seafloor environment and are replaced by sphalerite as the modified brine permeates the sediment. Precipitation of py<sub>2</sub> follows, from the cumulate modified brine in the sediment, and is focussed at the top of zones with locally high permeability or with abundant suitable nuclei.*

# Elements of the SEDEX Mechanism

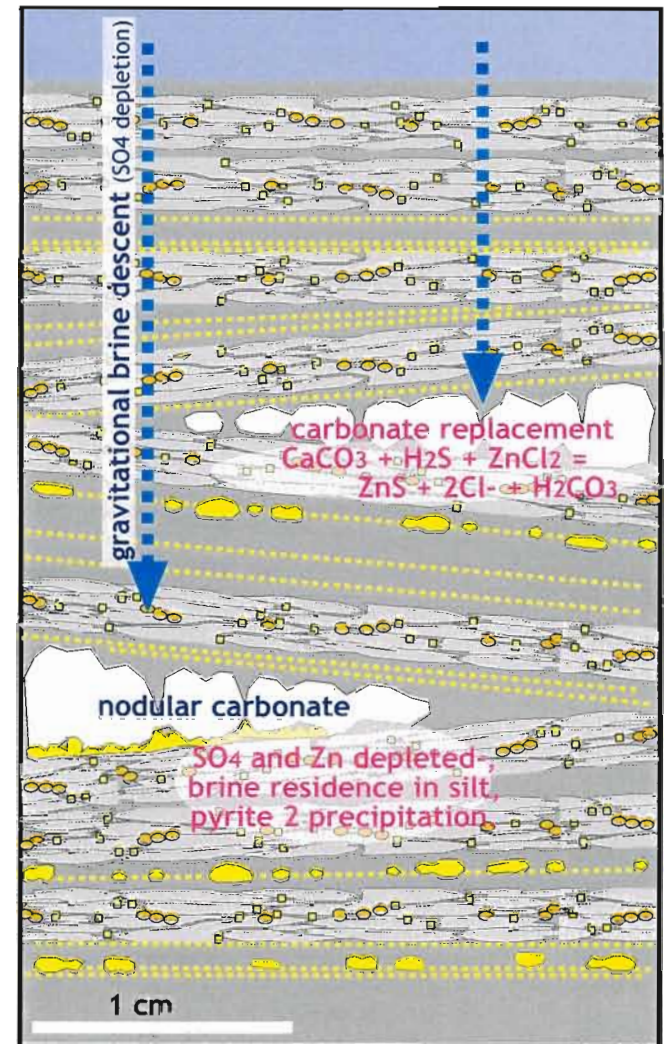
## I. Pelagic Sedimentation



## II. Basemetal Sulphide Precipitation

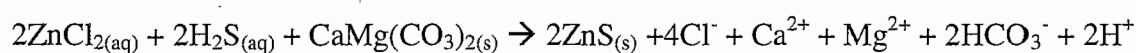


## III. In-situ Sulphide Precipitation



does not precipitate because iron is scarce in both fluids). Solubility equilibria predict that galena precipitates marginally earlier than sphalerite under these conditions (fig.3.1b; Cooke *et al.* 1998b) and the fluid becomes lead-depleted before each new influx of brine reaches the distal parts of the system, giving rise to broad metal zonation of proximal lead abundance.

The brine pulse does not immediately sink into the sediment (*cf.* Sangster, 2001) because of abundant impermeable sulphide and carbonate hardgrounds in the shallow sediment pile. On the side of the depocentre proximal to brine emission, solubility disequilibrium is so great that sulphides precipitate in the pore spaces of the top few millimetres of the seafloor sediment generating the diffuse-based *flooded* laminae characteristic of the northern part of 3LC (fig.3.8a, 3.7a-b, 3.12). Immediately above the seafloor, suspended basemetal sulphide crystallites coagulate electrostatically due to high salinity and consequent high ionic strength of the brine (Sholkovitz, 1976; Atkins, 1994) and fall from suspension. They collapse and compact together under their own weight once deposited, resulting in the characteristic anastomosing lamination of sp1. The amount of metal introduced into the basin in any one pulse, and the simultaneous rate of pelagic silt and pyrite 1 deposition control the amount of inclusions preserved in, and in between basemetal sulphide aggregates. Where sphalerite supersaturation is intense, locally the fluid pH drops and the smallest carbonate silt fragments are dissolved, summarized by the reaction:



After cessation of sphalerite precipitation, the pH re-equilibrates with the carbonate-buffered seawater and ankerite precipitates in the unconsolidated sphalerite lamina. At the same time, this intense sphalerite precipitation precludes incorporation of pelagic pyrite. However, pyrite may deposit in the upper part of the lamina as the sphalerite-ankerite precipitation process wanes, and thus create the characteristic zoned laminae (fig.3.8c-d). Only the most rapidly precipitated sphalerite aggregates preserve hypersaline pore fluid. At low temperatures, quartz precipitates during dilution (Rimstidt, 1997), and diffusive equilibration of pore fluid salinity (~25wt% NaCl eq.) with brine-modified anoxic seawater (5-10wt% NaCl eq. - normal seawater < modified seawater < brine) causes quartz precipitation in the sphalerite lamina. The newly introduced brine lens thins distally because of seafloor slope, and less metal is available for precipitation distally.

Sulphide mineral aggregates are smaller, and the volume of material is insufficient to exclude pelagic silt or pyrite, resulting in the wispy, diffuse laminae of the deposit fringe.

Reactions in the water column cause base metals to be scavenged from the system comparatively quickly, and sedimentation returns to background pelagic silt  $\pm$  pyrite until the next brine pulse. Terrigenous iron oxide colloids reach the seafloor as a component of pelagic sediment and react in situ with bacteriogenic sulphide to form wispy trails of pyrite crystals in the accumulating silt (e.g. Schieber, 1990). Nodular carbonates precipitate at very shallow depth within the laminated sediment, spatially confined to a zone controlled by a diffusive physicochemical gradient in the anoxic zone; between brine-like conditions in the deepest part and the anoxic seawater conditions in the shallowest part. The modified brine eventually permeates the sediment from above, reacts with, and partially replaces the nodular carbonates with sphalerite soon after they form. Now completely base-metal-depleted, the fluid concentrates in the permeable siltstone laminae and precipitates small quantities of pyrite (py<sub>2</sub>) in response to continuing addition of bacteriogenic sulphide. This completes the base metal mineralisation sequence.

## 4 NODULAR CARBONATES

### 4.1 Introduction

The finely laminated and very fine-grained nature of mineralised HYC siltstones is interrupted in the deposit fringe by globular aggregates and coarse (1-5 mm) laminae of carbonate minerals that are a distinctive feature of the deposit (fig.4.1a). Carbonates of this texture are not common in the McArthur Basin, but are a feature of both the Hilton deposits (Clark, 1993), and are texturally similar to a peripheral coarsely-laminated carbonate-sulphide ore facies at Lady Loretta (P. McGoldrick, pers. comm.). Approximate calculations (area x thickness x density) suggest that there are ~200 million tonnes of nodular carbonate material associated with the HYC deposit, and it is convenient to discuss the deposit in terms of a laminated sphalerite ore facies (LSOF), and a nodular carbonate ore facies (NCOF).

Previous discussion of the origin of nodular carbonates at HYC has been inconclusive beyond agreement on diagenetic timing. Early workers (Croxford and Jephcott, 1972; Logan 1979) recognised that the NCOF dominates weakly Zn-mineralised ore lenses and the southern fringe of the other lenses. The nodular carbonates were originally interpreted as mimetic pseudomorphs after a primary evaporite mineral (Croxford and Jephcott 1972, Williams 1978, Logan 1979), as concluded for nodular calcite at Hilton (Clark, 1993). Eldridge *et al.* (1993) suggested a hydrothermal origin associated with the base metal mineralising system, and reported a Mn-Fe-dolomite composition. Hydrothermal origin is supported by Perkins and Bell (1998) who also showed lateral stratigraphic equivalence between LSOF in the deposit centre and NCOF in the deposit fringe. Subsequent sedimentology (Bull, 1998) and biogeochemistry (Large *et al.* 1998; Logan *et al.* 2001) show conclusively that the Barney Creek Formation formed in a deep water environment, and preclude an evaporitic origin. Based on the spatial and stratigraphic association with stratiform base metal mineralisation, nodular carbonates are a feature of recent genetic models for HYC that are taken to represent a distal, lower temperature and higher pH expression of the envisaged mineralising system (Large *et al.* 1998; Hinman, 2001).

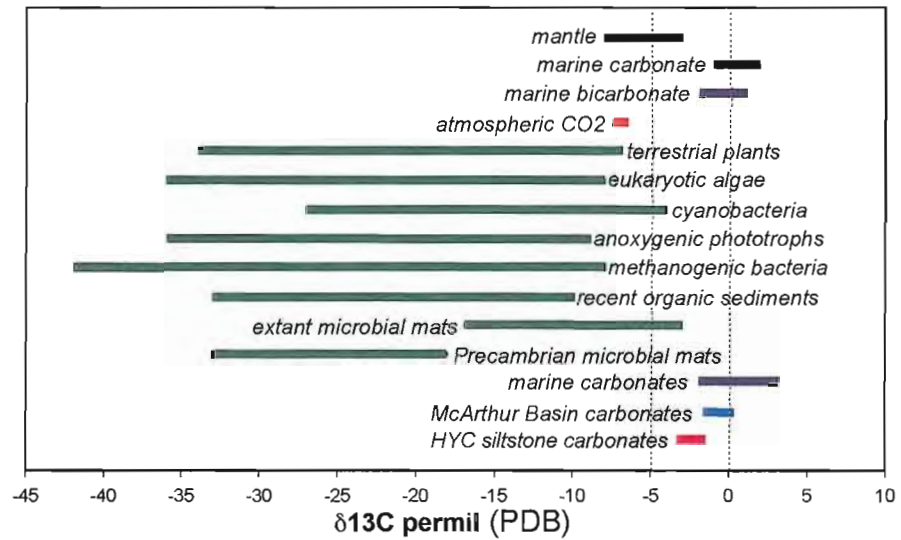
The isotopic composition of carbonates associated with the ore system can shed light on the mechanism and location of sulphate reduction.  $^{12}\text{C}$ -enriched carbon of organic origin (fig.6.1b)

*Figure 4.1 - (a) core specimen of typical HYC nodular carbonate facies siltstone. Note the macroscopic continuous laminar nature of carbonate aggregates; (b) C isotope distribution between common geological carbon pools. Compiled from Rollinson, 1993; Schidlowski, 2000; Large et al. 2000. (c) C-O isotope data from the McArthur Basin that defines the HYC ore halo of marginally lighter C and heavier O in carbonate minerals, from Large et al. 2001.*

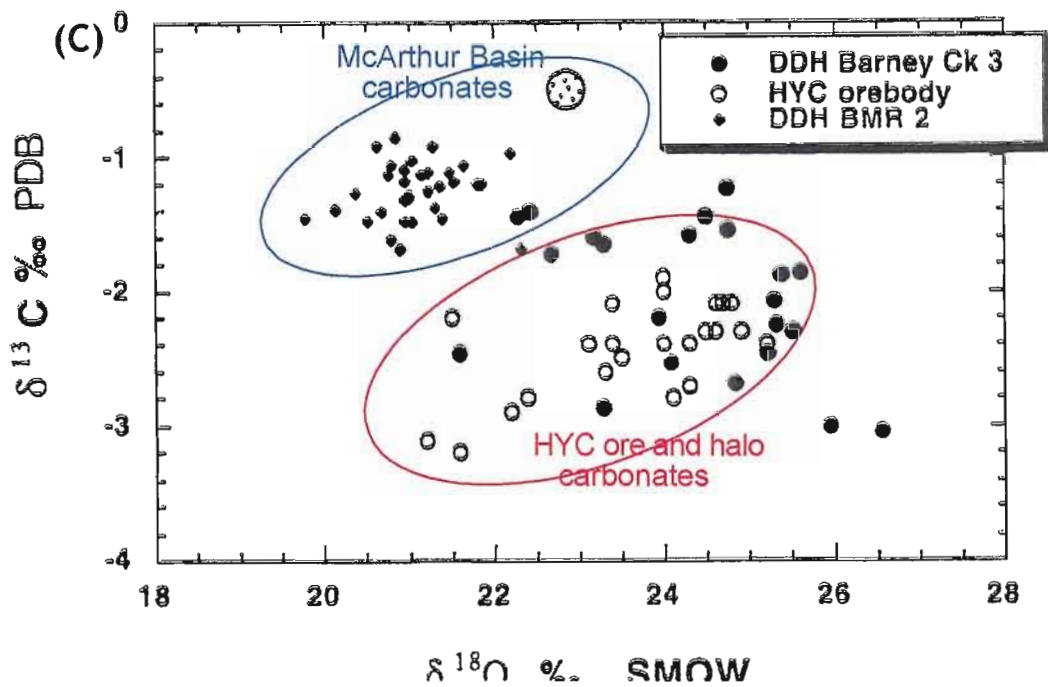
(A)



(B)



(C)



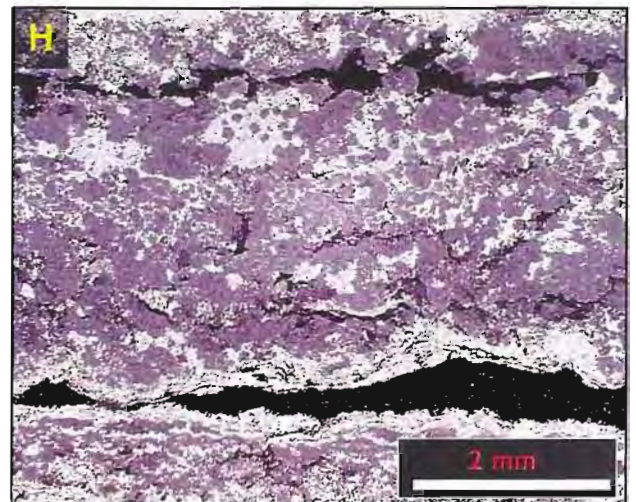
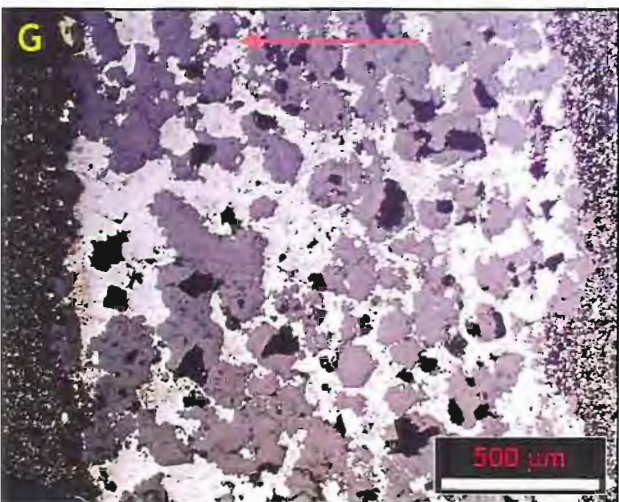
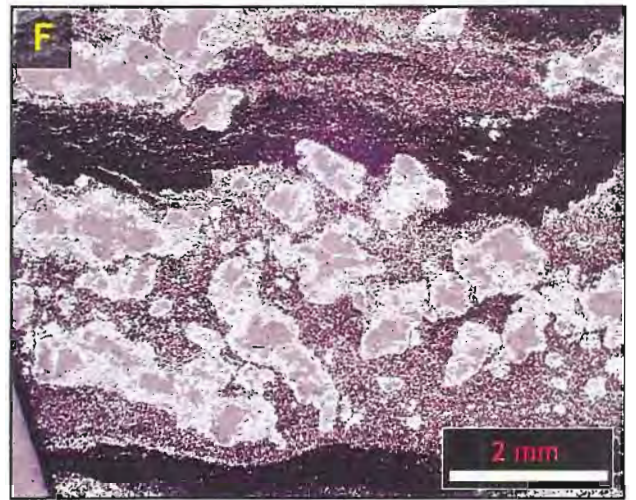
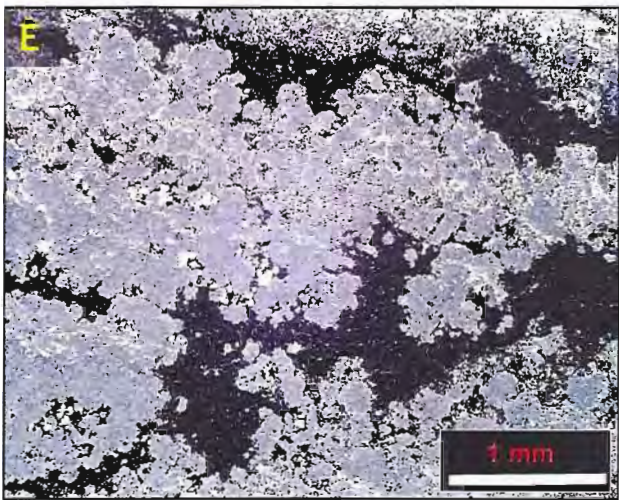
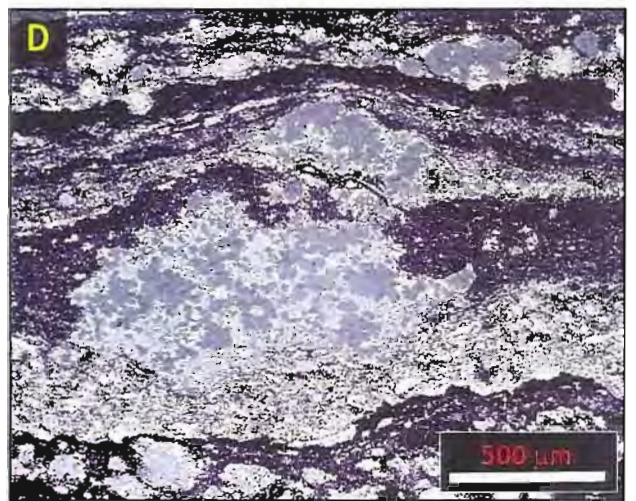
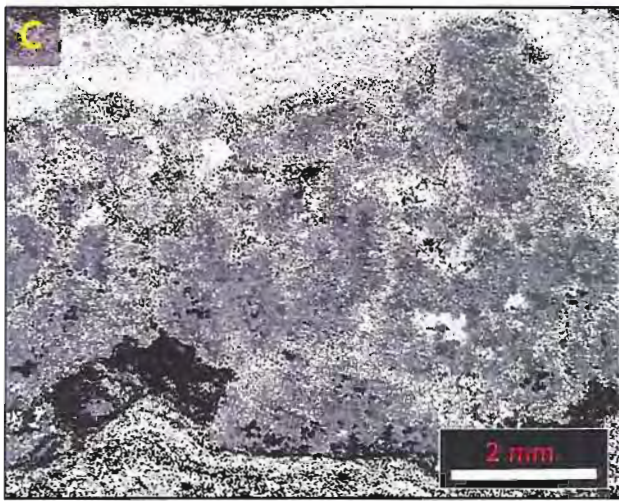
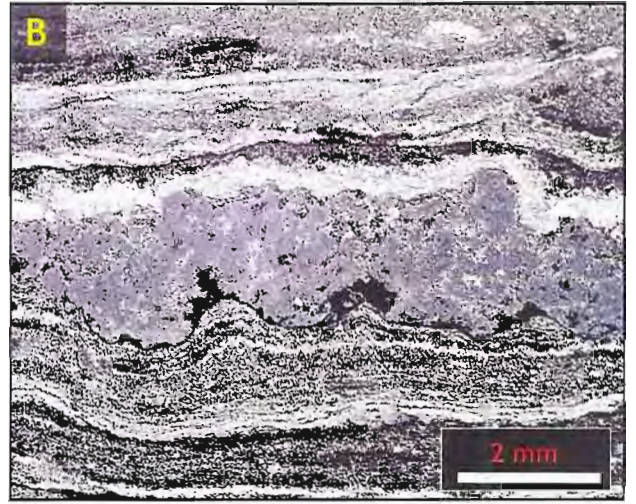
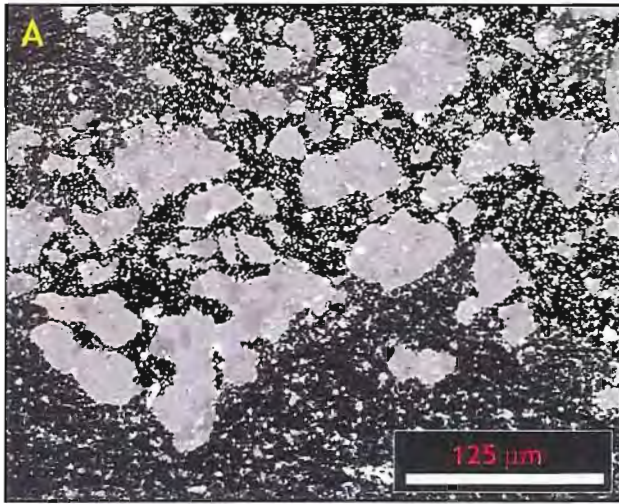
contributes to dissolved  $\text{HCO}_3^-$  if buried organic matter is the main reductant for TSR. This commonly results in a diagenetic carbonate  $\delta^{13}\text{C}$  shift 5-14‰ lighter than primary marine carbonate (Longstaffe, 1989; Ohmoto & Goldhaber 1997; Broadbent *et al.* 1998). If such an isotopic signature was to occur at HYC, it would be recorded in the nodular carbonates (Hinman 2001). The carbon-oxygen isotopic composition of all carbonates in the HYC deposit and surrounding halo (ch.3) show a definite trend to marginally heavier oxygen and lighter carbon (fig.4.1c). This is consistent with isotopic equilibration between McArthur Basin Proterozoic marine carbonates and a the likely hydrothermal fluid composition of  $\delta^{18}\text{O} = 5 \pm 5\%$  SMOW and  $\delta^{13}\text{C} = -6 \pm 1\%$  PDB (Large *et al.* 2001). Williams (1978) analysed nine nodular carbonate samples from throughout the HYC mineralised sequence and concluded that they were isotopically indistinguishable from associated dolomitic silt. Recent data of Hinman (2001) also plot in the field of HYC ore halo carbonates. Hinman (2001) also describes concomittant decline in iron and manganese substitution and increase in  $\delta^{18}\text{O}$  of nodular carbonates.

#### 4.2 **Methods and Sampling**

Nodular carbonate samples were taken from the I2/3 mine stratigraphic interval, and were selected for the presence of visible mode 2 sphalerite and to show the range of intensity of nodular carbonate development. Graphic drill logs have been compiled to show the lateral variation of nodular carbonate occurrence across and beyond the deposit margin.

Textures were identified using a petrological microscope with reflected light and the backscattered electron detector (BSED) of an environmental scanning electron microscope. Compositional variability was identified in BSED images, and compositional data was acquired using a Cameca SX100 electron microprobe; both at the University of Tasmania's Central Science Laboratory (CSL). Carbon and oxygen isotope ratios were also analysed at the CSL, using standard techniques including  $\text{H}_2\text{S}$  separation. Nodular material was isolated by drilling individual aggregates with a conventional dentists drill and collecting the rock powder generated (for detail carbon and oxygen stable isotope systematics, see Zheng and Hoefs, 1993; or Rollinson, 1993, for a summary).

**Figure 4.2** - Reflected light microphotographs (RLM); (a) incipient nodular carbonates in weakly mineralised siltstone; (b) nodular carbonate laminae showing displacement of under- and overlying sulphidic laminae; (c) detail of lamina in 'b', showing concentration of *pyl* inclusions along arcuate traces in the carbonate that record nodule sutures; (d) isolated nodules that displace the surrounding laminae and show strong replacement by *sp2*; (e) detail of a nodular lamina in weakly mineralised siltstone showing globular form and concentration of *pyl* on the sutures between individual nodules; (f) coronal *sp2* replacement of nodulaes and intimate association of *pyl* and nodular carbonates in discrete laminae separated by barren siltstone; (g) completely *sp-gn* replaced nodular laminae from the northern part of the deposit; (h) laminar form and *pyl* association of nodular carbonates.



### 4.3 **Composition and Mineralogy**

#### 4.3.1 **Textures and Timing of Nodule Growth**

The HYC “Nodular Carbonates” occur as 0.5-4mm globular, ‘blebby’ and elongate aggregates that amalgamate into laterally continuous laminae. There is a complete spectrum of nodular carbonate abundance, from sparse to pervasive, but they most commonly comprise 50-70volume% of the siltstone. Nodular carbonate laminae typically consist of interlocking anhedral crystalline carbonate grains 4-140µm across, and locally comprise diffuse zones of individual (?incipient) carbonate nodules (fig.4.2a). Elongate and dendritic subhedral potassic feldspar and quartz integrowths 1-10µm wide are irregularly developed in nodular carbonate aggregates. Aggregates of nodular carbonate displace primary siltstone lamination (fig.4.2b,c,d), and pyrite 1 crystals are commonly concentrated on the sutures between adjacent nodules (fig.4.2d,e). The laminae immediately underlying nodular carbonate laminae are commonly strongly pyritic (>50% py1), and often contain abundant ‘macroframboids’. Carbonate nodules are variably replaced by sphalerite ± galena, either as coronas about the edge of nodules or as pervasive textural replication (fig.4.2c,f,g; ch.3).

Very early diagenetic timing of nodule growth is apparent from earlier discussion of breccia intraclasts populations (ch.2) and sulphide paragenesis (ch.3). Nodules displace primary sphalerite 1 and pyrite 1 laminae both upward and downward, and must therefore form below the sediment-water interface, after precipitation of these sulphide phases. However, carbonate nodules are replaced by sphalerite 2 and are overprinted by pyrite 2, and must precede these phases. Further, pyrite 1 and nodular carbonates coexist (± minor sp1, sp2) in isolated mineralised laminae separated by barren siltstone in the extreme deposit fringe (fig.4.2f,h), which supports a genetic relationship between sulphides and nodular carbonates.

#### 4.3.2 **Elemental Composition**

The nodular carbonates are primarily homogenous, unzoned Fe-Mn-dolomite, but there are important compositional inconsistencies: in DDH 99/14 nodules are Mg-Mn-Fe-calcite; and in DDH M31/53, they are Ca-Mn-ankerite compositionally similar to that associated with sphalerite 1 (fig.4.3)

#### 4.3.2.1 Dolomite

41 new analyses from 15 nodular laminae fall in the range  $\text{Ca}_{52-55}\text{Mg}_{33-40}\text{Fe}_{3-10}\text{Mn}_{2-4}$ , and yield a mean cation composition of  $\text{Ca}_{53}\text{Mg}_{37}\text{Fe}_7\text{Mn}_3$ . This agrees with previous analyses of Large *et al.* (2000), but disagrees with those of Eldridge *et al.* (1993) that did not recognise significant calcium proportions  $>50\text{mol}\%$  (fig.4.3). High-Ca dolomites are considered indicative of formation temperatures below  $200^\circ\text{C}$  (Lumsden and Lloyd, 1997), and so the calcic nature of HYC dolomites is an important compositional feature. The ratio Ca/Mg is consistent in dolomite, and therefore transition metals substitute for magnesium and calcium in the same proportion. The ratio Fe/Mn varies only slightly, and tends to follow the total degree of substitution, such that there is relatively more manganese in dolomites that contain less total substituted metals.

Variations of the degree of  $\text{Fe}^{2+}$  and  $\text{Mn}^{2+}$  substitution vary laterally along a N-S section through the deposit (fig.4.4). The central part of the deposit, in which nodular carbonates are rare, has consistently moderate substitution ( $\text{Fe}+\text{Mn} \sim 7\text{mol}\%$ ). The distal fringes are asymmetric however; very low substitution characterises the southern fringe, and very high substitution (ankerite compositions) characterise the northern fringe.

#### 4.3.2.2 Ankerite

Ankerite compositions (i.e. carbonates with  $4*\text{Fe} > \text{Mg}$ ; Deer *et al.* 1992) are only recognised in nodular carbonates from drillholes in the north and northeast (DDH 99/08 and M31/53), whereas euhedral rhombic crystals associated with sp1 (ch.3) have this composition throughout the deposit. The average ankeritic composition falls very near the regression lines for variability of substitution ratios in dolomite (fig.4.5), and is therefore likely to be the Fe-rich end-member of a complete series of Fe-Mn-substituted calcian dolomites.

#### 4.3.2.3 Calcite

The calcite nodules are macroscopically identical to all other nodules (fig.4.6a), and share the same relationships to sulphide phases.. They comprise aggregates of euhedral to subhedral integrown crystals (50-200  $\mu\text{m}$  across) that have consistent magnesium content, but show strong micron-scale zonation of iron-manganese substitution for calcium (fig.4.6c). In these metal-rich zones, iron enrichment varies over two orders of magnitude and peaks at abundances similar to those of

*Figure 4.3 - Carbonate compositional tables; (a) average nodule compositions in samples from I2/3 in locational order S-N (top to bottom) across the deposit; (b) comparison of compositional data from this study and previous work, for all carbonate species present. Note that Ca is always > 50 mol%, indicative of formation below 200°C (Lloyd and Lumsden, 1997).*

(A)

Summary of Carbonate Compositions (by location)							
DDH	FeCO <sub>3</sub>	MnCO <sub>3</sub>	MgCO <sub>3</sub>	CaCO <sub>3</sub>	Fe/Mn	Ca/Mg	mineral
G8	3.56	2.47	38.91	54.58	1.44	1.40	dolomite
I14/00	6.16	3.16	36.97	53.51	1.95	1.45	dolomite
J-block	8.09	3.51	34.37	53.56	2.30	1.56	dolomite
99/14	2.12	1.82	6.28	92.85	1.17	14.78	calcite
I26/70	8.39	3.03	35.71	53.10	2.77	1.49	dolomite
99/17	6.35	2.40	37.51	53.23	2.65	1.42	dolomite
M31/53	13.18	3.64	30.04	51.47	3.62	1.71	ankerite

(B)

Summary of Carbonate Compositional Variability (by mineral)						
Mineral	FeCO <sub>3</sub>	MnCO <sub>3</sub>	MgCO <sub>3</sub>	CaCO <sub>3</sub>	Ca/Mg	Fe/Mn
<b>Calcite (nod)</b>	<b>2.12</b>	<b>1.82</b>	<b>6.28</b>	<b>92.85</b>	<b>14.97</b>	<b>0.90</b>
maximum	7.34	3.34	7.52	98.60	18.18	3.11
minimum	0.05	0.85	5.55	84.28	11.85	0.05
stat dev.	2.46	0.88	0.63	5.40	1.58	0.97
<b>Dolomite (nod)</b>	<b>6.65</b>	<b>2.81</b>	<b>36.78</b>	<b>53.48</b>	<b>1.46</b>	<b>2.36</b>
maximum	10.1	3.98	39.78	54.99	1.62	4.10
minimum	2.92	1.87	32.99	51.57	1.37	1.32
stat dev.	1.72	0.51	1.57	0.71	0.06	0.55
dolomite (Large et al. 2000)	~8.5	~3.5	~36	~53	~1.5	~2.3
dolomite (Eldridge et al. 1993)	7	2	41	50	1.2	3.5
<b>Ankerite (nod)</b>	<b>13.21</b>	<b>3.56</b>	<b>29.72</b>	<b>51.92</b>	<b>1.78</b>	<b>3.79</b>
maximum	16.11	4.25	35.39	57.71	3.29	6.63
minimum	9.18	1.61	27.58	40.06	1.45	2.88
stat dev.	1.18	0.27	0.95	3.42	0.08	0.30
<b>Ankerite (sp1)</b>	<b>13.35</b>	<b>3.05</b>	<b>27.65</b>	<b>54.72</b>	<b>1.29</b>	<b>4.80</b>
ankerite (sp1) (Eldridge et al. 1993)	15	3	33	50	1.5	5

*Figure 4.4 - Plot of Fe and Mn substitution into carbonates along a N-S section, with arrows for interpreted trends. Ankerite compositions in the north are possibly due to higher-temperature replacement during transient brine influx conditions, whereas declining Fe-Mn substitution in the south is due to decreased metal solubility in seawater that is less strongly modified by the mineralising brine.*

*Figure 4.5 - Variation of substitution with cation ratios for carbonates, showing consistent trends from dolomite to ankerite compositions for the same samples plotted in fig.6.4; (a) Ca/Mg v.  $\Sigma$ Fe,Mn; (b) Fe/Mn v.  $\Sigma$ Fe. Based on these plots, ankerite compositions are interpreted as the Fe-rich end member of a continuous series of carbonate compositions in the HYC ore system.*

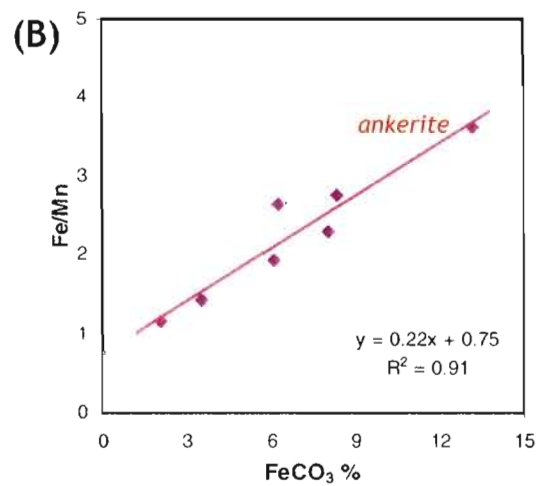
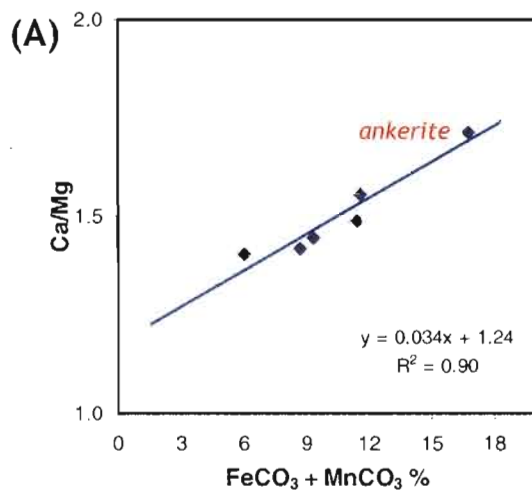
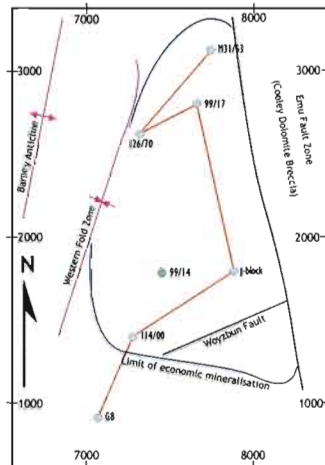
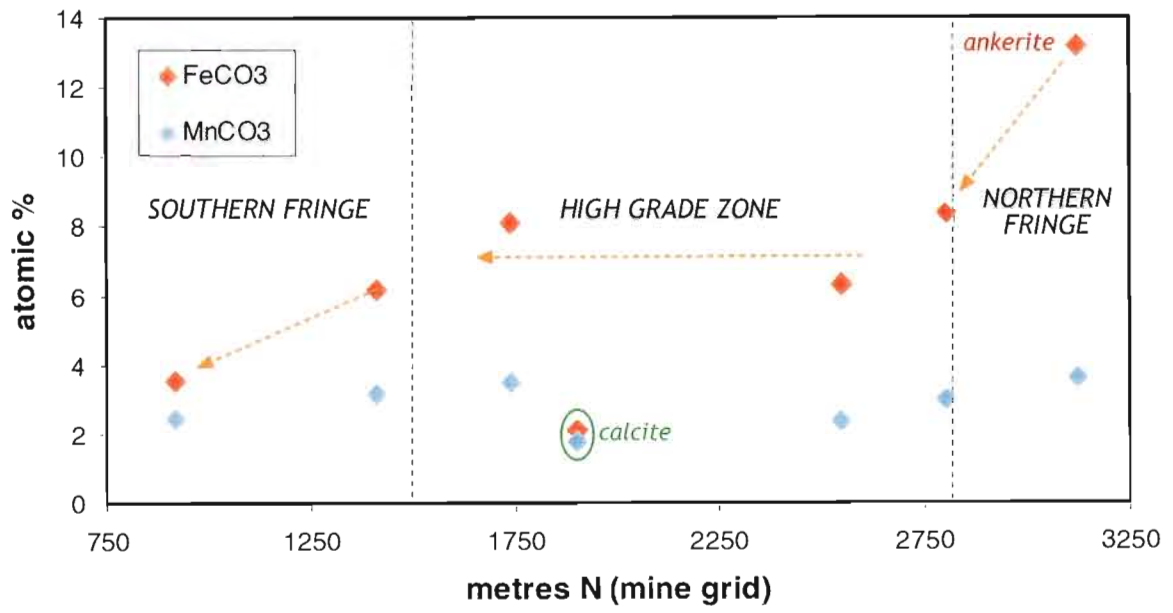
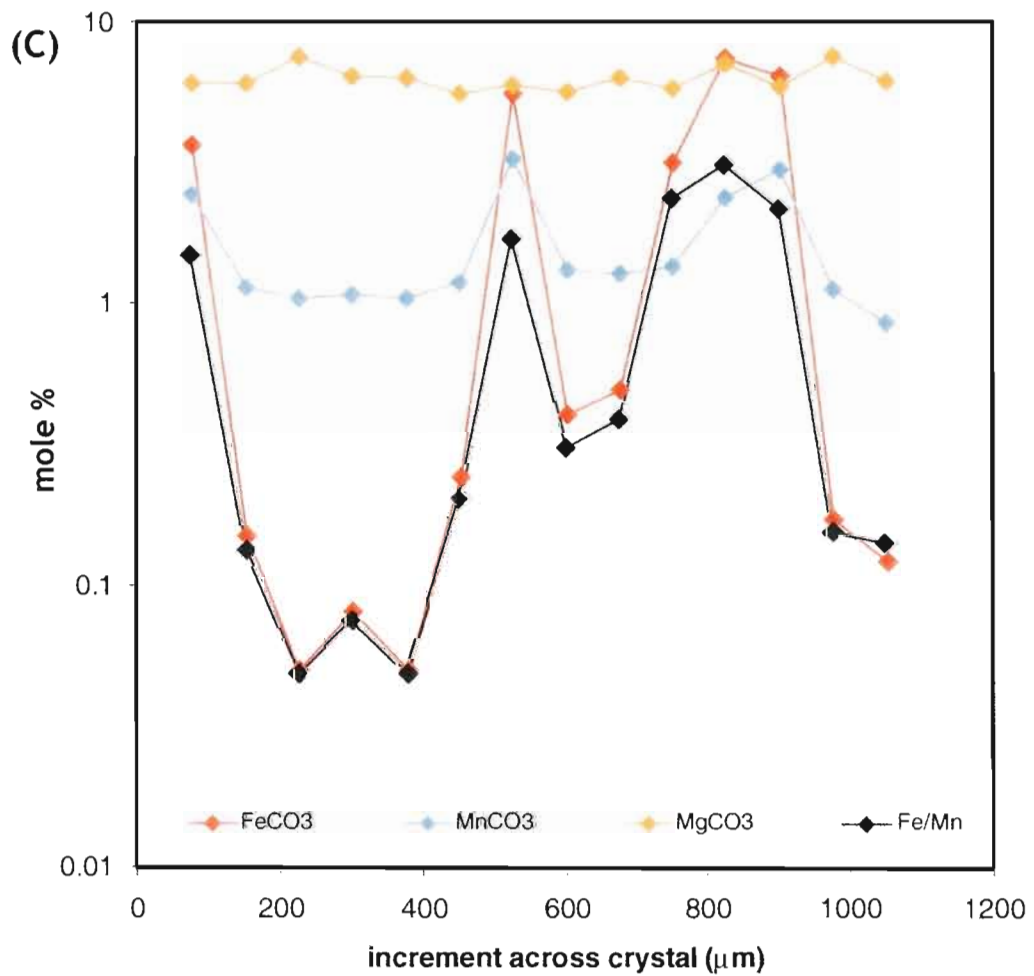
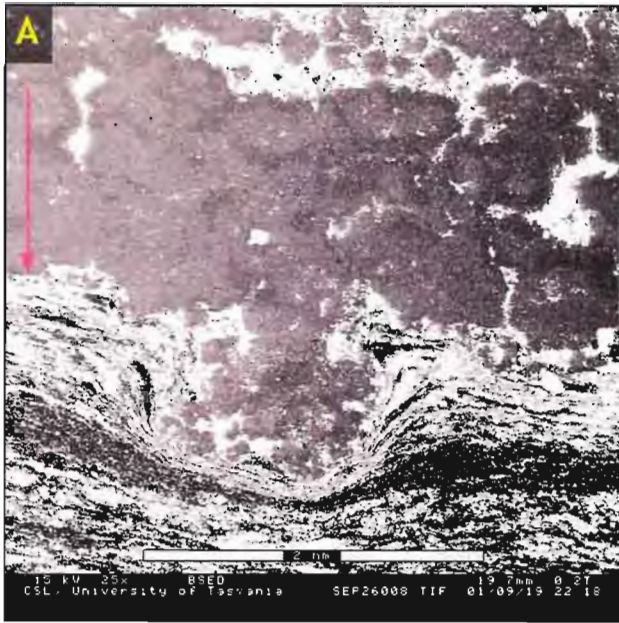


*Figure 4.6 - Backscattered electron images of zoned calcite nodules in DDH99/14; (a) showing morphology similar to other nodules, and (b) showing zonation of average atomic weight (and therefore transition metal substitution). (c) Plot of electron microprobe compositional data across a single zoned calcite crystal showing coincident enrichment of Fe and Mn, with far greater enrichment of Fe than Mn. Calcite nodules are extremely rare in the deposit, but preserved of compositional zonation suggests that all nodules precipitate as calcium carbonates. Later dolomitisation (ankeritisation) destroys the compositional zonation in most nodules.*



dolomite. Manganese is less variable, and is only slightly enriched in the metal-substituted crystal zones.

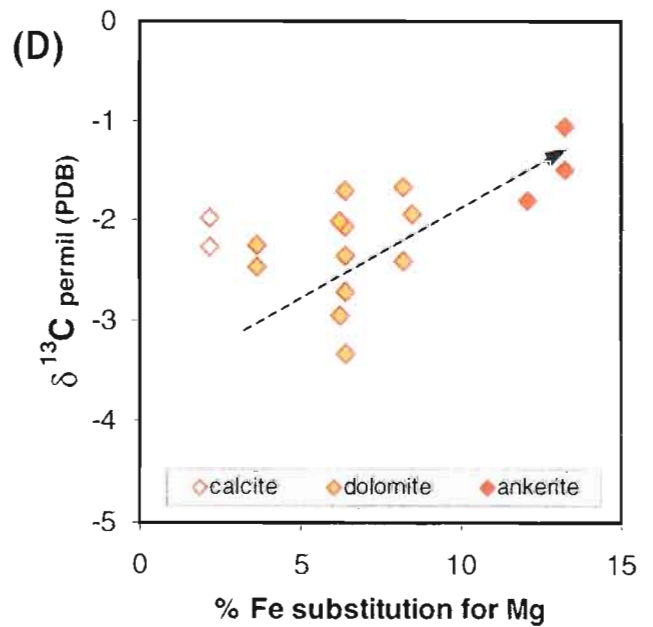
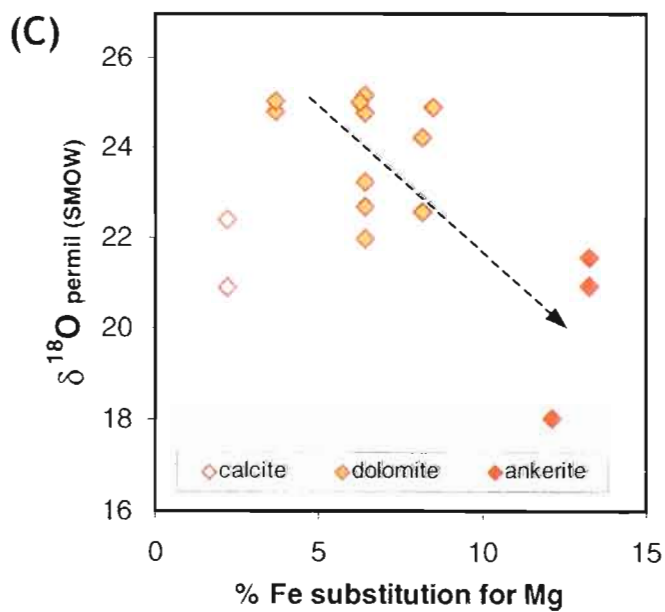
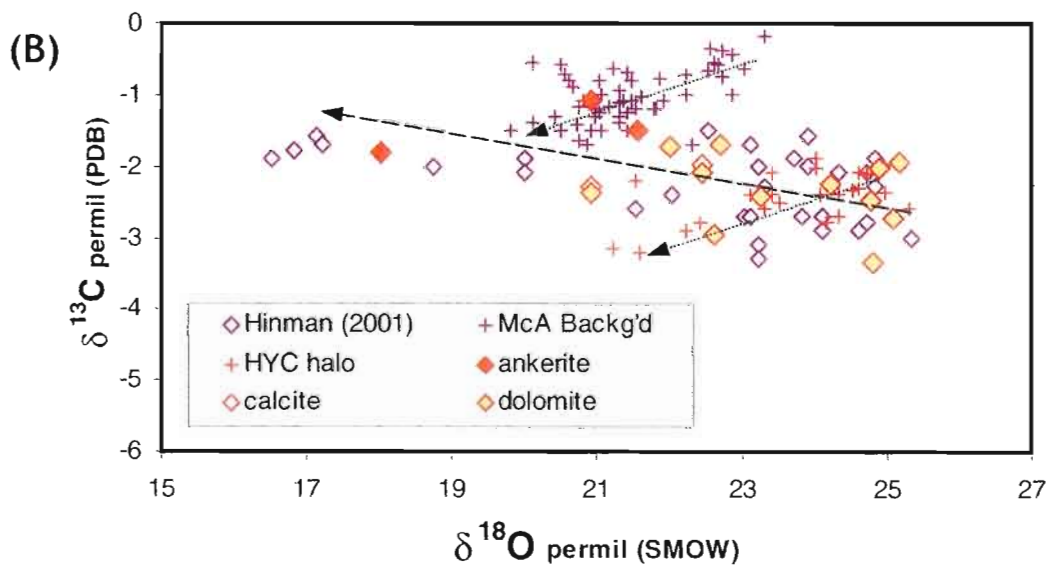
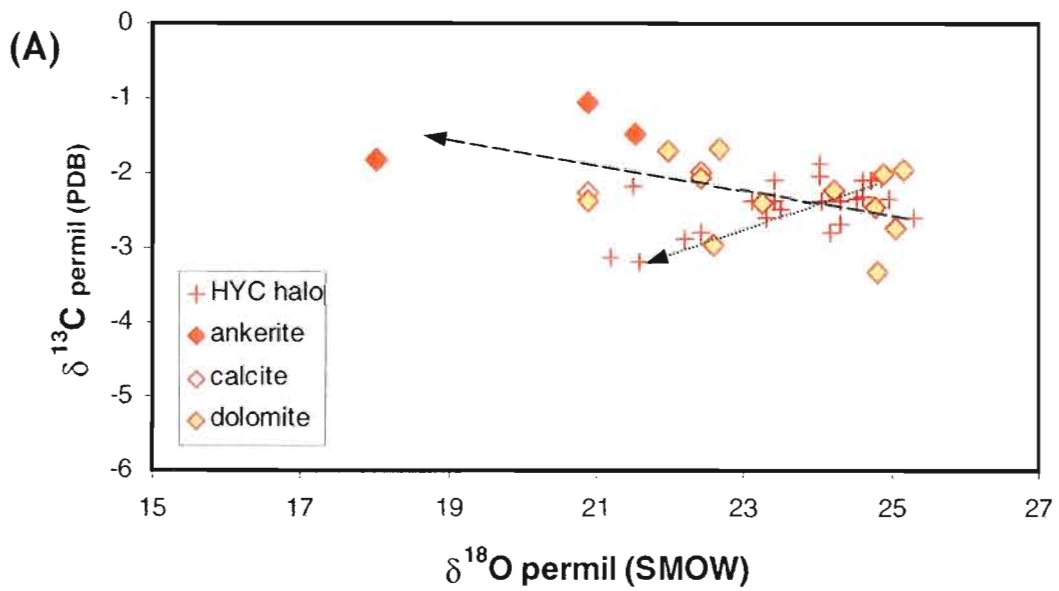
One sample of nodular calcite has been recognised previously in the Barney Creek Formation at Top Crossing (D.Cooke, pers. comm.) and primary aragonitic cements have been described from other McArthur Group carbonates (Coxco Dolomite; Winefield 1999). Strong elemental zonation is only known for primary and late diagenetic carbonates (Large *et al.* 2001). Therefore, in light of textural constraints on timing of nodule growth, nodular carbonates are interpreted as primary Mg-Mn-Fe-calcite.

#### 4.3.3 Isotopic Composition

The C-O isotopic compositions of nodular carbonates analysed in this study are graphically compared to previous data in figure 4.7. Nodular carbonates have a narrow range of  $\delta^{13}\text{C}$  (-1 to -3.5 ‰), but show wide spread in  $\delta^{18}\text{O}$  (+18 to +25‰). The data define a weak antivariant trend, but are concentrated in the field of values for 'siltstone' dolomites of the HYC C-O isotope halo (fig.4.7a; Large *et al.* 2001), and also overlap the range of values presented by Hinman (2001; fig.4.7b). Linear covariant trends for background McArthur Basin and HYC halo compositions are most likely caused by late diagenetic decarbonation (e.g. Winefield, 1999), and explain spread of the nodular carbonate data in this direction. Generally, nodular carbonates are isotopically similar to ore halo carbonates, and do *not* show a clear shift to lighter  $\delta^{13}\text{C}$ . Therefore, carbon dioxide from abiological oxidation of organic matter was not commonly incorporated into nodular carbonates under closed-system conditions associated with *in-situ* thermochemical sulphate reduction.

Dolomite and ankerite samples show a weak covariant trend between  $\delta^{18}\text{O}$  and Fe/Mn substitution (fig.4.7c) and a weak antivariant trend between  $\delta^{13}\text{C}$  and Fe/Mn substitution (fig.4.7d), i.e.,  $\delta^{13}\text{C}$  becomes lighter, and  $\delta^{18}\text{O}$  heavier, with increasing metal substitution. These trends are difficult to confirm with such a small sample set, but coincide with their findings of Hinman (2001), and are probably real despite considerable scatter in the middle of the compositional range. Calcite samples have isotopic characteristics in between the background McArthur Basin and the HYC ore halo dolomites, consistent with the slight differences in equilibrium isotope fraction between dissolved

*Figure 4.7 - Carbon and oxygen isotope data for different carbonates at HYC and in the McArthur Basin; (a) standard  $\delta^{13}\text{C}$  v.  $\delta^{18}\text{O}$  plot showing general isotopic similarity of nodular carbonates (coloured diamonds) to the HYC halo carbonates (red crosses). A few nodular carbonates define a weak trend to lighter oxygen and heavier carbon (long arrow), that is broadened by later diagenetic trends (short arrow; Winefield, 1999). (b) Similar diagram to 'a', overlain with previous nodular carbonate data of Hinman (2001), and the field for background McArthur Basin carbonates. The antivariant C-O isotope trend of nodular carbonates is supported by previous data, and appears to be related to nodule composition. (c) Variation of oxygen isotope composition of dolomite-ankerite series nodules with Fe; (d) variation of the carbon isotope composition of dolomite-ankerite series nodules with Fe. Trends between isotopic and elemental composition are taken to reflect localised higher temperature calcite replacement (ankeritisation rather than dolomitisation) in the part of the deposit closest to influx of the mineralising fluid.*



carbon dioxide and the isotopic composition of calcite and dolomite, respectively (Ohmoto and Goldhaber, 1997).

## 4.4 **Distribution**

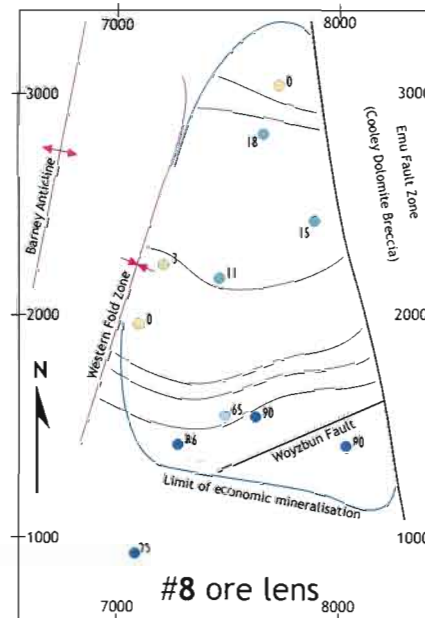
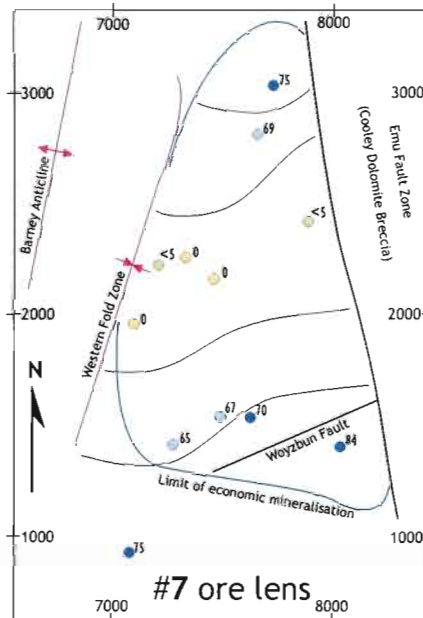
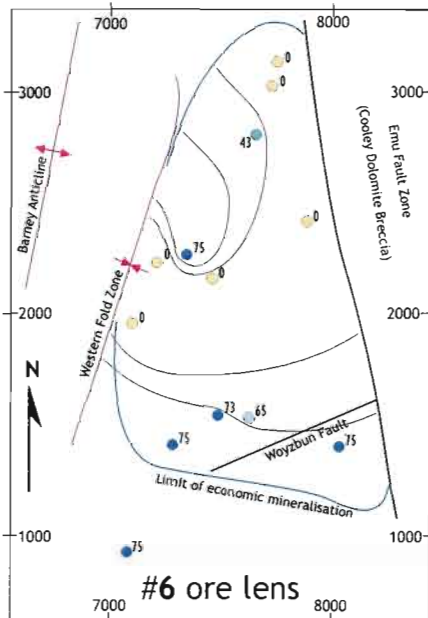
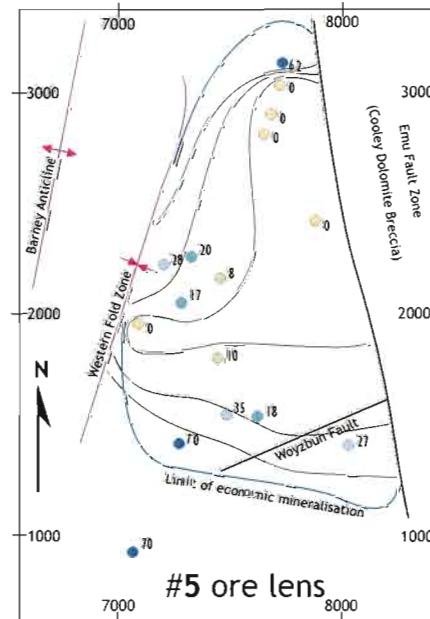
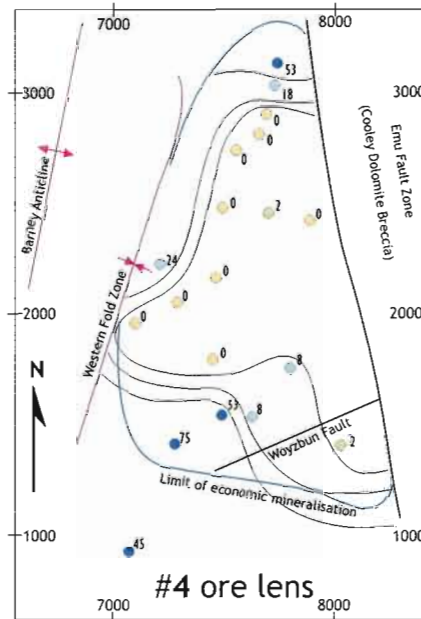
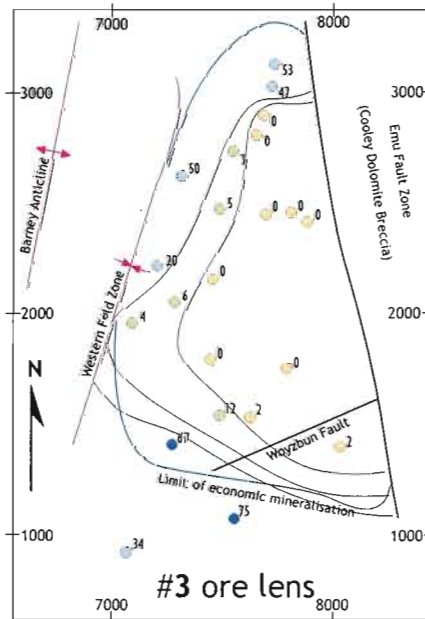
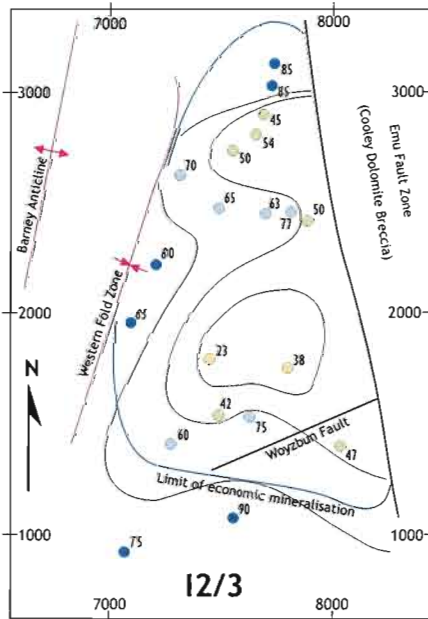
### 4.4.1 **Lateral Distribution**

Nodular carbonates dominate the HYC mineralised stratigraphy in a zone at least 700 metres wide that is peripheral to, and transitional with, the high grade laminated ore facies zone in every ore lens (fig.4.8). Extreme distal decrease in nodule abundance is only recognised in the stratigraphic level of 3 orebody for the spread of drillholes used in this study. However, specific association of the nodular carbonates and the mineralising system is unargued because this facies is uncommon elsewhere in the McArthur Basin and is a feature of other northern Australian stratiform base metal deposits (Clark, 1993).

The geometry of nodular carbonate distributions closely reflects both the geometry of declining base metal grades and changing sphalerite texture about the deposit fringe. In the lower ore lenses (#3-4), nodular carbonates are abundant in a zone that wraps around the deposit completely save the structurally truncated eastern boundary (Hinman, 1995). The central zones of low nodule abundance are elongate N-S consistent with distribution of high zinc grade and strong ILGF sphalerite textural development. The nodular zone is narrower in the north than elsewhere. Upsection, the distribution of nodular carbonates changes (fig.4.8) in accordance with upsection shifts in the distribution of base metals (fig.3.1a; Logan, 1979). The I2/3 interbeds are defined by unusually high abundance of nodular carbonates throughout the deposit, but this stratigraphic interval also exhibits significant reduction in nodule abundance in the central and southeastern part of the deposit spatially coincident with thickening of the under- and overlying mass flow facies in a local depocentre (ch.2). These relationships all indirectly suggest that the distribution of nodular carbonates is related to a depth-controlled zonation in the sedimentary environment of the HYC sub-basin.

Wholerock zinc content varies inversely with the abundance of nodular carbonates, but iron abundance is not systematically affected (fig.3.13a,b). The nodular carbonates therefore occur inside a broader system of pyrite mineralisation, but in the fringe of a more localised base metal mineralising system.

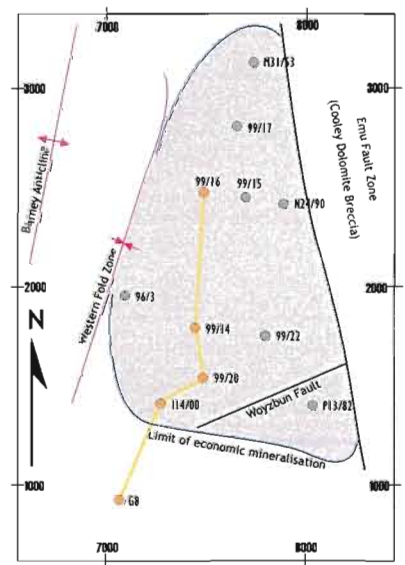
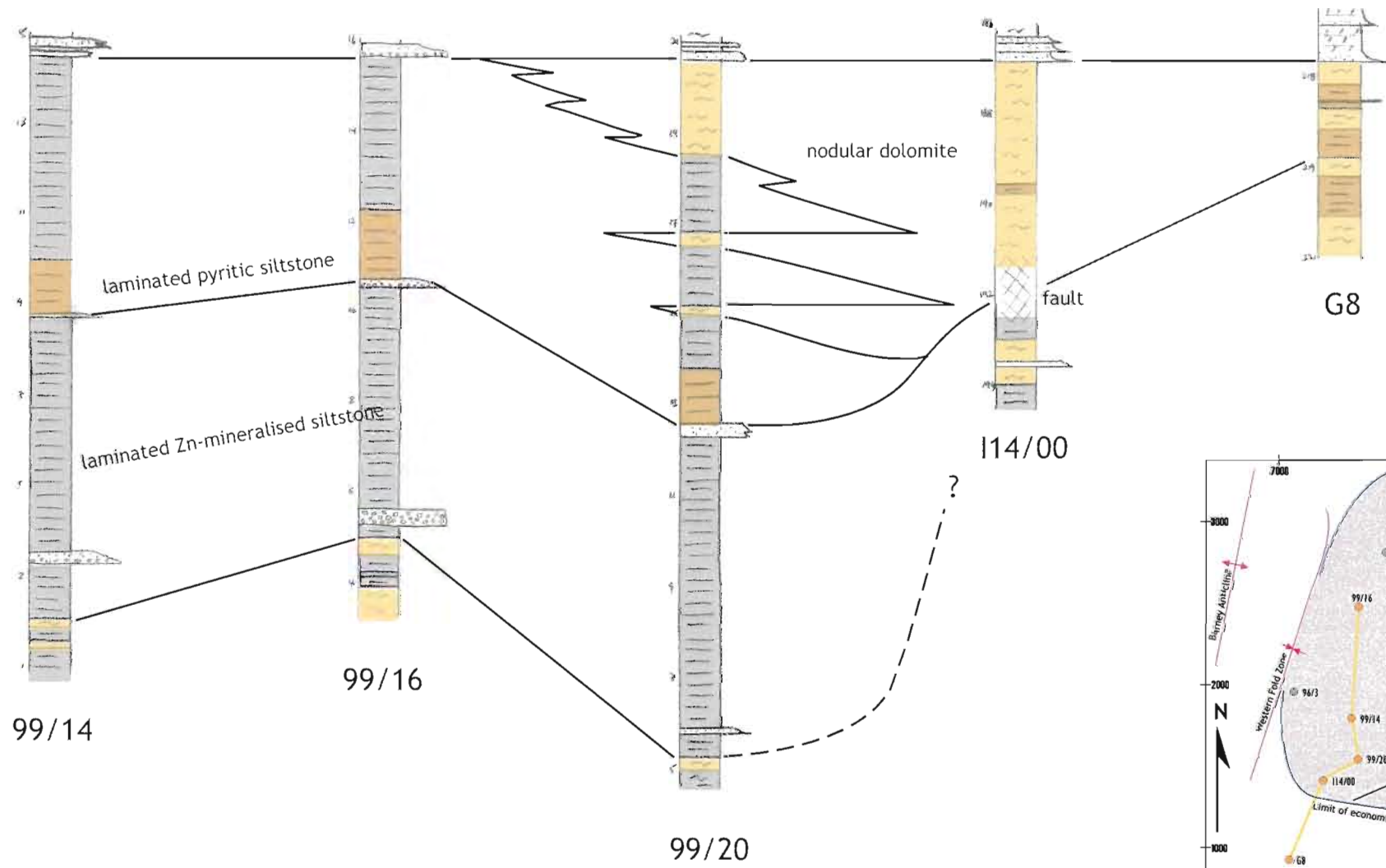
*Figure 4.8 – Plan view hand contoured plots of nodular carbonate distribution for each ore lens, revealing geometry very similar to distribution of sphalerite and sphalerite textures. Note the tighter constraint of contours in the lower ore lenses that are intersected by a greater number of drillholes. Concentric distribution of nodular carbonates about the high grade zone reflects similar geometry of physicochemical gradients during mineralisation, most easily explained by aqueous stratification of a small marine basin.*



*Nodular Carbonate Distribution: approximate volume percent*

*Figure 4.9 - Stratigraphic correlation of nodular carbonates across the southern fringe of the #3 ore lens, showing interpreted intercalated relationship with laminated sphaleritic siltstones of the central ore zone. Nodular carbonates are lateral equivalent of the laminated sulphide mineralisation, and the gradational facies boundary between the two cuts across stratigraphy at low angle reminiscent of the relationship between primary sedimentary facies.*

central zone      (proximal)      fringe zone      (distal)



Mineralised Facies, #3 Ore Lens

#### 4.4.2 Stratigraphic Relationships

Nodular carbonate laminae occur most commonly in discrete zones wherein they comprise more than 50 volume% of the rock, and in which there is minimal laminated sphalerite. However, the NCOF and LSOF are not mutually exclusive, and isolated nodular carbonate laminae may exist in strata dominated by laminated sphaleritic siltstone and *vice versa*. Intercalation of nodular carbonate and sphalerite laminae characteristically occurs over stratigraphic thickness of <1 metre, in between zones of dominance of the two ore facies.

The spacing of drillholes used in this study permits that only two or three drillholes span the transition between the two ore facies on any edge of the deposit. However, stratigraphic correlation of the southern margin of the #3 ore lens (fig.4.9) demonstrates that the diffuse boundaries it shares with the LSOF cut across bedding at low angle. This is reminiscent of the relationship between laterally equivalent primary sedimentary facies during fluctuating depositional conditions, but could be a manifestation of the reaction front of a mineralising fluid that permeated the sediment *in situ*.

### 4.5 S-C-Fe Relationships

#### 4.5.1 Introduction and Background

Relationships between sedimentary wholerock sulphur, organic carbon, and iron are useful indicators of the chemical environment of sedimentation (Raiswell & Berner 1985, Raiswell *et al.* 1987), may contribute to our understanding of benthic microbial behaviour (e.g. Goldhaber & Kaplan 1974, Berner 1970, 1983), and may be useful in recognising hydrothermal inputs to sedimentary systems (e.g. Williams 1978). In this study we analysed sulphur and carbon in unmineralised siltstone laminae from the NCOF and LSOF to determine if significant differences existed between the primary sedimentary and diagenetic processes relevant to each, and to discriminate possible origins of pyrite 1.

The sulphate reducing bacteria (SRB) are a common and diverse group of prokaryotes that utilise simple organic molecules or hydrogen as the reductant and energy source for a metabolic path which produces sulphide. They function most efficiently at temperatures between 20° and 70°C, may be planktonic or benthic, and are primarily limited by the presence of oxygen and simple

organic fuel (Trudinger, 1981; Peck, 1982). Sulphate is sufficiently abundant in the oceans to not inhibit SRB function in the top metre of sediment (Berner, 1983), and has been similarly abundant since the middle of the Archean (Ohmoto, 1992).

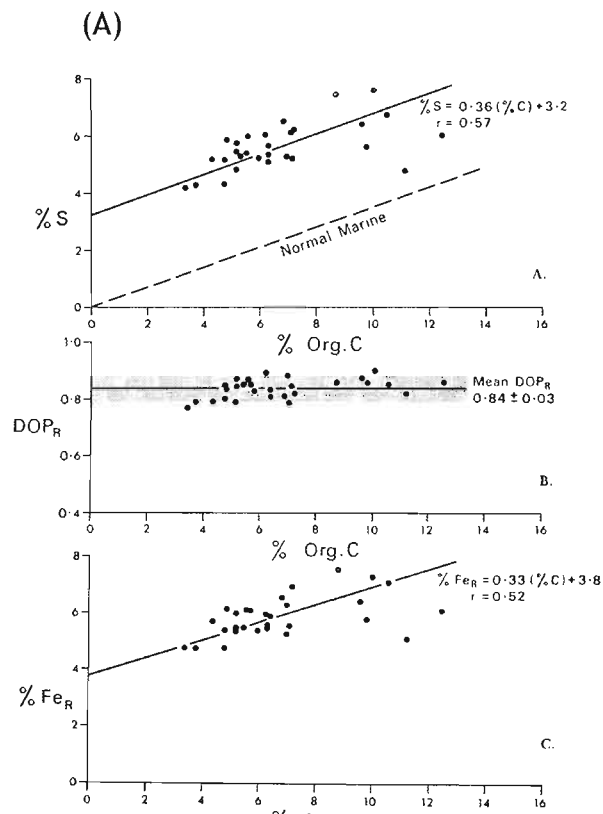
In ordinary marine sedimentary environments there is covariation between sulphur and organic carbon that defines a line through the origin (Berner, 1970), caused by SRB activity limited by available organic fuels. The slope of this line is influenced by the state of oxidative degradation of organic matter being deposited, and hence, by the sedimentation rate and the depth of oxic water through which pelagic material has fallen. A trend toward shallower slopes of the S/C covariant line through Phanerozoic time is probably directly related to the progressive oxygenation of the atmosphere (Berner, 1984). In stratified waters with basinal anoxia, SRB may exist in the water column as well as in the sediment, and aqueous biogenic sulphide builds up in the anoxic layer. Pyrite may therefore form in the water column, unrelated to deposition of organic matter. Simple organic carbon-limited diagenetic pyrite forms after burial and carbon and sulphur become covariant but define a line with a positive S intercept equivalent to the pyrite contributed from the water column (fig.4.10a; Raiswell & Berner, 1985). There are other scenarios in which this S-C relationship emerges (fig.4.10b), which can theoretically be discriminated by Fe-C and degree of pyritisation ( $DOP_t$ )-C relationships ( $DOP_t = \%Fe_{pyrite} / \%Fe_{total}$ ; Raiswell & Berner 1985). The  $DOP_t$  of mineralised sediments in DDH Te115 (HYC) is generally very high (~90%), and is taken to reflect anoxic-oxic stratification of the HYC sub-basin (Large *et al.* 1998).

#### 4.5.2 Analytical Methods and Sampling

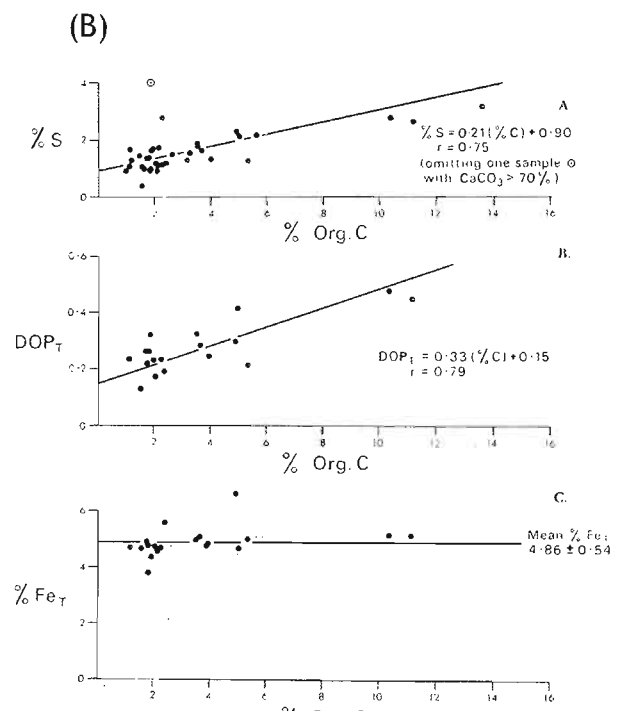
Sulphur and carbon analyses were performed at the CSL using a Carlo-Erba EA1108 Elemental Analyser. Analytical precision is reportedly  $\pm 0.1$  percent. However, standards analysed concurrently with samples used in this study show systematic analytical underestimation of S and C, and significantly decreased precision (appendix C). Organic carbon was determined using the difference method of Berner and Krom (1973); in which samples are crushed, and half gram sample splits are roasted in platinum crucibles at 400°C for 48 hours to volatilise organic carbon. Both the untreated and treated samples are then analysed and the difference calculated as percent organic carbon. We also analysed a subset of the original sample group by x-ray fluorescence (XRF, see Rollinson 1993), and back-calculated the mineralogy to determine  $DOP_t$  (assuming pyrite, sphalerite and galena are the only sulphides). These analyses also served as a check on the accuracy

*Figure 4.10 - Type example S-C-DOP-Fe plots used by Raiswell and Berner (1985) to explain diagenetic processes in anoxic basins; (a) indicating C-limited SRB productivity for the Mesozoic Jet Rock, UK and sulphide precipitation both in the water column and the sediment pile; (b) indicating Fe-limited sulphide precipitation in the Black Sea.*

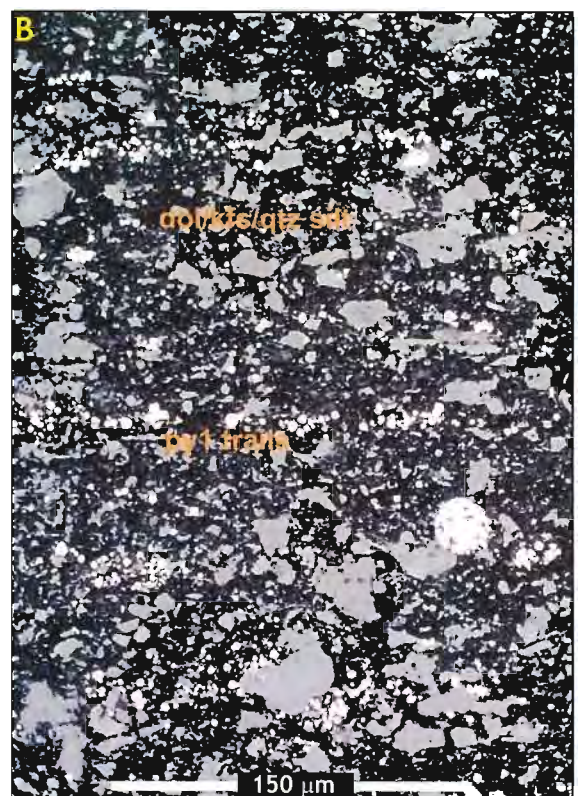
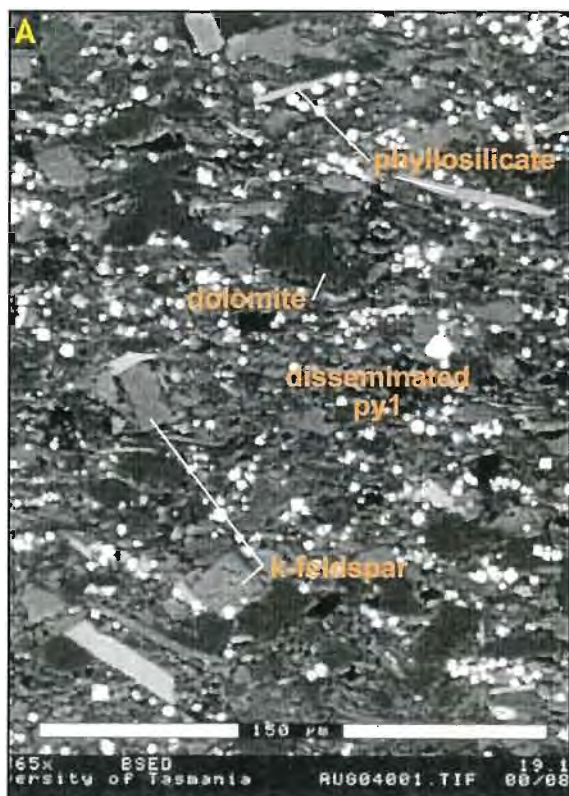
*Figure 4.11 - Typical unmineralised siltstones samples in this study for S-C-Fe geochemistry; (a) backscatter electron image showing random scatter of py1 crystals (Blake et al. 2001); (b) reflected light microphoto showing bedding-parallel trails of py1 crystals usually attributed to bacteriogenic formation in the sediment (eg Scheiber & Baird, 2000).*



C-limited (Jet Rock, UK)



Fe-limited (Black Sea)



of the chromatographic sulphur results and also confirmed that pyrite is the predominant sulphide mineral in the samples analysed.

Samples were selected that appear in hand specimen to be devoid of sulphide mineralisation and likely to be relatively high in organic carbon (fig 4.11). These were taken from different stratigraphic levels throughout the deposit, wherever unmineralised layers occurred in intimate association with either high grade laminated sphaleritic ore, or with strongly developed nodular carbonates. Individual bands of carbonaceous siltstone as thin as 3 mm were isolated from core samples using a diamond saw.

#### 4.5.3 S-C-Fe Results

The results of sulphur and organic carbon analyses are presented graphically (fig 4.12), with similar data for several drillholes outside the HYC mineralising system (R.Large, unpublished data). Organic carbon ranges between 0.3 and 1.2%, and sulphur 0.5 and 3.5%, which are similar to previous analyses of HYC samples (Williams 1978, Blake *et al.* 2001). Importantly, the data collected during this study only span an organic carbon range of ~0.8%, and so linear covariation must be interpreted with caution. Nonetheless, the data for samples from the laminated sphalerite ore facies (LSOF) appear to define separate linear S-C covariation from that defined by samples from the nodular carbonate ore facies (NCOF). Wholerock iron and degree of pyritisation ( $DOP_i$ ) are also covariant with organic carbon, but these relationships are stronger in the LSOF than in the NCOF.

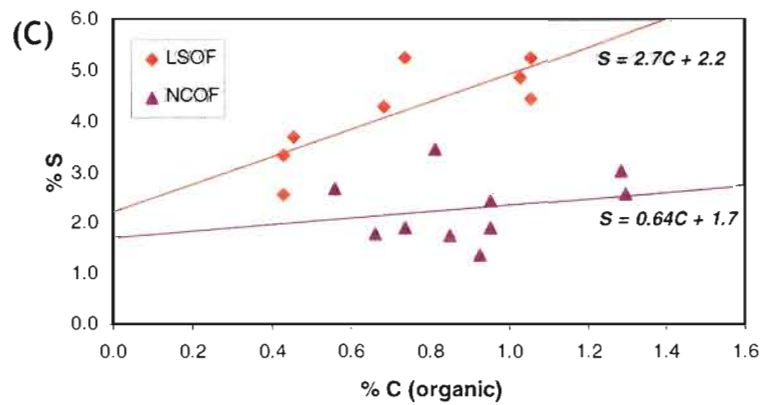
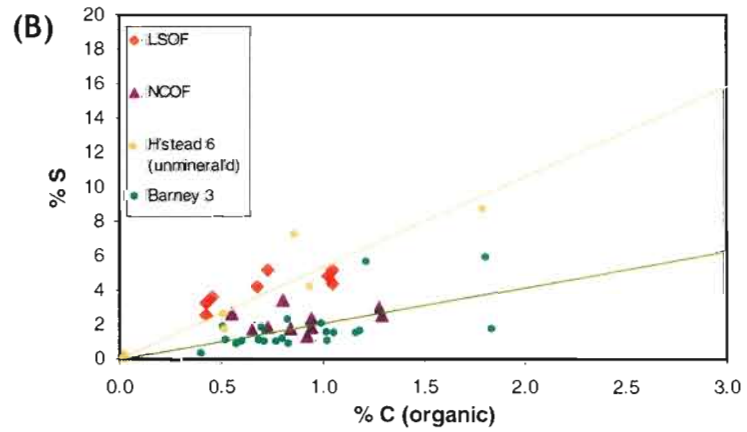
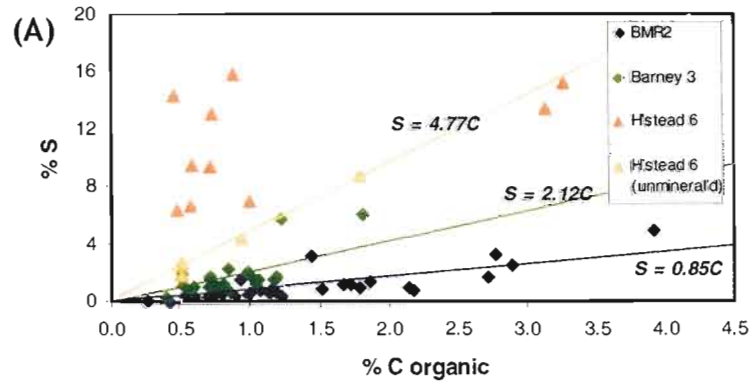
#### 4.5.4 Significance of S-C-Fe Results

##### *Hydrothermal S/C Control*

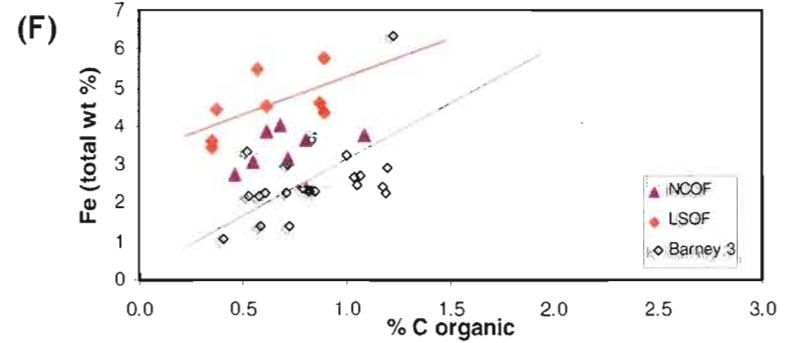
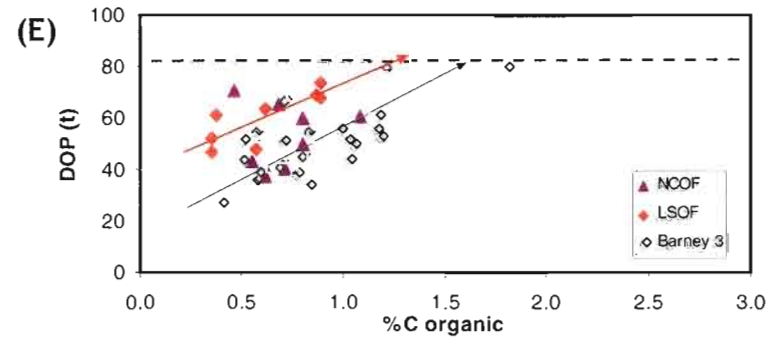
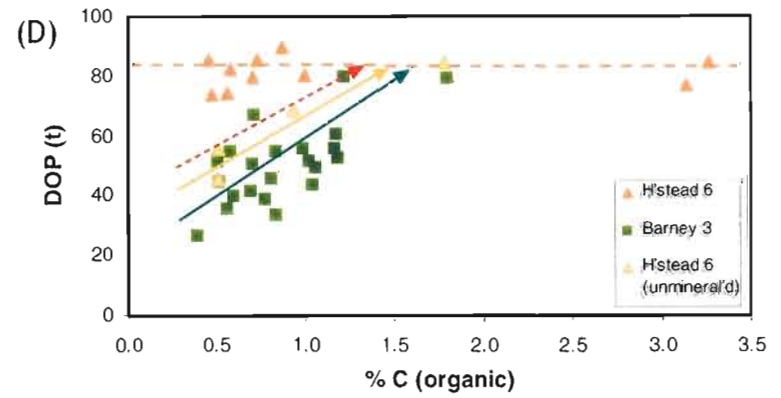
Fine grained, laminated and disseminated euhedral pyrite at Mt Isa and Century has been interpreted as hydrothermal in origin, based on sedimentology, petrography and S-isotope data (Painter *et al.* 1999; Broadbent *et al.* 1998). In these systems, iron is envisaged to be fixed preferentially (as pyrite) in sedimentary laminae containing reduced organic carbon, which acts to reduce sulphate in the fluid. If the proportion of buried organic material available as a reductant is constant, then

*Figure 4.12 - S-C-Fe plots for this study and for unpublished data from the wider McArthur Basin (courtesy R. Large); (a) S/C plot showing linear covariation outboard of HYC. Note that DDH Homestead 6 is closer to HYC than Barney 3, which is closer than BMR2, such that S/C increases with proximity to the deposit. Mineralised samples from Homestead 6 plot in a random scatter above the covariant line, indicating hydrothermal inputs to the system. (b) Plot of new data at the same scale, showing separation of LSOF and NCOF sample populations and their approximate coincidence on the regression lines for Homestead 6 and Barney 3, respectively. (c) Alternative interpretation, showing precise regression of the new data that have positive Y-intercept at ~2% S, and may indicate pelagic pyrite fallout from suspension. (d-f) DOP<sub>r</sub>- and Fe-C plots for the same datasets, showing covariation of both parameters that does not fit either of the model scenarios of Raiswell and Berner (1985). It is possible that Fe- and C-limitation can occur in the same system, in the water column and the sediment, respectively, which would yield relationships similar to those observed. Note that the DOP-C red line in 'd' is the LSOF regression line included for comparison with background unmineralised sediments. As is suggested by S/C relationships, a greater proportion of the iron deposited in the ore environment occurs as sulphides, and hydrothermal flooding of the system with sulphide causes DOP to be unrelated to organic carbon (orange line).*

Sulphur v. Carbon



DOP v. Carbon



covariant S/C and DOP/C trends will result from formation of pyrite by organic carbon-regulated thermochemical sulphate reduction. However, pyritic and pyrite-flooded siltstones at HYC do not share any systematic relationship with organic carbon (fig.4.12a), indicative of non-carbon regulated hydrothermal sulphide fixation (Berner, 1970; Williams, 1978). Further, hydrothermal formation of pyrite cannot explain the difference in S-C-Fe relationships between the nodular and laminate sulphide ore facies. This mechanism is anticipated to cause light-shifted carbon isotopic composition of related carbonates, and strongly positively skewed sulphur isotope distribution (due to Rayleigh distillation; Ohmoto and Goldhaber, 1997). As these predicted carbon and sulphur isotope trends are contrary to the data for HYC (fig.4.7a, 5.11), pyrite 1 is not likely to be of hydrothermal origin.

### ***Sedimentological S/C Control***

The data for the LSOF and the NCOF plot roughly on the covariant S/C lines in DDH Homestead 6 and Barney 3, respectively (fig 4.12b). In these drillholes, well established S/C trends through the origin indicate C-limited diagenetic precipitation of sulphides. The difference in slope between the two drillholes probably results from differences of organic flux or temperature, and subsequently of bacterial metabolic productivity, but may also arise from differences in the species composition of the bacterial community, or the relative proportions of Fe and C entering the sedimentary system. The same possibilities exist for differences between the ore facies at HYC. The lower slope of S/C in the peripheral NCOF could be due to lower sulphide productivity of SRB existing under cooler or non-ideal conditions, the nature of benthic microbial ecosystems specific to part of a stratified water body, or by enhanced fixation sulphur in elemental or organo-sulphur form.

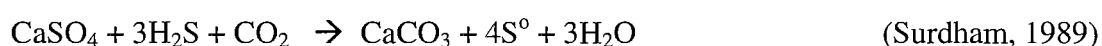
If the new data are treated rigorously, best fit regression lines maintain gradient distinction between NCOF and LSOF siltstones, but intercept the y axis at ~2% S (~5% pyrite; fig 4.12c). Therefore, it is possible that some pyrite precipitated in the water column (Berner & Raiswell, 1985) and was deposited uniformly across the LS and NC ore facies. This coincides with proposed pelagic pyrite deposition from the interface between aqueous layers (ch.3), while separate trends for the two ore facies still indicate lateral shifts in diagenetic sulphide production. Systematic differences between the S/C geochemistry of the NCOF and the LSOF strongly suggest that the distribution of nodular carbonates is ultimately controlled by the sedimentary environment.

## 4.6 Discussion

### 4.6.1 Primary Nodule Formation

The lateral distribution, stratigraphic relationships, and textural relationships presented here indicate that the nodular carbonates are a very early diagenetic product restricted to a zone peripheral to, and intercalated with basemetal-mineralised siltstones. The nodular carbonates formed in the top few metres of unconsolidated sediment, in between stages of basemetal mineralisation. The presence of (albeit rare) calcite nodules that preserve crystallographic zonation suggests that the nodular carbonates are not primary dolomitic precipitates, but have been dolomitised at some later stage.

Calcite nodules from Hilton have been interpreted to be mimetic replacement of calcium sulphate minerals (Clark, 1993), and can be explained by a reaction (below), in which organic carbon-mediated TSR generates the sulphide and carbon dioxide reactants.



This is attractive because primary calcite is unlikely to be preserved after burial by several kilometres of sediment and the rigors of 1.6 billion years of diagenetic processes; the vast majority of Precambrian carbonates have been pervasively dolomitised (Tucker, 1982; Kasting, 1992). However, iron and manganese do not substitute into calcium sulphate minerals (Deer *et al.* 1992, and references therein), and although it is possible for these metals to be introduced during carbonate replacement, it is unlikely that the crystallographic zonations of these metals (fig 4.7) would develop during carbonate replacement of sulphate mineral. Further, calcite nodules are anticipated to be abundant, not rare, if they formed by replacement of a common primary sulphate. Unfortunately, it has not been possible to take further samples from DDH 99/14 and determine if anomalous potassic feldspar or quartz alteration served to protect these nodules from dolomitisation. Nonetheless, it is most likely that the nodular carbonates precipitated as calcite and were locally protected from dolomitisation, because this is the only recorded occurrence of calcitic nodular carbonates at HYC among hundreds of analyses from all over the deposit (Logan, 1979; Rye and Williams, 1981; Eldridge *et al.* 1993, Large *et al.* 2000; Hinman, 2001, this study).

Atmospheric carbon dioxide was at least 10 times, and possibly 700 times more abundant during the Mesoproterozoic than at present (Holland, 1984; Kasting, 1987; Strauss *et al.* 1992b, Grotzinger,

1996), and therefore the activity of bicarbonate in the oceans would have been correspondingly greater. Winefield (1999) concluded that acicular structures in the Coxco Dolomite Member of the Teena Dolomite, stratigraphically below the Barney Creek Formation (BCF), were a primary seafloor aragonite precipitate. Dissolved iron and manganese inhibit calcite precipitation, and less oxidised fluid chemistry of Proterozoic oceans would have permitted higher concentrations of these species. McArthur Basin seawater was therefore likely to be permanently supersaturated with respect to carbonate due to a combination of high atmospheric carbon dioxide, and elevated dissolved metals (Winefield, 1999). However, primary carbonate precipitates are not a common feature of the BCF, and some other process must have acted to drive local carbonate precipitation. The distribution of nodular carbonates predicates that this 'trigger' must have been influenced by the base-metal mineralising system, but did not cause precipitation in the centre of that system.

*In situ* carbonate precipitation has been described from several modern and ancient sedimentary environments with prolific benthic microbial faunas (Lyons *et al.* 1984; Cafetz and Buczynski, 1992; Gerdes, 1994; Knorre and Krumbein, 2000; Sami and James, 1993, 2000), and ecological arguments suggest that prokaryotic microbial groups were probably extremely abundant during the Precambrian (e.g. Grotzinger, 1999). Many species of SRB generate bicarbonate and/or hydroxide as a product of their metabolism of sulphate (Peck, 1982; Widdel 1988), via the simplified reaction below, which leads to locally higher pH and enhanced carbonate supersaturation.



It is unlikely that a microbial community produces even a significant proportion of the carbonate precipitated, but that it initiates carbonate precipitation by locally influencing fluid chemistry is considered one of the fundamental processes in Precambrian carbonate formation (Sami and James, 1996; Castanier *et al.* 2000).

There is abundant evidence for the existence of a highly productive bacterial fauna during deposition of the BCF; microfossils in chert and pyrite (Oehler and Logan, 1977; Logan *et al.* 2001); textural identification of microbial mat fragments, lamalginite, and microbial pyrite laminations (Crick, 1992; Logan *et al.* 2001; this study); and diverse and distinctive biomarker occurrence (Logan *et al.* 2001). Further, the close spatial association between pyritic laminae containing macroframboids of probable microbial origin (ch.3) suggests that precipitation of

nodular carbonates at HYC may have been catalysed by a bacterial trigger. If we accept that the HYC sub-basin was a stratified hydrothermally-fed water body during Barney Creek time (Large *et al.* 1998, 2000; ch.3,5), then the distal limit of prolific SRB activity is likely to coincide with a critical physicochemical difference between strata; temperature, pH, redox potential, or a combination of these. In the anoxic layer, intense sulphide precipitation in a local depocentre would drive pore fluid compositions to mildly acidic conditions and prevent calcite precipitation. The distribution of nodular carbonates at HYC is possibly the result of varying and interdependent fluxes of bacterially generated bicarbonate and acidity on the fringes of the zone of major basemetal sulphide precipitation in the deepest part of the basin.

#### 4.6.2 Dolomitization

Penecontemporaneous diagenetic dolomitisation is a common feature of Precambrian carbonates, but iron and manganese content of dolomites from the HYC mineralised zone (ore and halo) are significantly greater than equivalent 'ordinary' McArthur Basin dolomite compositions. This is interpreted to reflect direct involvement of the mineralising fluid in the formation of dolomite at HYC (Large *et al.* 2001). Similarly, Davidson (1998) identified a characteristic phase of ankerite-*adularia* alteration related to base-metal mineralisation at HYC. In contrast to crystallographically zoned calcite nodules, dolomite (and ankerite) nodules at HYC are compositionally homogenous. Dolomite nodules contain approximately ten times as much iron and twice as much manganese as calcite nodules (and may reach ankerite compositions), in keeping with the relative ease of iron and manganese substitution into dolomite and calcite lattices, respectively (Reeder, 1983). This variation is unlikely to represent a change in the fluid composition in equilibrium with calcite and dolomite, and is thus unlikely to indicate long temporal separation between formation of the two.

Primary sedimentary dolomite is extremely rare, is usually compositionally similar across large areas, and is largely restricted to certain low-sulphate evaporitic settings (Deer *et al.* 1992, and references therein). It is therefore unlikely that the HYC nodular carbonates are primary dolomite precipitates. Dolomite formation is favoured under conditions of low dissolved sulphate and calcium, may be driven by magnesium release during alteration of smectite to illite, and is inhibited by amorphous silica precipitation (Machel and Mountjoy, 1986; Anovitz and Essene, 1987; Deer *et al.* 1992). These conditions may all have been enhanced in the proposed HYC ore fluid after

modification by precipitation of the early paragenetic phases. Local sulphate depletion due to precipitation of mode 2 (late) sulphides in the sediment pile is indicated by the relatively heavy sulphur isotopic composition of those phases (Eldridge *et al.* 1993, ch.5). Similarly, precipitation of primary calcium carbonates may cause local fluid calcium depletion. There is abundant (and enigmatic) illite in the HYC sedimentary host-rocks (Large *et al.* 2001), at least some of which was probably deposited as smectite of terrigenous origin. Lastly, (although not considered elsewhere in this study) fossiliferous sedimentary black cherts occur sporadically throughout the deposit and indicate that seafloor conditions were periodically suitable for precipitation of amorphous silica (Oehler and Logan, 1977). It is highly possible that dolomitisation of the nodules took place in the sediment pile shortly after primary calcite nodule formation, and was caused by a sulphate and calcium-depleted, magnesium-enriched modification of the original ore fluid. Detrital carbonates were unaffected because they had been dolomitised prior to resedimentation, as is suggested by C-O isotopes (Rye and Williams, 1981; Large *et al.* 2001).

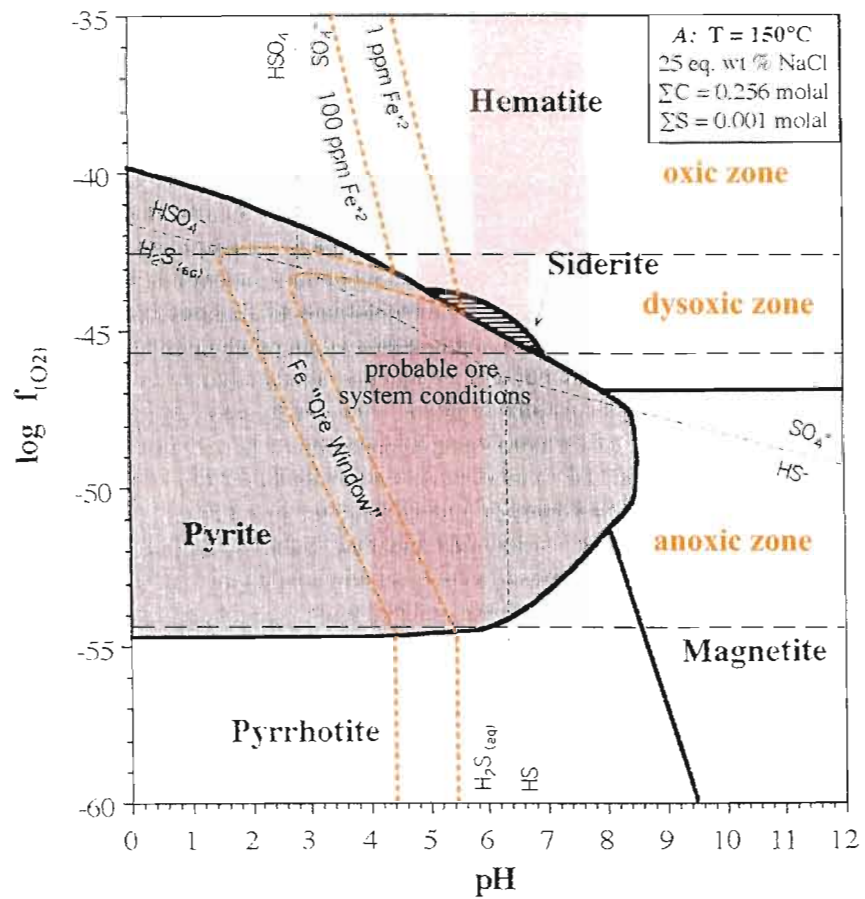
#### 4.6.3 Iron-Manganese Substitution

Solid solution between end-member carbonates is affected by the concentration of the various cations in solution and the precipitation temperature (Anovitz and Essene, 1987; Klein and Hurlbut, 1992). Cooke *et al.* (1998) used thermodynamics to determine that within the probable range of HYC ore fluid parameters, manganese solubility is enhanced by higher temperatures and low pH (fig 4.13b), whereas iron solubility is maximised near the sulphate-sulphide predominance boundary, at low pH (fig 4.13a), and high temperatures. Therefore, the total metal substitution will be controlled primarily by temperature whereas the ratio Fe/Mn will be controlled by the oxidation state of the fluid.

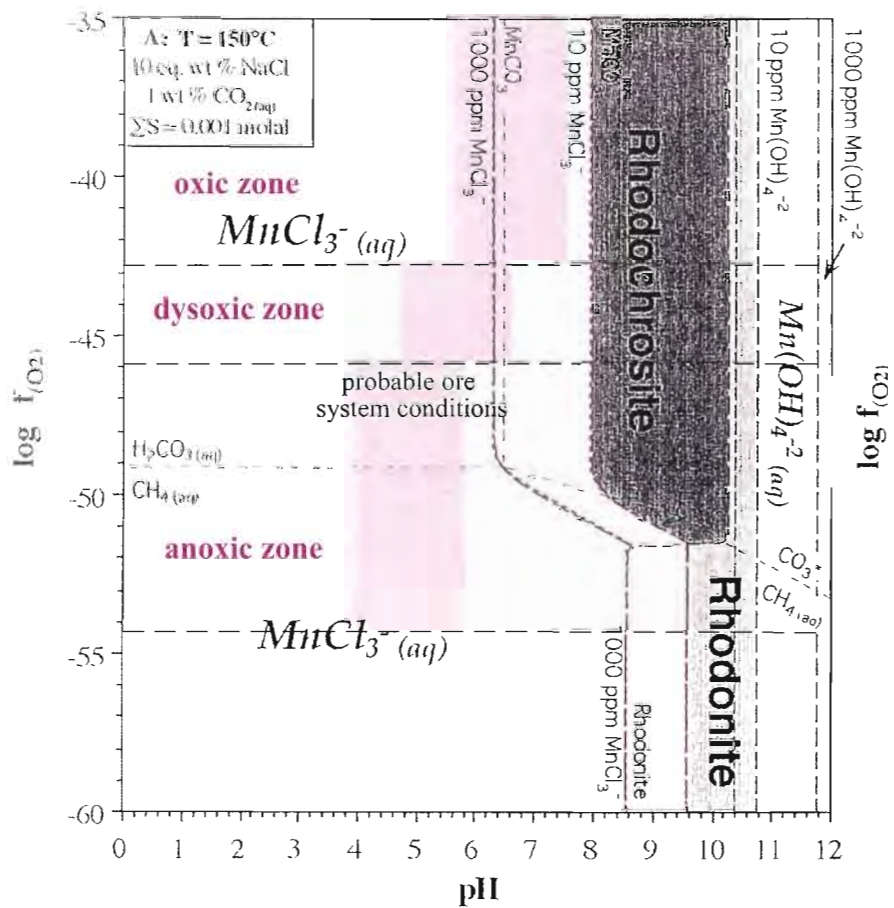
Concentric distribution of nodular carbonates around the high grade (Zn) zone, and similar spatial trends in sulphur isotopes on both the north and south fringes of the deposit (ch.5) suggest that mineralisation occurred in a thermal regime that was concentrically zoned rather than unidirectional. The N-S asymmetry of the degree of Fe-Mn substitution into dolomitic (and ankeritic) nodular carbonates is therefore unlikely to be caused by ambient, long-standing temperature variation. However, the similarity of ankeritic nodule compositions to carbonates intimately associated with strongly developed sphalerite 1 indicate that the two precipitated from a fluid with similar characteristics, i.e. largely unmodified ore fluid. Coincidence in the northeast of

*Figure 4.13 –  $fO_2$ -pH diagrams for proposed ore system fluid conditions, showing the likely ranges of conditions in each of the proposed layers of a stratified water body in the HYC Sub-basin, mineral stability fields, and the solubility contours for iron and manganese. Intersection of the condition fields and the solubility contours indicates strong redox control on iron solubility in contrast to pH control on manganese solubility.*

(A)



(B)



ankeritic nodule occurrence and the location of ore fluid influx into the #2-3 ore lens systems supports this suggestion. However, exceptionally rapid precipitation of base-metal sulphides also occurred in this part of the deposit and would have caused local decrease in pH, consistent with unusually complete sulphide replacement of nodular carbonates in the same area (fig.4.2f). Therefore, relatively hot, unmodified ore fluids were not permanently resident in the northern fringe of the system, or conditions would not have permitted formation of nodular carbonates at all in that part of the deposit. Instead, batches of ore fluid entering the system are envisaged to cause ankerite replacement of calcitic nodules *en route* to the deepest part of the basin without upsetting physicochemical stratification of the water column (fig 4.14b).

Dolomitic compositions in the central and inner fringe zones are fairly uniform, and precipitated under cooler and/or more alkaline conditions than ankerite. Covariation of Fe/Mn with total substitution also suggests that dolomitic compositions formed at conditions closer to the sulphate-sulphide predominance boundary than for ankerite, i.e., where the ratio of Fe/Mn in solution would also have been lower due to decreased iron solubility. Given the abundance of sulphide in the mineralising system, dolomite compositions probably formed under more reduced conditions than ankerite. This is consistent with a chemical and thermal gradient between warmer more oxidised primary fluid in the centre of the mineralising system and ambient cooler, more reduced seawater distally (fig.4.14). Decline of both total substitution and Fe/Mn in the far southern fringe probably relates to a continuation of this gradient to cooler temperatures and more reduced conditions away from concentration of ore fluids.

#### 4.6.4 Isotopic Variations

Departure of the isotopic composition of a few nodular carbonate samples toward lighter  $\delta^{18}\text{O}$  and marginally heavier  $\delta^{13}\text{C}$  is difficult to reconcile with the rather uniform isotopic composition of siltstone dolomites throughout the deposit. This isotopic trend is most pronounced for nodular carbonates of ankeritic composition, which indicates that it is related to the temperature of dolomitisation of primary nodules. Treated loosely, this coincides with modeling of water-rock interaction presented by Large *et al.* (2001), which shows a shift from  $^{18}\text{O}$  enrichment to depletion at about 150°C for the probable fluid composition (fig 4.15). Combined with simultaneous decrease in water-rock ratio (sediment pile v. water column conditions), this mechanism adequately predicts the pattern of observed nodular carbonate isotopic values. The apparent insensitivity of siltstone

*Figure 4.14* - Water-rock interaction modelling of the C-O isotopic effects on dolomite for the preferred ore fluid composition of Large et al. (2000). Orange line shows the anticipated trend for local interaction of carbonates with hot, unmodified fluids in the sediment pile. This hypothesis also accounts for covariation of Fe-Mn substitution with isotopic composition of nodular carbonates at HYC.

*Figure 4.15* - Schematic diagrams of a hypothetical hydrothermally-fed anoxic basal layer in a stratified water body; (a) usual steady-state conditions; (b) transient, hydrothermal influx conditions. Chemical gradients depicted control the location and cationic composition of nodular carbonates around the deepest part of the basin.

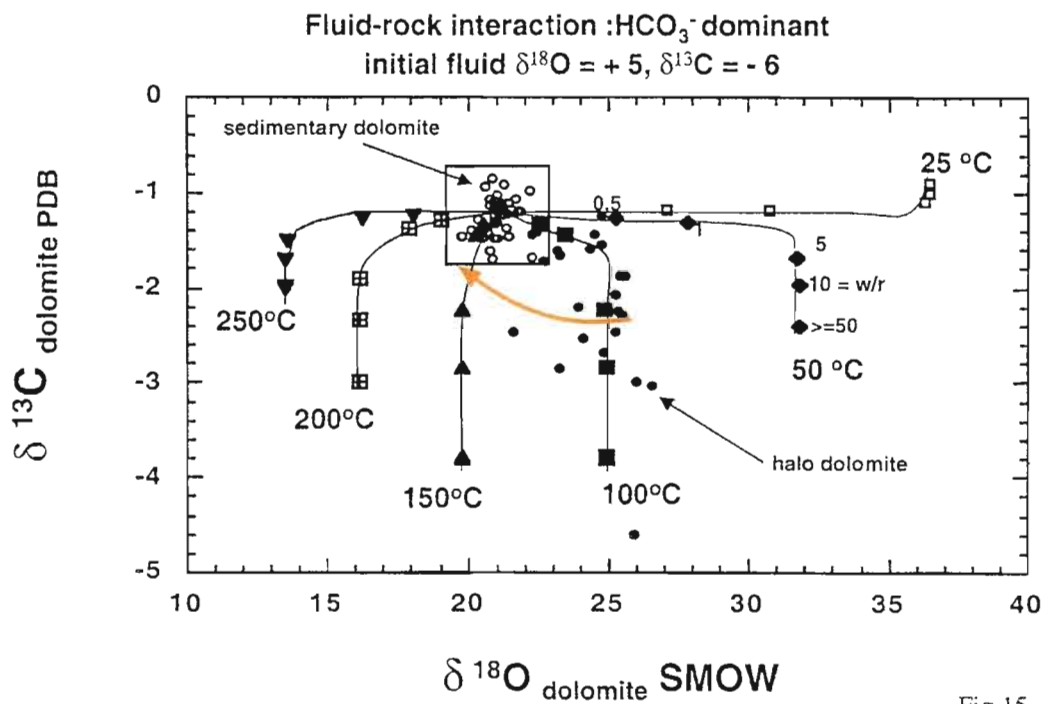
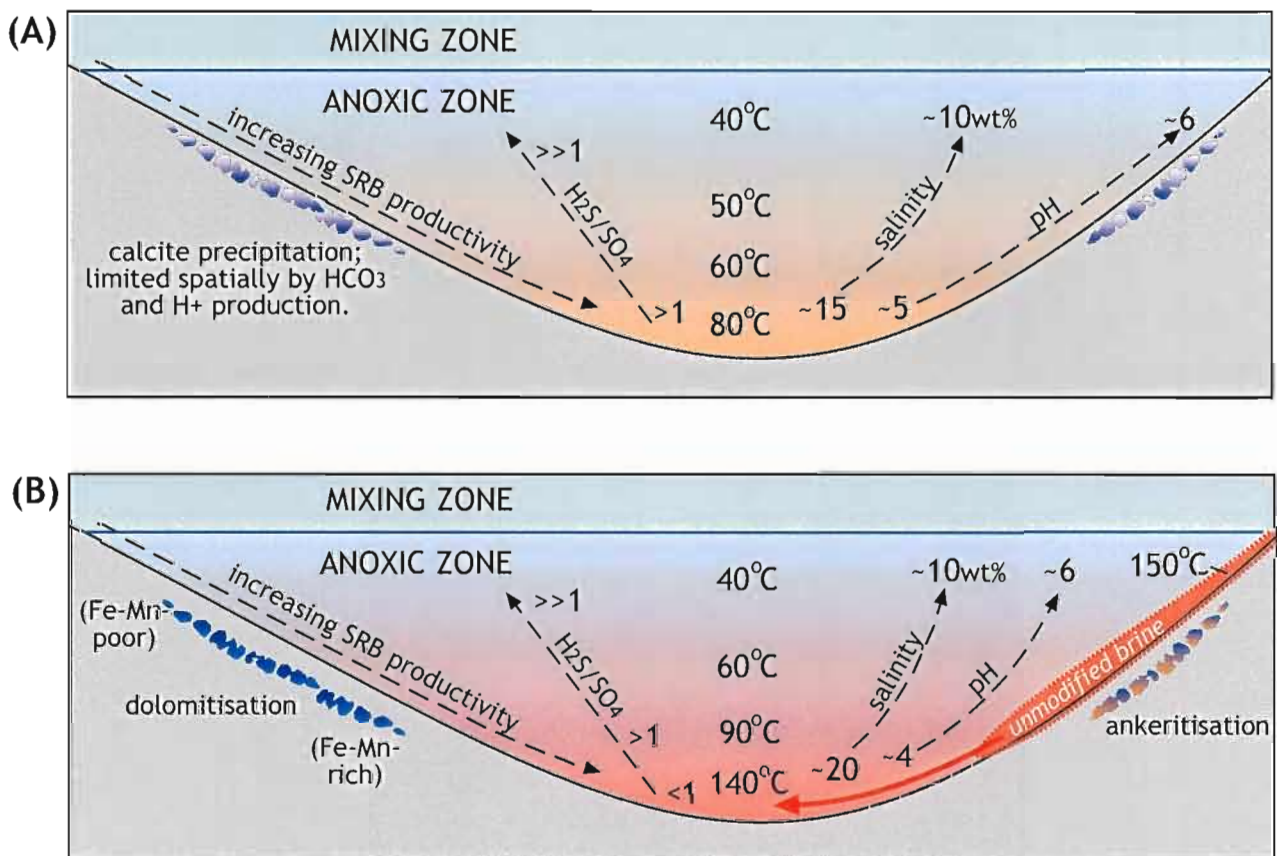


Fig 15



dolomite to whatever process causes the antivariant trend may arise because the process is intimately related to dolomitisation of calcite, or because the 'siltstone dolomite' field has been described from samples that do not originate in the northern part of the deposit and/or have ankerite composition.

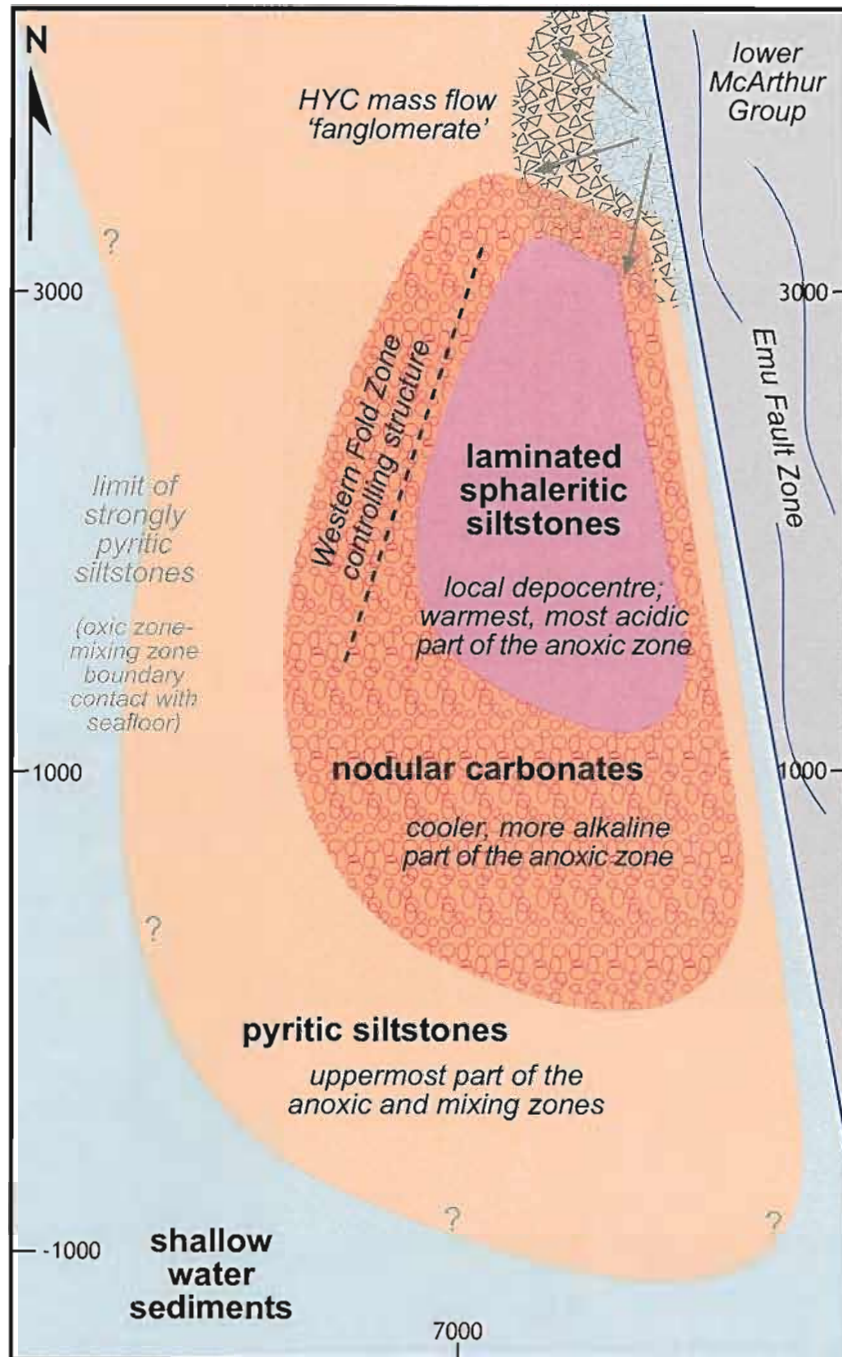
The effect of metal substitutions on carbonate isotope fractionation is anticipated to cause shifts of  $\delta^{18}\text{O}$  toward lighter values, but of less than one permil (Large *et al.* 2001), rather than the observed 4-7 permil. Rayleigh distillation of carbonate in the sediment pile might also cause lightening of carbonate oxygen isotope compositions, but this mechanism predicts lightening of both  $\delta^{18}\text{O}$  and  $\delta^{13}\text{C}$ , whereas the data trend to heavier  $\delta^{13}\text{C}$ . Ultimately, only 15 isotope analyses were made in this study (and only three on ankerite nodules) because it is not focussed specifically on the carbon and oxygen isotopic characteristics of the nodular carbonates. It is therefore premature to attempt to resolve the isotopic pattern rigorously.

#### 4.7 **Summary**

None of the individual results presented here go very far on their own to constraining processes of nodular carbonate formation. Together they reveal that the nodular carbonates are a complex and dynamic aspect of the HYC mineralising system that is strongly controlled by the interaction of the sedimentary environment and the flux of ore fluid into the basin (fig.4.14).

Microscopic textural relationships with sulphide phases necessitate that nodular carbonates formed temporally between mode 1 and mode 2 sulphides, and the presence of both laminated sulphide and nodular carbonate intraclasts in mass flow deposits constrains this mineralisation to the very shallow seafloor environment. The distribution of nodular carbonates concentric to the local depocentre, and the different S-C geochemistry of 'background' siltstones between the nodular and laminated ore facies suggest that there is a primary sedimentological control on nodule distribution. Although equivocal, stratigraphic relationships between laminated and nodular ore facies are also supportive of the primary sedimentological nature of nodular carbonates in the mineralised Barney Creek Formation.

*Figure 4.16 - Schematic plan view of the original distribution of the nodular carbonate ore facies relative to the other ore and sedimentary facies, and basin-controlling structures, prior to structural deformation. The distribution of facies is dictated by depth-controlled variations of the marine environment. In this interpretation, the outer limit of strongly pyritic siltstones corresponds to the point at which the mixing layer-anoxic zone boundary impinges on the palaeo-seafloor. The entire area studied here is located within the pyritic zone, and the location of the outer limit is unconstrained. HYC is located in the centre of a 10 km long-bouger gravity anomaly parallel to the Emu Fault Zone, which may in part be caused by anomalous density of the sulphidic sediments (Duffett, 1998). However, preliminary geophysical modeling indicates that the density contrast between pyritic siltstone and background McArthur Group sedimentary rocks is insufficient to alone generate a gravity anomaly of the magnitude observed.*



Variability in nodular carbonate composition is useful in constraining ideas of chemical and thermal gradients within the mineralising system (fig.6.14). For the concentric distribution to arise, there cannot have been a long-lived south-directed thermal and chemical gradient as has been interpreted from metal zonation. Had this been the case, rapid sulphide precipitation in the hottest part of the system would create local acidity and inhibit carbonate formation. Instead, the spatial distribution of nodular carbonates suggests thermal and chemical focussing in the local depocentre (fig.6.16). Rare crystallographically zoned calcite nodules indicate that calcium carbonate was the primary mineralogy, but was overprinted almost immediately by Mg-Fe-Mn carbonates. Broadly coincident spatial variation in the elemental and isotopic composition of this overprinting mineralogy is interpreted to reflect transient high-temperatures ( $\sim 150^{\circ}\text{C}$ ) near the point of ore fluid influx into the basin. The similarity of dolomite nodule and ore halo isotopic compositions further precludes widespread and dominant closed-system abiological oxidation of organic matter during mineralisation, and therefore places important constraints on sulphate reduction processes.

## 5 SULPHUR ISOTOPES OF THE #3 AND #4 ORE LENSES

### 5.1 Introduction

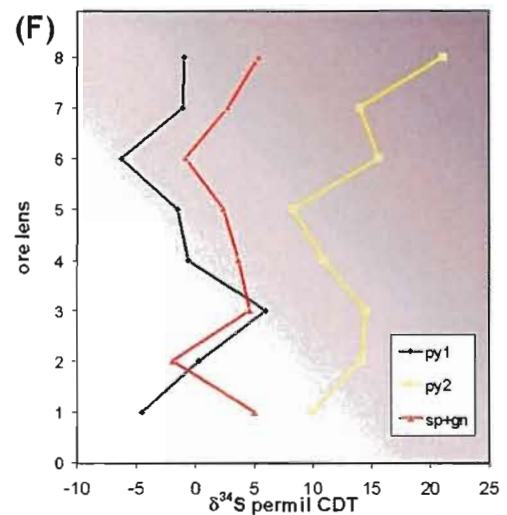
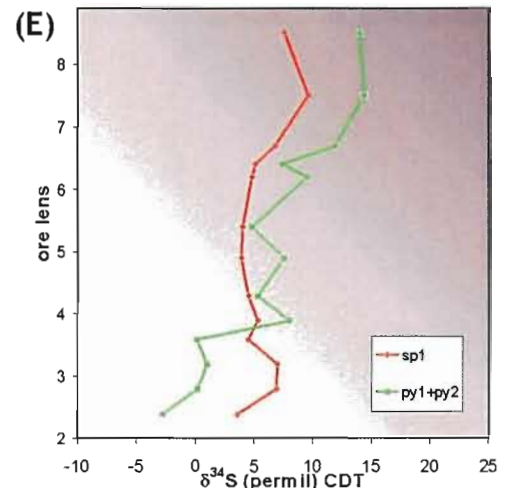
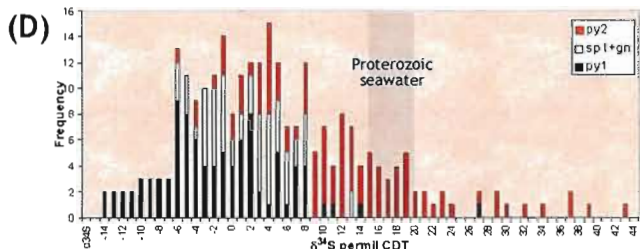
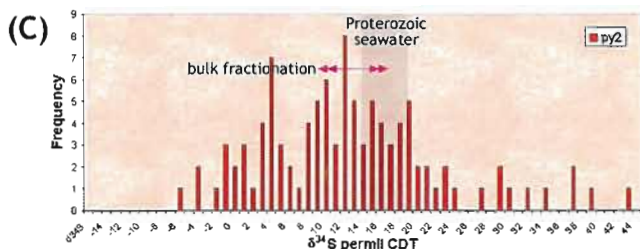
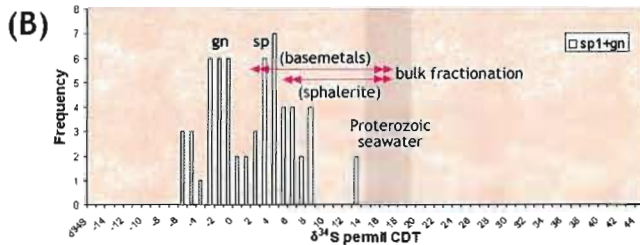
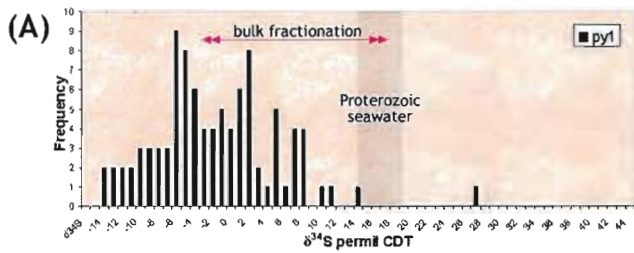
There have been extensive studies of the isotope characteristics of sulphide minerals at HYC (e.g. Smith and Croxford, 1973; Rye and Williams, 1981; Eldridge *et al.* 1993). These have produced complex and ultimately equivocal results that do not clearly constrain genetic hypotheses to one, or even a series of processes. It is generally accepted that seawater or evaporite sulphate was the major source of sulphur in the HYC mineralising system (Rye and Williams, 1981; Badham, 1981; Large, 1983; Cooke *et al.* 2000), and that Mesoproterozoic seawater had  $\delta^{34}\text{S}_{\text{SO}_4}$  in the range +15 to +20‰ (Muir *et al.* 1985; Strauss, 1993; Ohmoto and Goldhaber, 1997; Strauss *et al.* 2001). It is expected that lateral patterns in isotope distribution may more tightly constrain the interpretation of sulphur isotope data from HYC.

The different sulphide modes yield distinct populations of  $\delta^{34}\text{S}$  values (fig.5.1a-d). Pyrite (py1) values have normal distribution about a mean  $\sim$ -3‰ CDT, and pyrite 2 (py2) values have positively skewed broad distribution about a mean  $\sim$ +9‰. Values for base metal sulphides have bimodal distribution (probably  $\delta^{34}\text{S}_{\text{Ssp}} > \delta^{34}\text{S}_{\text{Sgn}}$ ) about a mean  $\sim$ +2‰, in between and overlapping the two pyrite populations. Therefore, if HYC sulphide sulphur is derived from Proterozoic seawater sulphate, then bulk sulphide-sulphate fractionation factors of 23‰ for pyrite 1; 15‰ for sphalerite 1; 11‰ for sphalerite 2; and 7‰ for pyrite 2 have been realised (assuming  $\delta^{34}\text{S}_{\text{SO}_4^{2-}} = +20\text{‰}$ ). In any one sample though, mode 1 sphalerite sulphur may be lighter, the same as, or heavier than co-occurrent pyrite 1, but is always lighter than co-occurrent pyrite 2 (Eldridge *et al.* 1993). Further, the  $\delta^{34}\text{S}$  of most phases varies upsection about an average value, whereas pyrite 2 shows a trend toward heavier  $\delta^{34}\text{S}$  values upsection (fig.5.1e-f; Smith and Croxford, 1973; Eldridge *et al.* 1993). Eldridge *et al.* (1993) also identified extreme isotopic disequilibrium of tens of permil in py2 aggregates and between sp1 and py1, illustrating apparent ‘...insensitivity of the sulphur isotope composition of the base metal sulphides to those of pyrite [1].’ (p16).

Most authors who have worked at HYC have suggested a possible sequence of sulphide mineralisation events based on the data available, variable textural investigation, and the prevalent

*Figure 5.1 - Previous sulphur isotope data for HYC, showing the bulk fractionation between estimated Mesoproterozoic seawater sulphate and the average value for each sulphide phase; (a) py1; (b) combined galena and sphalerite showing bimodal distribution probably caused by fractionation between the two; (c) py2 showing positive skew with a small number of very heavy isotopic values; (d) combined data showing overlap of the populations and overall positively skewed distribution, (e) upsection isotope trends reported by Smith and Croxford (1973); (f) upsection trends reported by Eldridge et al. (1993). All bulk population data is also from Eldridge et al.(1993).*

*Figure 5.2 - Summary table of previous interpretations of sulphate reduction processes and paragenesis at HYC, showing variation between syngenetic (SEDEX) models and various epigenetic replacement models (references included on table).*



### Summary of Sulphide Paragenetic Interpretations for HYC

Reference	Source of Reduced Sulphur	Timing of Mineralisation
Smith and Croxford (1973)	One for pyrite, another for base metal sulphides	Py, then Sp/Gn/Cpy simultaneously; most likely exhalative.
Williams and Rye (1974), Williams (1978)	Biogenic for pyrite 1, hydrothermal for pyrite 2 and base metal sulphides through thermochemical sulphate reduction by reduced carbon in sediments.	Py <sub>1</sub> , then Py <sub>2</sub> , then Sp/Gn/Cpy, Py <sub>1</sub> formed diagenetically before Py <sub>2</sub> , base metal sulphides formed later when metals and sulphur were introduced to the upper layers of sediment
Goodfellow and Jonasson (1986)	All biogenic	Py <sub>1</sub> , Sp/Gn/Cpy, Py <sub>2</sub> all simultaneous from exhalative brine introduction of metals into a waiting pool of H <sub>2</sub> S.
Maynard (1983)	Some of the pyrite must be biogenic, but the rest of the pyrite and base metal sulphides have hydrothermal source.	Because the sulphides form monomineralic layers and are conformable, they must be exhalative and syngenetic.
Eldridge <i>et al.</i> (1993)	Pyrite 1 and 2 are biogenic, base metal sulphides are hydrothermal but unspecified.	Py <sub>1</sub> , followed by Py <sub>2</sub> in later diagenesis, then Gn/Sp/Cpy simultaneously as replacement by hydrothermal fluid permeation of the sediment.
Perkins & Bell (1998)	Pyrite 1 and 2 are biogenic, base metal sulphides are hydrothermal but unspecified.	Py <sub>1</sub> , then followed by Py <sub>2</sub> later in diagenesis, the Gn/Sp/Cpy simultaneously as replacement after lithification.
Large <i>et al.</i> (1998)	Pyrite 1 is biogenic, base metal sulphides have mixed hydrothermal-biogenic source, and pyrite 2 is from sulphate introduced during mass flows and biogenically reduced.	Py <sub>1</sub> , immediately followed by Gn/Sp/Cpy, then Py <sub>2</sub> in late diagenesis.
Druschel <i>et al.</i> (in press)	The texturally inferred paragenetic sequence is consistent with numerical modelling of biogenic processes.	Py <sub>1</sub> , then in sequence and overlapping Gn-Sp-Py <sub>2</sub> .
Logan <i>et al.</i> (in press), Hinman (2001).	Pyrite 1 and 2 are biogenic, but the base metal sulphides have a hydrothermal source from thermochemical reduction by organic carbon in the unconsolidated sediment pile.	Py <sub>1</sub> , followed by Py <sub>2</sub> later in diagenesis, then after 10-20m burial, Gn/Sp <sub>1</sub> /Sp <sub>2</sub> /Cpy simultaneously. Sp modes are only texturally differentiate d.

school of thought (fig.5.2). Further suggestions have arisen from numerical modelling of modern biogenic sulphide-precipitating systems (Druschel *et al.* in press). These hypotheses vary mostly in terms of the timing relationships between phases (ch.3) and method of reduction of seawater (and evaporite) sulphate: bacterial sulphate reduction (BSR), or thermochemical reduction (TSR). Determination of the dominant process responsible for the generation of reduced sulphur is important for exploration as it controls interpretation of whether restricted, local depocentral sedimentary basin conditions are a fundamental aspect of the deposit genesis. This is the case if biogenic reduction is envisaged and mineralisation is directly linked to the sedimentary environment. If thermochemical reduction was the dominant process however, any large source of organic (reduced) carbon may act as a redox trap, and mineralisation is not necessarily linked to sedimentation (e.g. Broadbent *et al.* 1998). As reduced carbon can accumulate in a wide range of sedimentary rocks and in structurally controlled hydrocarbon traps, determination of post-sedimentation thermochemical reduction as the dominant process widens the range of potential exploration targets.

## 5.2 **Methods and Sampling**

### 5.2.1 **Analytical Method**

The stable sulphur isotope ratios of various sulphide phases were analysed at the University of Tasmania's Central Science Laboratory (CSL), using a laser ablation technique and 200 $\mu$ m-thick polished section samples. This apparatus uses an yttrium aluminium garnet (YAG) laser to ablate spots ~300 $\mu$ m wide (fig.5.3a), and the resultant SO<sub>2</sub>-containing gaseous mixture is then cleaned of water and CO<sub>2</sub> in a series of freezing-vaporization steps before analysis in a mass spectrometer. Analytical precision is reported at  $\pm 0.100$  permil.

Ablation targets were always selected on grounds of mineralogical purity, as the very fine-grained intergrown nature of sulphides at HYC prevents absolute exclusion of subsidiary phases. Pyrite 1 never forms aggregates > 10 $\mu$ m, and zones of flooding by this phase with minimal other sulphides (~60% py1, ~40% silicates and carbonates) were selected (fig.5.3b). Sphalerite 1 very rarely occurs without inclusions of galena and pyrite 1 (fig.5.3c), and decreased precision has been calculated

*Figure 5.3 - RLM of sulphide targets showing the size of the ablated spot; (a) ablated spot on a sp2 sample. The grey halo is zinc oxide deposited during ablation, and the brown halo is probably lead oxide from galena inclusions; (b) py1-flooded target; (c) sp1 target with quartz and organic impurities; (d) sp2 target with minimal impurities.*

*Figure 5.4 - Summary table of recalculated precision for laser ablation sulphur isotope data presented in this study, based on estimated mineralogical impurities and variation with a single lamina.*



### Effective Precision Estimation for Sulphur Isotope Data

Target Sulphide	$\delta^{34}\text{S}$ (CDT)	Average $\delta^{34}\text{S}$	Lam. $\sigma$	Impurities (wt% x nS)	Impurity $\delta^{34}\text{S}$ (wrt target)	Calc. Var.	Effective Precision
Pyrite 1	1.04 2.84 4.38	2.75	1.68	sp <sub>1</sub> + py <sub>2</sub> <5%	sp <sub>1</sub> +3 ‰ py <sub>2</sub> +15 ‰	+ up to 1 ‰	+ up to 2.5 ‰ - up to 1.5 ‰
Sphalerite 1	5.54 6.27 4.64	5.48	0.82	py <sub>1</sub> <10% gn <10%	py <sub>1</sub> -5 ‰ gn +6 ‰	± 0.8 ‰	± 1.6 ‰
Sphalerite 2	11.14 11.07 8.78	10.33	1.34	py <sub>1</sub> <10% gn <10%	py <sub>1</sub> -5 ‰ gn +8 ‰	+ up to 0.3 ‰ - up to 1.2 ‰	+ up to 1.7 ‰ - up to 2.6 ‰

based on estimation of modal abundances of these inclusions. Sphalerite 2 is generally monomineralic (fig.5.3d).

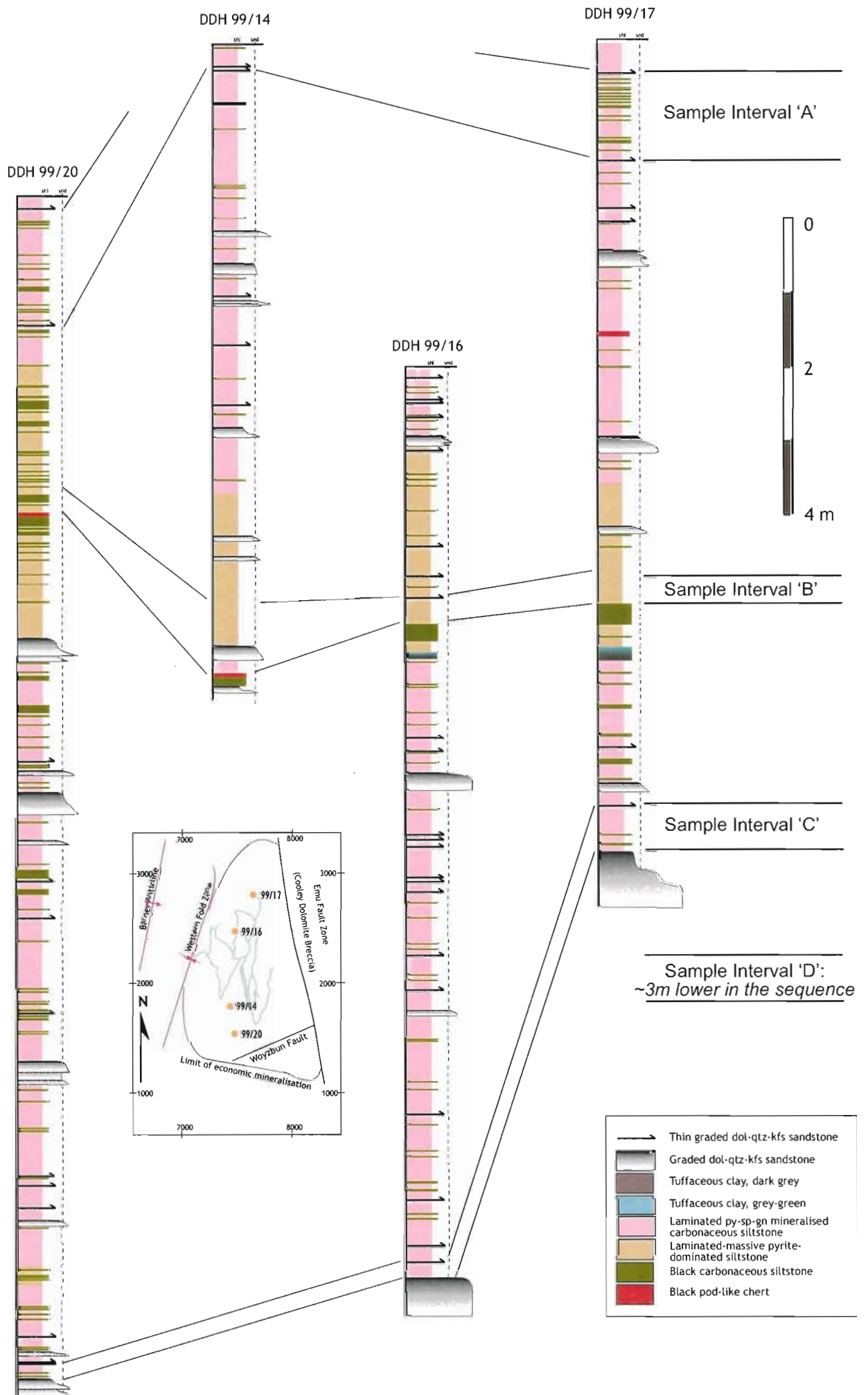
To constrain variability within a single lamina, three targets were analysed separately for one lamina of each target sulphide phase. Thereafter, the ablated gas from three spots per sample was analysed simultaneously to yield average values, for which effective precision has been recalculated (fig.5.4). This procedure is a conscious trade-off between statistical integrity and time and money constraints. The 40 new analyses performed during this study will be presented with 66 unpublished analyses of sphalerite from the #2 and #4 ore lenses, that were acquired using the same apparatus at the University of Tasmania, by Mike Blake, Ross Large, and Peter McGoldrick.

### 5.2.2 Sampling

The #3 ore lens was chosen for this sampling as it was intersected by a suitable array of drillholes throughout the deposit, and the core had largely not been used for metallurgical testing (unlike #2 and #4 ore lenses). Due to up-section variations in S isotope ratios (Smith and Croxford 1976, Eldrige *et al.* 1993), stratigraphic control was an important consideration in sampling. The #3 ore lens was logged at 1:10 scale in four drillholes so as to test lateral continuity of thin-bedded strata in the deposit, and to allow construction of a generalised stratigraphy on which sampling could be based (fig.5.5). Samples were taken from four locations identified in these sections and considered to be identifiable in most drillholes: (A) a 1 m zone of regular laminated sulphide interruption by thin black carbonaceous siltstones immediately below the I3/4 graded beds; (B) a zone of massive to laminated pyrite-dominated siltstone immediately above a 8-15 cm thick black carbonaceous shale, variably overlain by a black chert or accompanied by a characteristic green-black tuffaceous shale in the underlying metre of stratigraphy; (C) a 30 cm zone of high grade laminated sphalerite mineralisation immediately above the dominant graded bed in the lower part of #3 lens (3LC); (D) the first 50 cm of nodular carbonate mineralisation at the base of #3 ore lens. Sample location (A) has relatively loose stratigraphic control and was sampled as a reserve set. Samples from stratigraphic location (B) have been used for pyrite 1 sulphur isotope analysis, and those from location (C) have been used for sphalerite 1 isotope analysis. Samples from location (D) have been used for co-occurring sphalerite 1-2 pairs.

*Figure 5.5 - Stratigraphic correlations used in sampling for sulphur isotope analysis. Note that the chert (red) and carbonaceous siltstone couplet is the most distinctive marker bed in the northern part of the deposit, whereas the zoned tuff is the best marker in the southern part. The author is confident in the stratigraphic correlation within the ore zone, within a 50 cm range, but correlation of pyritic units (3M) is much more tenuous outboard of mineralisation (e.g. DDH G8). The potential for local, centimetre scale, upsection variation is unquantified and has been assumed to be minor in this study.*

# Sulphur Isotope Sampling Stratigraphy



### 5.3 Results

The bulk data presented here (fig.5.6) are the results of this study combined with similar laser ablation results of recent unpublished work on the #2 and #4 ore lenses by M. Blake and R. Large. Data presented in spatial context are exclusively the results of this study. All data are reported with respect to Cañon Diablo Troilite.

#### 5.3.1 Pyrite 1

The  $\delta^{34}\text{S}$  composition of py1 in the 3M stratigraphic unit has a mean value of 4.2‰; heavier than the bulk mean for py1 from throughout the deposit by ~7‰ (fig.5.6a). The new data vary between -3.3‰ and +8.0‰, consistent with previous data, and well within the established range of values (fig.5.1; Eldridge *et al.* 1993). The 3M unit is >50% pyrite, and the data are most probably shifted to heavier values due to kinetic partial system closure during rapid sulphide precipitation (Machel *et al.* 1995).

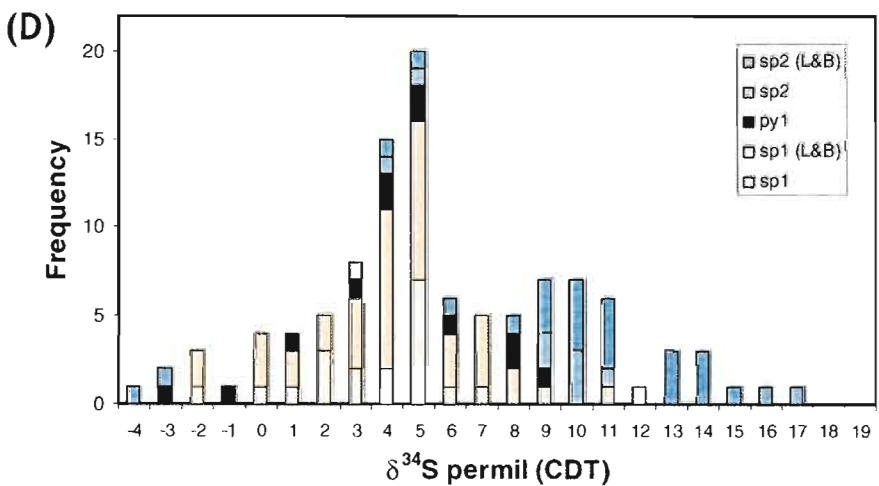
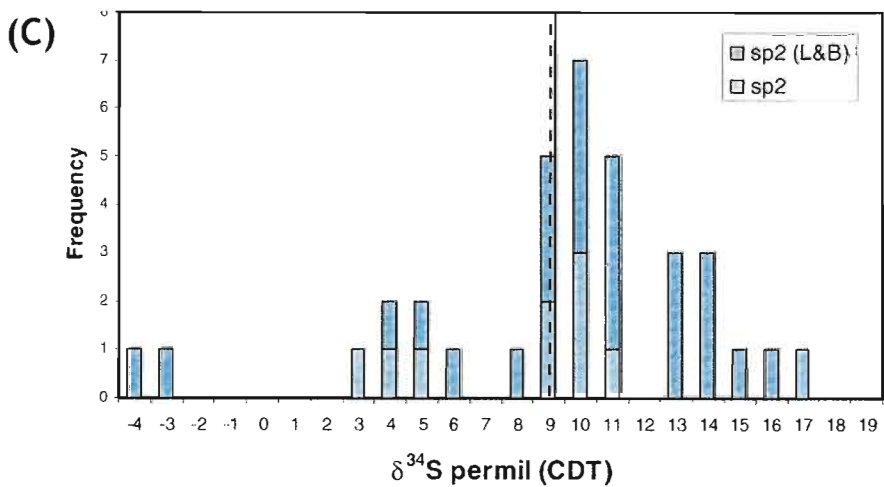
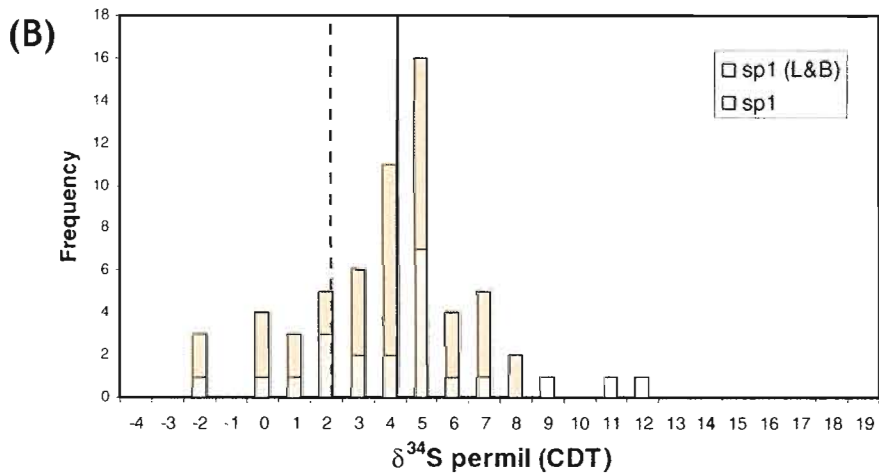
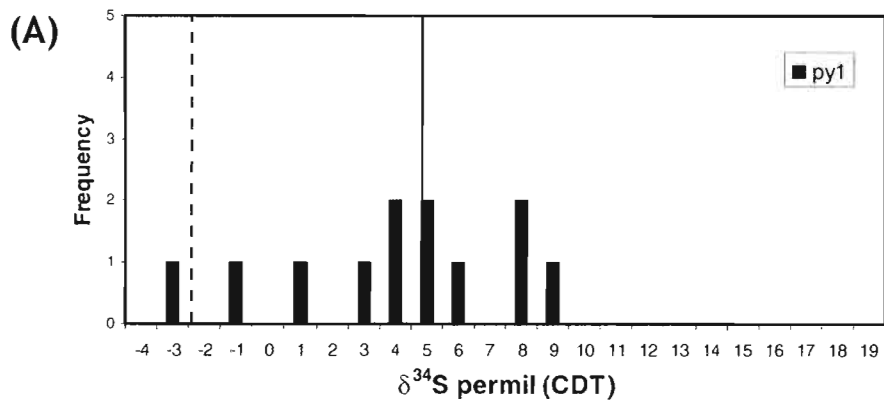
The py1  $\delta^{34}\text{S}$  values in 3M vary within a range of 11‰ along a 2 kilometre N-S section through the deposit. The isotopic composition is limited in the range +4 to +8‰ through the high grade (Zn) part of the deposit and is <0‰ in the moderate grade fringes of the deposit (fig.5.7). The one sample analysed from the very distal southern fringe zone is also heavy, but this is likely to be an artefact of poor stratigraphic correlation in this area. No significant variation is apparent along a NW-SE section, in which  $\delta^{34}\text{S}$  values are limited in the range +2 to +6‰

#### 5.3.2 Sphalerite 1

The  $\delta^{34}\text{S}$  composition of sphalerite 1 (sp1) analysed in this study, and that of Blake and Large, has mean value 4.2‰; marginally heavier than the bulk mean for sp1 from throughout the deposit (fig.5.6b). The new data vary between -2.4‰ and +12.1‰, but have relatively tight normal distribution ( $\sigma = 2.83$ ) and do not represent a departure from the previously determined range of values (fig.7.6b; Eldridge *et al.* 1993).

Sp1  $\delta^{34}\text{S}$  in 3LC vary across an 8‰ range along a N-S section through the deposit. Within the high grade (Zn) zone, the isotopic composition becomes gradually heavier toward the south (changing

*Figure 5.6 - Histograms of bulk sulphur isotope data produced in this study and in unpublished work of M.Blake and R. Large. Solid line is mean for combined new data, dashed line is mean value from Eldridge et al. (1993). The dashed line on the sp2 histogram is the mean value for py2, suggesting that sulphur supply to sp2 and py2 is similar. Py1 analysed in this study is heavier than the bulk average, probably because the 3M unit is pyrite-flooded and represents a period of unusually rapid sulphate reduction (and hence restricted fractionation of reduced sulphur). Sp1 data analysed in this study is also heavier than the bulk average, probably because that figure is the pooled average of galena and sphalerite together.*



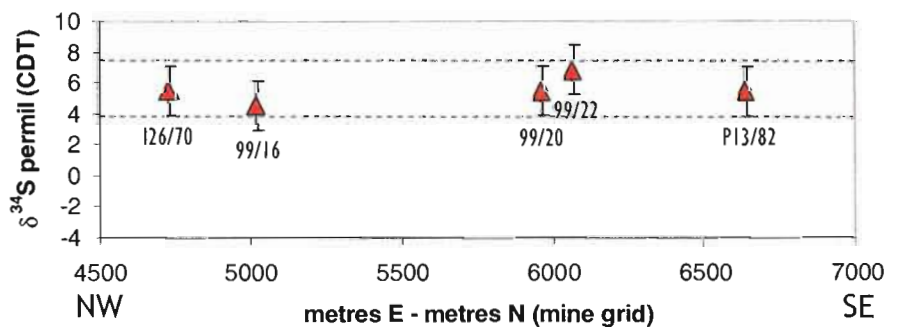
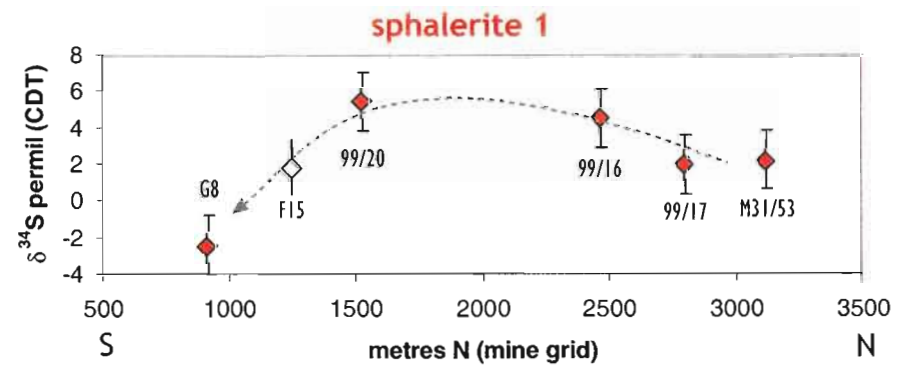
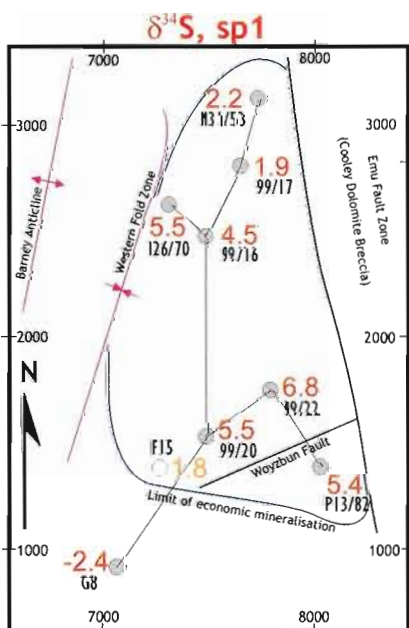
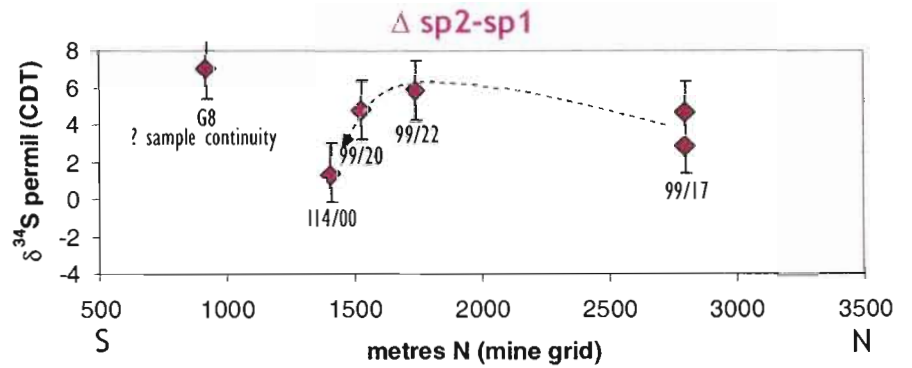
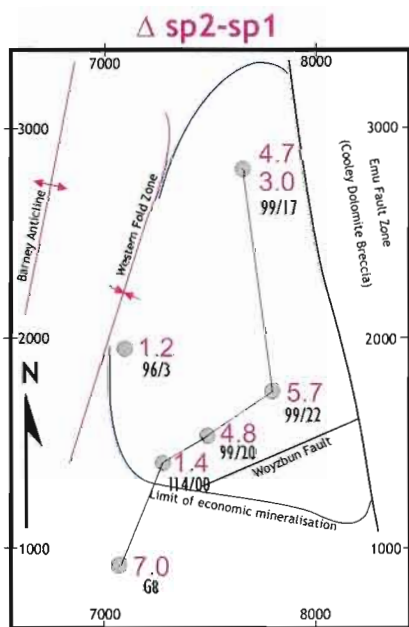
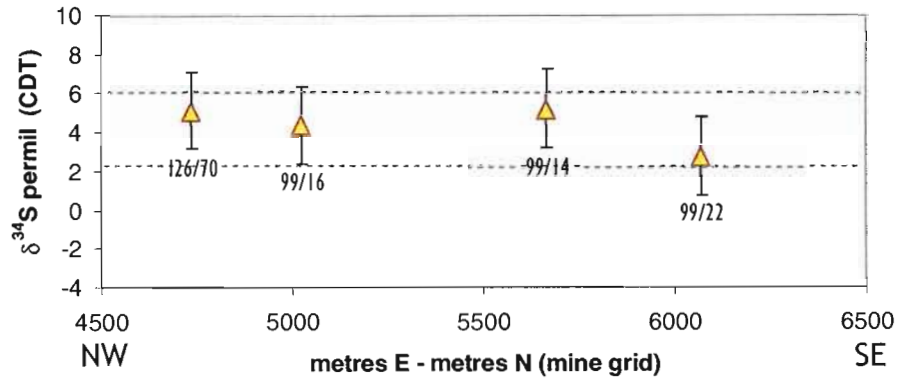
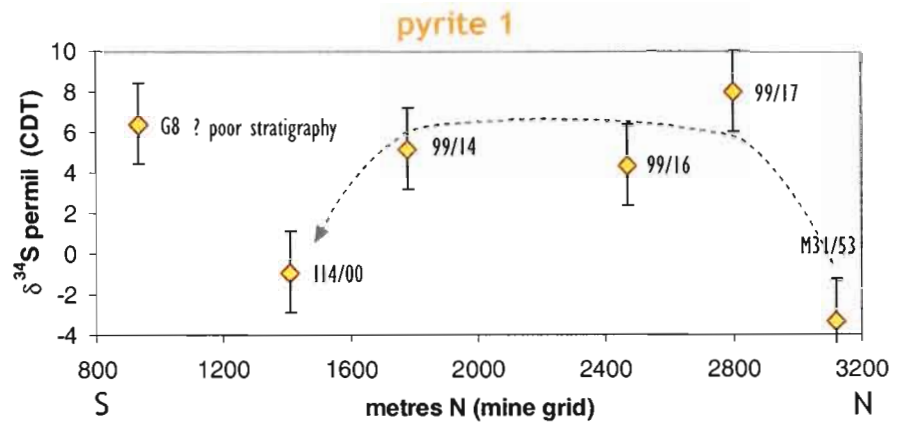
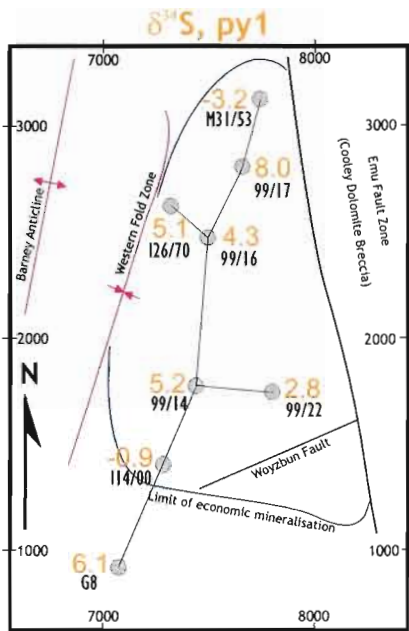
from  $\sim 2\text{‰}$  to  $\sim 6\text{‰}$ ), and then lightens in the distal environment to be  $<0\text{‰}$ . Stratigraphic correlation in DDH G8, to the south of economic mineralisation, is less convincing than elsewhere, and is important because it is the lone sample location in this area. However, the trend to lighter values south of economic mineralisation is maintained even if the upsection variability between ore lenses 2, 3 and 4 (Eldridge *et al.* 1993) is extrapolated from DDH F15 to this drillhole. Further, inclusion of un-stratigraphically constrained #3 ore lens data from DDH F15 (Eldridge *et al.* 1993), confirms the lightening trend south of high grade mineralisation (fig.5.7). There is no systematic variation in the sp1 isotopic composition along a NW-SE section, and  $\delta^{34}\text{S}$  values are limited within the narrow range  $+4$  to  $+7\text{‰}$ . In line with textural information (ch.3), this is interpreted to reflect confinement of sampling within the high grade zone, rather than absence of isotopic trends on these deposit margins.

### 5.3.3 Sphalerite 2

The  $\delta^{34}\text{S}$  composition of sphalerite 2 (sp2) has mean value  $9.3\text{‰}$ ; heavier than the bulk mean for sp1 from throughout the deposit by  $\sim 7\text{‰}$ . The data range between  $-3.9\text{‰}$  and  $+18.6\text{‰}$  ( $\sigma = 4.8$ ), the upper limit of which falls outside the previously recognised range of sphalerite values (fig.5.1, 5.6; Eldridge *et al.* 1993). Statistical analysis confirms that these data represent a discrete population and are not a subset of the previously established sp1  $\delta^{34}\text{S}$  population (fig.5.8).

Pairs of analyses conducted on coexisting sp1 and sp2 (spatially separated by  $<5\text{mm}$ ) show that although the respective  $\delta^{34}\text{S}$  populations overlap, sp2 is consistently heavier than sp1 in any given sample. Isotopic distinction of sp1 and sp2 is maintained for samples in which the two phases occur in immediately adjacent laminae (fig.3.9d,f). This parameter,  $\Delta_{\text{sp2-sp1}}$ , varies laterally across the deposit from  $>4$  in the high grade (Zn) central part of the deposit, to  $<2$  in the moderate grade deposit fringe (fig.5.7). The result for the southernmost drillhole is contrary to the apparent trend, but is probably an artefact of poor sample continuity; the two laminae analysed were by necessity separated by several centimetres because sphalerite is scarce in this drillhole.

*Figure 5.7 - Plans and sections showing lateral variability in sulphur isotope ratios of  $py1$  (top),  $\Delta_{sp1-sp2}$  (middle), and  $sp1$  (bottom). Dashed lines are interpreted trends and limits, made under the gross assumption that six data points adequately characterise the lateral variation. Unfortunately, higher sample frequency could not be acquired because of the lack of well preserved drillcore inclusive of the relevant intersections. Hollow datapoint for DDH F15 is taken from Eldridge et al. (1993).*



## 5.4 Sulphur Geochemistry and Marine Chemical Environments

### 5.4.1 Sulphate Reduction

The resolution of sulphate reduction mechanisms based solely on sulphide data can be complex and equivocal (Machel *et al.* 1995). Traditionally, dissimilatory bacterial sulphate reduction (BSR; Peck, 1982; Trudinger, 1992) has been cited in cases of extremely large kinetic isotopic fractionation between aqueous sulphate and sulphide ( $\Delta\text{SO}_4\text{-S}_2 = 4\text{-}46\text{‰}$ , but usually 15-30‰), because sulphate reducing bacteria (SRB) preferentially utilise sulphate containing  $\text{S}^{32}$  (Kaplan and Rittenberg, 1964; Chambers *et al.* 1975; Ohmoto and Rye, 1979). The largest fractionation from direct biological sulphate reduction is realised under conditions of unlimited sulphate supply and low metabolic productivity (Ohmoto, 1992; Canfield and Thamdrup, 1994). Conversely, there are two instances in which bacteriogenic isotopic fractionation may be diminished ( $\Delta\text{SO}_4\text{-S}_2 = 0\text{-}20\text{‰}$ ): in a system partially closed to sulphate, such that sulphate reduction progresses toward completion (Rayleigh distillation); and conditions of rapid sulphate metabolism wherein isotopic selectivity of sulphate is diminished (Machel *et al.* 1995; Ohmoto, 1992; Ohmoto and Goldhaber, 1997).

Many of the same bacterial groups have the ability to metabolise (by disproportionation) both elemental sulphur and thiosulphate ( $\text{S}_2\text{O}_3^{2-}$ ), and can engender cumulative isotopic fractionations in excess of 65‰ (Ohmoto and Rye, 1979; Jorgensen, 1990). Sulphate is not reduced directly to intermediate oxidation state sulphur compounds (Machel *et al.* 1995), and therefore these processes require either dissolved oxygen or iron/manganese oxide minerals as an oxidant for sulphide (Canfield and Thamdrup, 1994), or the presence of sulphur-oxidising bacteria. Elemental sulphur is generated in sediments in which sulphide production exceeds consumption (i.e. precipitation or re-oxidation) and is also commonly recognised to form at the redoxcline in stratified waters. The reaction stoichiometry and kinetics of partial sulphide oxidation causes elemental sulphur to be marginally heavier (0-7‰) than associated sulphide (Machel *et al.* 1995). Metabolic disproportionation proceeds via thiosulphate or polythionate intermediates and generates sulphide 7-8‰ lighter than precursor elemental sulphur (Canfield and Thamdrup, 1994). Importantly, the major biological sulphur-cycle processes are confined to the thermal regime in which SRB metabolize efficiently; 20-80°C (Stetter *et al.* 1987; Trudinger, 1992).

Thermochemical (abiological) sulphate reduction (TSR) is restricted by the kinetics of the inorganic redox reactions to temperatures above 100°C, becoming more efficient with increasing temperature. The subsequent isotopic fractionation relates inversely to temperature: resultant sulphide formed at 100°C is 20‰ lighter than precursor sulphate, but sulphide formed at 200°C is only 10‰ lighter (Machel *et al.* 1995). In practise, maximal TSR isotopic fractionations are rarely observed because of near-complete consumption of sulphate (Rayleigh distillation - Ohmoto and Goldhaber, 1997), or due to slow reaction kinetics and minimal sulphide yield at low temperatures. However, the intermediate oxidation state sulphur species (thiosulphate, polythionate, sulphur) catalyse the inorganic reduction of sulphate (Machel *et al.* 1995) and may permit TSR to operate effectively within the thermal regime usually assigned to BSR.

#### 5.4.2 Stratification of Water Bodies

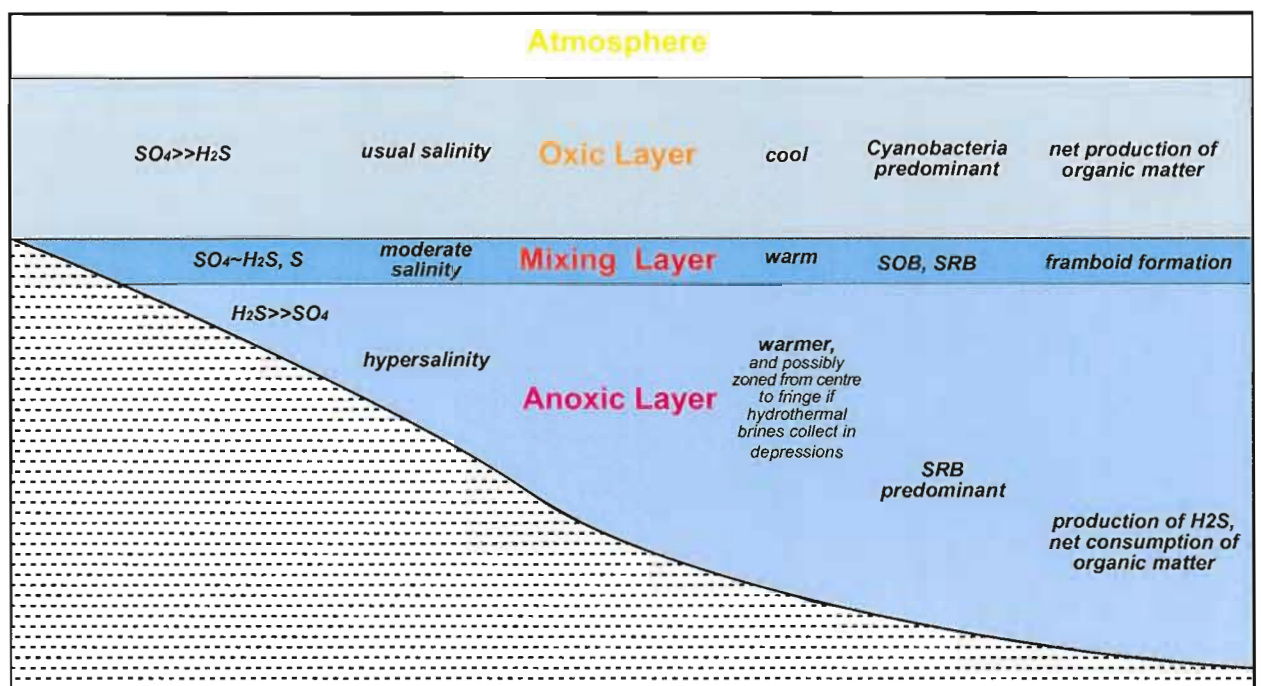
Stratification of restricted and closed water bodies usually results in three distinct aqueous strata: an oxic surficial zone which includes the photic zone; a deep anoxic zone; and a narrow (<10m) mixing layer (fig.5.9). Internally, these zones have uniform chemistry, and the layer boundaries are characterised by steep chemical gradients (Degens and Ross, 1969; Degens *et al.* 1973). The photic zone (oxic) is the site of most prolific biological productivity (mostly due to cyanobacteria, Ohmoto, 1992; Ramsing *et al.* 1996), and biomarkers isolated from HYC samples suggest that much of the organic material preserved in the Barney Creek Formation is cyanobacterial detritus (Logan *et al.* 2001). The thickness of the oxic zone is consistent basin-wide, and the only significant lateral variations in the amount of organic detritus generated and/or oxidatively degraded in the oxic zone occur where the oxic zone impinges on the seafloor.

The mixing layer is intermediate in temperature, Eh, pH and salinity, but it may attain anomalously high dissolved iron concentrations through redox cycling between layers (Craig, 1969). The mixing layer is the lowermost location of biological sulphide oxidation, and SRB may coexist with sulphur oxidising bacteria (SOB) because of chemical communication with both the oxic and anoxic layers. Consequently, up to 90% of the dissolved sulphur immediately below the oxic-mixing zone boundary may be elemental sulphur (Suits and Wilkin, 1998). The mixing layer is the zone of most prolific pyrite framboid formation (via the ferromagnetic precursor phase, greigite, Fe<sub>3</sub>S<sub>4</sub>; Kribek, 1975), and of pyrite replacement of organic debris (Schieber and Baird, 2001). Given the likely seafloor slopes for HYC-host sedimentation (north – 4°, south – 1°; ch.2), and the likely

*Figure 5.8 - Statistical calculations used to prove individuality of the sp1 and sp2 populations. Equations from Witte (1985).*

*Figure 5.9 - Summary diagram of the physical, chemical and biological characteristics of stratified water bodies, compiled from Degens and Ross (1969); Degens et al. (1973); Horodyski and Donaldson (1980); Keunen and Bos (1987); Canfield and Thamdrup (1994).*

	$\delta^{34}\text{S}$ sp1	$\delta^{34}\text{S}$ sp2
<b>n</b> (number of samples):	58	26
$\bar{x}$ (sample mean):	4.13	9.28
$\sigma$ (standard deviation):	2.83	4.79
$s^2$ (variance):	8.0	23.0
$\mu$ (hypothetical $\Delta\text{sp1-sp2}$ mean)		0.0
$s_p^2$ (pooled variance):	$= \sqrt{\frac{(n_1 - 1)s_1^2 + (n_2 - 1)s_2^2}{(n_1 - 1) + (n_2 - 1)}}$ $= 3.55$	
$s_{\bar{x}_1 - \bar{x}_2}$ (variance of means):	$= \sqrt{\frac{s_p^2}{n_1} + \frac{s_p^2}{n_2}}$ $= 0.444$	
<b>t</b> (test for 2 populations)	$= \frac{(\bar{x}_1 - \bar{x}_2) - (\mu_1 - \mu_2)_{hyp}}{s_{\bar{x}_1 - \bar{x}_2}}$ $= 11.67$	
<p>now, (with 95% confidence), the populations are significantly different if:</p> <p style="text-align: center;"><math>t &gt; 1.99</math></p> <p style="text-align: center;"><math>11.67 &gt; 1.99</math></p> <p>therefore, there is statistical separation of the two populations.</p>		



thickness of a mixing layer (5-10 m; Ramsing *et al.* 1996), approximately 100 and 600m of seafloor would have been directly influenced by a mixing layer on the northern and southern edges of the HYC sub-basin, respectively.

The basal anoxic zone is defined by the absence of free oxygen and the potential for residence of dissolved sulphide in the water column. It is usually warmer, more saline, contains more sulphate, and has lower Eh and pH than the upper layers (Craig, 1969; Degens *et al.* 1973; Sweeney and Kaplan, 1980). If it is fed by a hydrothermal brine, e.g. the Red Sea Deeps, the basal layer stabilises at a temperature below that of brine emission (Craig, 1969). The bacterial community is dominated by SRB, both in the water column and the upper few metres of sediment, and by fermentative bacteria below this depth (Peck, 1982; Suits and Wilkin, 1998). Fluxes of simple organic substrates and reactive iron are usually both dominated by pelagic rain of colloidal particles, and complex relationships emerge between SRB productivity and subsequent consumption of organic substrates and fixation of iron as pyrite (Raiswell and Berner, 1985; Suits and Wilkin, 1998).

## 5.5 Discussion

### 5.5.1 Lateral Isotope Patterns

The sulphur isotope data presented here indicates trends to lighter  $\delta^{34}\text{S}$  values for both pyrite 1 and sphalerite 1 across the fringes of the #3 ore lens. These trends are anticipated to continue right around the deposit, because the northern and southern fringes of the #3 ore lens represent opposite mineralogical and textural extremes within the deposit (ch.3). Absence of these trends in the NW-SE section sampled indicates only that the section did not penetrate the distal edges of the deposit.

#### 5.5.1.1 Lateral Sediment Permeation

Several genetic models for HYC have proposed that the mineralising fluid enters the unconsolidated sediment pile at the stratigraphic level of basemetal mineralisation (Eldridge *et al.* 1993; Perkins and Bell, 1998; Hinman, 2001). Metal zonations in the deposit (fig 3.1a) show that the #3 ore lens is enriched in lead and copper in the north-northeast, and that the tenor of these metals decreases southward. Based on thermodynamics and metal solubilities, this is interpreted to represent higher

temperatures and metalliferous fluid influx into the system from the north-northeast (Logan, 1979; Hinman, 2001).

Organic carbon-mediated TSR is only likely to be viable at temperatures above 100°C (although the catalytic effects of mid-oxidation state sulphur species is unquantified), and so the mineralising fluid must enter the sediment package at greater than 100°C if TSR is the dominant reduction mechanism, and then cool as it moves away from a point of influx. The temperature dependence of isotopic fractionation during TSR would cause greater fractionation in the cooler, distal parts of the system, i.e. sulphides precipitated would be isotopically heavier near the influx point, and lighter away from it. Further, closed-system sulphate consumption (Rayleigh Distillation; Ohmoto and Goldhaber, 1997) could also drive sulphide isotopic compositions to very heavy values in the extreme distal zone.

The pattern of distally lightening sulphide sulphur isotopes observed at HYC can therefore be generated by thermal effects and TSR. If this was the case (assuming  $\delta^{34}\text{S}_{\text{sulphate}} = +20\text{‰}$  and unlimited  $\text{SO}_4$ ), the observed fractionation (using sphalerite 1) in the deposit centre ( $\sim 15\text{‰}$ ) and the fractionation in the deposit fringe ( $\sim 22\text{‰}$ ) would equate to temperatures of  $\sim 150^\circ\text{C}$  in the centre (Machel *et al.* 1995), and  $80^\circ\text{C}$  in the deposit fringe (the fractionation between aqueous sulphide and sphalerite is negligible; Ohmoto and Goldhaber, 1997). However, the location of highest temperature, and hence also fluid influx, must have been in the centre of the deposit for the observed concentric pattern to result. This cannot be reconciled with the metal zonation that suggests fluid influx from the north-northeast. Likewise, the predicted temperatures (and the thermal range of TSR) do not match the results of recent carbon-oxygen isotope work (Large *et al.* 2001) that suggests carbonates equilibrated with fluids at temperatures in the range  $80\text{--}25^\circ\text{C}$ . The lateral isotopic patterns indicated by this study do not support a genetic model that involves post-sedimentation TSR.

#### 5.5.1.2 *Chemical Sedimentation*

Given the inexact state of our knowledge about Proterozoic biotas, there are numerous ways of explaining the observed concentric, distally lightened sulphur isotope pattern in terms of chemical sedimentary processes, bacterial sulphur-cycle effects and water stratification that impinges on the seafloor. Isotopic disequilibrium and spatial decoupling of the two dominant sulphide phases (pyrite

1 and sphalerite 1) suggests that different processes were responsible for their precipitation despite similar laterally variant isotope distribution (ch.3).

### ***Thermochemical Sulphate Reduction (TSR)***

If we assume that TSR can occur at temperatures in the range 25-80°C (ambient ore system T°C proposed by Large *et al.* 2001), then thermal variation between aqueous strata, or within a basal high-salinity layer, can account for distally lightened isotope patterns. If hot metalliferous fluid is introduced in batches to the basin and later cools and diffuses into a basal layer (ch.3; fig.5.10), thermal communication between brine and seawater could generate a thermal gradient (McDougall, 1984) in the basal layer. Oxidation associated with TSR has been shown to be the likely cause of anomalous maturity of organic matter and unusual alkane distributions recognised in mineralised laminae (Crick, 1992; Logan *et al.*, 2001). The density contrast between proposed mineralising fluids and seawater is such that a fluid pulse will flow on the seafloor almost independent of the ambient environment (Sangster, 2001; ch.3), and temperature gradation may develop concentric to a local depression, rather than along the flow path.

TSR therefore probably took place in the HYC mineralising system, but there is considerable evidence that it was not the dominant sulphate reductive process. Oxidation of organic matter generates isotopically light dissolved carbonate, which is not recorded in any of the ore system carbonates (ch.4). The amount of dissolved carbonate produced during TSR must therefore have been negligible compared to the abundance of ordinary marine bicarbonate. Furthermore, the temperatures anticipated for ore formation are far below the accepted range for TSR. Fine grained sulphide textures indicate very rapid precipitation and necessitate efficient sulphate reduction, which is unlikely if TSR operated near its lower thermal kinetic limit.

### ***Pure Bacterial Sulphate Reduction (BSR)***

The isotopic fractionation caused by BSR is inversely related to the rate of sulphide production (Ohmoto, 1992; Canfield and Thamdrup, 1994), in turn controlled by the amount of available simple organic fuel and the ambient temperature. As the bulk of organic detritus is generated in the oxic layer, the flux of organic fuels to the deeper layers is laterally consistent. Distinct thermal zonation controlled by stratification of the water would influence benthic bacterial productivity (Peck, 1982; Schidlowski, 2000), the nature of which is bacteria-dependent. There are thermophilic species that metabolise sulphate more rapidly at higher temperatures, and others that

are inhibited at high temperature (Peck, 1982; Trudinger, 1992). Therefore it is possible to generate either distally light, or distally heavy isotopic patterns concentric about the local depocentre as a result of bacterial comfort in the different aqueous layers.

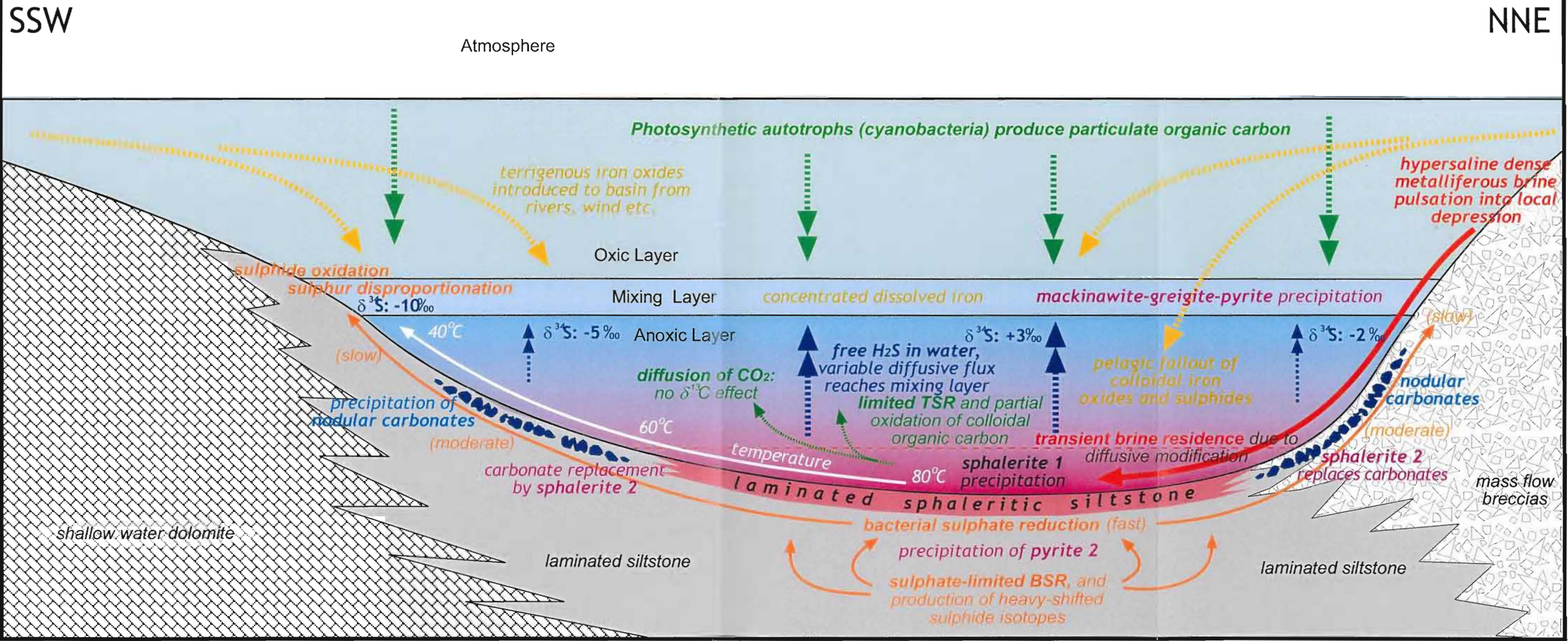
It is also possible that sulphate consumption in the warmest part of the anoxic zone caused greater local sulphate depletion, and hence greater Rayleigh distillation, than in the cooler fringes of the anoxic zone. Slower sulphate reduction at lower temperature distally is less likely to exceed the rate of sulphate replenishment, and open-system fractionation would result in isotopically lighter sulphides. This could also generate a concentric distribution of isotopically lighter sulphides around a heavier central zone.

The magnitude of the difference in isotopic fractionation cannot realistically be estimated because the relationship between productivity and fractionation is not quantitatively understood. However, Ohmoto (1992) has suggested that temporal decline in bulk organic fluxes into the oceans is reflected in the magnitude of sulphate-sulphide fractionation; from 5‰ in the Archean to >30‰ currently. For the Proterozoic this curve predicts maximum fractionation of ~20‰, which is consistent with the observed ~10-20‰ range observed for pyrite 1 and sphalerite 1 at HYC.

### ***Complex Microbial Communities***

The different physicochemical characteristics of layers in a stratified water body creates potential for several communities; benthic and planktonic in each thermal and chemical zone. If there is systematic difference between the sulphur isotope fractionation caused by different bacterial groups, then bacterial distribution based on environment would generate concentric isotope patterns around the local depocentre. A likely scenario is that SOB inhabit the mixing zone, and SRB therein are forced to use secondary metabolic pathways because they are unsuited to this environment. Therefore, whereas sulphate reduction may be the dominant process in the anoxic layer, sulphur disproportionation may be important in the mixing zone (fig.5.10). Sulphide re-oxidised to elemental sulphur by SOB retains its isotopic character (Machel *et al.* 1995), but elemental sulphur disproportionated by SRB becomes 7-8‰ lighter than source sulphur (Canfield and Thamdrup, 1994). The majority of modern SOB communities are benthic, and hence sulphide precipitated on the seafloor in the mixing zone would be isotopically lighter than that precipitated in the anoxic zone. It is also possible that metalliferous fluids entering the basin are toxic to some microbes

*Figure 5.10 - Schematic diagram (not to scale), depicting complex interaction of processes relevant to the marine and diagenetic sulphur cycle during mineralisation at HYC. Note the primary thermal control over the rate of sulphate reduction and hence the degree of sulphur isotopic fractionation, and the potential for BSR and TSR to occur simultaneously in the hottest part of the system. For clarity, sub-seafloor processes shown much deeper than top few metres of sediment in which they are envisaged to occur.*



(Truper, 1969), and cause repeated retreat and recolonisation in response to brine accumulation in a local depocentre. This also has potential to cause concentric variation of microbial communities, and hence of sulphide isotopes also.

### 5.5.2 Two Isotopically-distinct Sphalerite Populations

The two sphalerite modes are distinct texturally (fig.3.9), are separated temporally, and are always in isotopic disequilibrium; the extent of which decreases distally. However, both modes are variably associated with ankerite and quartz precipitation, and therefore precipitated from a chemically similar fluid. If sp2 was the product of remobilisation of sp1, it follows that the two should be isotopically indistinguishable. This is clearly inconsistent with the findings of this study.

There is inverse correlation between the isotopic  $\Delta_{sp2-sp1}$  and total modal abundance of sphalerite (and hence basemetal sulphides generally), and it has been shown that sp2 formed later than, and deeper in the sediment pile than sp1 (ch.4). Sulphate-depletion of the fluid from which sp1 precipitates would be related to the rate of sulphate reduction, and ultimately, to the amount of sulphide precipitated. Therefore, Rayleigh distillation effects are likely to be more pronounced in the zone of strongest sphalerite precipitation. If the mineralising fluid resides in the sediment porosity after precipitation of sp1 has finished, it is then available for sp2 formation with  $\delta^{34}\text{S}_{\text{sulphate}}$  character evolved to heavier values in the central high-grade zone than in the deposit periphery. In this way the fluid characteristics that drive gangue mineral precipitation are preserved, and the isotope trends of the deposit fringe can be explained.

## 5.6 Conclusion

Concentric isotopic patterns around the deposit are best explained by variations in local fluid sulphide flux and composition, driven by benthic bacterial colonisation and productivity, and related to chemical gradients and stratification of the basin. The patterns are difficult to reconcile with a TSR and point-source, lateral influx of mineralising fluid into the sediment pile. It has been shown that the high grade and thickened zone at HYC closely correlates with the probable depocentre during deposition of the host sediments (ch.2), and hence patterns concentric to zinc grade are also concentric to water depth during sedimentation. It is proposed here that sulphate

*Figure 5.11 - Compilation of bulk sulphur isotope data from this study, unpublished laser ablation data of Blake and Large, and SHRIMP data of Eldridge et al. (1993), showing relative heavy sulphur enrichment during the sulphide paragenetic sequence from mode 1 phases formed in the water column, to mode 2 phases formed in the sediment pile.*

reduction at HYC was largely mediated by thermophillic bacteria, and took place at the time of sedimentation, spatially limited by the ambient marine environment (fig.5.10). TSR probably occurred on the seafloor in the hottest part of the system and caused locally anomalous organic maturity. Partial closed-system conditions in the uppermost sediment pile caused isotopic distinction of sp1 and sp2 (fig.5.11) that is accentuated in the deposit centre because of greater bulk sulphide precipitation (fig.5.10). Progressive assimilation of evolved isotopically heavy sulphate-bearing pore fluids during deposition of the host sequence is responsible for upsection increase in the  $\delta^{34}\text{S}$  of py2 (fig.5.1e,f, fig.5.11).

## 6 CONCLUSIONS

### 6.1 *Constraints and Conclusions*

The sedimentological environment of the Barney Creek Formation host to HYC has received considerable previous attention (Logan, 1979; Logan and Williams, 1984; Jackson *et al.* 1987; Crick 1992; Bull, 1998; Davidson, 1998; Logan *et al.* 2001). This study contributes to precise understanding of the immediate sedimentological environment of the HYC deposit, confirms that mineralisation was focussed about a local depocentre, and unequivocally constrains mineralisation to syn-sedimentation timing. The important lines of evidence are:

1. textural and isotopic criteria that distinguish between sulphidic replacement and laminated sulphide clasts in mass flow breccias, which indicates that laminated sulphide clasts are primary intraclasts;
2. presence of a complete primary sulphide association in laminated intraclasts, which suggests that mineralisation was complete prior to seafloor erosion;
3. spatial coincidence of sphaleritic (dark) matrices in breccias overlying primary mineralised siltstone, which is consistent with a mineralised seafloor sediment origin for matrix sphalerite;
4. occurrence of laminated sphalerite fragments in thin (<2cm) graded beds, which indicates mineralisation took place either on the seafloor or at shallow depth (<3 metres), and that sulphidic laminae behave as partially consolidated hardgrounds;
5. spatial coincidence of thickened turbidite silty tops and the highest grade zinc-mineralised siltstone, consistent with a fundamental sedimentary basin control on focussing of mineralisation processes;
6. spatial coincidence of variations of S/C geochemistry and the intensity of mineralisation, which also suggests influence of the sedimentary environment on the mineralising system;
7. subtle change in the provenance of mass flow breccias and the geometry of ore lenses above the largest mass flow unit (I4/5), indicating some degree of basin geometry control over mineralisation;
8. absence of a consistent relationship between siltstone grainsize and sphalerite abundance, which discounts a critical element of epigenetic models that rely on small-scale permeability variations between silt and 'mud' laminae to cause sulphide lamination.

Syn-sedimentary timing of mineralisation is also indicated by geochemistry and textures documented in this study. The similarity of all ore system carbonates (ch.4) necessitates that organic oxidation responsible for anomalous organic maturity and distinctive biomarker compounds (Logan *et al.* 2001) occurred under open system conditions w.r.t CO<sub>2</sub>. In contrast, systems in which TSR occurs *in-situ* (partially closed conditions) are characterised by a 5-14‰ shift to lower carbonate δ<sup>13</sup>C values, which is not apparent at HYC. In addition, the geometry of sulphur isotope trends is inconsistent with a point-source fluid influx into the sediment pile, and instead supports concentric thermal zonation more akin to physicochemical stratification in the sedimentary environment (ch.3-5). Likewise, there are systematic changes of laminated sphalerite texture, the abundance of nodular carbonates, and the presence of pyrite 1 macroframboids in the deposit fringe on all preserved edges of the deposit. Concentric distribution about the local depocentre constrains the conditions under which mineralisation occurred to a zoned system that was centred according to sedimentology rather than to directed fluid flux through the system.

There is significant evidence that mode 1 sphalerite and pyrite did not form together *in-situ*. In addition to extreme isotopic disequilibrium between coexistent sp1 and py1 (Eldridge *et al.* 1993), the spatial distribution of sp1 and py1 is decoupled both at microscopic and macroscopic scales. Diffuse spherical pyrite framboids form in the water column, and suggest that at least part of the py1 at HYC forms in this environment. Sp1 excludes py1 when associated with contemporaneous quartz and ankerite, and consequently there is an intimate relationship between the intensity of sp1 precipitation and the inclusion of py1 in sp1. Mass balance calculations from wholerock geochemistry preclude carbonate dissolution as the cause of the anastomosing internal lamination in sp1. These complex textural, chemical and mineralogical relationships are best explained by seawater precipitation of sp1 in a marine environment amid pelagic fallout of py1 crystallites (ch.3). There is also clear isotopic and textural distinction of mode 1 and mode 2 sulphides. Mode 1 sulphides are syn-sedimentary and formed under open conditions with respect to sulphate, whereas mode 2 sulphides are diagenetic and formed under partially closed conditions with respect to sulphate. Taken together, these aspects of the deposit indicate sulphide precipitation in three different but adjacent physicochemical environments; a dysoxic seawater environment (py1); an anoxic hypersaline seawater environment (sp1); and a sub-seafloor, partially closed-system, modified metalliferous brine environment (sp2 & py2).

The conclusions suggested here have clear ramifications for ore genesis. Genetic models for HYC have largely been variations on three themes: syn-deformational replacement (Perkins and Bell, 1998); diagenetic replacement (Williams, 1978; Eldridge *et al.* 1993; Logan *et al.* 2001), and syngenetic chemical sedimentation (Large *et al.* 1998, 2001). The strong sedimentological controls and concentric spatial features identified here all support syn-sedimentary mineralisation related to a stratified water body in a local depocentre, and are extremely difficult to reconcile with post-sedimentation replacement models. Further, there are numerous less tightly constrained findings in this study that lead to interpretation of a complex and dynamic sedimentary mineralisation system in which geochemical variations are influenced both by depth-controlled elements of the sedimentary environment, and by transient temperature and chemical kinetic conditions related to batch-wise introduction of warm (100-150°C) mineralising fluid into the system at some point distant from the location of eventual fluid residence.

## 6.2 ***Implications for Exploration and Further Work***

The extensive pool of knowledge now established for SHS base metal deposits is such that only subtle differences exist between genetic models. The findings of this study suggest that basin geometry and sedimentology are critical to the formation of deposits like HYC. Exploration could benefit from greater concentration on these aspects of geology, which is anticipated to reduce the number of potential targets in a given region. The basinal brines thought responsible for SHS deposits and MVT deposits are very similar (Sangster, 1983), and it is perhaps the potential for a complete spectrum of deposits between these two types, i.e., that form in a range of redox traps including hydrocarbon accumulations (e.g. Century; Broadbent *et al.* 1998 ) that will most affect the future of zinc exploration in northern Australia, and therefore reward further investigation.

Nonetheless, this study has raised at least as many questions as it has answered. Time limitations have meant that much of what is presented here needs to be confirmed by analysis of a larger number of samples. Ultimately this is restricted by the paucity of quality drillcore through relevant parts of the deposit, and is not likely to be possible until McArthur River Mining undertake a new drilling program aimed at better defining the lateral limits of the economic reserve.

Aspects of the deposit that warrant further study are:

- Confirmation of lateral S isotope and carbonate compositional trends;
- Petrographic study of the calcite-bearing zone in DDH 99/14 to determine what distinguishes it from the rest of the deposit;
- Description of the quartz and potassium feldspar intergrowths in nodular carbonates;
- Definition of the relationships between potassic phases (illite, adularia, orthoclase, smectite, micas);
- Continued comparison of organic biomarkers between sedimentary deposit types to refine understanding of the contemporaneous marine microbiological environment.